

CARDIFF UNIVERSITY

DOCTORAL THESIS

**Four-wave mixing heterodyne
interferometric imaging of gold
nanoparticles in cells**

Author:

Panagiota
GIANNAKOPOULOU

Supervisors:

Prof. Paola BORRI
Dr. Peter WATSON

*A thesis submitted in fulfillment of the requirements
for the degree of Doctor of Philosophy*

in the

Group of Biophotonics
School of Biosciences



February 20, 2019

*Four-wave mixing heterodyne interferometric
imaging of gold nanoparticles in cells*

a dissertation presented
by
PANAGIOTA GIANNAKOPOULOU
to
the School of Biosciences of Cardiff University

in partial fulfillment of the requirements
for the degree of
DOCTOR OF PHILOSOPHY
in the subject of
Biophotonics

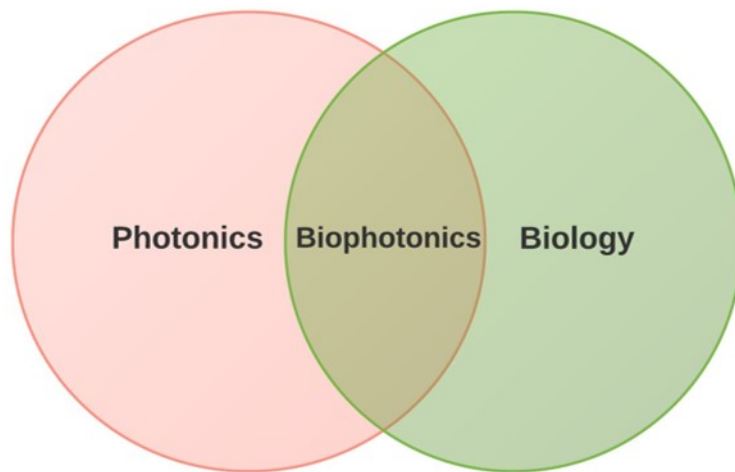
2018

Copyright © 2018 Panagiota Giannakopoulou- All rights reserved.

*'I was born not knowing, and have only had a little time to change that here to
there.'*

R. Feynmann
1918-1988

To my family



The emerging field of Biophotonics occurred by the intersection of the research fields of Photonics and Biology.

DECLARATION

I, Panagiota Giannakopoulou, declare that this thesis titled, “Four-wave mixing heterodyne interferometric imaging of gold nanoparticles in cells” and the work presented in it are my own. I confirm that:

- This work was done wholly or mainly while in candidature for a research degree at this University.
- Where any part of this thesis has previously been submitted for a degree or any other qualification at this University or any other institution, this has been clearly stated.
- Where I have consulted the published work of others, this is always clearly attributed.
- Where I have quoted from the work of others, the source is always given. With the exception of such quotations, this thesis is entirely my own work.
- I have acknowledged all main sources of help.
- Where the thesis is based on work done by myself jointly with others, I have made clear exactly what was done by others and what I have contributed myself.

Signed:

Date:

FOUR-WAVE MIXING HETERODYNE INTERFEROMETRIC IMAGING OF GOLD NANOPARTICLES IN CELLS

Doctorate Thesis

PANAGIOTA GIANNAKOPOULOU

ABSTRACT

Gold nanoparticles (NPs) are widely utilised for bio-imaging applications owing to their facile synthesis, ease of surface functionalisation and bio-conjugation, as well as bio-compatibility. However, when embedded in highly heterogeneous and fluorescing environments such as biological cells and tissues, these NPs have to be large (typically >50 nm diameter) to be distinguished optically against backgrounds via their linear absorption and scattering at the surface plasmon resonance (SPR). As a result, cell imaging protocols often adopt the use of fluorophore tags attached onto the NP, and assume that the fluorophore is a reliable reporter. These constructs are routinely used in correlative microscopy techniques such as Correlative Light Electron microscopy (CLEM) and presume that the fluorophore colocalises well with the electron dense NP. In this thesis, I present the application of our recently developed four-wave-mixing (FWM) imaging modality to investigate the spatial correlation between a gold NP and a fluorescently labeled biomolecule attached onto it on a variety of gold NPs-fluorophore conjugate constructs inside biological cells. Owing to the specific nature of the FWM process, which is a non-linear light matter interaction with the free-electron gas in the gold metal, I was able to detect single gold NPs down to 10 nm diameter background-free and with high 3D spatial resolution even in highly heterogeneous and fluorescing cellular environments. The FWM signal from gold was spatially correlated with the fluorescence signal of the fluorophore attached onto the biomolecule of the construct. Surprisingly, even covalently attached conjugate constructs exhibited low colocalization highlighting the limitations of fluorescence tagging as a means to address fundamental questions about intracellular pathways of high biological interest. This study opens new prospects to the use of FWM microscopy for imaging small gold NPs potentially even in live cells and to the understanding of the cellular uptake of bio-conjugated gold NPs.

Keywords: Gold nanoparticles, four-wave mixing, nonlinear microscopy, correlative microscopy.

ACKNOWLEDGMENTS

The realization of this project was a joint venture of experimental physicists, biologists and synthetic chemists, which I am proud to have been part of. From the beginning of this project I have had the opportunity to carry out research in the emerging fields of Biophotonics which I was dreaming since the end of my undergraduate studies in Greece.

I would like to begin by thanking my supervisor Professor Dr. Paola Borri for giving me the opportunity to work on such an interesting project. Her guidance and continuous encouragement have been catalytic throughout these years alongside her understanding and support to me especially during the writing up months. I would also like to thank my co-supervisor, Lecturer Dr. Peter Watson for shedding light to the biological part of this multi-disciplinary work and for his time preparing the last family of samples measured in this work. Special thanks also go to Professor Dr. Wolfgang Langbein; thank you Wolfgang for your scientific insight, your time and for being scientifically tough on me. I have learnt a lot from all of you.

Importantly, I would like to express my gratitude to our collaborators, Dr. Paul Moody and Dr. Johannes P. Magnusson from Cardiff School of Pharmacy and Nottingham School of Pharmacy respectively, for providing the initial samples and for our scientific discussions during the first years of my PhD.

Thanks to all members of the Group of Biophotonics and Quantum optoelectronics, Watson and Dale groups. In particular, Dr. Iestyn Pope for always being eager to assist me when I needed you in the lab, for teaching me how to use MultiCARS and for all your support during my thesis - I have really appreciated it Iestyn!-, Dr. George Zorinants for teaching me how to use the FWM set-up, the implementation of the MATLAB algorithm and our mathematical discussions, Dr. Lukas Payne for teaching me the Piranha cleaning procedure and various co-operations throughout the years. Many thanks also to Dr. Francesco Masia who although not being in the same building, he has always been helpful and kind to me and taught me the microscopy principles.

A generous thank-you to all the gang sharing the E 3.19 office. Attilio (Dr. A. Zilli now!): you are special to me for a number of reasons that I cannot even put

down to paper. Thanks for our discussions, for sharing FINON travels with me and for listening patiently to my moaning throughout the years, I know you will be a friend for life; Anika (Dr. Anika Offegenld), thanks for your support and for letting me borrow chemicals whenever I needed, but mainly thanks for being there the late evenings listening to my worries; Yisu Wang, you are a hard worker and I wish you all the best for your future. Many thanks also go to my roommate, colleague and friend Mela (Dr. Pamela Reister) who taught me tissue culture techniques, how to use the wide-field epi-fluorescence microscope and for sharing many happy moments throughout my years in Cardiff. Thanks also to Nadia Tzelepi, Dr. Josie Bradley and Dr. Marian Thomas, Bleddyn Williams, Dr. Luned Bared, Dr. Kez Cleal and Dr. Mark Robinson for sharing some really good moments in rainy Wales!

A very special thank-you part goes to the FINON family and especially to my fellow ESR colleagues with whom I am very glad to have shared some of the best experiences in my life. For over three and a half years we have shared happy moments but unfortunately some very sad as well. In no particular order: Carolina, Alberto, Marie, Alex, Diana, Michael, Amala, Xiao, Vitalis, Siyuan, I would like to thank you guys for sharing our scientific (and not only!) thoughts. I consider myself very lucky to have met all of you! My home is your home wherever life finds us! Juris, you will be missed. Acknowledgements also go to all the principal investigators of FINON (again with no particular order:): Dr. Anna Forsl w (AstraZeneca Ab), Prof. Dr. Paola Borri (Cardiff University), Prof. Dr. Annika Enejder (Chalmers University of Technology), Prof. Dr. Silvie Roke (EPFL), Dr. Sophie Basselet (Institut Fresnel) and Dr. Katrin F. Domke (Max Planck Institute for Polymer Research) for creating the FINON network which enabled my project's existence and fostered tight collaboration with each other's labs and students.

Personally, I am grateful to my dear friends, Eleni and Georgia for always being there for me, despite the distance separating us. You have proved companions for life and you are family to me!

Finally I owe my deepest thanks to my parents, Kostas, Eleni and my sisters Georgia and Ioanna, for making me the person I am today, for teaching me to work hard and fight to pursue my dreams and foremost showing me the really important things when I lose my way. I lastly owe a huge thank-you to you, Dimo for listening to my worries, making them yours till they are resolved and importantly advising me. I would not have managed writing and working at the same time without your support and patience to my stubborn character.

This work was supported by the European Commission, Research Executive Agency Marie Curie Actions 607842 FINON ITN-2013.

CONTENTS

Declaration	xi
Abstract	xiii
Acknowledgements	xv
Abbreviations	xx
List of Figures	xxix
List of Tables	xxxii
1 Introduction	1
2 Background concepts	7
2.1 Linear optical properties of AuNPs	7
2.1.1 Optical cross-sections	8
2.1.2 The dielectric function of metals	10
2.1.3 Simplifying general Mie theory	12
2.2 Elements of nonlinear optics	16
2.2.1 Introductory concepts	16
2.2.2 Nonlinear optical signals in microscopy	18
2.2.3 The principle behind our FWM technique	20
3 Set-ups and methods	23
3.1 The multi-modal imaging set-up: DIC, FWM and confocal fluorescence microscopy	23
3.1.1 Description of the FWM set-up	24
3.1.2 Confocal fluorescence implementation	28
3.1.3 FWM measurements: Alignment and settings	28
3.2 Commercial microscopes	30
3.2.1 Wide field epi-fluorescence microscope	30

3.2.2	Confocal fluorescence microscopes	32
3.3	Data Analysis	33
3.3.1	FWM Data Analysis	33
3.3.2	Correlation analysis	33
3.4	Miscellaneous materials	38
3.4.1	Miscellaneous materials used in Chemistry Laboratory	39
3.4.2	Miscellaneous materials used in Tissue Culture Laboratory	39
4	Imaging of bio-conjugated AuPsn human and mouse cells	41
4.1	Introduction	41
4.2	Measurements of AuNPs conjugated with transferrin in HeLa cells	43
4.2.1	Sample description and experimental flow	43
4.2.2	Results and discussion on Hela cells incubated with 40nm AuNP-SA:Bi-Tf(A647)	47
4.2.3	Results and discussion on HeLa cells incubated with 10nm AuNP-SA(A488):Bi-Tf(A647)	53
4.3	Measurements of polymer coated 15nm AuNPs uptaken by HeLa cells	61
4.3.1	Sample description	61
4.3.2	Results and discussion	64
4.4	Imaging 20 nm AuNPs conjugated with antibodies in 3T3-L1 cells	72
4.4.1	Sample description	72
4.4.2	Results and discussion	74
4.5	Summary	89
5	Study of AuNP's diffusion in Agarose matrix gel	93
5.1	Motivation	93
5.2	Sample description	96
5.3	Experimental details	97
5.4	Data Analysis	98
5.5	Results and discussion	101
6	Summary and Outlook	109
A	Appendix A	113
A.1	Investigation of thermoresponsive PC-50 nm AuNPs via absorption spectroscopy	113
A.1.1	Introduction	113
A.1.2	Samples	114
A.1.3	Temperature dependent spectroscopy measurements	115

A.1.4 Summary	121
B Appendix B	123
B.1 Optical resolution of FWM imaging	123
C Appendix C	127
C.1 Competition of 15nm AuNP-PC-Tf(A488) with excess Tf	127
D Appendix D	129
D.1 Preliminary experiments on FWM imaging of 20nm AuNPs in live 3T3-L1 cells	129
Bibliography	i
Publications, Oral and Poster presentations	xvii
Curriculum Vitae	xix

ABBREVIATIONS

A488	AlexaFluor488
A647	AlexaFluor647
AOM	Acousto-Optic Modulators
AS	Agarose-in-water Aolution
Au	Gold
AuNPs	Gold Nanoparticles
BF	Bright Field
CARS	Coherent Anti-Stokes Raman Scattering
CLEM	Correlative Light Electron Microscopy
DAPI	4',6-diamidino-2-phenylindole
DF	Dark field
DIC	Differential Interference Contrast
FBS	Fetal Bovine Serum
FCS	Fluorescence Correlation Spectroscopy
FRAP	Fluorescence Recovery After Photobleaching
FWHM	Full Width at Half Maximum
FWM	Four-Wave Mixing
GVD	Group Velocity Dispersion
HEPES	4-(2-Hydroxyethyl)-1-piperazineethanesulfonic acid

JACoP	Just Another Colocalization Plugin
LCST	Lower Critical Solution Temperature
LSPR	Localised Surface Plasmon Resonance
MPC	2-Methacryloyloxyethyl phosphorylcholine
NA	Numerical Aperture
NLO	Non Linear Optical
NP	Nanoparticle
NPBS	Non-polarising Beam Splitter
OPO	Optical parametric Oscillator
PBS	Phosphate Buffered Saline
PC	Pearson coefficient
PEG	Polyethylene glycol
PFA	Paraformaldehyde
PI	Physik Instrumente GmbH & Co
PNIPAm	Poly(N-isopropylacrylamide)
PSF	Point-Spread Function
PTI	Photothermal Imaging
RME	Receptor mediated endocytosis
ROI	Region of Interest
sCMOS	Scientific CMOS camera
SEM	Scanning Electron Microscopy
SFG	Sum Frequency Generation
SHG	Second Harmonic Generation
SPT	Single Particle Tracking
STED	Stimulated Emission Depletion

STORM	Stochastic Optical Reconstruction Microscopy
TEM	Transmission Electron Microscopy
Tf	Transferrin
TfR	Transferrin Receptor
THG	Third Harmonic Generation
Ti:Sa	Titanium Sapphire
TIRF	Total Internal Reflection Fluorescence
UCST	Upper Critical Solution Temperature

LIST OF FIGURES

1.1	Schematic presentation of the two AuNP surface structures commonly employed in delivery applications.	2
1.2	Example of far-field optical imaging of mitochondria in live cells without the use of any labels from Ref.[41].	4
2.1	The Lycurgus Cup in reflected and transmitted light as displayed in the British Museum of London.	8
2.2	Plot of the real and imaginary dielectric constant data for gold) . . .	11
2.3	Schematic illustration of the localised surface plasmon resonance (LSPR) in AuNPs.	13
2.4	Tuning of the relative contribution of surface plasmon absorption and scattering by changing the particle size.	14
2.5	Absorbance spectrum of nominally spherical AuNPs of 80 nm diameter in aqueous solution (BBI Solutions) shown alongside the one of AuNRs of 25 nm diameter with an aspect ratio x/y axis of 2.3 (Nanopartz)also in aqueous environment.	15
2.6	Illustration of nonlinear optical (NLO) modalities employed for the visualization of nanomaterials.	17
2.7	The P-E relation for (a) a linear dielectric medium, and (b) a nonlinear medium	18
3.1	Photographs of the microscope body and the multi-modal imaging technique optical components during operation.	24
3.2	Sketch of the four-wave mixing microscopy set-up in heterodyne detection	29
3.3	Example of FWM imaging and pump-probe delay dependence on the reference sample Au film.	31
3.4	The wide-field epi-fluorescence microscope	32
3.5	Example of confocal fluorescence background subtraction	35
3.6	Evaluation of the re-registration algorithm	36

4.1	The sequential labelling protocol	44
4.2	Sketch of the 40nm AuNP-SA:Bi-Tf(A647) construct bound to TfR on the cell membrane	46
4.3	Experimental flowgram for the measurements of AuNPs conjugated with transferrin in HeLa cells	48
4.4	Example of fixed HeLa cells cultured on a gridded coverslip imaged via DIC on a tile mode on the Zeiss LSM 880 confocal fluorescence microscope.	48
4.5	Proof of FWM signal for the 40nm AuNP-SA:Bi-Tf-A647 sample . . .	50
4.6	Results: 40nm AuNP-SA:Bi-Tf(A647): Cellular DIC, FWM, reflection and fluorescence 3D imaging.	51
4.7	Results: 40nm AuNP-SA:Bi-Tf(A647): Cellular DIC, FWM, reflection and fluorescence 3D imaging.	52
4.8	Widefield fluorescence imaging on the 10nm AuNP-A488-SA:Bi-Tf-A647 sample	56
4.9	ROI Overview 1: Retrieval of the fluorescently imaged region on the multi-modal microscope via DIC imaging	56
4.10	ROI Overview 2: Retrieval of the fluorescently imaged region on the multi-modal microscope via DIC imaging	57
4.11	Results 1: 10nm AuNP-SA(A488):Bi-Tf(A647): Comparison of FWM imaging with widefield fluorescence	58
4.12	Results 2: 10nm AuNP-SA(A488):Bi-Tf(A647): Comparison of FWM imaging with widefield fluorescence	59
4.13	Results 3: 10nm AuNP-SA(A488):Bi-Tf(A647): Comparison of FWM imaging with widefield fluorescence	60
4.14	Proof of FWM signal for the 10nm AuNP-A488-SA:Bi-Tf-A647 sample	61
4.15	The 15nm AuNP-PC-Tf(A488) construct.	62
4.16	Results of 15nm AuNP-PC-Tf(A488): Cellular DIC overview, FWM, reflection and fluorescence 3D imaging.	66
4.17	Weak fluorescent signal coming from the 15nm AuNP-PC-Tf(A488) .	67
4.18	Results of 15nm AuNP-PC-Tf(A488) with DAPI nuclear counterstain: Cellular DIC overview, FWM, reflection and fluorescence 3D imaging.	69
4.19	Examples of confocal fluorescence images of the 15nm AuNP-PC-Tf(A488) with DAPI nuclear counterstain.	70
4.20	Proof of FWM signal for the 15nm AuNP-PC-Tf(A488) sample . . .	71

4.21	Co-polarised FWM field amplitude for a 15nm AuNP-PC-Tf(A488) at the focus center versus pump-probe delay time τ for a pump (probe) power measured before the microscope entrance 31 μ W (15.5 μ W).	71
4.22	Schematic Sample Description	73
4.23	Sample 1: False colour overlay image of the reflection and FWM channel showing lack of receptor-mediated endocytosis.	78
4.24	Sample 1 -Example 1: Cellular DIC, FWM, reflection and fluorescence 3D imaging.	79
4.25	Sample 1 - Example 2: Cellular DIC, FWM, reflection and fluorescence 3D imaging.	80
4.26	Comparison of fluorescence images acquired in our home-built microscopy set-up with the ones acquired on the commercial wide-field epi fluorescence microscope.	81
4.27	Sample 2 - Example 1: Cellular DIC, FWM, reflection and fluorescence 3D imaging.	82
4.28	Sample 2- Example 2: Cellular DIC, FWM, reflection and fluorescence 3D imaging.	83
4.29	Sample 3- Example 1: Cellular DIC, FWM, reflection and fluorescence 3D imaging.	84
4.30	Sample 3- Example 1 overlay: Cellular FWM, reflection and fluorescence 3D imaging.	85
4.31	Sample 3-Example 2: Cellular DIC, FWM, reflection and fluorescence 3D imaging.	86
4.32	Sample 3-Example 3: Cellular DIC, FWM, reflection and fluorescence 3D imaging.	87
4.33	Two cell regions of Sample 3 imaged on the commercially available wide-field epi fluorescence microscope for A647 and A568 channels.	88
4.34	Proof of FWM signal via raster scan imaging with negative pump-probe delay	88
4.35	Co-polarized FWM field amplitude (V) for a 20 nm diameter AuNP at the focus center versus pump-probe delay time.	89
5.1	Nanometric localisation using optical vortices	95
5.2	Sample Layout of 50nm AuNPs in AS / DIC images at the interface and in the gel's volume	97
5.3	Experimental FWM measurements on 50nm AuNP rotating in 5% w/v AS.	99
5.4	Axial dependence of the Φ_{FWM}^+ retrieved from rapid 3D scan	100

5.5	Montage of A_{2r}^+ and A_{FWM}^+ channels over $z = 7.5 \mu\text{m}$ at the 50 nm AuNPs in 5 % AS sample	102
5.6	FWM imaging of rotational motion of a single 50 nm AuNP in % AS	103
5.7	Hypothesis scetch: AuNP rotating while being enclosed or jumping between the agar's network pockets	103
5.8	Histogram of the derived AuNP's axial position alongside the corresponding amplitude co-circularly polarised field	104
5.9	Histogram of the z coordinates of multiple <i>tracing</i> scans and fitted lines for each one of the center bin peaks alongside a cumulative fit for all the center bins of the above histogram.	105
5.10	Time traces of the amplitude and phase of co-circularly polarised FWM signal	106
5.11	Autocorrelated data of the axial position of a single AuNP in AS fitted with anomalous diffusion functions	107
5.12	MSD analysis of axial position time traces acquired at 0.2 ms time per point	108
A.1	Scheme of the change of the conformational structure of the polymer chain on the AuNP's surface. In our case the external stimulus of the PC-AuNPs under investigation is the temperature. [FIGURE REPRODUCED WITH PERMISSION FROM REF [141].]	114
A.2	Vis-NIR absorption spectra of the firstly received 50 nm polymer coated AuNP sample, JPM 400, from 20 °C to 70 °C.	117
A.3	Maximum absorbed intensity at the LSPR peak of 531 nm versus temperature. The transition temperature is found to occur at 50 °C. .	117
A.4	Vis-NIR absorption spectra of the firstly received 50 nm polymer coated AuNP sample, JPM 400, from 30 °C to 70 °C one day after the first cycle of heating shown on Fig. A.2.	118
A.5	Vis-NIR absorption spectra of JPM 400 at temperatures between 35 °C and 55 °C with 5 minutes intervals in each temperature.	118
A.6	Multiple Vis-NIR absorption spectra of JPM 400 sample at each of the shown temperatures for longer timescale (indicated at the bottom).	119
A.7	Control measurement. Vis-NIR absorption spectra of JPM 400 for 45 minutes at constant temperature (room temperature). The behaviour of the investigated solution, i.e. PBS, was found to be stable over time.	119
A.8	Vis-NIR absorption spectra of sample JPM 487 from 20 °C to 65 °C.	120
A.9	Vis-NIR absorption spectra of sample JPM 491 from 20 °C to 65 °C.	120
B.1	Experimental determination of the lateral resolution of FWM	124

B.2	Experimental determination of the axial resolution of FWM	124
B.3	Experimental determination of both lateral and axial resolution of FWM when imaging AuNPs in cells	125
C.1	0 $\mu\text{g}/\text{ml}$ non-fluorescent Tf-Bi. 10 μm scalebar.	128
C.2	50 $\mu\text{g}/\text{ml}$ non-fluorescent Tf-Bi. 10 μm scalebar.	128
D.1	Preliminary experimental results on simultaneous FWM-fluorescence of 20nm AuNPs in live 3T3-L1 cells.	131
D.2	Montage of <i>fast scans</i> on simultaneous FWM-fluorescence of 20nm AuNPs in live 3T3-L1 cells.	132

LIST OF TABLES

3.1	The combined excitation and emission Chroma filter-sets of the inverted Olympus IX73 used in this thesis. For each one the center wavelength alongside its FWHM is indicated.	31
4.1	Bioconjugated fluorescently labelled AuNPs used in this study. SA: streptavidin, Bi: biotin, PC: polymer coat, Tf: transferrin, Ab: antibody, A488: AlexaFluor488, A647: AlexaFluor647, cb: covalent bond, ad: adsorbed	42
4.2	Samples' specifications according the antibody and labelling bio-conjugation achieved.	73
A.1	Summary of thermoresponsive PC-AuNPs measured via absorption microscopy manufactured by our collaborators at Nottingham University.	115

1

INTRODUCTION

The application of nanotechnology¹ in biomedical sciences has vastly changed the landscape of drug delivery methods as well as broadening the horizons of bioimaging techniques over recent years. Metallic nanoparticles (NPs), and in particular the gold NPs, are amongst the most promising nanomaterials in nanomedicine. In 1971, W.P. Faulk and G.M. Taylor published –possibly– the first biomedical application of metal nanoparticles as they described a technique to conjugate antibodies with colloidal gold for imaging of Salmonella surface antigens via electron microscopy [2]. Since then, there have been tremendous research advances dealing with the applications of functionalised (or not) gold NPs in nanomedicine² [3], [4], [5], [6], [7], biochemistry [8], [9], and bioimaging [10], [11], [12], [13].

Unlike other nanostructures, such as quantum dots, carbon nanotubes or polymeric NPs, gold nanoparticles (AuNPs) exhibit unique optical properties derived from the localised surface plasmon resonance (LSPR). This resonance originates from the collective oscillation of the conduction band electrons and for spherical AuNPs lies in the visible region of the spectrum and can be easily tuned by their shape and size³ [14], [15]. As a result, AuNPs exhibit strong optical absorption and scattering cross-sections at the LSPR which render them capable platforms for optical labeling and therapeutic agents in biomedical applications [16], [9], [17] [6],

¹The term of nanotechnology includes the Greek word *nanos* –meaning dwarf– and refers to “the engineering and manufacturing of materials at the atomic and molecular scale”[1].

²referring mainly to photothermal and gene therapy research fields.

³LSPR is also a function of the surrounding’s dielectric function, which for this sentence is considered constant.

[7], [5], [18], [19], [13].

AuNPs are ideal optical labels and attractive ‘vehicles’ in cellular environments for delivery applications as they are proven to be chemically inert and low-toxic, hence biocompatible. They can be easily fabricated in a wide range of sizes (usually 1-120 nm) and shapes (spherical, rods, nanoshells etc.) in a controlled and reproducible way [20], [21], [22], [23]. There are numerous ways to synthesize gold NPs with the most known to be the citrate reduction method firstly introduced in 1951 by Turkevich et al. [24], [25]. In addition to their facile synthesis, AuNPs can be functionalised with a variety of molecules, such as ligands, biomolecules, surfactants, polymers etc. [17]. Figure 1.1, reproduced by the review article of Rana et al. [5], illustrates the most commonly employed surface functionalisation practices depending on the intended delivery application. A common way of attaching oligonucleotides, peptides and PEGs (polyethylene glycol) on the NP’s surface is with the aid of thiolates using the strong Au-S bond. For a detailed review on functionalisation methods of NPs, which is out of the scope of this work, one can refer to Ref. [5], [7], [6].

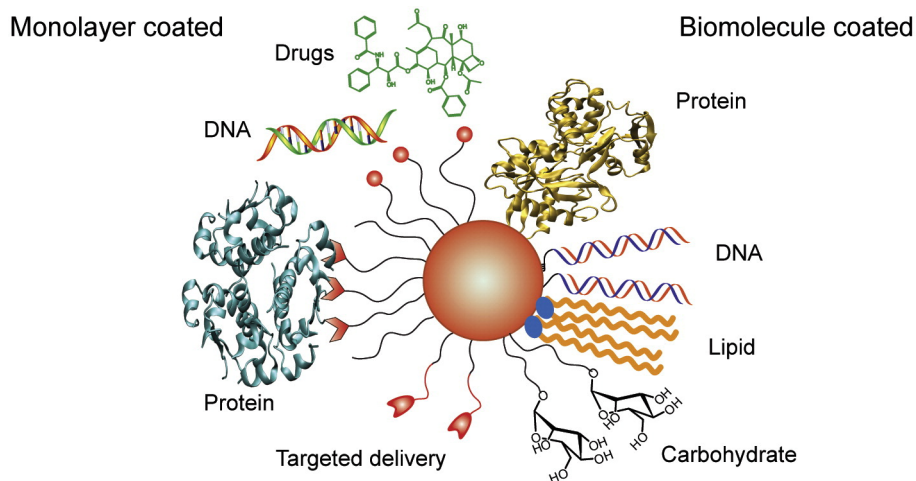


Figure 1.1: Schematic presentation of the two AuNP surface structures commonly employed in delivery applications. [FIGURE AND CAPTION REPRODUCED WITH PERMISSION FROM REF. [5]]

Bioimaging is generally dominated by fluorescence-based techniques which require the labeling of cellular structures with fluorescent molecules. However, the use of organic fluorophores suffer from a number of drawbacks including photobleaching, photoblinking, non-specific binding and in many cases perturbation of the biological system as well as phototoxicity. Up to date there is a wide range of fluorescence techniques (far-field and near-field) which can achieve high chemical specificity and sensitivity at single molecule level. Some of those are: confocal microscopy with/without stimulated emission depletion (STED) [26], [27], stochastic

optical reconstruction microscopy (STORM) [28], photoactivated localisation microscopy (PALM) [29], and in the case of near-field fluorescence techniques [30], total internal reflection fluorescence microscopy (TIRF) [31]. Despite the high spatial resolution and/or single molecule localisation achievements of the mentioned techniques which can reach the order of tens of nm, they are eventually limited by the inherent nature of the fluorescence itself.

On the contrary AuNPs –and metallic NPs in general– own superior photostability and their LSPR can be further exploited to image with high spatial resolution and probe the region around the NP’s vicinity, via the so-called local field enhancement effect. Thus, they are among the most promising non-fluorescent optical imaging agents. Both linear and nonlinear microscopy techniques have been developed for the imaging of AuNPs in cellular environments over the past years. As mentioned earlier, in the linear regime the LSPR results in strong optical properties, absorption and scattering, of metallic NPs. In fact, the extinction coefficients are 5-6 orders of magnitude larger than those of organic dyes [17], [19], [32]. For large AuNPs (diameter > 40 nm) the scattering process dominates over absorption. Conversely, absorption dominates over scattering for AuNPs with diameter below 20 nm [19]. This difference is crucial to the type of optical microscopy associated with the choice of size and type of metallic NPs used for bio-imaging. Among the most straightforward light scattering imaging methods is darkfield (DF) which simply detects light scattered by the object of interest against a dark background, owing to the use of a high-angle illumination which cannot enter the collection optics unless it is scattered [33], [34]. The research group of El-Sayed et al. has shown imaging of gold NPs in cancer cells via dark-field microscopy [13] even in living cells [35]. However, in order to achieve image selectivity to AuNPs, elaborated cleaning methods of the sample are required to avoid background from additional scattering since any refractive index heterogeneity (e.g. debris) causes scattering. In addition to having strong scattering properties, AuNPs are capable of converting the absorbed light (near UV to NIR) to heat via non radiative processes [14]. This property is the central idea of photothermal interference contrast (PIC) microscopy and extensively of photothermal therapy [36], [37]. PIC is actually a variation of the differential interference contrast (DIC) method where the temperature increase of the NP and its surrounding upon illumination leads to a modification of the local refractive index around the NP which is then probed by an off-resonant laser beam [38], [39], [40]. Although this technique is sensitive and capable of detecting AuNPs down to 5 nm diameter, it lacks selectivity also as it is challenging to discriminate cellular background provoked by endogenous absorption (for example in mitochondria, Figure 1.2) even in the absence of AuNPs [41], [42].

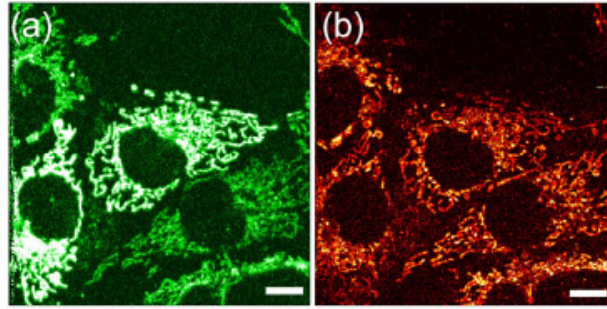


Figure 1.2: Example of label-free optical imaging of mitochondria in live cells via a photothermal technique called (Light Induced Scattering Around a NanoAbsorber) LISNA [39], as demonstrated in Lasne et al. [41].

(a). Fluorescence (Mitotracker Deep Red) and (b) LISNA images of COS-7 cells. The scale bar represents 10 μm . FIGURE AND CAPTION REPRODUCED WITH PERMISSION FROM REF. [41].

Alternatively to the methods mentioned above, and with the aim to develop a background-free imaging modality, the strong intrinsic nonlinear optical (NLO) signals of AuNPs alongside the recent developments in NLO microscopy, provide an attractive tool for imaging these non-fluorescent nanoparticles, based on their intrinsic nonlinearity, without the need to add a fluorophore tag, with inherent 3D spatial resolution and high optical contrast in biological samples [43]. Multiphoton microscopy techniques capable to image non-fluorescent AuNPs include second harmonic generation (SHG), third harmonic generation (THG), four-wave mixing (FWM) and pump-probe techniques which exploit the higher orders nonlinearities imposed to a medium by high-intensity light sources such as lasers. Extensive research has been conducted over the last decade in NLO response of various gold NPs both outside and inside of biological environments with most of the references to be included in the recent reviews of E.C. Dreaden et al. [16] and E. Boisselier et al. [17] for further reading.

In this thesis, a novel phase-sensitive degenerate FWM microscopy technique in heterodyne detection, built in-house (including acquisition and data analysis software) at Cardiff School of Biosciences [44], [45], [46], has been used to image functionalised AuNPs with various diameter sizes (from 10 nm to 40 nm) internalised in cells background-free. In recent years, FWM microscopy, a coherent third-order optical imaging technique, has opened new prospects as a tool for the non-invasive investigation and further analysis of several biological procedures. As a general microscopy implementation, FWM imaging has naturally evolved from the coherent anti-stokes Raman scattering (CARS) microscopy; however, it is by no means limited to the measurement of vibrational modes. The FWM signal is in principle sensitive to both electronic and vibrational properties of the material. Although,

FWM imaging does not offer the high resolution of an electron microscope, it can achieve a spatial resolution of beyond one photon diffraction, less than 200 nm, at power levels that cannot harm the biological functions of the specimens. Notably, the FWM technique developed in our laboratory is triply resonant to the LSPR, and operates at power levels (10 – 100 μ W) typically one to two orders of magnitude lower than CARS, SHG or THG techniques.

Driven by the recent achievements of our collaborators [47], where fluorescently labelled AuNPs conjugated to membrane specific ligands were utilised as platforms to regulate site specific tracking of components to subcellular organelles (i.e. lysosomes), in this thesis I studied similar nanostructures via correlative FWM-fluorescence imaging.

In recent years, fluorescently labelled NPs are routinely employed as reliable tools for drug delivery and intracellular imaging studies and are also extensively used in correlative microscopy methods such as Correlative Light Electron Microscopy (CLEM) where it is presumed that the fluorescent label is colocalised with the electron dense gold core. Only recently, a scientific report by Miles et al. [48] demonstrated lack of colocalisation between fluorescent labels and the AuNPs for a commercially available product (i.e. streptavidin labelled with Alexa 633 attached onto 10 nm diameter gold NPs). To do do, they combined single molecule fluorescence microscopy with optical detection of the scattering from the 10 nm AuNPs on an interferometric cross-polarisation microscope (ICPM) [49], [50]. Far from being a trivial question, there are many reasons for a fluorophore label to fail to colocalise with a gold NP, ranging from physical instability of the nanoparticle-fluorophore construct, through to the fact that several studies indicate quenching of the fluorophore when it resides in close proximity to the metallic NP [51], [52], [53].

In this work, the aim is to shed new light to the degree of spatial colocalisation between AuNPs located by FWM imaging and the position of fluorescently labelled bio-molecules attached onto the NPs, based on their fluorescence signal. We present a detailed study of correlative FWM-fluorescence imaging of a variety of AuNPs (40 nm, 15 nm and 10 nm diameter) fluorescently labelled bio-conjugated constructs internalized in cells using four different strategies, inspired by examples and common practice in the literature. Three types of the constructs entered cervical cancer cells (HeLa type) via clathrin-mediated endocytosis using the ligand transferrin (Tf) which was fluorescently labelled, while one construct contained a fluorescently labelled antibody which entered 3T3-L1 type of cells via unspecific uptake. All cells were imaged fixed at different time points following cell entry and the preparation protocols and results of each sample-category are discussed separately.

Thesis Outline

This thesis is organised as follows:

Chapter 2 provides theoretical background concepts regarding the linear and nonlinear interaction of gold NPs with light which are necessary for the description of the FWM technique, and the discussion of the results obtained during this research study. The experimental set-ups and the analysis' rationale used in this work are described in **Chapter 3** along with some standard sample preparation methods used across this work. **Chapter 4** encompasses the core results on correlative FWM and confocal fluorescence imaging measurements of various bio-conjugated AuNPs in fixed cancer cells and is divided in sub-chapters where each sample/construct is analysed separately. In addition, **Chapter 5** demonstrates FWM imaging and tracking of a freely rotating single AuNP in an agarose gel network alongside a primary study of its axial diffusion, as a proof of principle investigation of single particle tracking analysis via FWM. Finally, **Chapter 6** summarises the main findings of this thesis and provides an outlook for future applications.

2

BACKGROUND CONCEPTS

This chapters aims at providing an introduction to the physical concepts needed to understand the optical properties of AuNPs. Discussed are firstly the linear optical response of AuNPs and secondly the concepts on nonlinear optics and the principles of the resonant four-wave mixing microscopy technique mainly used in this work.

2.1 Linear optical properties of AuNPs

Noble metallic NPs have fascinated men since antiquity who had observed the unique colour of gold when used in microscopic dimensions and had exploited this property in a number of artistic endeavors. Possibly, one of the first examples of artistic implementation of the optical properties of nano-sized metallic NPs, is the Roman Lycurgus Cup dated back to 4th century AD depicting the legend of King Lycurgus. The cup is vastly known for the different colour that shows depending on the direction of illuminating light; an effect attributed to glass staining methods with a mixture of colloidal gold and silver NPs resulting in the dichroic effect shown in Figure 2.1 [54].

Since then, tremendous advances have been carried out around the understanding and the applications of the optical properties of metallic NPs and particularly gold NPs. A systematic scientific approach in this field is firstly accredited to M. Faraday in 1857, however the full mathematical description was later given by G. Mie in 1908 who solved the Maxwell's equations with the appropriate boundary conditions for



Figure 2.1: The Lycurgus Cup contains tiny portions of gold and silver NPs of about 50 nm diameter size and therefore exhibits dichroism. On the left the cup is shown in reflected light and on the right in transmitted. It is displayed at the Department of Prehistory and Europe in the British Museum of London. [55]

nanospheres and established the *Mie theory*.

This section reviews the foundations of the linear optical properties of spherical AuNPs and is based on the following references [56], [57],[14], [58], [59].

2.1.1 Optical cross-sections

In general, the linear optical interaction with NPs can be described by their *absorption* and *scattering* cross-sections which depend on the nano-object's morphology (size and shape), its material's composition as well as on the surrounding medium.

Let's start by considering the simplest illumination scheme where we have a nanosphere (in our case will always be composed by gold) embedded in a homogeneous medium illuminated by a plane light wave. What we expect to happen is a portion of the illuminating energy to be re-radiated (scattering) and another part to be transformed to another energy source, for example heat (absorption) resulting in the total *extinction* of the illuminated light to be the sum of *scattering* and *absorption*.

In order to mathematically describe and solve the problem of scattering and absorption of light by NPs, one needs to solve Maxwell's equation taking into account the boundary conditions of the problem. This was firstly shown by G. Mie (1908) for spherical particles – *Mie theory* – and has found wide applicability in explaining experimental results due to its simplicity till nowadays. In addition, *Gans theory* [60] (1912) expands to describing the optical response of spheroidal NPs, like nanorods in the dipole approximation (i.e. much smaller than the wavelength of light) [61], whilst a popular computational modeling alternative technique is the *discrete dipole*

approximation (DDA) which can provide solutions for particles of arbitrary shape.

The optical cross-sections ¹ can be derived by Mie theory for a spherical particle with dielectric function ϵ_p and are important quantities for single particle spectroscopy and microscopy measurements. They are defined as effective geometrical areas of light-NP interaction which relate the incident light intensity to the extincted, scattered and absorbed power and are given by Eq. 2.1.1. [59], [56], [62]

$$\sigma_{\text{ext}} = \frac{P_{\text{ext}}}{I_{\text{inc}}}; \sigma_{\text{sca}} = \frac{P_{\text{sca}}}{I_{\text{inc}}}; \sigma_{\text{abs}} = \frac{P_{\text{abs}}}{I_{\text{inc}}} \quad (2.1.1)$$

where I_{inc} is the incident intensity, and P_{ext} the power loss in the forward direction, induced by both absorption and scattering. As also mentioned above, the extinction cross section is the sum of the scattering and absorption ones.

$$\sigma_{\text{abs}} = \sigma_{\text{ext}} - \sigma_{\text{sca}} \quad (2.1.2)$$

The general expressions for the scattering and extinction cross-sections from Mie theory are given by Bohren and Huffman [59] as below

$$\sigma_{\text{sca}} = \frac{2\pi}{k^2} \sum_{n=1}^{\infty} (2n+1) \{|a_n|^2 + |b_n|^2\} \quad (2.1.3)$$

$$\sigma_{\text{ext}} = \frac{2\pi}{k^2} \Re(a_n + b_n) \quad (2.1.4)$$

The factors a_n and b_n of Eq. 2.1.3 and 2.1.4 are given by [59]

$$a_n = \frac{\psi'_n(mx)\psi_n(x) - m\psi_n(mx)\psi'_n(x)}{\psi'_n(mx)\zeta_n(x) - m\psi_n(mx)\zeta'_n(x)} \quad (2.1.5)$$

$$b_n = \frac{m\psi'_n(mx)\psi_n(x) - \psi_n(mx)\psi'_n(x)}{m\psi'_n(mx)\zeta_n(x) - \psi_n(mx)\zeta'_n(x)} \quad (2.1.6)$$

where ψ_n and ζ_n are n^{th} order Ricatti-Bessel functions, $x = kR$ (with R the particle's radius and k the wave number of light in the medium) is a size parameter and $m = n/n_m$ a parameter relating the particle's refractive index n with the medium's refractive index n_m . Notably, the terms of Eq. 2.1.3 and 2.1.4 correspond to dipole ($n = 1$), quadrupole ($n = 2$), hexapole ($n = 3$) etc contributions.

An exact solution of the optical cross-sections for the case of small spherical

¹The term cross section is generally used in physics in order to describe the probability of particle-particle interactions.

AuNPs will be discussed after the following section which covers the dielectric function of metals and especially gold.

2.1.2 The dielectric function of metals

Gold (Au)² belongs to the 11th group of the periodic table along with other metals such as copper (Cu) and silver (Ag). The elements of this group have their d-bands filled while their outer s-bands are under-filled resulting in an sp-hybridised band which is filled up to the Fermi energy, E_F . The electrons in this band can be treated as a free electron gas relative to the ions of the lattice which act as scattering centers. One of the simplest realistic models which describes the response of metallic NPs when exposed to an external electromagnetic field is the classical Drude-Lorentz which was later corrected by Sommerfeld and is known as *Drude-Sommerfeld* model.

In this classical description we start with an electromagnetic wave with a corresponding electric field $\mathbf{E}(\mathbf{r}, \omega)$ that interacts with a metallic NP. The free electron cloud of the metal will start oscillating and create a polarization $\mathbf{P}(\mathbf{r}, \omega)$ which expresses the degree of displacement of the electrons relative to the core lattice. In turn a depolarising field described by the electric displacement $\mathbf{D}(\mathbf{r}, \omega)$ is linked to the excitation field by the relationship:

$$\mathbf{D}(\mathbf{r}, \omega) = \varepsilon_0 \varepsilon(\omega) \mathbf{E}(\mathbf{r}, \omega) \quad (2.1.7)$$

where $\varepsilon(\omega)$ is the complex dielectric function of the metal and depicts its response to the electromagnetic excitation and ε_0 is the permittivity of free space.

The *Drude* model determines the dielectric function $\varepsilon(\omega)$ by solving a damping oscillator model for a single electron and multiplying the result by the number of electrons per unit volume [58][14]:

$$\varepsilon(\omega) = 1 - \frac{\omega_p^2}{\omega^2 + i\gamma_b \omega} \quad (2.1.8)$$

where $\omega_p = \sqrt{n_e e^2 / \varepsilon_0 m_e}$ is the *plasma frequency*, n_e is the electron density, m_e is the effective electron mass accounting for the coupling of the free electrons to the ion core and γ_b is the bulk damping constant. The latter one equals to $\gamma_b = u_F / l$ where u_F is the Fermi velocity and l the mean free path of electrons.

For metallic NPs with a diameter less than the mean free path of their bulk material the overall conductivity and its dielectric function need to be corrected and take into account electron-surface scattering which is done by modifying the the damping constant γ_b (a more detailed overview is given in Ref. [14]).

²[Xe] 4f¹⁴5d¹⁰6s¹

Overall, this model provides accurate results for infrared frequencies but it fails in the visible regime as it does not take into consideration interband transitions [62] [58] [14].

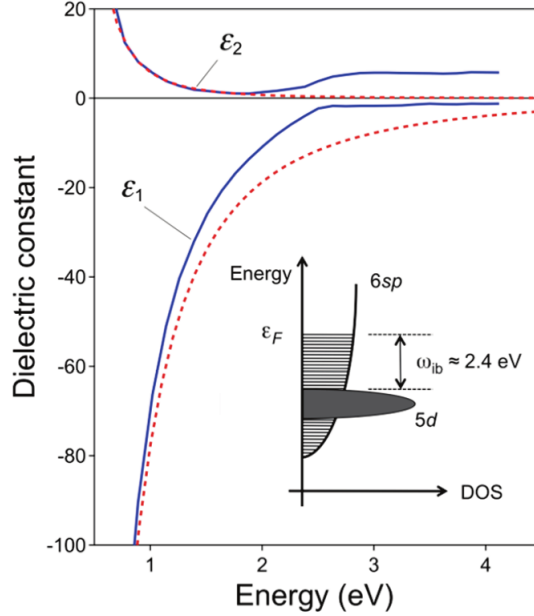


Figure 2.2: Plot of the real (ϵ_1) and imaginary (ϵ_2) dielectric constant for gold as measured from Ref [63] (blue solid line). The dashed red lines show a fit to the data using the Drude model (eq. 2.1.8). The insert shows a cartoon of the band structure of gold, where ϵ_F is the energy of the Fermi level, and ω_{ib} is the frequency of the gold interband transitions.[FIGURE AND CAPTION REPRODUCED WITH PERMISSION FROM REF. [14]]

In this case, a frequency dependent extra term $\epsilon_{ib}(\omega)$ has to be added in equation 2.1.8 correcting for the interband transitions.

$$\epsilon(\omega) = \epsilon_{ib}(\omega) + 1 - \frac{\omega_p^2}{\omega^2 + i\gamma_b\omega} \quad (2.1.9)$$

Therefore, for metals the complex dielectric function can be expressed as:

$$\epsilon(\omega) = \epsilon_1(\omega) + i\epsilon_2(\omega) \quad (2.1.10)$$

and for non magnetic materials ($\mu = 1$) is related to the complex refractive index via the relation $\epsilon(\omega) = \tilde{n}^2 = (n + ik)^2$.

The complex component is related to damping and is significantly increased by the presence of interband transitions in energies above 2.4 eV (around 516 nm) for gold as shown in the figure's 2.2 insert [63][14]. In Figure 2.2 which is taken from Ref [14], plots of the real and imaginary part of the dielectric function of bulk gold are presented alongside a fit for the low frequencies in order to compare with the Drude model based on equation 2.1.8. The data which were used for these plots are taken

from experiments done in the 70's and specifically by Johnson and Christy in 1972 [63] who measured the dielectric constants of copper, silver and gold as functions of photon energy.

The dielectric function can also be expressed in terms of electric susceptibility via the formula:

$$\varepsilon(\omega) = 1 + \chi_d(\omega) + \chi_{ib}(\omega) \quad (2.1.11)$$

where $\chi_d(\omega)$ stands for the free electron model susceptibility and $\chi_{ib}(\omega)$ stands for the complex interband susceptibility.

2.1.3 Simplifying general Mie theory

Although there are exact solutions given by general Mie theory for the cross-sections of spherical particles, simpler formulas can be obtained for particles of radius R much smaller than the wavelength λ of light they interact with [56],[59]. This approximation is known as *Rayleigh limit* and requires:

$$2\pi R \ll \lambda \quad (2.1.12)$$

In this regime, the NP is treated as an ideal dipole in a uniform external electric field \mathbf{E}_0 with an induced dipole moment $\mathbf{p} = \varepsilon_m \alpha \mathbf{E}_0$. The polarisability α is then given by [15] [64] [62]

$$\alpha = 4\pi\varepsilon_0 R^3 \frac{\varepsilon_p - \varepsilon_m}{\varepsilon_p + 2\varepsilon_m} \quad (2.1.13)$$

also known as *Claussius-Mossotti* homogenization. In Eq. 2.1.13 ε_p defines the dielectric function inside the particle and ε_m the dielectric function of the surrounding medium.

Considering now the external electromagnetic field to be a plane wave, the exact solutions of the optical cross-sections are presented below [56],[59].

$$\sigma_{\text{abs}} = k\Im(\alpha) = 4\pi k R^3 \Im\left(\frac{\varepsilon_p - \varepsilon_m}{\varepsilon_p + 2\varepsilon_m}\right) \quad (2.1.14)$$

$$\sigma_{\text{sca}} = \frac{k^4}{6\pi} |\alpha|^2 = 8\pi k^4 R^6 \left| \frac{\varepsilon_p - \varepsilon_m}{\varepsilon_p + 2\varepsilon_m} \right|^2 \quad (2.1.15)$$

Localised surface plasmon resonance (LSPR)

As can easily be predicted by Eq. 2.1.14 and 2.1.15 maximum extinction occurs

when their denominator is minimised, i.e. $\varepsilon_p = -2\varepsilon_m$, which is possible for the real part of the dielectric function of metals. The frequency for which the above relationship is true, is called localised surface plasmon resonance (LSPR) and dominates the spectra of noble metallic NPs, such as Au and Ag. Figure 2.3 illustrates the phenomenon of the collective plasma oscillation of the free electron gas induced by the external electromagnetic field. A dipole oscillation is formed due to the charge separation between the free electrons and the ionic lattice as shown. The frequency for which the oscillation amplitude reaches its maximum is the LSPR [19] [14].

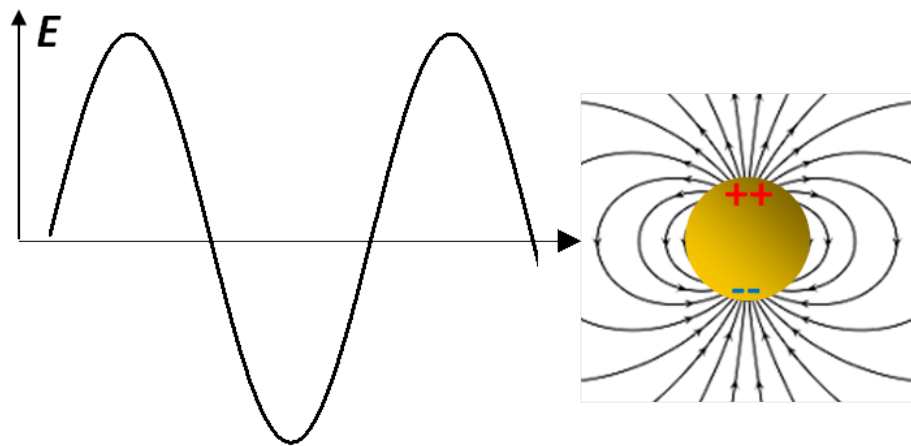


Figure 2.3: Schematic illustration of the localised surface plasmon resonance (LSPR) in AuNPs. The conduction band electrons of the metal will collectively oscillate upon exposure to the external electromagnetic field \mathbf{E} and under the restoring force from the field created by the resulting charge displacement at the NP edges. The amplitude of the oscillation reaches its maximum at the surface plasmon resonance frequency, which depends on the NP shape, size and dielectric environment.

The LSPR intensity, position and bandwidth depend strongly on the NP's material, its size and shape as well as the refractive index of the environment [15], [65] [62], [56]. For $R \approx 30$ nm spherical gold NPs in aqueous solutions, the LSPR band appears in the visible region at around 530 nm wavelength.

Figure 2.4 gives a better description on how the size affects the LSPR's position, bandwidth and magnitude. Mie theory (Eq. 2.1.14) indicates that the absorption cross-section is dependent on the particle's size $\propto R^3$. Extended research conducted over the years has experimentally confirmed this and further shown that there is a red shift of the resonance peak while the NP's size increases [66], [15],[67], [32], [19], [68]. El-Sayed and co-workers have calculated –via full Mie theory– the optical absorption and scattering cross-sections of AuNPs of various sizes and plotted their

ratio dependence as shown on Fig. 2.4 [19], [32]. From Fig. 2.4.D it can be observed that the scattering cross-section increases with increasing particle's size whilst nearly vanishes for particles with a diameter below 40 nm. This is specifically shown: for 20 nm AuNP (Fig. 2.4.A) where the extinction is purely dominated by absorption, for 40 nm AuNP (Fig. 2.4.B) where the extinction is yet nearly all contributed by absorption and finally for 80 nm AuNP (Fig. 2.4.C) where the scattering contribution has largely increased and both processes are contributing to the extinction. Notably, the LSPR wavelength is red shifted for these large NPs. It is also worth mentioning that the spectra are quite asymmetrical with a plateau appearing for low wavelengths because of the absorption by the interband transitions [64].

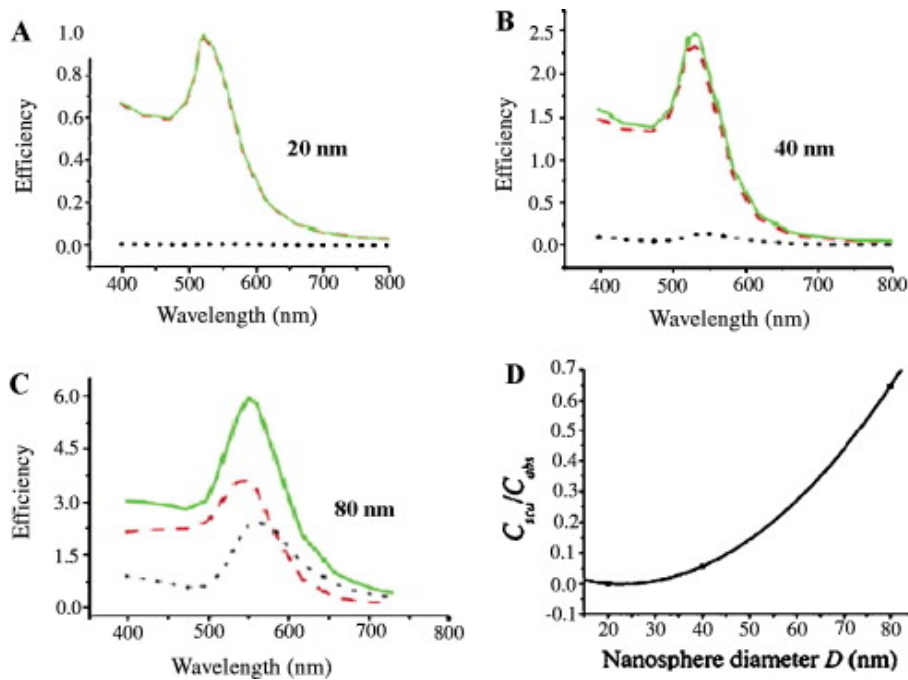


Figure 2.4: Tuning of the relative contribution of surface plasmon absorption and scattering by changing the particle size. The calculated surface plasmon absorption (red dashed), scattering (black dotted) and total extinction (green solid) efficiencies of gold nanoparticles in diameter of (A) 20 nm; (B) 40 nm and (C) 80 nm. (D) The dependence of the ratio of the scattering to absorption cross-sections to on the diameter of gold nanoparticles. Increase particle sizes lead to increased contribution from Mie scattering. The calculations are made by using full Mie theory. FIGURE AND CAPTION REPRODUCED WITH PERMISSION FROM REF. [19]

In addition to the size dependence, the surrounding medium plays also crucial role to the optical cross-sections (Eq. 2.1.14 and 2.1.15) and hence the spectra of plasmonic NPs. Comparison of absorption spectra of AuNP of 60 nm diameter for increasing refractive indexes, varying from air ($n = 1$) to oil ($n = 1.5$) can be found in Ref. [64] showing red shifts of the LSPR wavelength as well as significant intensity increase. The red shift can be attributed to enlarged charge screening as

the surrounding material's refractive index is rising [62]. Effectively, the oscillation of the free electron gas is expected to slow down given a higher polarised surrounding medium leading to a red shift of the LSPR position.

Fine tuning of the optical properties of NPs based on shape control has fascinated scientists for decades, who have used synthetic control mechanisms to create and control the aspect ratio of elongated NPs, e.g. nanorods (NRs) [69], [23], [70] [71], [32], [72], [73], [74]. Extinction cross-sections for ellipsoidal particles have been analytically computed by Bohren and Huffman in the quasistatic regime ($\sigma_{\text{sca}}/\sigma_{\text{abs}} \propto V/\lambda^3 \ll 1$ in this regime and V is the particle volume) [59] [57]. Figure 2.5 shows the absorption spectra of nominally spherical AuNPs of 80 nm diameter in aqueous solution along with the one of AuNRs of 25 nm diameter with an aspect ratio x/y axis of 2.3 (i.e. a long axis of 57.5 nm) also in aqueous environment. For the later (AuNR), the spectrum is characterised by two bands, as the SPR splits into a transverse mode, which is perpendicular to the long axis of the AuNR and corresponds to the short-wavelength band (close to 520 nm), and a longitudinal mode that is parallel to the long axis of the AuNR and corresponds to the long-wavelength band [75], [66]. With increasing the aspect ratio, it has been observed (experimental results can be found among others in Ref. [75]) that the 'transverse mode' band shifts slightly to shorter wavelengths while the 'longitudinal mode' band increases in intensity as well as red-shifts linearly with the rod length [75].

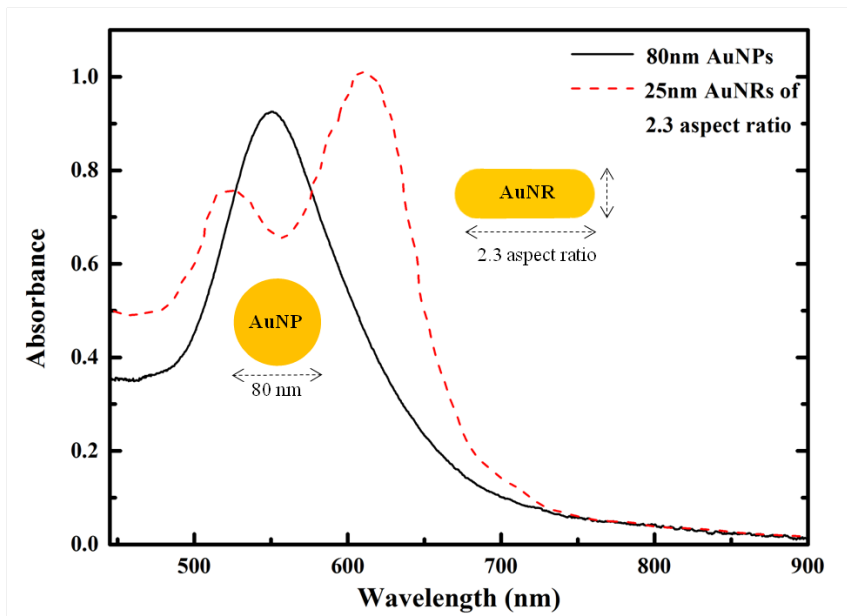


Figure 2.5: Absorbance spectrum of nominally spherical AuNPs of 80 nm diameter in aqueous solution (BBI Solutions) shown alongside the one of AuNRs of 25 nm diameter with an aspect ratio x/y axis of 2.3 (Nanopartz) also in aqueous environment.

2.2 Elements of nonlinear optics

Metallic nanostructures exhibit also strong optical responses in the nonlinear regime and are therefore promising systems in the field of biophotonics and especially in bio-imaging [43], [76]. Examples of nonlinear processes used in microscopy and spectroscopy techniques include among others, second harmonic generation [77], [78], [79], third harmonic generation ([80], [81], sum and difference frequency generation (SFG and DFG), four-wave mixing [82], [83], [84], and Coherent anti-stokes Raman scattering [85]. This section gives a brief introduction to the field of nonlinear optics, the nonlinear effects associated with the experiments and the general research field of this work. For an extensive reading one can refer to the references [86], [87], [88] and [89].

2.2.1 Introductory concepts

Nonlinear optics is the field that describes phenomena where the polarisation, \mathbf{P} , of a medium responds nonlinearly to an external electric field \mathbf{E} . Typically, laser sources can produce an adequate intensity in order to provoke nonlinear effects. Therefore these effects were firstly observed -with the discovery of SHG in 1961 by Franken et al.- after the invention of the first experimental laser by Maiman in 1960. In order to elucidate these nonlinear effects we shall start from the principles of light matter interaction. This part is based on [86], [87], [62].

Nonlinear optical phenomena are mostly described with the polarisation \mathbf{P} in terms of the applied field. As mentioned earlier, in the linear regime the polarisation density \mathbf{P} of a dielectric medium equals to $\mathbf{P} = \mathbf{dp}/dV$, where \mathbf{dp} is the change of dipole moment within a certain volume element dV in the material. The polarisation depends linearly on the strength of the applied electric field \mathbf{E} –Fig. 2.7– via the relationship:

$$\mathbf{P}(t) = \varepsilon_0 \chi^{(1)} \mathbf{E}(t) \quad (2.2.1)$$

In 2.2.1 $\chi^{(1)}$ is known as the *linear* or *first order susceptibility*.

In the nonlinear regime the polarisation \mathbf{P} can be expressed as a power series of the field as follows:

$$\mathbf{P}(t) = \varepsilon_0 [\chi^{(1)} \mathbf{E}(t) + \chi^{(2)} \mathbf{E}^2(t) + \chi^{(3)} \mathbf{E}^3(t) + \dots] = \mathbf{P}^{(1)}(t) + \mathbf{P}^{(2)}(t) + \mathbf{P}^{(3)}(t) + \dots \quad (2.2.2)$$

where $\mathbf{P}^{(n)}(t)$ represents the n -th order polarisation given by $\varepsilon_0 \chi^{(n)} \mathbf{E}^n(t)$. In 2.2.2 $\chi^{(2)}$

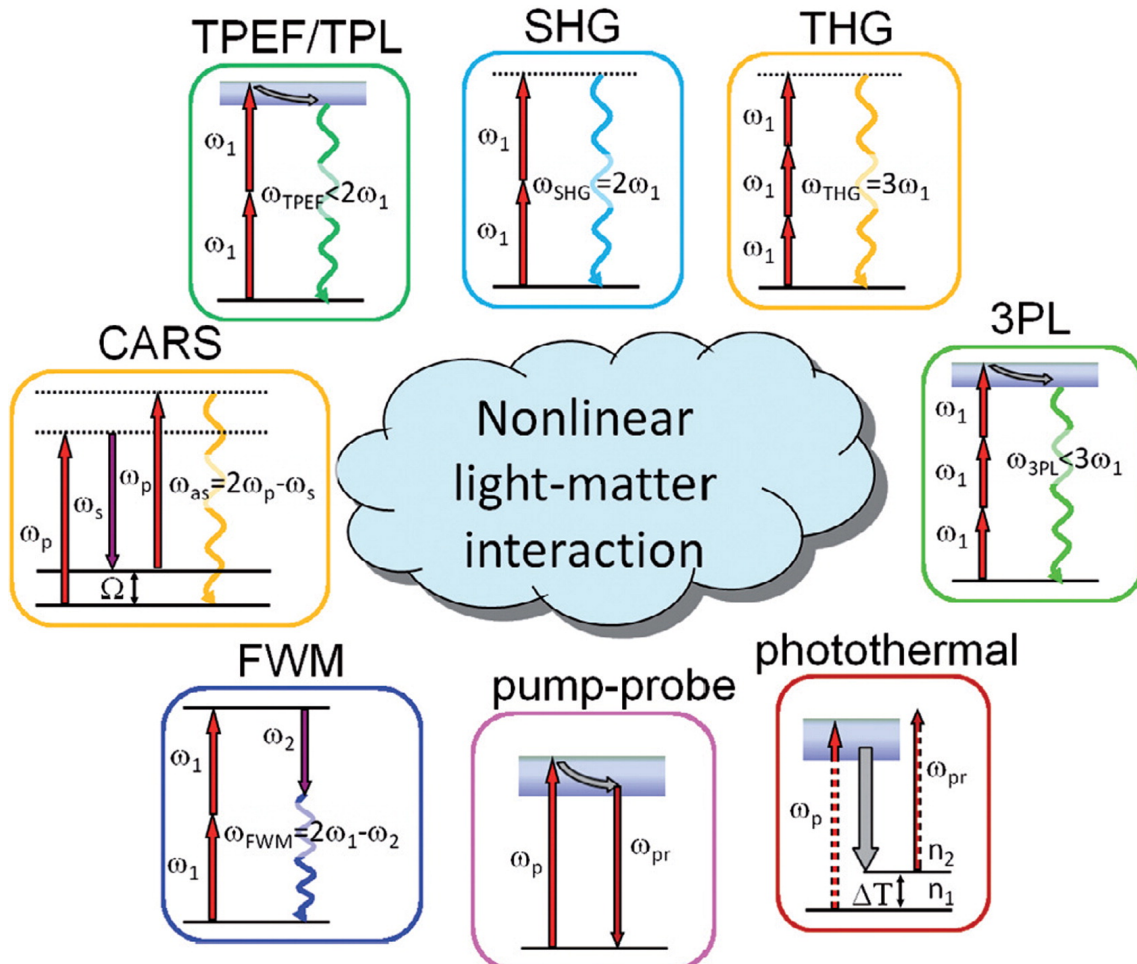


Figure 2.6: Nonlinear optical (NLO) modalities employed for the visualization of nano-materials. Horizontal solid lines represent electronic and vibrational energy levels of molecules. Dashed lines are virtual states. The straight and wavy arrows are excitation and output signal beams, respectively. The gray arrows represent relaxation in electronically excited states. ω_1 and ω_2 are excitation beams. ω_p and ω_s are pump and Stokes beams for CARS. Ω is the frequency of vibrational transition between vibrational ground state and vibrationally excited state. ω_p and ω_{pr} are the pump and probe beams for pump-probe and photothermal modalities. ΔT is the temperature change due to excitation. n_1 and n_2 are the refractive indices of the material before and after excitation, respectively. TPEF: Two-photon excited fluorescence. TPL: Two-photon luminescence. SHG: Second harmonic generation. THG: Third harmonic generation. 3PL: Three-photon luminescence. CARS: coherent anti-Stokes Raman scattering. FWM: Four-wave mixing. FIGURE AND CAPTION REPRODUCED WITH PERMISSION FROM REF. [43]

and $\chi^{(3)}$ are known as second and third order nonlinear susceptibility respectively while the $\mathbf{P}^{(2)}(t)$ and $\mathbf{P}^{(3)}(t)$ as second and third order nonlinear polarisation. In the case of a linear and isotropic medium, the susceptibility is a scalar quantity while in anisotropic media becomes a second rank tensor. In general $\chi^{(n)}$ is a $n + 1$ rank tensor [86].

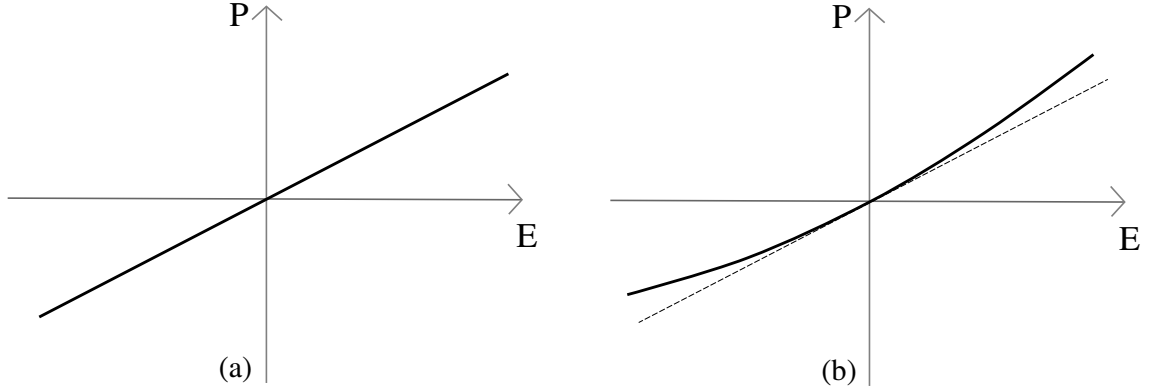


Figure 2.7: The $\mathbf{P} - \mathbf{E}$ relation for (a) a linear dielectric medium, and (b) a nonlinear medium

2.2.2 Nonlinear optical signals in microscopy

Among the most popular label-free microscopy techniques are the ones that derive from nonlinear optical signals such as Second Harmonic Generation, Third Harmonic Generation, Coherent Anti-stokes Raman Scattering and Four-Wave Mixing (Fig. 2.6). In this subsection a brief description of the mathematical background of some of these techniques is given along with some recent application of those in bioimaging.

Second order nonlinear optics

Second Harmonic Generation (SHG)

SHG is in fact a special case of sum frequency generation (SFG) where photons with frequency (ω) interact with a nonlinear medium and are converted to photons with twice the energy and thus frequency (2ω). This can be mathematically described by considering an external monochromatic electric field, $\mathbf{E}(t) = \Re[\mathbf{E}(\omega)e^{i\omega t}] = \frac{1}{2}\{\mathbf{E}(\omega)e^{i\omega t} + \mathbf{E}^*(\omega)e^{-i\omega t}\}$ and calculate the second order polarisability given by

$$\mathbf{P}^{(2)} = \varepsilon_0 \chi^{(2)} \mathbf{E}^2(t) \quad (2.2.3)$$

where by substituting

$$\mathbf{E}^2(t) = \frac{1}{4}[\mathbf{E}^2(\omega)e^{2i\omega t} + 2\mathbf{E}(\omega)\mathbf{E}^*(\omega) + \mathbf{E}^{*2}(\omega)e^{-2i\omega t}] \quad (2.2.4)$$

in 2.2.3 we get

$$\mathbf{P}^{(2)} = \varepsilon_0 \chi^{(2)} \frac{1}{2} \mathbf{E}(\omega) \mathbf{E}^*(\omega) + \varepsilon_0 \chi^{(2)} \frac{1}{4} [\mathbf{E}^2(\omega) e^{2i\omega t} + \mathbf{E}^{*2}(\omega) e^{-2i\omega t}] \quad (2.2.5)$$

$$= \underbrace{\varepsilon_0 \chi^{(2)} \frac{1}{2} |\mathbf{E}(\omega)|^2}_{P(0)} + \underbrace{\varepsilon_0 \chi^{(2)} \frac{1}{2} \Re[\mathbf{E}^2(\omega) e^{2i\omega t}]}_{P(2\omega)} \quad (2.2.6)$$

Application of a high intensity field $\mathbf{E}(t)$ of frequency ω to a $\chi^{(2)}$ material creates a second harmonic polarisation $P(2\omega)$ at twice frequency of the incident field and a steady (dc) component $P(0)$ also known as optical rectification. Importantly SHG effects arise from noncentrosymmetric structures and have been used to probe interfaces, surface defects, as well as for label-free imaging of microtubules or collagens in cells and tissues [43] [78]. With specific reference to AuNPs, since SHG is forbidden for a perfect spherical particle much smaller than the wavelength of light, this non-linearity has been utilized to characterize large particles and/or complex anisotropic structures [90].

Third order nonlinear optics

Third order nonlinear effects are present also in media possessing centrosymmetry³ and this nonlinearity has the form of

$$\mathbf{P}^{(3)} = \varepsilon_0 \chi^{(3)} \mathbf{E}^3(t) \quad (2.2.7)$$

These materials interact with optical fields by generating sum and differences of triplets of frequencies as well as third harmonics [87]. In this category belong the THG, FWM and CARS effect which are among the most popular label free imaging techniques and are vastly used in biomedical research nowadays.

Third Harmonic Generation (THG)

Similar to the SHG principal, THG is a third-order nonlinear process where photons with energy ω interact with the nonlinear medium and produce photons of energy 3ω and in accordance with 2.2.5 the third order polarisation $\mathbf{P}^{(3)}$ is given by

$$\mathbf{P}^{(3)} = \varepsilon_0 \chi^{(3)} \mathbf{E}^3(\omega) \quad (2.2.8)$$

With reference to AuNPs, THG has been utilised to detect single nominally spherical AuNPs down to 40 nm diameter in Ref. [80], however it required significant

³these materials are also called Kerr mediums.

excitation powers (≈ 70 mW) and pixel integration times (600 ms) rendering this method unpractical for imaging AuNPs within biological specimens.

2.2.3 The principle behind our FWM technique

This work focuses on the exploitation of an innovative phase-resolved triply resonant FWM microscopy technique developed in the Biophotonics and Quantum Optoelectronics group at Cardiff University for imaging various AuNPs in cellular environments. It is therefore of great importance to discuss the rationale behind this third-order nonlinear process. Important concepts are the fact that $\chi^{(3)}$ nonlinearities act as a modification of the dielectric function [62] of the material under investigation and that the scheme used is degenerate with $\omega_1 = \omega_2 = \omega_3 = \omega_p$ and tuned very close to the AuNP's LSPR. This section is based on Ref. [45] where one can find the full model describing the ultrafast changes of the real and imaginary parts of the dielectric function of single spherical AuNPs (15 nm to 40 nm) via the transient electron and lattice temperature in gold taking into account both intraband and interband transitions.

In the following description, the pump and probe fields of the experimental set-up will be noted with \mathbf{E}_1 and \mathbf{E}_2 respectively. Let us start from the induced polarisation at the particle

$$p = \varepsilon_0 \varepsilon_p \alpha \mathbf{E}_2 \quad (2.2.9)$$

where the polarisability α of a spherical AuNP of radius R in the Rayleigh limit is given by (as previously discussed in section 2.1.3)

$$\alpha = 4\pi\varepsilon_0 R^3 \frac{\varepsilon_p - \varepsilon_m}{\varepsilon_p + 2\varepsilon_m} = 4\pi R^3 \tilde{\varepsilon} \quad (2.2.10)$$

with the particle dielectric constant ε_p , defining the effective dielectric constant $\tilde{\varepsilon}$. In our experimental configuration⁴, upon excitation of the NP with the intensity modulated pump field \mathbf{E}_1 the dielectric function $\tilde{\varepsilon}$ changes. It is the pump-induced change of $\tilde{\varepsilon}$, denoted as $\Delta\tilde{\varepsilon}$ which creates a FWM field \mathbf{E}_{FWM} proportional to the change of polarisation,

$$\mathbf{E}_{\text{FWM}} \propto \Delta\tilde{\varepsilon} \mathbf{E}_2 \quad (2.2.11)$$

Since the $\Delta\tilde{\varepsilon}$ is proportional to the pump's intensity, $I_1 = |\mathbf{E}_1|^2 = \mathbf{E}_1 \mathbf{E}_1^*$, the FWM signal is hence proportional to

$$\mathbf{E}_{\text{FWM}} \propto \mathbf{E}_1 \mathbf{E}_1^* \mathbf{E}_2 \quad (2.2.12)$$

⁴section 3.1.1

and has the dependence form of a third-order nonlinearity as described previously in 2.2.8.

A quantitative description based on the modeling of the dielectric function $\tilde{\epsilon}$ of gold, described in 2.1.9 is given by Masia et al.[45], where the transient electron temperature T_e and lattice temperature T_l are modeled using a two temperature model [91], [92]. Briefly, the change of $\tilde{\epsilon}$ of a AuNP (Eq. 2.1.9) is associated with the change of the electron relaxation time γ_b and the contribution of interband transitions ϵ_{ib} . Since this experiment involves a complex interaction of electrons and the lattice with the exciting optical fields, it is worth mentioning the ultrafast dynamics of AuNPs which have been studied extensively and have been found to evolve in a series of steps [92] [14], [56], [45].

Upon excitation of the NP at the LSPR with the pump pulse (top sketch of Fig. 2.8), a non-equilibrium electron distribution is formed after a rapid (around 10 fs) energy transfer from the coherently oscillating electrons to single electron excitation. A subsequent thermalisation via electron-electron scattering (within a few hundred femtoseconds) of the hot electron gas described by the electron temperature T_e will in turn lead to thermalisation with the lattice in about 1 ps described by the lattice temperature T_l . Finally, the cooling of the lattice through heat diffusion to the environment comes over hundreds of picoseconds. This behaviour is imprinted in the FWM dynamics versus pump-probe delay as shown in Fig. 2.8 where the measured along with the simulated FWM dynamics are plotted.

Importantly, the *average* temperature increase at the NP's surface was found to be only 1.3, 1.9 and 4.7 K for the 15, 20 and 38 nm diameter AuNPs respectively used in previous experiments which were performed with a pulse train of 76 MHz repetition rate for which 1 kW/cm² average intensity (equal to an incident average power of 10 μ W over 1 μ m² focused area) corresponds to a pulse fluence of 0.13 J/m² [45].

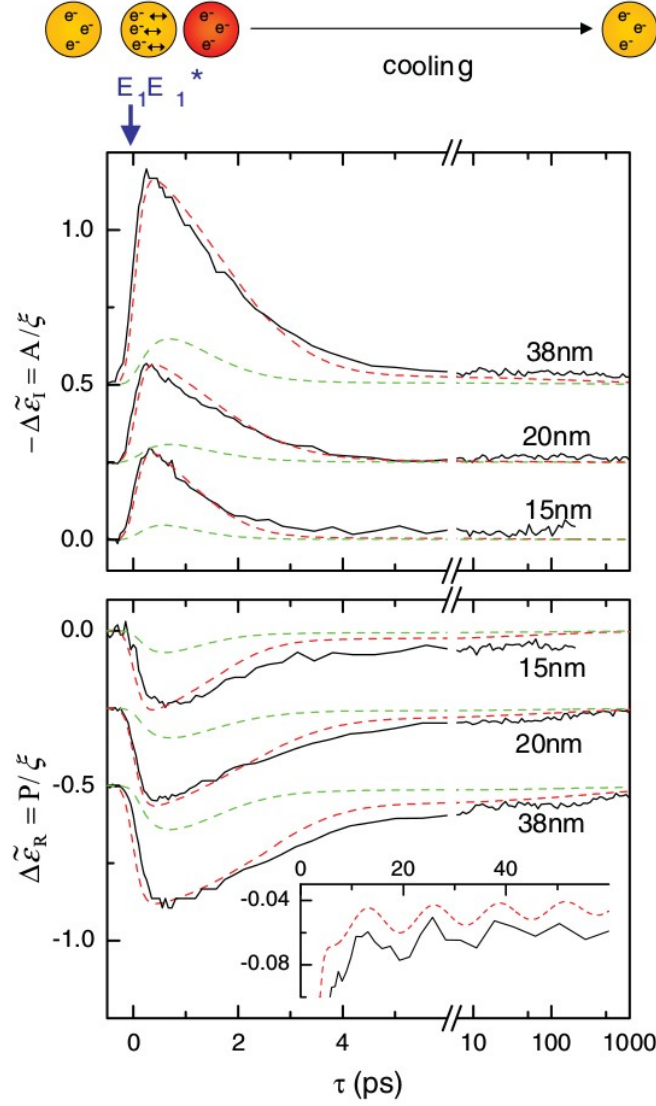


Figure 2.8: Transient changes of the real ($\Delta\tilde{\epsilon}_R$) and imaginary ($\Delta\tilde{\epsilon}_I$) parts of the dielectric function of a single gold NP resonantly excited and probed at 550 nm for different NP diameters as indicated. Pump (probe) fluence is 0.60 J/m^2 (0.11 J/m^2) for the 15 and 20 nm NPs and 0.65 J/m^2 (0.05 J/m^2) for the 38 nm particle. Acquisition time per point is 200 ms. Dashed lines are corresponding calculations, with the green lines neglecting the heating by interband absorption. Curves are vertically displaced for clarity. The top sketch illustrates the LSPR excitation by the pump (E_1) and the subsequent heating and cooling dynamics monitored by the probe. The inset shows coherent phonon oscillations for the 38 nm NP. FIGURE AND CAPTION REPRODUCED WITH PERMISSION FROM REF. [45]

3

SET-UPS AND METHODS

3.1 The multi-modal imaging set-up: DIC, FWM and confocal fluorescence microscopy

All samples were imaged on the multi-modal experimental set-up shown during FWM operation on Figure 3.1. The set-up is composed of an inverted Nikon Ti-U microscope equipped with a 100 W halogen lamp for wide-field illumination, a selection of microscope objectives, an oil condenser of 1.34 numerical aperture (NA) with a removable home-built dark-field illumination of 1.1-1.34 NA, sliders of polarizers and analyzers inserted into the optical pathway before the condenser and after the objective, respectively, enabling Differential Interference Contrast (DIC) microscopy, as well as a choice between 1x and 1.5x tube lens. A xyz piezoelectric stage, also referred to as nanostage, (Mad City Laboratory model NanoLP200) is used to control the sample's position with nanometric accuracy over 200 μm range. A consumer Canon EOS 40D color camera (2592 x 3888 pixels of 5.7 μm pixel pitch, and full-well capacity $N_{\text{fw}} = 4 \times 10^4$) is coupled to the left port of the microscope alongside a scientific-CMOS PCO Edge 5.5 gray scale (b/w) camera water cooled (2560 x 2160 square pixels of 6.5 μm pitch and a $N_{\text{fw}} = 3 \times 10^4$ full-well capacity) for rapid image acquisition (100 frames per second for full sensor) which is attached at the eyepiece side port.

Overall, the inverted Nikon Ti-U microscope is capable of Bright field (BF), Dark field (DF), DIC imaging as well as optical extinction measurements as has

been shown in recent work of our group [93], [94]. The right port of the microscope is coupled with the beam path of the FWM set-up described in the following section.

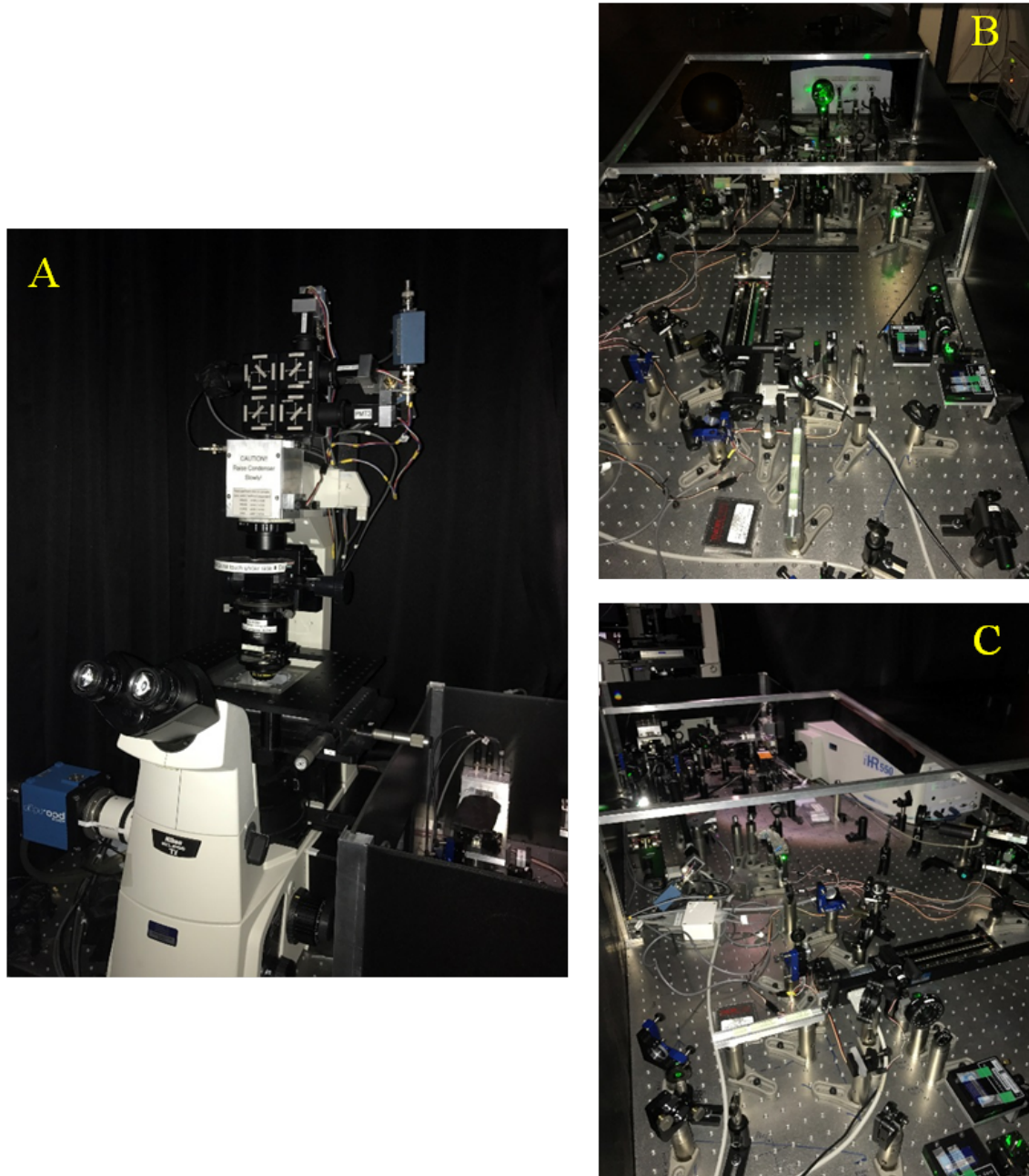


Figure 3.1: Photographs of the microscope body (A) and the multi-modal imaging technique optical components (B and C) during operation.

3.1.1 Description of the FWM set-up

Phase-sensitive FWM microscopy in heterodyne detection, triply resonant to the LSPR of gold NPs, able to resolve the ultrafast changes of the real and imaginary part of the dielectric function of single spherical gold NPs has been previously

shown by our group [45] alongside background-free detection of gold NPs in highly scattering and fluorescing environments [84].

For the work presented in this thesis, a new generation of FWM microscopy set-up –also described in [44] [62]– was used comprising epi-collection (reflection) geometry and a dual-polarisation heterodyne detection scheme. A sketch of the FWM set-up used in this work is shown in Figure 3.2. Optical pulses of 150 fs duration and repetition rate $v_L = 80$ MHz, centered at $\lambda = 550$ nm are provided by the signal output of a Newport/Spectra-Physics Inspire optical parametric oscillator (OPO), pumped by the frequency-doubled output of a femtosecond MaiTai Titanium:Sapphire (Ti:Sa) laser. The train of laser pulses is split into three beams (pump, probe and reference) all having the same center wavelength (550 nm) which is approximately resonant to the LSPR of spherical AuNPs resulting in a degenerate FWM scheme. Initially the beam passes through a $\lambda/2$ plate ($\lambda/2-1$ in Figure 3.2) which converts it from being vertically to horizontally polarised with respect to the lab reference axis. Straight after, the laser beam passes through a prism pulse compressor which negatively chirps ¹ the pulses in order to pre-compensate for the positive chirping due to the various optical components in the beam path. The reason for rotating the polarisation to being horizontal is in order to minimise reflections while the beam travels through the prism compressor (p-polarisation has zero reflection at the Brewster angle). It is important not to have chirped pulses on the sample for best time resolution, hence the use of the compressor. It is also important to ensure that pump and probe pulses have the same chirp in the beam path so that they can be equally pre-compensated, and be Fourier limited at the sample. For this purpose, appropriate glass blocks were inserted in the beam path. Moreover, there are glass blocks added on the beam path of the reference beam in order to equalize the chirping of the reference with the collected signal outside the sample for maximum interference. After the pulse compressor, the train of optical pulses passes through $\lambda/2-2$ resulting in 45° polarised light which then enters the polarising beam splitter (PBS 1) and results in having horizontally (H) polarised transmitted and vertically (V) polarised reflected beams of equal intensity. The V polarised beam acts as pump and excites the gold NPs at the LSPR with an intensity which is temporally modulated by an acousto-optic modulator (AOM_1). AOM_1 is driven at the carrier frequency $v_1 = 83$ MHz with a square-wave amplitude modulation of frequency $v_m = 0.4$ MHz. The change in the NP's optical properties is resonantly probed by the probe beam derived from the H-polarised beam transmitted by PBS1, arriving at an adjustable delay time τ after the pump pulse.

¹The chirp of an optical pulse usually refers to the temporal broadening of the pulse occurring due to group velocity dispersion.

The probe optical frequency is also upshifted via a second AOM (AOM₂) which is driven with a constant amplitude at $\nu_2 = 82$ MHz. The first order diffraction of the AOMs are used for both pump and probe pulses which are upshifted by ν_1 and ν_2 respectively. The zero order diffraction of AOM₂ is used as the frequency-unshifted reference beam, with field \mathbf{E}_{ref} , in the heterodyne detection scheme. Pump and probe beams, cross-linearly polarised, are recombined onto PBS2 and are then reflected by a non-polarising beamsplitter (BS 80:20 T:R) into a pair of λ plates ($\lambda/2$ -4 and $\lambda/4$) resulting into circularly polarised beams at the sample plane. The recombined beams are then reflected by a dichroic beam splitter (DBS) into the right port of the inverted Nikon Ti-U microscope. Notably, the DBS allows us to couple beams of different wavelengths into the microscope when performing other experiments such as CARS (albeit CARS was not performed within the work in this thesis). The sample is positioned onto the piezoelectric stage and can be moved with respect to the focal volume of the objective by scanning the sample-nanostage in all three dimensions. For all samples consisting of fixed cells embedded with various bio-conjugated AuNPs, pump and probe fields called \mathbf{E}_1 and \mathbf{E}_2 respectively are focused onto the sample by a 100x oil-immersion microscope objective of 1.45 NA in order to achieve high spatial resolution². The epi-detected FWM field, $\mathbf{E}_{\text{FWM}} \propto \mathbf{E}_1 \mathbf{E}_1^* \mathbf{E}_2$ is collected by the same objective alongside the reflected probe field \mathbf{E}_{2r} . FWM and reflection signals travel backwards through the same $\lambda/2$ and $\lambda/4$ waveplates, such that upon reflection through a planar surface the probe returns V polarised with respect to the lab reference. The reference beam is polarised at 45° by using the $\lambda/2$ -3 waveplate in order to provide equal reference fields of H and V polarisation. The reference beam is recombined with the epi-detected signals at the non-polarising beamsplitter (NPBS). The resulting interference is detected by two pairs of balanced photodiodes, as detailed below. The dual-polarisation detection of reflected and FWM signal will be firstly discussed in the following, while the heterodyne detection will be secondly analysed.

A Wollaston prism is used to separate H and V polarised components for each arm of the NPBS interferometer. The two pairs of balanced photodiodes shown on Figure 3.2 enable polarisation resolved detection with the top (bottom) pair detecting the photo-current difference of the H (V) polarised beams for common-mode noise rejection. In this way the cross-circularly (-) and co-circularly (+) polarised components of \mathbf{E}_{FWM} and \mathbf{E}_{2r} , relative to the incident circularly polarised probe \mathbf{E}_2 are detected.

We will now discuss the heterodyne detection applied in this scheme after introducing the general principles of heterodyne interferometry which can also be found

²in some cases the 1.5x tube lens were also used

in Ref [95].

Let's first simplify matters by considering the real parts of two electromagnetic fields, $E_1(t)$ and $E_2(t)$, with frequencies $\omega_1 = 2\pi\nu_1$ and $\omega_2 = 2\pi\nu_2$ respectively, as well as real amplitudes α_1 and α_2 . The above electric fields can then be represented as:

$$E_1(t) = \alpha_1 \cos(\omega_1 t + \phi_1) \quad (3.1.1)$$

$$E_2(t) = \alpha_2 \cos(\omega_2 t + \phi_2) \quad (3.1.2)$$

The intensity of the resulting interference can be calculated as follows by using the trigonometric identities of $\cos A \cos B = \frac{1}{2} \cos(A - B) + \frac{1}{2} \cos(A + B)$ and $\cos^2 A = \frac{1}{2}(1 + \cos 2A)$.

$$\begin{aligned} I(t) &= [E_1(t) + E_2(t)]^2 \\ &= (\alpha_1^2/2) + (\alpha_2^2/2) \\ &\quad + (1/2)\alpha_1^2 \cos[2(\omega_1 t + \phi_1)] \\ &\quad + (1/2)\alpha_2^2 \cos[2(\omega_2 t + \phi_2)] \\ &\quad + \alpha_1\alpha_2 \cos[(\omega_1 + \omega_2)t + (\phi_1 + \phi_2)] \\ &\quad + \alpha_1\alpha_2 \cos[(\omega_1 - \omega_2)t + (\phi_1 - \phi_2)] \end{aligned} \quad (3.1.3)$$

The output of higher order terms $2\omega_1$, $2\omega_2$, $\omega_1 + \omega_2$ from 3.1.3 are rapidly oscillating and average to zero over the time response of the detector. In our set-up, these terms would correspond to $2\omega_s$, $2\omega_{ref}$, $\omega_s + \omega_{ref}$, while the remaining detected term is $\omega_s - \omega_{ref}$. The radial frequency ω_s corresponds to the frequency upshifted signal $\omega_s = \omega_{ref} + \Delta\omega$, hence the difference detected term is $\omega_s - \omega_{ref} = \Delta\omega + \omega_{ref} - \omega_{ref} = \Delta\omega$. Now, this shift $\Delta\omega$ can be chosen considering that we have a pulse train at ν_L repetition rate, hence the spectrum consists of a series of modes separated by ν_L . We can therefore choose to detect the interference between signal and reference at appropriate sideband, modulo ν_L . As a result, for the reflected probe a signal at $\nu_2 - \nu_L = 2$ MHz is detected via a multi-channel lock-in amplifier (Zurich Instruments HF2LI). With the same amplifier, two sidebands are simultaneously detected at $\nu_2 \pm \nu_m - \nu_L = 2 \pm 0.4$ MHz corresponding to the FWM field, due to the amplitude modulation of the pump at ν_m and the frequency upshift of the probe at ν_2 . The lock-in amplifier provides both the in-phase (\Re) and in-quadrature (\Im) components for each detected frequency, and in turn we are able to resolve amplitude and phase of both co- and cross-circularly polarised com-

ponents of \mathbf{E}_{2r} and \mathbf{E}_{FWM} indicated in this thesis as A_{2r}^{\pm} and A_{FWM}^{\pm} , and, Φ_{2r}^{\pm} and Φ_{FWM}^{\pm} .

The reference and probe delay stages are the models M403.6 and M403.8 from Physik Instrumente (PI) GmbH & Co (Karlsruhe, Germany) and they have translational ranges 150 mm and 200 mm respectively with a minimum incremental motion $0.2 \mu\text{m}$. In addition, the AOMs used are model ASM-802B67 from IntraAction Corp (Illinois, U.S.A).

Four-wave mixing images of the samples under investigation were acquired using a custom-written software called MultiCARS implemented in LabWindows CVI (W. Langbein, Cardiff School of Physics and Astronomy) which permits hardware-software interfacing as well as remote control of the set-up. For the data display of FWM and reflection images shown in this work the MultiCARS software was used as well which allows to represent the acquired data as 2D or 3D images, and also provides some data processing options (for example detector offset subtraction).

3.1.2 Confocal fluorescence implementation

The confocal epi-fluorescence detection was implemented during the last months of the project and allows us to measure confocal fluorescence at the same time as FWM imaging. In fact, fluorescence is collected via the same objective, is spectrally separated by a dichroic mirror DBS2 (610-720nm) and travels through a confocal pinhole of adjustable opening in front of a photomultiplier detector, Epi-PMT of Figure 3.2, (Hamamatsu H10770A-40) where there is also a bandpass filter (Semrock FF02-650/100) transmitting in the 600-700 nm wavelength range.

3.1.3 FWM measurements: Alignment and settings

The alignment of the set-up was performed in several steps using a gold film sample as our *reference sample*. Initially, all three beams were aligned with the aid of several pinholes placed in the beams' pathways as well as with observation cameras positioned to image a plane conjugated to the sample (near field) and its Fourier plane (far field directional space). Importantly, pump and probe beams had to spatially overlap both in direction (far field) and position (near field). The laser power applied to the sample was controlled by adjusting the amplitude of radio-frequency wave in the AOMs and was measured before the entrance to the microscope (after the DBS1 on figure 3.2). The polarization state onto the sample was controlled via rotation of the pair of $\lambda/2$ -4 and $\lambda/4$ waveplates in order to achieve minimum detected cross-polarised signal. The pump-probe delay which yields the strongest FWM signal is set to 0.5 ps for gold NPs and it is related to time with which the

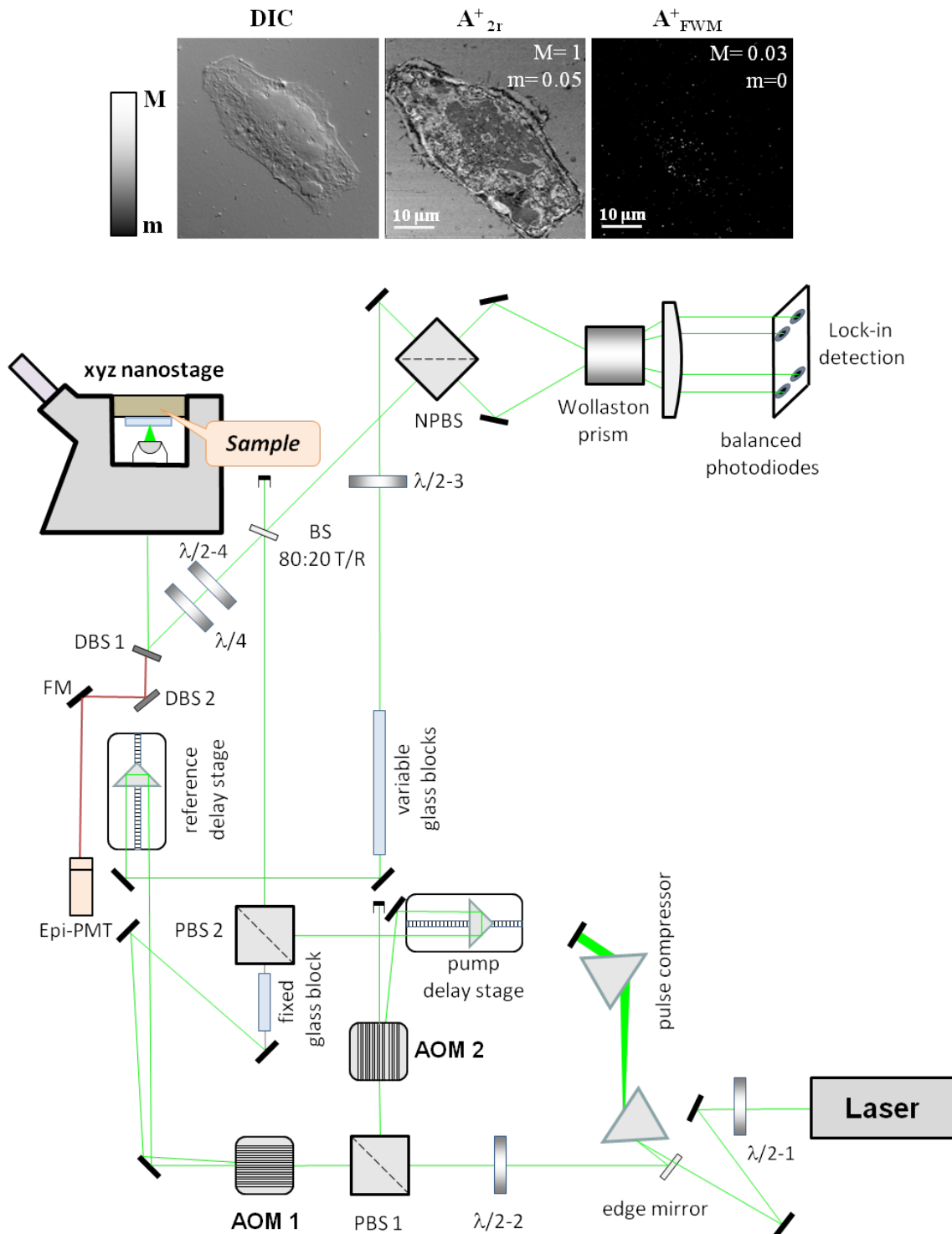


Figure 3.2: Four-wave mixing microscopy set-up in heterodyne detection

A full description of the set-up is given in the text. The top inset shows a fixed HeLa cell incubated with bio-conjugated 15 nm AuNPs imaged on the set-up via DIC imaging and FWM. Amplitude of the co-polarised reflection field (A_{2r}^+) and the co-polarised FWM amplitude (A_{FWM}^+) indicating the presence of AuNPs are shown alongside their linear grey scale from m to M .

hot electron gas reaches its maximum temperature [45] (see also 2.2.3).

Three kinds of measurements were acquired on this setup:

- xy scans, referred as *raster scans*, indicating a two dimensional transverse to the objective spatial scan.
- xy-z scans, referred as *z-stacks*, indicating a raster scan acquired in the axial direction, producing a 3D sample representation.
- xy- τ , referred as *delay scans*, indicating a raster scan over the pump delay time (τ).

An example of the FWM imaging of the reference sample is shown in Figure 3.3 alongside a pump delay scan. Bright field transmission imaging under wide field illumination aids to bring the Au film in ‘rough’ focus (Figure 3.3 (a)) which is further optimized by nano movements of the nanostage in order to detect the maximum reflection signal possible (A_{2r}^+). Co (+) and cross (-) polarized reflection (2r) and FWM amplitudes are then measured and the raster scans of Figure 3.3 (c) are produced after data display with the MultiCARS home-built software. The strength of the reflection and FWM signal is a way of evaluating the quality and reproducibility of our alignment. Notably, there is a difference of about two orders of magnitude between reflection and FWM signal amplitude. In addition to the raster scans, as a further proof of detecting FWM signal, a pump-probe delay dependence is acquired (Figure 3.3 (b)) and indicates the pump-induced change of the sample’s polarizability as explained in 2.2.3.

3.2 Commercial microscopes

3.2.1 Wide field epi-fluorescence microscope

The wide-field epi fluorescence images presented in this thesis were acquired on the inverted Olympus IX73 shown on Figure 3.2.1. The microscope is equipped with a Prior Proscan 220 light source and a CMOS Hamamatsu Camera (ORCA-flash 4.0 V2) which are controlled via the HCImage software package. The fluorophore tags used in each sample defined the filter cubes (Chroma) which were chosen for the image acquisition. Table 3.1 summarizes the filter cube sets used in the experiments. The acquisition time varied per sample and per fluorescence channel and therefore this parameter is stated on each respective image’s caption. A 100×1.4 NA oil immersion objective and 2×2 binning readout effect was used on all images corresponding to a $0.13 \mu\text{m}$ pixel size (unless stated otherwise).

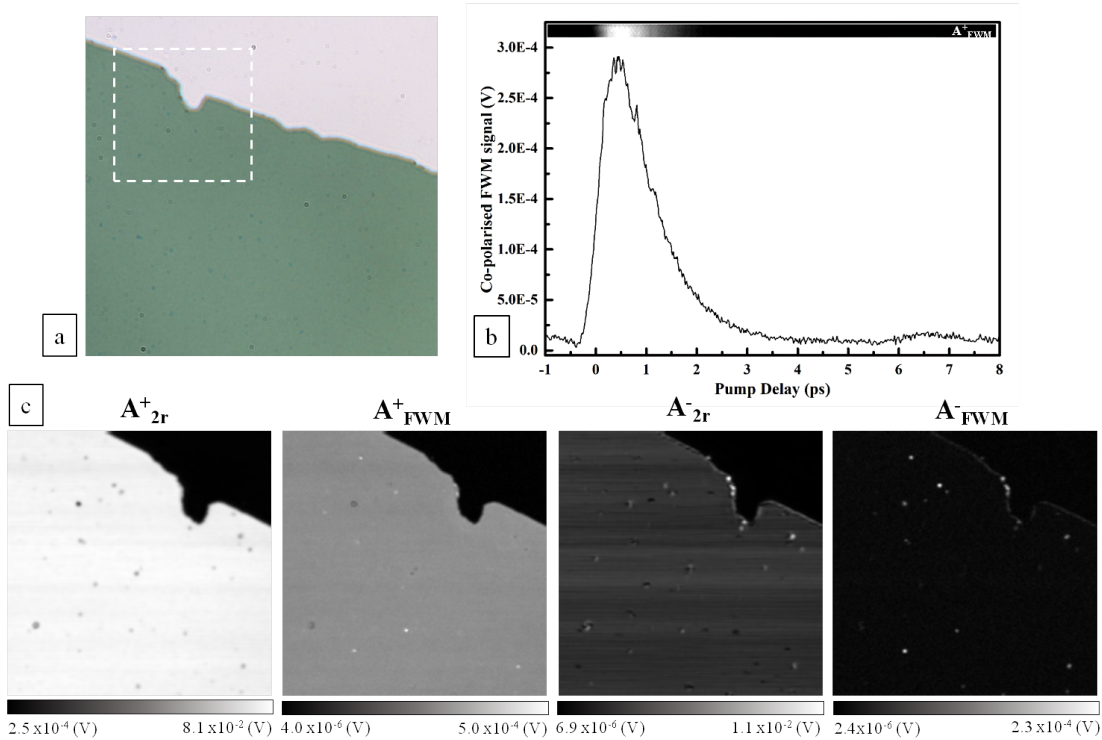


Figure 3.3: Example of FWM imaging and pump-probe delay dependence on the reference sample Au film.

(a) Brightfield image of the Au film, (b) pump-probe delay dependence of the co-polarised FWM field amplitude acquired from -1 ps to 8 ps with 1 ms dwell time, (c) 20 x 20 μm raster scans with 63 nm lateral pixel size of co (+) and cross (-) polarized reflection (A_{2r}^+) and FWM amplitude (A_{FWM}^+) channels. Pump (probe) power before the microscope entrance equals to 20 μW (10 μW). A 100 \times oil-immersion microscope objective of 1.45 NA is used.

Fluorophore	excitation wavelength (nm)	emission wavelength (nm)
DAPI	350/50	455/50
GFP	490/20	525/36
A568	555/25	605/52
A647	645/30	705/72

Table 3.1: The combined excitation and emission Chroma filter-sets of the inverted Olympus IX73 used in this thesis. For each one the center wavelength alongside its FWHM is indicated.

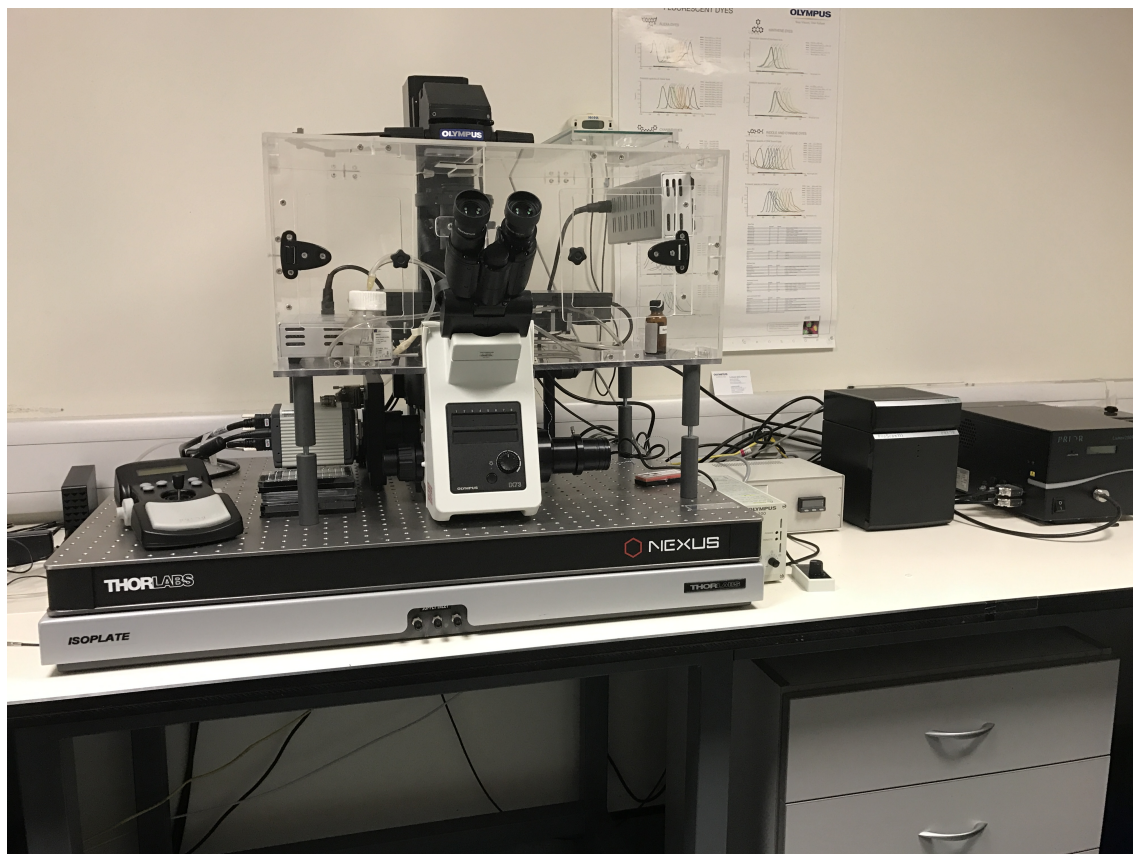


Figure 3.4: The wide field epi-fluorescence Olympus IX73 microscope in Cardiff School of Biosciences.

3.2.2 Confocal fluorescence microscopes

Two commercially available confocal fluorescence microscopes were used for fluorescence imaging of the samples presented in this thesis.

- **Leica SP5 - Cardiff School of Pharmacy**

Confocal fluorescence images of sections 4.2.2 and 4.3 were acquired on a Leica SP5 confocal laser-scanning microscope equipped with a 488 nm Ar laser and a 543/633 nm HeNe laser. A 100x 1.4 NA immersion oil objective was used alongside a 152 μm confocal pinhole. Images were acquired at 400 Hz line scan speed, with 3D voxel size of 76 nm \times 76 nm \times 250 nm. AlexaFluor488 (A488) and AlexaFluor647 (A647) were excited using 488 and 633 nm lasers respectively. These measurements were performed by Dr. Paul Moody in Cardiff School of Pharmacy prior to the FWM measurements.

- **Zeiss LSM 880 - Cardiff School of Biosciences**

A state-of-the art Zeiss LSM 880 upright confocal microscope comprising a fully-motorised (x, y, z) Zeiss Axio Imager and supporting various imaging

modalities –in addition to confocal fluorescence, BF and DIC– such as Fluorescence correlation spectroscopy (FCS) and Fluorescence-lifetime imaging microscopy (FLIM) was used for the images shown on section 4.3.2. The 405 nm and 483 nm laser lines were used to excite the DAPI ³ and A488 fluorescence tags alongside the plan apochromat 20x, 0.8 NA air and the plan apochromat 63x, 1.4 NA oil objectives.

3.3 Data Analysis

3.3.1 FWM Data Analysis

The display of the FWM and the epi-confocal measurements was all made via the the MultiCARS home-built software, as previously stated. This software enables to export the displayed images as bitmap files for subsequent image analysis, using for example the publicly available software ImageJ.

3.3.2 Correlation analysis

From the beginning of the project a major challenge was the need for a correlation analysis (a set of analysis steps) of images taken on different microscopes. Even when using gridded coverslips with marked areas to aid finding the same region on the sample, confocal and FWM microscopy were performed mostly through non simultaneous image acquisitions and implied different sample mounting (potentially with small rotation differences) as well as different lateral and axial resolution, and z-sectioning. In order to analyze these images for the purpose of determining spatial correlation, the following steps were performed after the acquisition of the FWM images and fluorescence images and will be from now on mentioned as *correlation analysis*.

Slice Registration

Initially, the StackReg [96] ImageJ plug-in was run on both 3D fluorescence and FWM datasets consisting of a sequence of 2D images at different z-planes, in order to rectify misalignments mainly of the z-axis and produce a stack of correctly registered image slices.

Maximum intensity z projection

The next step was to produce maximum intensity projections (a volume visualization method that projects in a 2D plane the voxels with maximum intensity from the

³DAPI is the scientific abbreviation for 4',6-diamidino-2-phenylindole and serves as fluorescent dye which binds strongly to A-T rich regions in DNA. Its absorption/emission wavelengths are 358/461 nm.

data encountered by a ray cast through the 3D object from the viewer's eye to the plane of projection) of the corrected z-stacks on both fluorescence and co-circularly polarized FWM amplitude images. In such way, 2D fluorescence and FWM images containing information regarding the localization of fluorophore tags and nanoparticles respectively were ready to be further analyzed. Note that a maximum intensity projection is a common way to transform a 3D information into a 2D image, best used when the objects of interest are the brightest objects in the image, and widely utilized for example in computer tomography. It was used here to eliminate the need to identify precisely the same z-plane position from 2D images sequentially acquired in different microscopes.

Background subtraction

An important part of this analysis was to isolate the pixel intensity coming from the fluorophores of interest and neglect the very low pixel intensities (looking as haze in the images) due to cell autofluorescence or glass slide's autofluorescence. There are various methods available for background subtraction in image processing, such as the Rolling ball background subtraction algorithm available on ImageJ. To minimize processing complexity (and possible resulting artifacts) I used here a simple background correction where the mean intensity in regions without cells (mostly due to autofluorescence from the glass substrate) was calculated and subtracted from the fluorescence images, using ImageJ's mathematics functionality that allows to subtract a numerical value from an image. An example of a 2D maximum intensity z projection of the fluorescence signal from the fluorophore A647 (see Chapter 4) embedded in fixed HeLa cells before and after background subtraction is shown on Figure 3.5.

Re-registration algorithm

This analysis step was implemented in order to overlay two images which might have a rotation and/or translation mismatch. The re-registration algorithm was written in Matlab by Dr. George Zorinians.

It is based on the following equation which aims to re-register two two-dimensional images based on a set of chosen coordinates from both images:

$$\mathbf{r}_a = \begin{bmatrix} a_1 & a_2 \\ a_3 & a_4 \end{bmatrix} \mathbf{r}_b + \begin{bmatrix} t_1 \\ t_2 \end{bmatrix} \quad (3.3.1)$$

Matrix $\mathbf{A} = \begin{bmatrix} a_1 & a_2 \\ a_3 & a_4 \end{bmatrix}$ contains rotation, stretching and/or squeezing mechanisms whilst vector $\mathbf{t} = \begin{bmatrix} t_1 \\ t_2 \end{bmatrix}$ describes lateral translations. In order to fully solve equation 3.3.1 we need to determine the values of the six unknown variables $(a_1 \dots a_4, t_1, t_2)$.

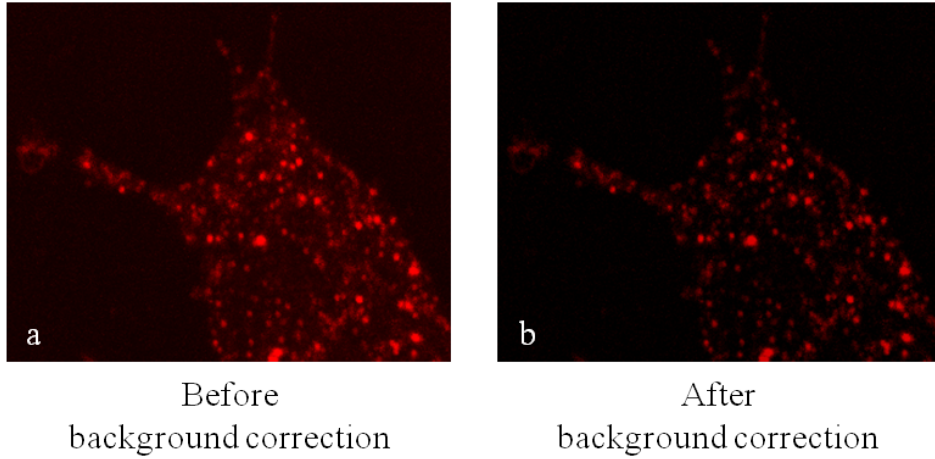


Figure 3.5: Example of confocal fluorescence background subtraction

Maximum intensity z projection images of fixed HeLa cells embedded with 40 nm AuNPs-SA:Bi-Tf-A647 imaged via confocal fluorescence microscopy. (a) Original maximum intensity projection image (b) maximum intensity projection image after background subtraction. Images are shown as RGB on a 0-255 intensity scale.

Given one pair of points (one from each image, assumed to represent the same position if the images were registered), $\mathbf{r}_a = (x_a, y_a)$ and $\mathbf{r}_b = (x_b, y_b)$, equation 3.3.1 leads to:

$$\begin{bmatrix} x_a \\ y_a \end{bmatrix} = \begin{bmatrix} a_1 & a_2 \\ a_3 & a_4 \end{bmatrix} \begin{bmatrix} x_b \\ y_b \end{bmatrix} + \begin{bmatrix} t_1 \\ t_2 \end{bmatrix} \quad (3.3.2)$$

Equation 3.3.2 can be re-written as a product of matrices as follows:

$$\begin{bmatrix} x_a \\ y_a \\ 1 \end{bmatrix} = \begin{bmatrix} a_1 & a_2 & t_1 \\ a_3 & a_4 & t_2 \\ 0 & 0 & 1 \end{bmatrix} \begin{bmatrix} x_b \\ y_b \\ 1 \end{bmatrix} \quad (3.3.3)$$

We can combine the unknown variables into a vector $[a_1, a_2, a_3, a_4, t_1, t_2]^\top$. In the general case of N pairs of points $(x_{a1}, y_{a1}), (x_{b1}, y_{b1}) \cdots (x_{aN}, y_{aN}), (x_{bN}, y_{bN})$, equation 3.3.3 applied for all pairs takes the form below:

$$\begin{bmatrix} x_{b1} & y_{b1} & 0 & 0 & 1 & 0 \\ 0 & 0 & x_{b1} & y_{b1} & 0 & 1 \\ \vdots & \vdots & \dots & \vdots & \vdots & \vdots \\ x_{bN} & y_{bN} & 0 & 0 & 1 & 0 \\ 0 & 0 & x_{bN} & y_{bN} & 0 & 1 \end{bmatrix} \begin{bmatrix} a_1 \\ a_2 \\ a_3 \\ a_4 \\ t_1 \\ t_2 \end{bmatrix} = \begin{bmatrix} x_{a1} \\ y_{a1} \\ \vdots \\ x_{aN} \\ y_{aN} \end{bmatrix} \quad (3.3.4)$$

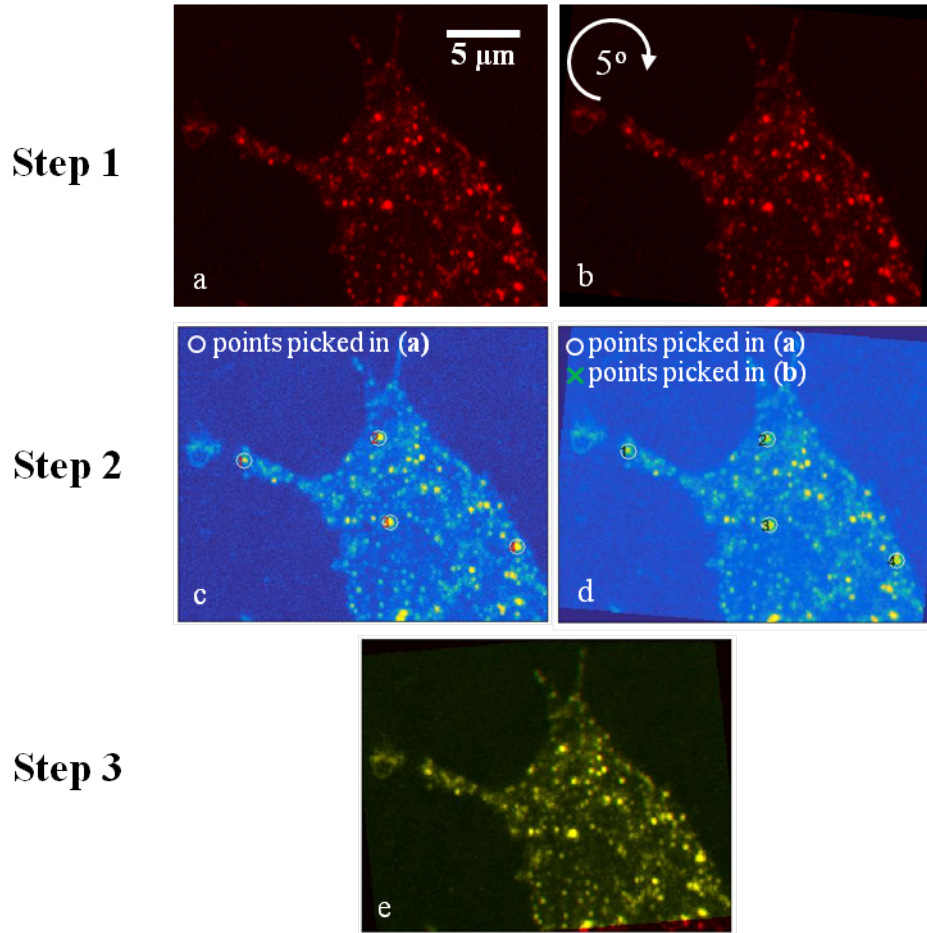


Figure 3.6: Evaluation of the re-registration algorithm

Step 1: image (b) is the rotated by 5° image (a), Step 2: image (c) shows the (x,y) points picked in image (a), whilst image (d) shows the points on both images (a and b) on top of image (b), Step 3: image (e) is the re-registered image (b) on top of image (a).

which can take the general form of

$$Ax = b \quad (3.3.5)$$

where, in our case, $x = [a_1, a_2, a_3, a_4, t_1, t_2]^T$ contains the unknown parameters to be identified. We compute x as the least squares solution of equation 3.3.5. ⁴

In the end the algorithm produces three images, one where the chosen points (x_{1n}, y_{1n}) of Image 1 are shown, a second one where the chosen pairs of points from both images are shown on the ‘transformed’ image and a third one which is an overlay of the initial image with the transformed or re-registered one, where the first one appears in red and the second one in green and hence the result is produced based on pixel intensity overlapping with the maximum overlay appearing yellow for visualization purposes.

⁴ $x^* = \min_x (Ax - b)^T (Ax - b)$ which in Matlab is equivalent to $x = A \setminus b$.

In order to validate the algorithm's accuracy on our experimental results, since the procedure is based on manual selection of coordinates, we performed the test whose results are depicted in Figure 3.6. There, we start with the maximum intensity projection of a confocal fluorescence z-stack of images as the image number 1 of the pair that we wish to register and overlay. Image number 2 is image 1 rotated clock-wise by 5° . Four well-recognized points of the images are chosen as given points – (x,y) pairs of both images– and are shown in Step 2 (Figure 3.6 (c),(d)). In Step 3 of the figure, we see the re-registered image (b) on top of image (a) which comes along with a calculated root mean squared error⁵ of 12.6 nm indicating the accuracy of the manual coordinate selection (since we know that the two images are identical upon rotation). These results suggest that the re-registration algorithm is a simple way capable of re-registering the fluorescence images obtained in different microscopes with respect to the FWM images and produce an overlay image where further colocalization analysis can be performed.

Colocalization analysis

This analysis was inspired and practiced via the S. Bolte & F.P.Cordelieres' toolbox named JACoP (Just Another Colocalization Plugin) available on ImageJ. JACoP is an integrated toolbox of all the current quantitative subcellular colocalization methods in fluorescence microscopy where the user is able to choose the analysis that fits better to his needs. For a detailed review of the toolbox as well as a general overview of colocalization approaches in light microscopy, see Ref [97].

A number of colocalization analysis methods spanning from qualitative ones based on overlapping pixels to rather complex and tailored approaches whom their vast majority is based on global statistic analysis of pixel intensity distributions [98] [99] [100] are available nowadays. However, these methods are usually applied to fluorescence microscopy and arise from the question whether two fluorophores overlap and hence reside in the same biological structure. The question becomes more challenging for the 3D space or even more for 4D (live imaging). Diffraction limitations imposed by Abbe law (xy resolution $\lambda/2NA$, z resolution $2\lambda/NA^2$), as well as the nature of the sample –for example biological samples are not 2D limited– and optimum imaging acquisition (avoid oversampling or downsampling for best results) need to be taken into account beforehand and in the chosen image analysis.

For the work in this thesis, I chose to perform correlation analysis on the linearly transformed overlaid images derived from the Matlab algorithm described in the previous subsection, based on the Pearson's coefficient (PC) and the Manders' coef-

⁵Error S= $\sqrt{\frac{1}{N} \sum |\mathbf{r}_b - (A\mathbf{r}_a + \mathbf{t})|^2}$

ficient (M) with the last to be applied only for the FWM channel. Both coefficients shown on the results of sections 4.2.2 and 4.3 were calculated via JACoP plugin. These coefficients evaluate colocalization by using statistics to assess the relationship between pixel intensities. In our case, PC (here is represented by the letter r_p) measured the linear correlation of the grey values of the intensity pixels of the FWM and fluorescence image pairs, while the Manders' coefficient measured the ratio of the 'summed intensity of FWM pixels for which the intensity of the fluorescence pixels is above zero' to the total intensity of the FWM channel [97][98]. Let's assume a dual channel image where A_i represents the pixel intensity in grey values of voxel i in channel A and B_i corresponds to the respective values for channel B. The average image intensities of each channel are also noted as a and b . The formulas 3.3.6 below calculate the PC (r_p) and Manders for each channel (M_A and M_B). For M_A and M_B , we define $A_{i,col}$ as A_i for $B_i > 0$ and 0 for $B_i = 0$, similarly $B_{i,col}$ as B_i for $A_i > 0$ and 0 for $A_i = 0$. The Manders' coefficient is very sensitive to noise. To circumvent this limit, M_A and M_B may be calculated by setting a threshold to the estimated value of the background instead of zero⁶.

$$r_p = \frac{\sum_i (A_i - a) \times (B_i - b)}{\sqrt{\sum_i (A_i - a)^2 \times \sum_i (B_i - b)^2}} \quad (3.3.6)$$

$$M_A = \frac{\sum_i A_{i,col}}{\sum_i A_i} \quad (3.3.7)$$

$$M_B = \frac{\sum_i B_{i,col}}{\sum_i B_i} \quad (3.3.8)$$

3.4 Miscellaneous materials

A significant part of the work for this thesis was also dedicated to producing different kind of samples from simple drop-casted AuNPs on 'piranha' etched glass coverslips to biological samples where appropriate biological protocols had to be followed. Due to the fact that the samples shown in this work involved usage of different materials and implementation of different techniques, they will be described in separate subsections in their corresponding results chapter. However, here miscellaneous materials and general information is given regarding products used in the chemistry and tissue culture laboratories used for the realization of this work.

⁶The threshold values in the analysis of Manders' coefficients were picked by the JACoP Image-J plugin. Alterations of the plugin's default values did not impact our data.

3.4.1 Miscellaneous materials used in Chemistry Laboratory

Various chemicals and appropriate glassware were used as part of samples' preparation. In more details, acetone, methanol, ethanol, sulphuric acid, 30% hydrogen peroxide were mainly used for cleaning purposes of glass slides and coverslips. They were purchased from Sigma-Aldrich along with silicon oil (refractive index $n = 1.518$) for embedding samples and matching the refractive index of the oil-immersion microscope objective. Glass coverslips varied from square $25 \times 25 \text{ mm}^2$ of thickness No. 1.5 obtained from Menzel-Glaser to circular ones of No. 1.5 and 25 mm diameter. All the glassware used in this thesis, such as 5 and 10 ml glass graduated cylinders, various sizes of borosilicate glass beakers as well as 50ml falcon tubes used for storage, were obtained from Fisher Scientific (Loughborough, UK). Bare gold nanoparticles of different sizes were obtained from BBI Solutions (Cardiff, UK).

3.4.2 Miscellaneous materials used in Tissue Culture Laboratory

Part of the samples shown in Chapter 4 were produced by our collaborators on this part of the project in Cardiff School of Pharmacy (Dr. P. Moody) and Nottingham School of Pharmacy (Dr. J.P. Magnusson). However partly due to the occurrence of unexpected results but also for requirements of repeatability, many of the samples were produced directly by myself and tissue culture protocols had to be implemented leading to regular use of the tissue culture facilities. This part concerns the maintenance and growth of human cervical cells known as HeLa.

Materials

HeLa cells were obtained from the American Type Culture Collection (Teddington, UK), Modified Eagle Medium (MEM GlutaMAXTM-I), Fetal Bovine Serum (FBS), were purchased from Life Technologies (Warrington, UK) as well as Trypsin (0.25%) and phosphate buffered saline (PBS, pH 7.4).

Cell culture

HeLa cells were maintained in a humidified 5 % CO₂ environment at 37° C using the media recipe described below. Cells were split twice weekly using 0.25% Trypsin for 5 min to detach cells from the growth plate. Cells were plated in 10 cm plastic dishes (Fisher, Chirchester, UK) at concentrations of 1:5, 1:10 and 1:20 dilution in growth medium. For microscopy experiments cells were grown on glass coverslips in 6 well dishes.

Media 'recipe':

- 1x MEM GlutaMAXTM-I
- 1x NEAA (Non-Essential Amino Acid)
- 1x Na Pyruvate
- 10% FBS

4

IMAGING OF BIO-CONJUGATED AuPsN HUMAN AND MOUSE CELLS

4.1 Introduction

All samples studied in this thesis involved fluorescently labelled bioconjugated AuNPs. These were generated either using in-house developed protocols, where the AuNPs were attached to a fluorescently labelled ligand via a polymer coat, or via the streptavidin-biotin (SA:Bi) bond, or using commercially available kits where the AuNPs were attached to fluorescently labelled antibodies. Specifically, four types of constructs were investigated and are summarised in Table 4.1 based on the protocol used, the AuNP core and the fluorescent biomolecule used in each case. Three of the constructs aimed at clathrin-mediated endocytosis in HeLa cells via the ligand transferrin (Tf) which was fluorescently labelled, while the fourth type of constructs encompassed antibodies, one specific to the transferrin receptor (TfR) (non fluorescent) and one non specific (fluorescently labelled) in mouse cells (3T3-L1). From the last type, only the construct containing the fluorescent antibody for unspecific uptake is presented in Table 4.1 for consistency with the overall summary of fluorescently labelled samples.

In order to better address the different characteristics of the samples used alongside their results, this chapter is divided into three sections based on the biological protocol/strategy employed in each construct. The first section *Measurements*

Sample	AuNP diameter	Shell	Sequential labelling
40nm AuNP-SA:Bi-Tf(A647)	40nm	SA (cb)	Bi-Tf(A647)
10nm AuNP-SA(A488):Bi-Tf(A647)	10nm	SA(A488)(ad)	Bi-Tf(A647)
15nm AuNP-PC-Tf(A488)	15nm	PC-Tf(A488)(cb)	No
20nm AuNP-PC-Ab(A647)	20nm	PC-Tf(A647)(cb)	No

Table 4.1: Bioconjugated fluorescently labelled AuNPs used in this study. SA: streptavidin, Bi: biotin, PC: polymer coat, Tf: transferrin, Ab: antibody, A488: AlexaFluor488, A647: AlexaFluor647, cb: covalent bond, ad: adsorbed

of AuNPs conjugated with Transferrin in HeLa cells presents a correlative FWM-fluorescence study of fluorescently labelled constructs of 40 nm and 10 nm AuNP embedded in HeLa cells and used for cellular uptake studies. Gold NPs were purchased already bound to streptavidin, either via a covalent bond (40 nm AuNP-SA, Innova Biosciences), or via adsorption (10 nm AuNP-SA-A488, Molecular Probes). Tf was purchased covalently bound to biotin (Sigma-Aldrich) and was attached to the fluorophore A647, using a protocol developed in house. This project involved close collaboration with A.T. Jones group in Cardiff School of Pharmacy where the biological concept behind the preparation protocol of this sample group was first introduced to the scientific community in their recent work [47]. The samples outlined in section (4.2.2) were fabricated and imaged via confocal fluorescence in Cardiff School of Pharmacy and were later sent to our lab for FWM measurements and correlative analysis which I performed.

The second section *Measurements of polymer coated 15 nm AuNPs uptaken by HeLa cells* shows correlative FWM-fluorescence results on polymer coated (PC) 15 nm AuNPs attached to a fluorescently labelled Tf using the fluorophore A488 (see Table 4.1). The PC-AuNPs were fabricated by our collaborators in Nottingham School of Pharmacy while the cell culture protocols alongside the confocal fluorescence measurements were conducted in Cardiff School of Pharmacy. Similar to the previous section, the samples were sent to our lab for FWM measurements and correlative analysis which I performed (section 4.3.1).

In addition to the samples produced by our biology-expert collaborators, there are samples shown in this chapter which were fabricated solely by myself. During my PhD years I learned basic tissue culture techniques and was able to reproduce the biological protocols and make new samples in order to perform additional measurements and/or validate results. These experiments led to the results shown in sections 4.2.3 and 4.3.2.

Finally, the last section *Imaging of 20 nm AuNPs conjugated with various types of antibodies in 3T3 cells* shows samples prepared (by my co-supervisor Dr. P. Wat-

son) using a commercially available bio-conjugation kit (Innova Biosciences, see also Table 4.1). Simultaneous FWM and confocal fluorescence imaging measurements were performed by myself on an array of three different samples having different antibody combinations and the fluorophore label A647 (see Table 4.2). These additional measurements aimed at investigating further the co-localization between fluorescence and FWM signal on state of the art samples, as well as performing simultaneous FWM and confocal fluorescence measurements on the same experimental set-up without the need of post acquisition image registration analysis.

4.2 Measurements of AuNPs conjugated with transferrin in HeLa cells

4.2.1 Sample description and experimental flow

As mentioned in the *Introduction* of this chapter, the core of the sample protocol for the bioconjugated AuNPs attached to Tf via SA:Bi bond lies on the recent work [47] of our co-workers in Cardiff School of Pharmacy. Tf-mediated endocytosis is a type of receptor mediated endocytosis (RME), i.e. clathrin-mediated, and is the major iron uptake route for cells [101]. In the research field of drug delivery systems it has been thoroughly characterised for targeting therapeutics in subcellular organelles such as lysosomes. Briefly, the trafficking route of Tf includes first the binding of the ligand with the transferrin receptor (TfR) and their internalisation from the cell membrane via clathrin coated pits. These pits mature to endosomes which can either recycle back to the membrane or follow the endolysosomal pathway and end up in the lysosomes for degradation [102], [103],[104].

Our collaborators demonstrated enhanced lysosomal trafficking of three administrative proteins (transferrin, anti-MHC class I antibody and anti-Her2 antibody trastuzumab) via formation of SA:Bi complexes on the cell membrane. To do so, they developed the *sequential labelling protocol*, shown on Figure 4.1 which involved several washing steps and incubation on ice (described in the following) in order to prevent (i) formation of clusters, and (ii) early Tf-Bi-A647 endocytosis before the SA addition. Notably, there are 4-8 molecules of Biotin per transferrin molecule (based on the manufacturer product's specifications) and moreover streptavidin can bind up to 4 Biotin which results in the formation of Tf-Bi-A647:SA aggregates if the counter parts are co-incubated. This is why the sequential labelling protocol is needed, as opposed to creating SA:Bi conjugates in a vial, prior administration to the cell. It is also important to mention that the published results in [47] were obtained in live cells and without any usage of gold NPs attached to the streptavidin

as opposed to our case.

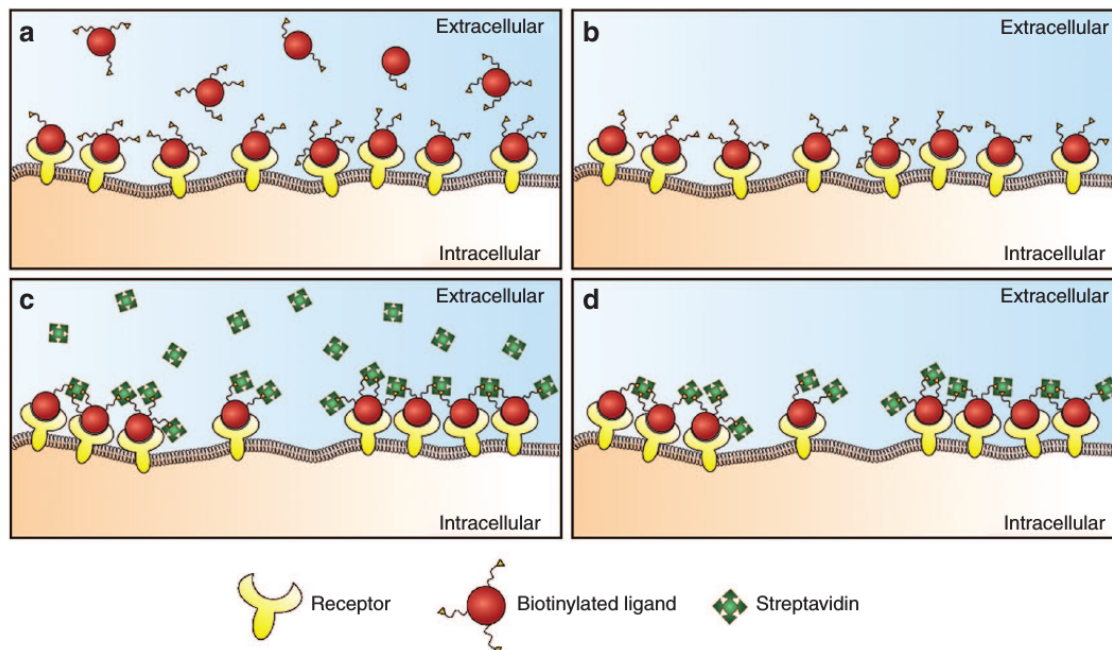


Figure 4.1: The sequential labelling protocol

(a) Exogenous biotinylated protein is added to cells kept at 4 ° C. (b) Excess unbound protein is removed by washing. (c) Streptavidin is added to cells, which has the capacity to cluster receptors by formation of extended cross-links between receptor:ligand–biotin complexes. (d) Excess streptavidin is removed by washing prior to incubation at 37 ° C. [FIGURE AND CAPTION REPRODUCED WITH PERMISSION FROM REF [47]]

Sequential labelling of HeLa cells with Tf-Bi-A647 and AuNPs-SA

HeLa cells obtained from ATCC were passaged every third day and were maintained as a subconfluent monolayer in normal media under standard tissue culture conditions¹. HeLa cells were grown on 24 x 24 mm photoetched gridded square coverslips of thickness No.2 purchased by Electron Microscopy Sciences for the 40 nm AuNP sample and on 25 mm diameter circular coverslips (not gridded) of thickness No. 1.5 purchased from Fisher Scientific for the 10 nm AuNP sample. The fluorescently labelled biotinylated transferrin² (Tf-Bi-A647) was generated as per protocol described by Moody et al. [47] and is also repeated here. Lyophilized biotinylated Tf (5 mg) was suspended in 1 ml PBS pH 7.4 and then added directly to 1 mg NHS-A647 and reacted for 1 hour at room temperature to generate Tf-Bi-A647. The conjugate was later purified from unreacted A647 into PBS pH 7.4 using a G-50 sephadex gel filtration column (Life Technologies, Paisley, UK). As mentioned earlier, a sequential labelling protocol was used in order to avoid aggregation [105]

¹Miscellaneous materials and standard processes are described in section 3.4.2

²Moody et al.[47] showed that biotinylation does not affect the rate of Tf recycling.

and lack of functionality of the Tf and is described below:

On the day of the experiment, cells were starved for 30 min in serum-free medium to allow recycling of serum-derived transferrin. For the **40 nm AuNP sample**, cells were placed on ice for 10 min to inhibit endocytosis. They were after incubated with 50 µg/ml Tf-Bi-A647 in ice-cold serum-free medium for 8 min and then washed 3 times in ice-cold PBS pH 7.4. Cells were after incubated with 1 in 10 dilution of the stock concentration of the SA-AuNPs solution in ice-cold serum-free medium for 10 min and then again washed 3 times in ice-cold PBS pH 7.4. For the **10 nm AuNP sample**, cells were incubated for 30 min in serum-free medium and they were after placed on ice for 15 min to inhibit endocytosis. They were then incubated with 20 µg/ml Tf-Bi-A647 in ice-cold serum-free medium for 15 min and washed 3 times in ice-cold PBS pH 7.4. Cells were then incubated with the 10 nm diameter AuNP-SA(A488) at a protein concentration of 1 µg/ml (this corresponds to 1 in 30 dilution from the stock solution) in ice-cold serum-free medium for 15 min, and washed 3 times in ice-cold PBS pH 7.4.

The SA-conjugated AuNPs solutions were purchased from Innova Biosciences for the 40 nm AuNPs-SA and from Molecular Probes for the fluorescently labelled 10 nm AuNPs-SA-A488, where the streptavidin molecule was labelled with the A488 dye.

Final Incubation part and fixation

40 nm AuNP-SA:Bi-Tf(A647)

After the last washing step, cells were incubated in pre-warmed imaging medium, containing phenol red-free DMEM pH 7.4 with 25 mM HEPES and supplemented with 10 % v/v heat inactivated FBS, for 6 hours (*chase part*). They were then fixed in 3 % PFA at room temperature for 10 min, washed 3 times with room temperature PBS pH 7.4 and then mounted on microscope glass slides with 80 % DAKO medium purchased from Dako UK Ltd.

10 nm AuNP-SA(A488):Bi-Tf(A647)

Differently from the 40 nm AuNP sample, cells were not chased but were fixed in ice-cold 4 % PFA for 20 min after the last part of the sequential labelling protocol and washed 3 times with ice-cold PBS pH 7.4 before mounted with Mowiol³ medium (produced in house) on microscope glass slides. The direct fixation was chosen in

³Mowiol (n= 1.41 - 1.49) is a widely utilised mounting medium which is known to excel over other media due to the fact that is liquid when first mounting the sample and then it solidifies after several hours. It is ideal for fluorescence imaging as it has been observed to keep the fluorescence stable when the sample is held in dark and at 4 °C [106].

order to ‘capture’ the AuNP-SA(A488):Bi-Tf(A647) labelled construct on the cell surface, as opposed to the internalised 40 nm AuNP samples that had trafficked for 6 hours inside live cells, prior fixation.

Figure 4.2 is a representative illustration of the structure of the 40 nm AuNP-SA:Bi-Tf-A647 construct when it binds to the TfR on the cell membrane.

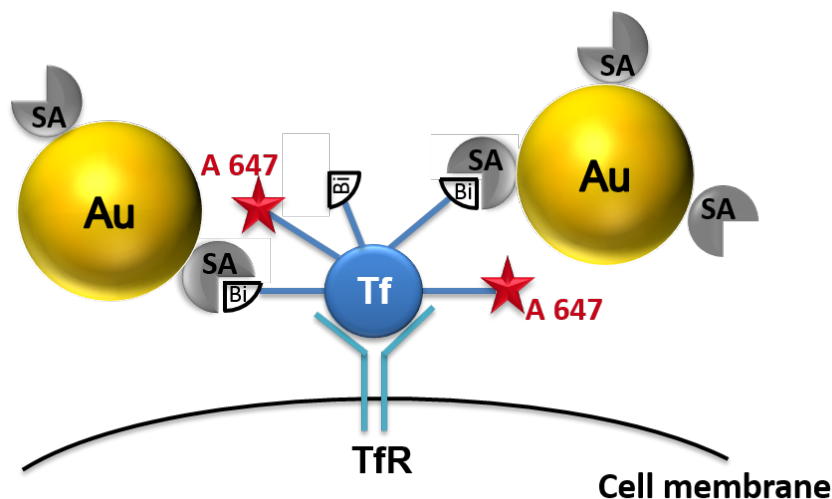


Figure 4.2: Sketch of the 40nm AuNP-SA:Bi-Tf(A647) construct bound to TfR on the cell membrane before internalisation. For the 10nm AuNP-SA(A488):Bi-Tf(A647), the streptavidin protein would be also fluorescently labelled using the A488 fluorophore.

There is an important distinction between the two SA-conjugated AuNPs commercial solutions used, which is the type of AuNP-SA bond. In the case of the 40 nm AuNP-SA construct the nanoparticles are covalently attached to the unlabelled SA while the 10 nm AuNPs are non-covalently bound (adsorbed) to the fluorescently labelled SA (see Table 4.1). As a result, the 40 nm AuNP-SA:Bi-Tf(A647) is expected to be a more robust construct (in terms of AuNP-SA bonding) which can supposedly be internalised as one entity and proceed to endosomal trafficking. Conversely, the non-covalent bond between the 10 nm AuNPs and SA may disassociate under the same conditions. However, according to the biological protocol used the 10 nm AuNP construct is not expected to undertake internalisation as it was fixed straight after the sequential labelling protocol. Nonetheless, this distinction is important when these constructs are chosen as probes for cellular uptake experiments.

Experimental flow

The workflow for the realization of these experiments is illustrated on Figure 4.3 and explained below. Initially, HeLa cells with the 40 nm AuNP-SA:Bi-Tf(A647) (10 nm AuNP-SA(A488):Bi-Tf(A647)) were prepared by our collaborators in Cardiff School of Pharmacy (by myself) and then imaged shortly after being mounted on a

glass slide on a confocal (widefield) fluorescence microscope. For the 40 nm AuNP sample, specific cell regions were indicated by our collaborators using combinations of numbers and letters of the gridded coverslip. Figure 4.4 is a representative example of the grid's and letters'/numbers' visibility as well as how cell regions cultured on these coverslips and treated by the sequential labelling protocol look like on a commercially available confocal microscope via DIC imaging. In many regions of the sample, cells were 'missing' due to the multiple washing steps of the protocol while others were sometimes 'shrunk' (if surrounded by others) because of the ice steps involved. In fact, there were cases in which the sample preparation had to be repeated several times in order to achieve a worth-investigating sample.

After the sample arrived in our lab, the same regions were found via DIC microscopy on our multi-modal microscope and were after imaged via FWM. In the case of the 10 nm AuNP sample (no gridded coverslips used), the cell regions imaged on the widefield fluorescence microscope, were found after laborious DIC imaging under low magnification objective on our multi-modal microscope. The last part of the workflow comprised the correlation analysis, described in 3.3.2, via the application of the re-registration algorithm on the confocal fluorescence image in order to match the FWM image and the calculation of the correlation coefficients on the merged produced image of the two modalities. This analysis was applied only to the samples that exhibited distinct fluorescence and FWM signals on both images. In cases where the results revealed no correlation between the two signals, this analysis was not applied and the comparison remained to a qualitative level.

4.2.2 Results and discussion on Hela cells incubated with 40nm AuNP-SA:Bi-Tf(A647)

In this section, the results on correlative FWM-confocal fluorescence imaging on HeLa cells incubated with 40 nm AuNP-SA:Bi-Tf(A647) are presented.

Figures 4.6 and 4.7 constitute representative results of two different regions including one or more cells on the sample. FWM imaging succeeded the DIC imaging and was acquired using the 100x 1.45 NA oil-immersion objective and 1.5x tube lens, pump (probe) power 31 μW (15.5 μW) at the sample with a pump-probe delay time of 0.5 ps (corresponding to the maximum FWM signal as a result of the ultrafast heating of the electron gas in gold[45]), 2 ms pixel dwell time and in plane pixel size of 94 nm. Furthermore, FWM acquisition was performed in z-stack from the coverslip-cell interface upwards till no AuNPs can be observed, with the axial step size set to 250 nm. In Figures 4.6 and 4.7, DIC images of the cell regions show spatially varying contrast derived from thickness and refractive index inhomogeneities

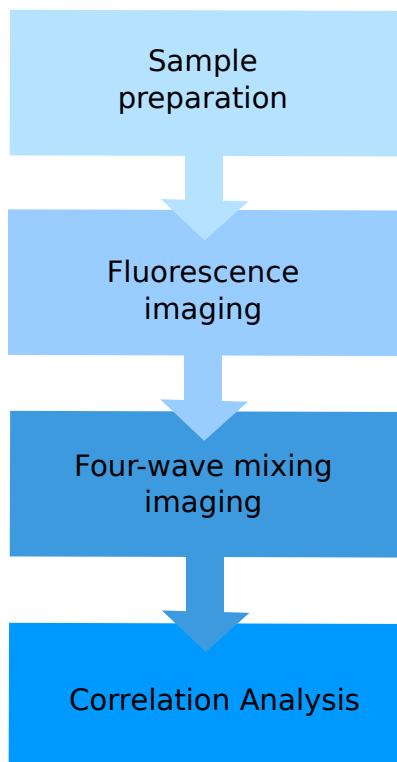


Figure 4.3: Experimental flowgram for the measurements of AuNPs conjugated with transferrin in HeLa cells shown in sections 4.2.2 and 4.3.2.

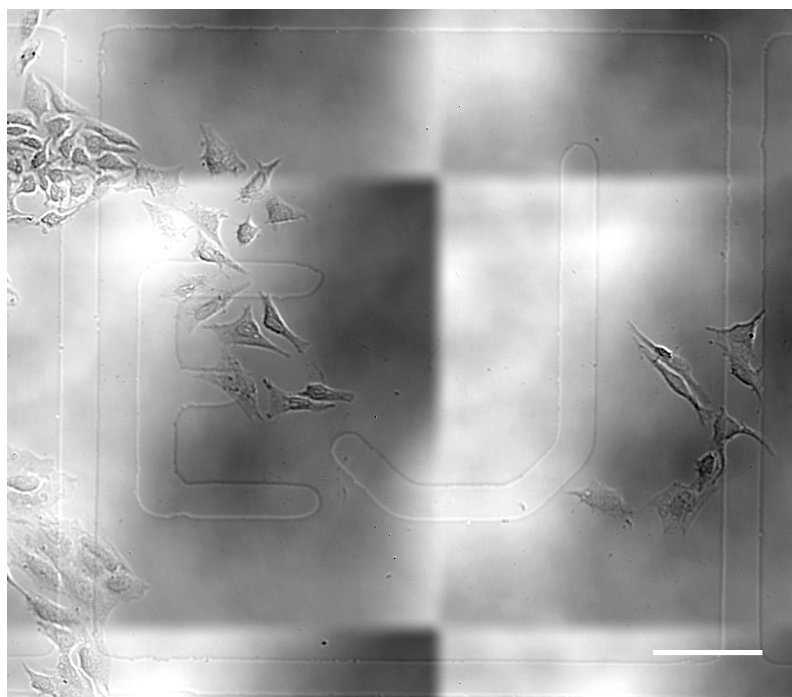


Figure 4.4: Example of fixed HeLa cells cultured on a gridded coverslip (different sample than the ones shown later on this chapter) imaged via DIC on a tile mode on the Zeiss LSM 880 confocal fluorescence microscope with a plan-apochromat 20x air objective with 0.8 NA. Photoetched squares with alphanumeric pattern assisted our correlative imaging measurements carried out on different microscopes. The scale bar of the image is 100 μm , while its contrast has been adjusted to enhance the pattern's visibility.

in the biological sample. Dashed rectangles on the DIC images highlight the region of interest (ROI) imaged via FWM and fluorescence and can easily be correlated with the cell contour of the co-circularly polarised reflection images. Each figure set also comprises sets of maximum intensity projection images originating from the co-polarised FWM amplitude (A_{FWM}^+) analysed z-stack images and the corresponding confocal fluorescence ones, alongside the co-circularly polarised amplitude reflection (A_{2r}^+) shown on a single xy plane and finally the re-registered overlay of the previous two as a product of the Matlab algorithm described in part 3.3.2. As explained in Chapter 3, we can also detect the cross-circularly polarised reflection and FWM components. These carry information regarding the particle asymmetry, as detailed in [44]. For the scope of the work in this thesis, namely imaging the position of AuNPs correlatively with that of bio-conjugated fluorophores, such cross-polarised detection does not add further information and is therefore not discussed in the following.

For each region the calculated ⁴ co-localisation coefficients of Pearson's (r_p) and Mander's (M_{FWM}) for the FWM channel based on the re-registered overlay image are given next to each data set. Both calculated values indicate negligible spatial co-localisation between the FWM image and the re-registered confocal fluorescence one. Note that, in most published works the PC values that are considered to prove significant degree of co-localisation, beyond the noise in the data, are above 0.7. Moreover, the low M_{FWM} values (which quantify the proportion of FWM pixels for which the pixel intensity of the corresponding fluorescent ones is above zero (or the set background threshold)) proved that most AuNPs did not co-localise with a fluorescence intensity, i.e. either they did not longer have the fluorophore attached, or the fluorescent dye at the NP was quenched.

The absence of co-localisation between the FWM signal (AuNPs) and the confocal fluorescence (fluorescently labelled Tf), is surprising considering that SA is covalently attached to the AuNP which in turns binds to Bi with extraordinary affinity ($K_d = 10^{-14}\text{M}$ [107]); yet the found correlation was minimal. There are regions of the cell that exhibit distinct fluorescent signal that can be attributed to the Tf-A647 label but do not show FWM signal and thereby presence of AuNPs, as well as the contrary. Generally, we observe a significantly larger number of fluorescent spots than AuNPs. These findings could be explained by a number of reasons, as follows. Unbound streptavidin might be present in the commercially available stock solution of 40 nm AuNP-SA, which in turn binds Bi-Tf(A647). This could explain the observation of fluorescence from A647 as expected from internalized Tf, but not co-localised with AuNPs. The entry of the 'bulky' 40 nm AuNP-SA:Bi-Tf(A647)

⁴as described in 3.3.2

construct is inhibited, as compared to the unbound SA:Bi-Tf(A647). This could explain the larger number of fluorescent spots compared to AuNPs. There is a dissociation of the 40 nm AuNP-SA:Bi-Tf(A647) construct while undergoing endocytosis as well as a potential degradation of the Tf-A647 by the lysosomes due to the 6h trafficking (chase part of the biological protocol) similar to what suggested by Wu et al. [108] for quantum-dot nucleic acid conjugates. Finally, the fluorophore might be quenched near the surface of AuNPs, similar to what reported by Miles et al. [48] on commercial 10 nm AuNPs-Alexa633 fluorophore conjugates. For comparison, Hela cells incubated with the 10 nm AuNP-SA(A488):Bi-Tf(A647) discussed in the following had no chasing part and mostly membrane labelling by fixing the cells straight after the sequential labelling part.

Notably, Figure 4.5 shows that FWM signal is detected when the pump-probe delay is set to 0.5 ps while there is no signal generation for negative delay (in this case $\tau_{\text{pump}} = -1$ ps) as expected from the physical origin of this electronically resonant FWM in gold which vanishes over a few hundred ps time scale [45], as opposed to long-lived photothermal effects that could persist beyond the 13 ns time-interval between pulses, and would manifest as a signal at negative pump-probe delay.

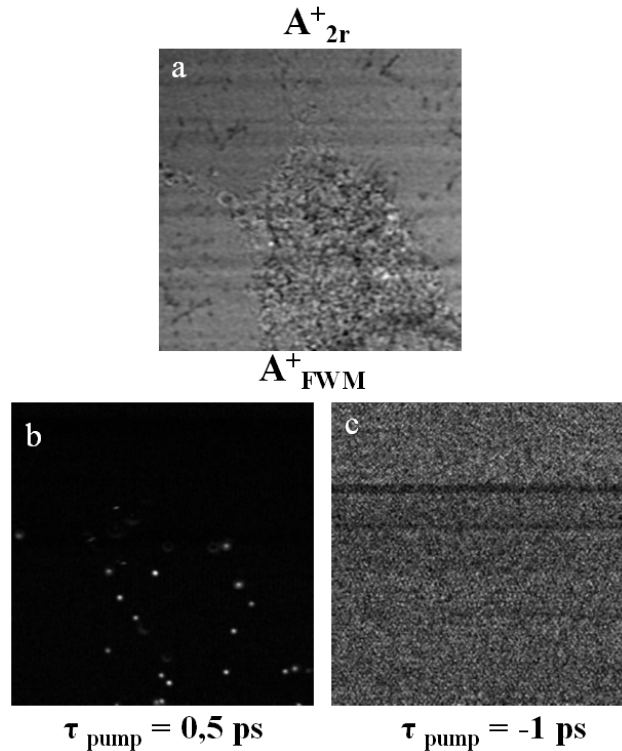


Figure 4.5: Representative example of xy raster scan with 0.5 ps and -1 ps pump-probe delay. Image (a) refers to the co-circularly polarized amplitude reflection while (b) and (c) refer to the co-circularly polarized FWM amplitude. When the pump-probe delay is negative the FWM signal originating from the AuNPs can not be observed.

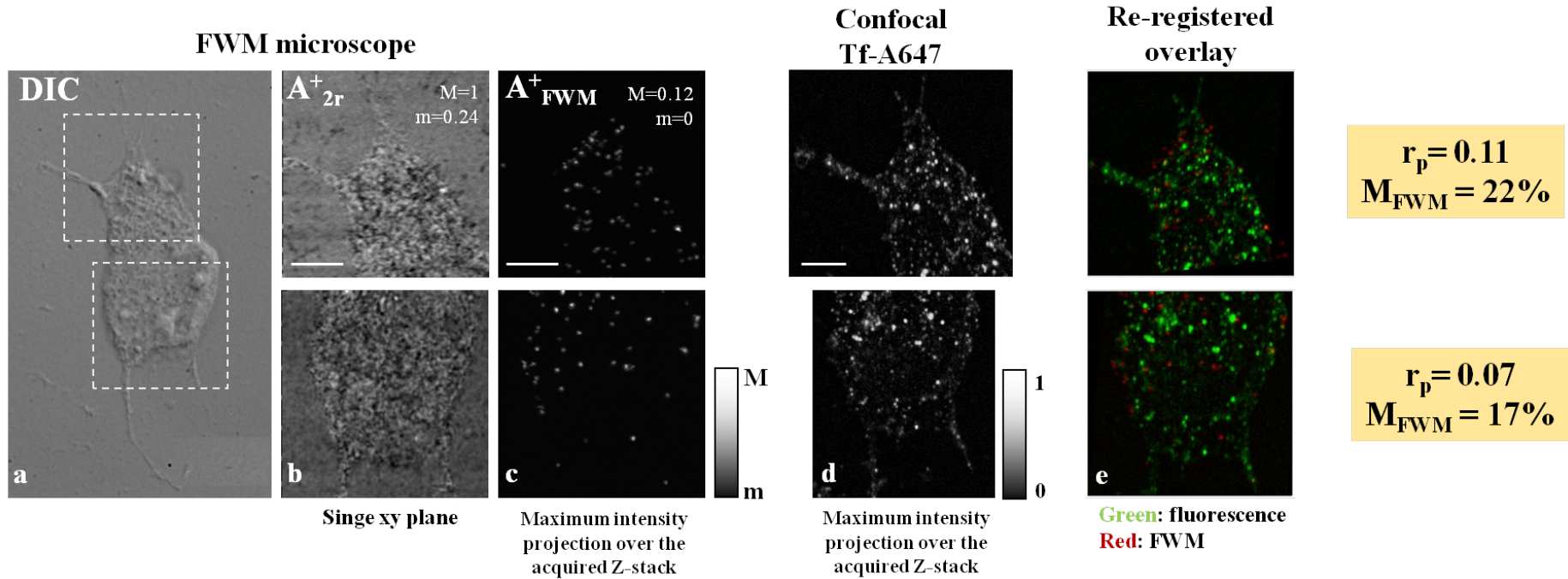


Figure 4.6: 40nm AuNP-SA:Bi-Tf(A647) - Region 1

(a) DIC image of a fixed HeLa cell where two dashed rectangulars show $20 \times 20 \mu\text{m}$ cellular regions imaged in 3D via reflection and FWM (b,c) and confocal fluorescence (d). The co-circularly polarised reflection (b), A_{2r}^+ , is shown as a single (x,y) plane while the co-circularly polarised FWM, A_{FWM}^+ , (c) and confocal fluorescence (d) channels are shown as maximum intensity projections over $5 \mu\text{m}$ axial direction. Amplitude scales from m to M are indicated in each image for the FWM acquisition while in fluorescence the scale spans from 0 to 1 corresponding to 255 grey levels. Fluorescence was background subtracted as explained in Fig.3.5. The scale bar for the FWM and reflection images is $5 \mu\text{m}$. The re-registered overlay (e) of the confocal fluorescence (green) –representing the fluorescently labelled Tf– on top of the FWM signal (red) –representing the location of gold NPs in the cell– is shown alongside the calculated correlation coefficients.

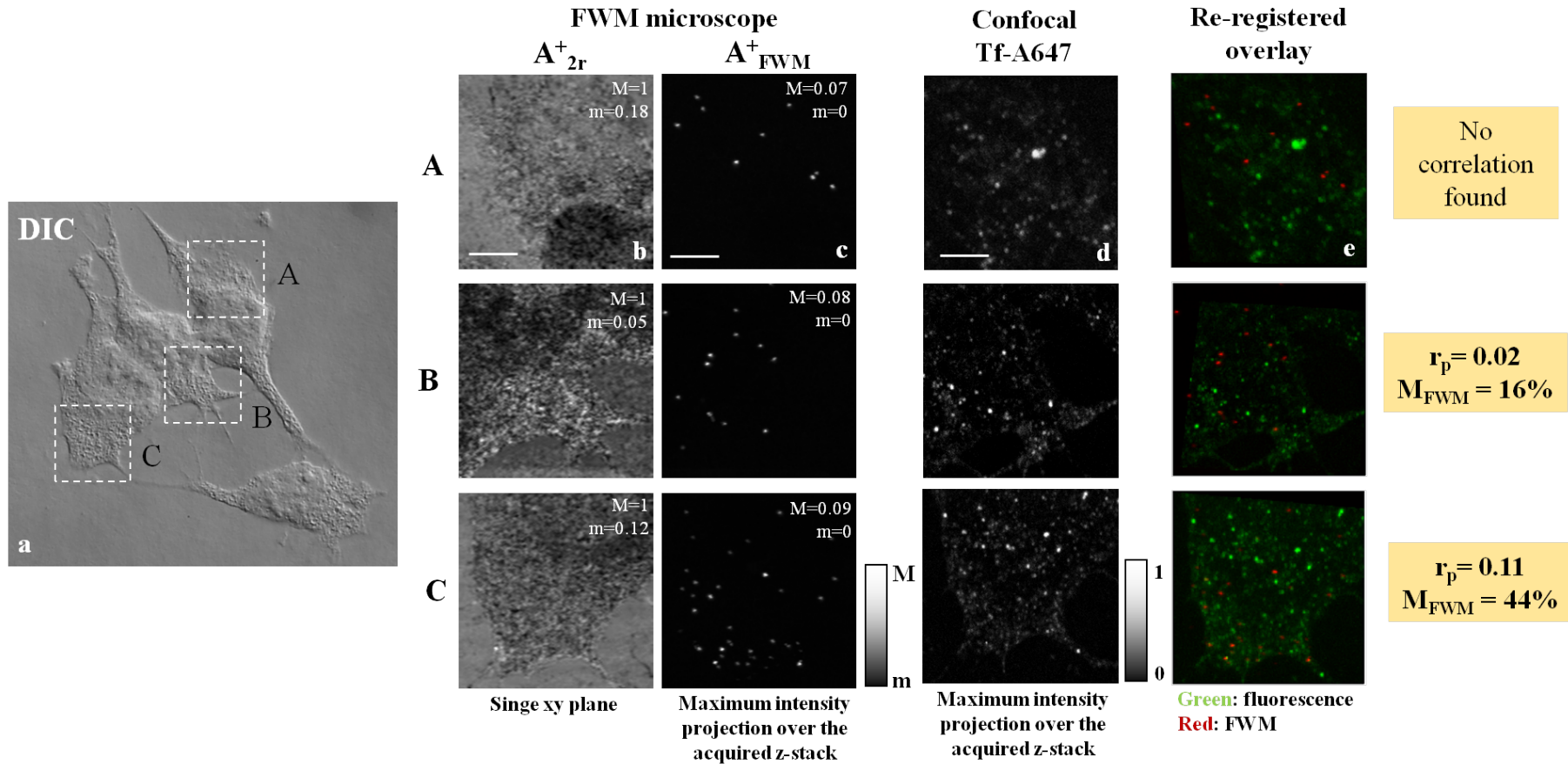


Figure 4.7: 40nm AuNP-SA:Bi-Tf(A647) - Region 2

(a) DIC image of fixed HeLa cells where three dashed rectangulars show $20 \times 20 \mu\text{m}$ cellular regions of interest in different cells imaged in 3D via reflection, FWM (b,c) and confocal fluorescence (d). The co-circularly polarised reflection (b), A_{2r}^+ , is shown as a single (x,y) plane while the co-circularly polarised FWM, A_{FWM}^+ , (c) and confocal fluorescence (d) channels are shown as maximum intensity projections over $5 \mu\text{m}$ axial direction. Amplitude scales from m to M are indicated in each image for the FWM acquisition while in fluorescence the scale spans from 0 to 1 corresponding to 255 grey levels. Fluorescence was background subtracted as explained in Fig.3.5. The scale bar for the FWM and reflection images is $5 \mu\text{m}$. The re-registered overlay (e) of the confocal fluorescence (green) –representing the fluorescently labelled Tf– on top of the FWM signal (red) –representing the location of gold NPs in the cell– is shown alongside the calculated correlation coefficients.

4.2.3 Results and discussion on HeLa cells incubated with 10nm AuNP-SA(A488):Bi-Tf(A647)

In order to further investigate the reasons of lack of co-localisation between the fluorescently labelled Tf ligand and the FWM signal coming from gold nanoparticles observed, as described previously, similar measurements were performed on 10nm AuNP-SA(A488):Bi-Tf(A647) and are shown in this section. The motivation behind the implementation of these experiments lies on the advantage of using a significantly smaller diameter size –as a further potential for easier internalisation– of AuNPs (10 nm instead of 40 nm) as well as having dual fluorophore tagging (both Tf and AuNP are labelled in this case) which enables direct comparison of FWM signal with both fluorophores and thereby gaining more information. In this case the co-localisation of the two fluorescent labels can be assessed via fluorescence imaging. Since here HeLa cells were fixed after the sequential labelling protocol, a successfully prepared sample imaged via widefield fluorescence should exhibit punctuated fluorescent signal on the cell membrane (no internalisation is expected) and importantly a high degree of pixel overlapping when channels are merged.

In fact, Figure 4.8 shows a dual colour widefield fluorescence image captured on the widefield fluorescence microscope in Cardiff School of Biosciences where the A647 and A488 exhibit high degree of co-localisation with a Pearson coefficient of 0.913. This can also be appraised qualitatively by the merged false colour overlay image (4.8 (e),(f)) with the majority of pixels appearing yellow. Fluorescence images of a control sample ⁵ are also displayed on Figure 4.8 and compared with the respective colour channels on the same scale. These images were captured while focusing on the cell surface and strongly suggest that the Tf ligand is bound to the TfR and that AuNP-SA is also bound to the biotinylated Tf and therefore made this sample a promising candidate for further correlative FWM-fluorescence imaging study.

In order to proceed with the FWM imaging of the sample, the same regions had to be found firstly via DIC on our multi-modal microscope. However, this sample was prepared on non-gridded coverslips and therefore the experimental finding of the fluorescently imaged regions on our multi-modal microscope via DIC was a laborious and meticulous process. Figures 4.9 and 4.10 demonstrate that the cellular regions imaged on the fluorescence microscope were retrieved via DIC imaging and the white dashed rectangles indicate the regions where the FWM results (shown below) were acquired. The regions were chosen because they indicated high degree of co-localisation between the fluorescently labelled Tf and the AuNPs, hence we

⁵a sample which is treated identically to the sample under examination but is not fluorescently labelled

would also expect significant correlation between the FWM signal and the fluorescent signals.

Results of the FWM imaging of the 10nm AuNP-SA(A488):Bi-Tf(A647) sample are presented on Figures 4.11–4.12.

For these experiments, it is important to note that the pump (probe) power at the sample was increased to 93 μW (46.5 μW), the dwell time was set to 3 ms or 5 ms and the pixel size was reduced to 38 nm in order to increase the number of points per resolution (and in turn the signal to noise ratio) when detecting the 10 nm AuNPs. All the experimental parameters (laser power, dwell time, pixel resolution) were gradually changed in order to identify the above settings which would enable the detection of the 10 nm AuNPs. As a consequence of these values the time of our measurements raised significantly. For example, a 1 μm z-stack of $10 \times 10 \mu\text{m}$ area with 100 nm axial step completed in 38 minutes. As a notable comparison, it is worth mentioning that 40 nm AuNPs were previously detected with pump (probe) power set to 31 μW (15.5 μW), 2 ms dwell time (we have experimentally found that this parameter could be even lower than 1 ms to still achieve sufficient signal to noise ratio and image contrast) and in plane pixel size of 94 nm. Last but not least, the proof that the measured signal was electronically resonant FWM from Au was confirmed –as a standard experimental practice– via changing the pump-probe delay time toward negative delays and a representative example is shown on Figure 4.14.

A striking result from the FWM imaging (Fig. 4.11 and Fig. 4.12) is that on the regions with high correlation Pearson’s coefficient, for example an $r_p=0.913$ was found for Figure 4.8, between the A488(SA-AuNP) and A647(Tf-Bi) indicating colocalisation of AuNPs and Tf, when measuring with our FWM technique this is actually not the case. The image data set of figure 4.11, shows regions imaged on our multimodal microscopy set-up via DIC (a), reflection (b) and FWM (c) alongside the respective previously acquired widefield fluorescence images. Z-stacks over 1 μm with 100 nm axial step size were acquired. Maximum intensity projections of the FWM images are overlapped (in false colour) with each fluorescence channel highlighting the poor colocalisation between them with visual means. The regions to be overlapped were determined by selecting the cell contour from the reflection image that matches the contour seen in fluorescence. The density of AuNPs imaged with FWM is tremendously different to the one that one would assume based solely on the A488 widefield fluorescence image. There are surprisingly just a few AuNPs in the FWM images, as opposed to our expectation from the fluorescence images.

On the next data sets (Figure 4.12 and 4.13) similar results are presented. Another region of interest (ROI) of the sample is shown where high correlation is also

expected judging by the fluorescence image. This set of images is composed of $15 \times 15 \mu\text{m}$ single xy raster scan images of the reflection (a) and FWM amplitude (b) along with a fine z-stack acquired over a $6 \times 6 \mu\text{m}$ area with 100 nm axial step size. The FWM imaging (d) better highlights one nanoparticle through the z-stack which was weakly visible on the $15 \times 15 \mu\text{m}$ FWM image at a single z plane (b). Notably, no other particles are found through the z-stack. This example highlights further the sparse density of AuNPs and the absence of significant correlation between the fluorescence and the FWM signal.

Overall, despite the evident co-localisation of the fluorescent signals for the SA-A488 and the Tf-Bi-A647 conjugate, FWM imaging on the same regions indicate that the number of AuNPs effectively present is actually much smaller than the number of fluorophore labels observed. Moreover, of these AuNPs, only a few are co-localising with the A488 and A647 fluorophores. These results indicate that there was likely a disassociation between the non-covalent bond of the SA-A488 and the 10 nm AuNP during the cell incubation steps. Furthermore, the stock 10 nm AuNP-SA-A488 solution used most probably contained multiple unbound fluorophores. In other words, it is likely that the observed fluorescence of the A488 well co-localised with the A647 label originates from SA-A488 molecules not attached to AuNPs. These SA-A488 can strongly bind to Tf-Bi-A647 at the cell surface, and saturate the available binding sites. As a result, only a few AuNPs are actually present on the cell surface, and of those only a few are attached to SA-A488 and bind to Tf-Bi-A647. Notably, although the supplier data sheet for the AuNP-SA-A488 mentions that fluorescently-labeled SA proteins may dissociate from the colloid gold particles during storage, there is no reference to a mandatory protocol that must be followed to remove unbound proteins prior use. Indeed, our biology collaborators have typically used the stock solution of this product, without additional centrifugation steps to separate and remove unbound proteins. It is worth mentioning that I made subsequent efforts to prepare new samples after adding ‘washing’ steps on the 10 nm AuNP-SA-A488 stock solution which however resulted in much reduced detected fluorescence (very close to the autofluorescence control levels). This suggested that the washing steps themselves might cause disruption of the construct and loss of label, and thus are not a straightforward procedure to resolve the issue⁶.

⁶As a further note, an investigation of the AuNP-SA-A488 stock solution has been carried out as part of a following PhD project and has confirmed the presence of a large amount of unbound SA-A488 in the stock solution, via correlative fluorescence and extinction analysis on individual AuNPs deposited onto a glass surface. Even after 3x washes (a procedure suggested as ‘optional’ by the manufacturer) there was still a significant number of unbound fluorophores.

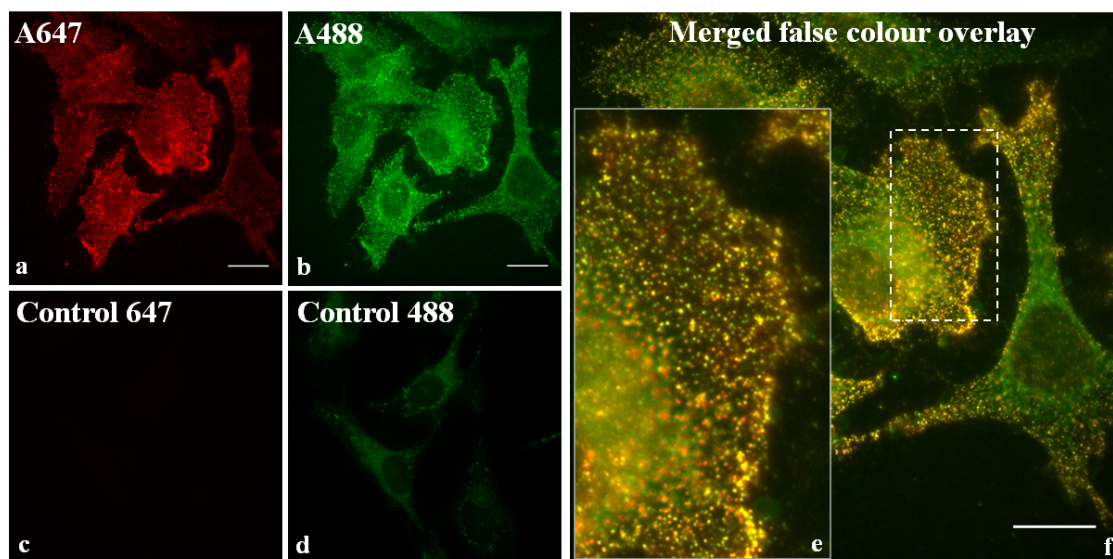


Figure 4.8: Representative dual colour widefield fluorescence microscopy images of HeLa cells loaded with fluorescently labelled 10 nm AuNP (**AuNP-SA-A488**)–(b)– linked to biotinylated fluorescently labelled Tf (**Tf-Bi-A647**) –(a)–. A merged false colour overlay image of the red and green fluorescent channels is shown on (f) alongside a zoom inset (e). A Pearson coefficient of 0.913 on image (f) was found indicating high degree of co-localisation between Tf-Bi-A647 and SA-A488. ‘Control’ fluorescent images are shown on (c) and (d) for comparison. Images were acquired while focusing on the cell surface and are shown here in RGB format with values spanning from 0 to 255. Scale bar is 20 μm .

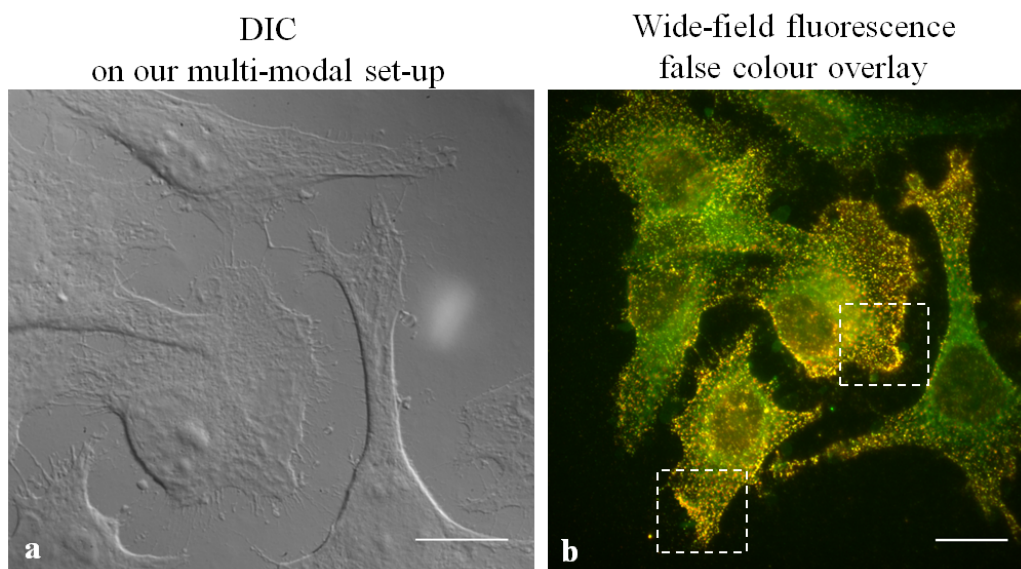


Figure 4.9: ROI Overview 1: On the right, the merged false colour overlay fluorescence image captured on the widefield fluorescence microscope is shown (b), while on the left the same region was retrieved via DIC imaging on our multi-modal microscope. The white dashed rectangles show regions imaged via FWM in the next experimental step and were chosen because they indicate high degree of co-localisation between the fluorescently labelled Tf and the SA-A488 (supposed to be attached onto AuNPs). Scale bar on both images is 20 μm .

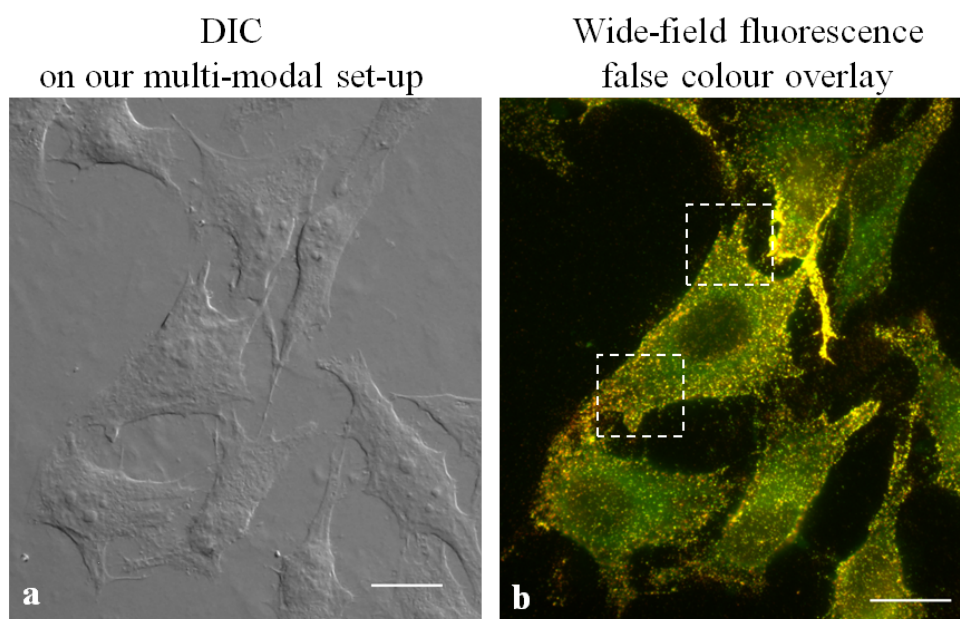


Figure 4.10: ROI Overview 2: On the right, the merged false colour overlay fluorescence image captured on the widefield fluorescence microscope is shown (b), while on the left the same region was retrieved via DIC imaging on our multi-modal microscope. The white dashed rectangles show regions imaged via FWM in the next experimental step and were chosen because they indicate high degree of co-localisation between the fluorescently labelled Tf and the SA-A488 (supposed to be attached onto AuNPs). Scale bar on both images is 20 μm .

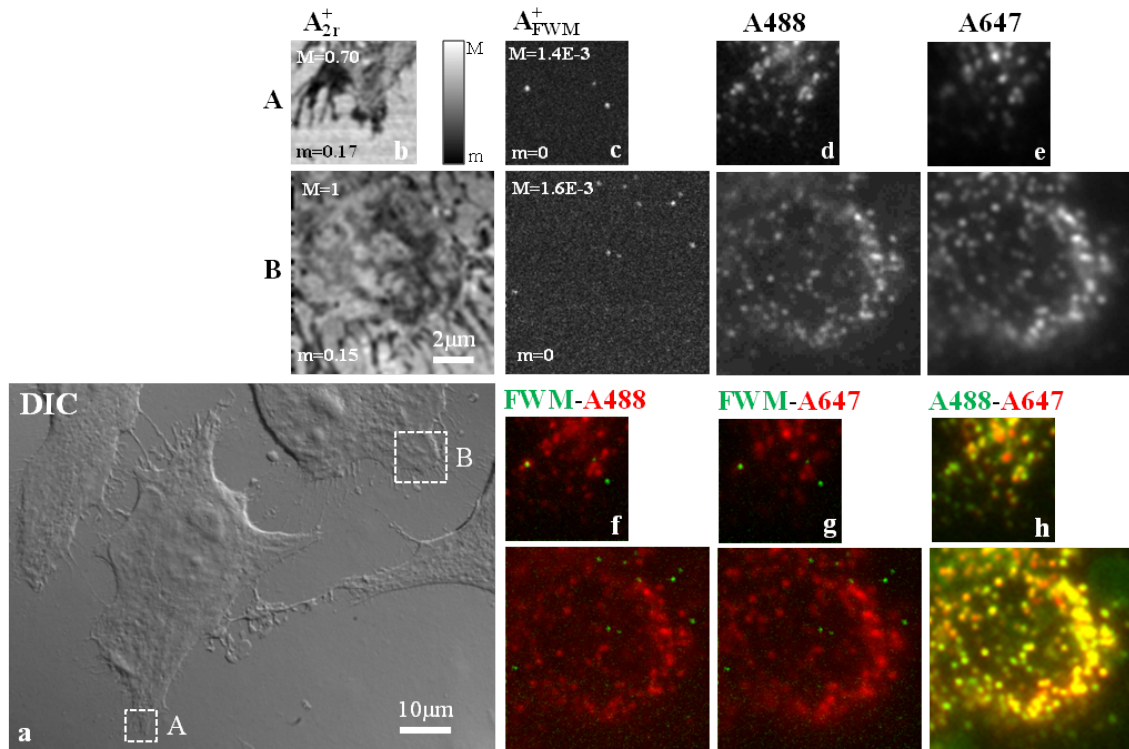


Figure 4.11: Results 1: Comparison of FWM imaging with widefield fluorescence on the 10nm AuNP-SA(A488):Bi-Tf(A647) sample

(a) DIC image of fixed HeLa cells that have internalised 10nm AuNP-SA(A488):Bi-Tf(A647) where regions A and B are highlighted with white dashed rectangles. FWM/reflection was acquired with a pump (probe) power set to 93 μ W (46.5 μ W), a dwell time equal to 5 ms for region A and 3 ms for region B and the in plane pixel size measures 38 nm. Z-stack was acquired over 1 μ m with 100 nm step size. Co-circularly polarised reflection (b), A_{2r}^+ , is shown at the cell-coverslip interface while maximum intensity projection of the FWM, A_{FWM}^+ , (c) over the z-stack. Grey scales are linear from m to M for field amplitudes as indicated. Widefield fluorescence images of the A488 (d) and A647 (e) are shown scaled to their maximum intensity next to each acquired FWM/reflection areas. Merged false colour overlay images of FWM-A488 (f), FWM-A647 (g) and both A488-A647 (h) are also re-scaled to maximise colour overlap.

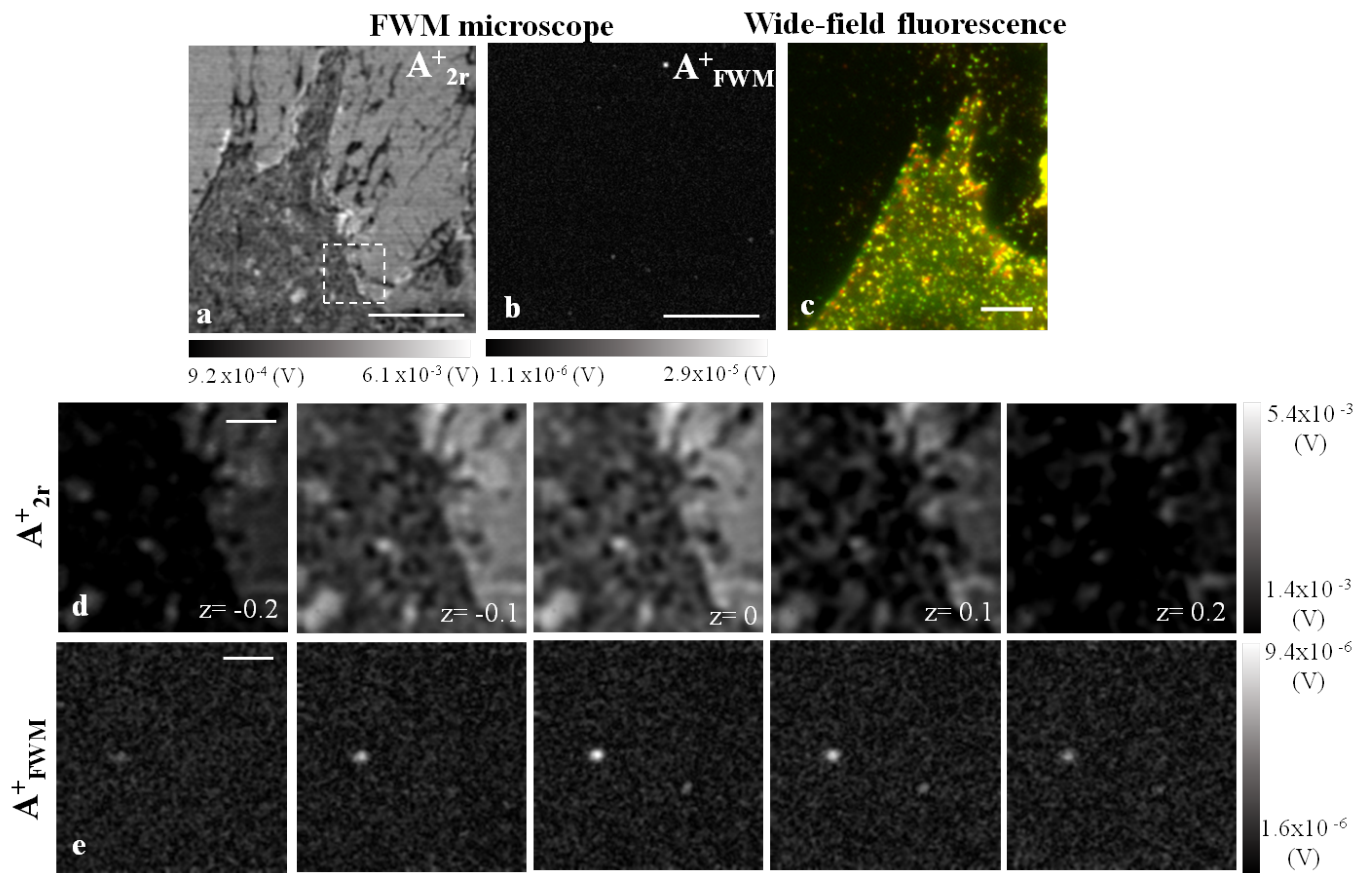


Figure 4.12: Results 2: Comparison of FWM imaging with widefield fluorescence on the 10nm AuNP-SA(A488):Bi-Tf(A647) sample. On the top, $15 \times 15 \mu\text{m}$ single xy co-circularly polarised reflection (a), A_{2r}^+ , and co-circularly polarised FWM amplitude (b), A_{FWM}^+ , are shown alongside the merged false colour overlay widefield fluorescence image of the same region (c). Below $6 \times 6 \mu\text{m}$ reflection (c) and FWM (d) images of five z-planes of a z-stack acquired with 200 nm axial step alongside their scale in volts. FWM imaging parameters: pump (probe) power set to 93 μW (46.5 μW), dwell time equal to 3 ms (5 ms) for the top (bottom) images and in plane pixel size measures 38 nm. Scale bar on (a-c) images is 5 μm while the scale bar on (c-d) is 1 μm .

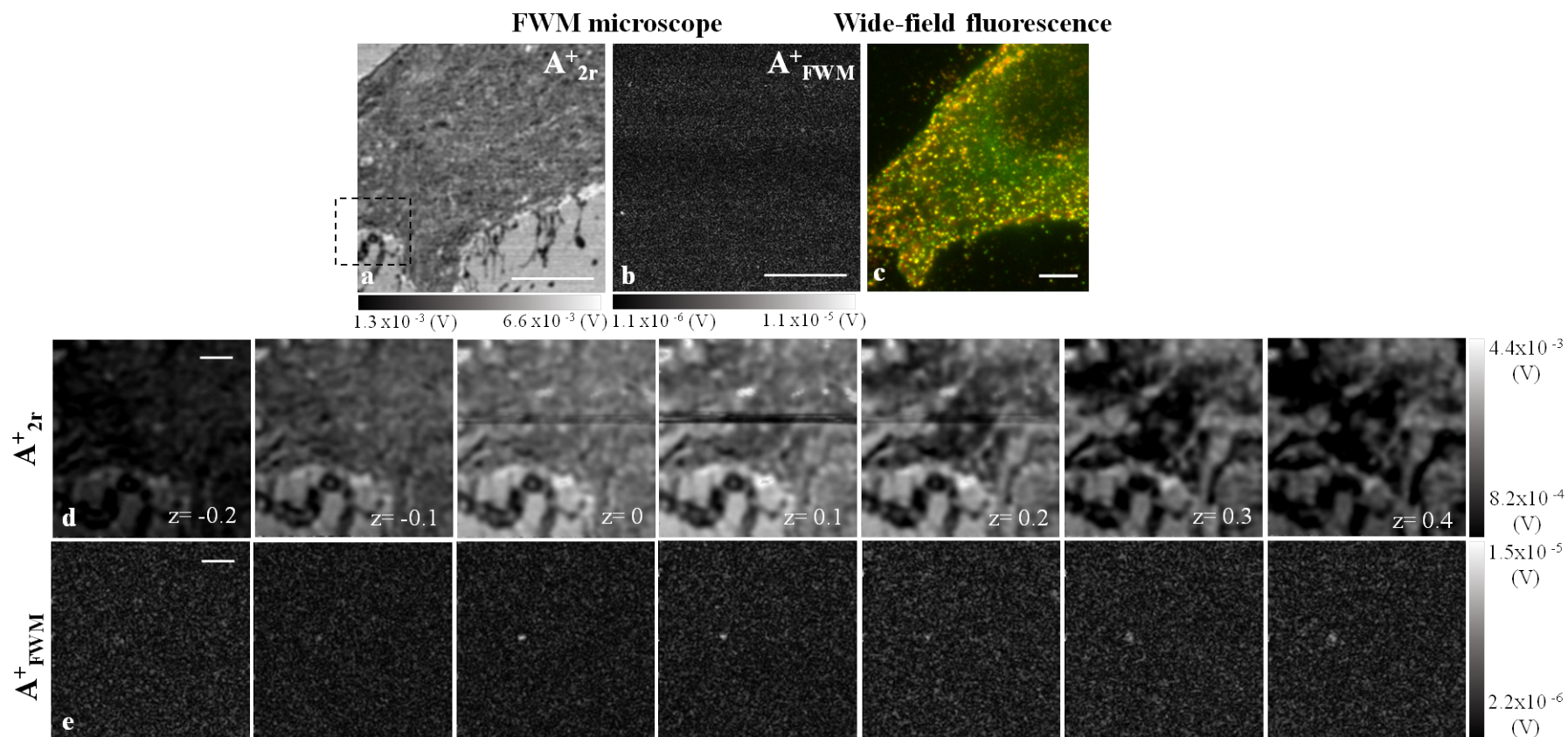


Figure 4.13: Results 3: Comparison of FWM imaging with widefield fluorescence on the 10nm AuNP-SA(A488):Bi-Tf(A647) sample. On the top, $15 \times 15 \mu\text{m}$ single xy co-circularly polarised reflection (a), A_{2r}^+ , and co-circularly polarised FWM amplitude (b), A_{FWM}^+ , are shown alongside the merged false colour overlay widefield fluorescence image of the same region (c). Below $6 \times 6 \mu\text{m}$ reflection (c) and FWM (d) images of five z-planes of a z-stack acquired with 100 nm axial step. FWM imaging parameters: pump (probe) power set to $93 \mu\text{W}$ ($46.5 \mu\text{W}$), dwell time equal to 3 ms (5 ms) for the top (bottom) images and in plane pixel size measures 38 nm. Scale bar on (a-c) images is $5 \mu\text{m}$ while the scale bar on (c-d) is $1 \mu\text{m}$.

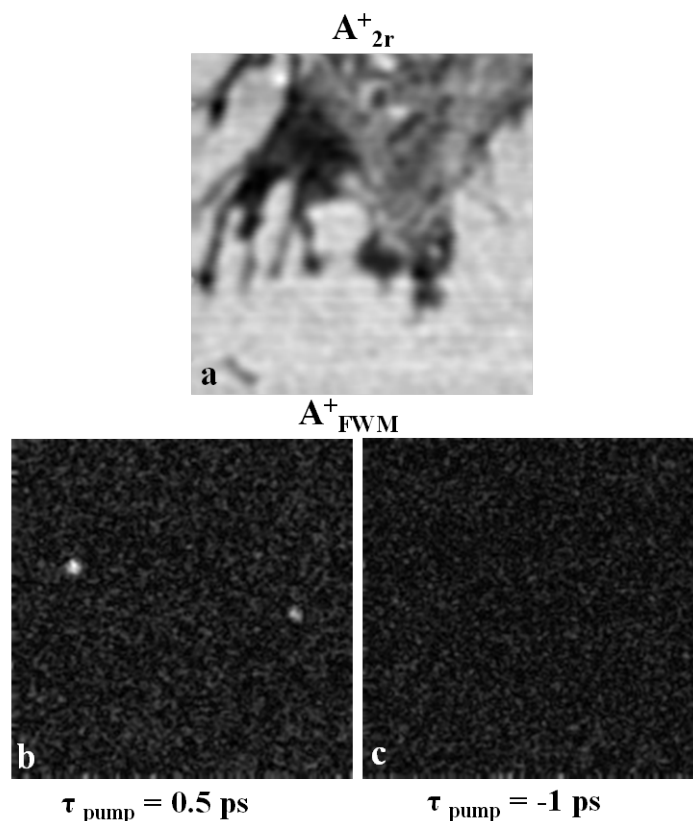


Figure 4.14: Representative example of xy raster scan with 0.5 ps and -1 ps reference pump delay. Image (a) refers to the co-circularly polarized amplitude reflection while the (b) and (c) refer to the co-circularly polarized FWM amplitude. When the pump-probe delay is negative, no FWM signal is generated.

4.3 Measurements of polymer coated 15nm AuNPs uptaken by HeLa cells

In this section, a correlative FWM and confocal fluorescence imaging study on 15 nm polymer coated (PC)-AuNP covalently attached to fluorescently labelled Tf (Tf-A488) ligand is presented.

4.3.1 Sample description

The 15nm AuNP-PC-Tf(A488) construct consists of 15 nm diameter AuNPs covalently bound to a polymer coating shell onto which fluorescently labelled Tf-A488 is covalently bound. An illustration of the 15nm AuNP-PC-Tf(A488) construct is given on figure 4.15.

This construct was fabricated in house by our collaborators in Nottingham School of Pharmacy and it is described in Sayers et al.[109] as ‘Tf-AuNP-3’. During the

project, we received various batches of PC-AuNPs of different sizes and with different polymer structures and properties which were initially aimed at temperature dependent clathrin-mediated endocytic studies based on the thermoresponsive properties of the polymer cell [110]. Prof. C. Alexander's group in Nottingham School of Pharmacy has conducted extensive research in responsive polymer coated NPs with some of the most recent work to be [111] [112] [113]. Ideally, we were aiming for a PC-AuNP construct where the polymer would enable to "reveal" ("hide") the attached Tf due to collapse (extension) of the polymer shell depending on the increase (decrease) of the environment's temperature. This would lead to a controlled clathrin-mediated cellular uptake via temperature dependent exposure of the target ligand (Tf). To that direction, a series of 50 nm PC-AuNPs without Tf was initially characterised (by myself) in its thermoresponsivity by absorption spectroscopy upon several heating cycles. The results of this study can be found on Appendix A.1. The thermoresponsive behaviour of the PC-AuNPs solution appeared not sufficiently reversible for its subsequent use in cellular applications and therefore this aim of the project was aborted within the work in my PhD thesis.

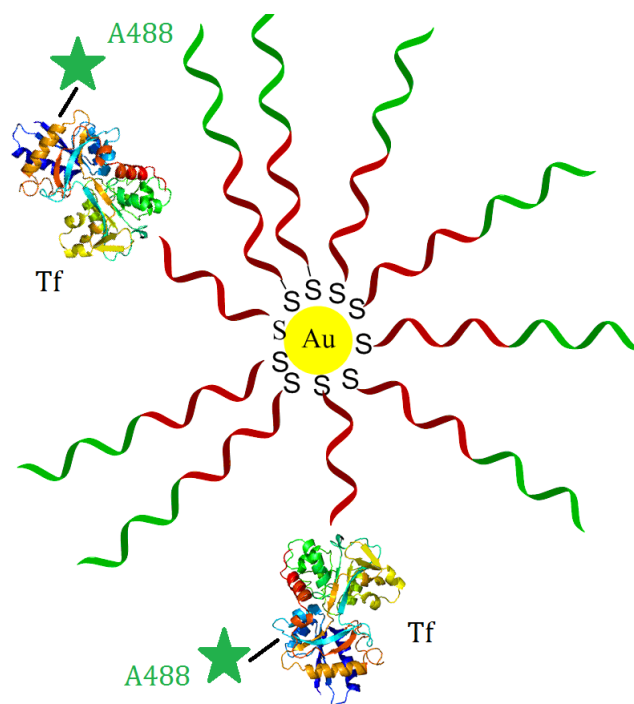


Figure 4.15: Illustration of the 15nm AuNP-PC-Tf(A488) construct fabricated in Nottingham School of Pharmacy following in house chemistry protocols. Gold nanoparticles of 15 nm diameter size decorated with thiolated polymeric shell onto which fluorescently labelled (A488) transferrin (Tf) is attached. An average value of 3 molecules of Tf per AuNP was calculated by our collaborators.

The samples, whose results are shown in this section, comprise a series of non-thermoresponsive PC AuNPs-Tf-A488 which were proven to internalize via clathrin-

mediated endocytosis without exhibiting any thermoresponsivity (tested by our collaborators in Cardiff School of Pharmacy and can be found in Appendix C.1). The stock solution has a particle concentration of 1.27×10^{14} AuNPs/mL and an average value of 3 molecules of Tf per AuNPs. The Tf ligand is always exposed for cellular uptake and the construct has a hydrodynamic diameter of 48-50 nm⁷.

Protocol 1: *Sample preparation protocol for 15nm AuNP-PC-Tf(A488) embedded in HeLa cells whose results are shown in 4.3.2 - First results.*

The tissue culture part of the preparation of this sample was conducted in Cardiff School of Pharmacy where the sample was also imaged via confocal fluorescence microscopy by Dr. P.Moody. HeLa cells were grown on photoetched square gridded coverslips of thickness No.2 (Electron Microscopy Sciences). On the day of the experiment, cells were firstly incubated in serum-free medium for 30 min, to allow recycling of serum-derived transferrin, and then were incubated with 1 in 10 dilution of the 15nm AuNP-PC-Tf(A488) stock solution into serum-free medium for 2 hours. After incubation, cells were washed 3 times in PBS pH 7.4 and incubated in imaging medium for 4 hours ('chased') and then fixed in 3% PFA for 10 min at room temperature. Sample was finally washed 3 times in PBS pH 7.4 at room temperature and then mounted onto microscope glass slides with 80% DAKO medium (similar to the 40 nm AuNP sample).

Protocol 2: *Sample preparation protocol for 15nm AuNP-PC-Tf(A488) embedded in DAPI stained HeLa cells whom results are shown in 4.3.2 - Further studies.*

These samples were prepared by myself as part of *Further Studies* on these constructs. Similar to the protocol described above, HeLa cells grown on gridded coverslips and on the day of the experiment were incubated with 1 in 30 dilution of the 15nm AuNP-PC-Tf(A488) stock solution medium into serum-free medium for 2 hours, following a first step of 30 min incubation in serum-free medium. They were then incubated in serum-free medium for 30 min (no wash step after the 'chase' part) and subsequently fixed in 4% PFA for 10 min at room temperature. Cells were then washed 3 times in PBS pH 7.4 at room temperature and a 1 in 10000 dilution of DAPI stain solution was added for 10 min in room temperature. Finally, cells were washed 3 times with PBS pH 7.4 at room temperature mounted onto microscope glass slides with mowiol medium containing 200 nm diameter multi-fluorescent polystyrene beads. The polystyrene beads were purchased from Polysciences, Inc.

⁷these numbers were measured by Dr. J.P. Magnusson in Nottingham School of Pharmacy

and are designed to have emission fluorescence peaks at 479, 546, and 612 nm. The estimated number of fluorescent beads used per coverslip was 10^7 . The used volume was calculated as such in order to have the beads approximately 50 μm apart on the 24×24 mm square coverslips used.

The usage of the beads in Protocol 2 aimed at having 3D fiducial points in both fluorescence and reflection (FWM set-up) imaging modalities which would serve as correlative reference points. Based on the visibility of the fluorescent beads in each axial raster scan of each modality we aimed at being able to match (re-register) the x,y coordinates and z-planes of the two imaging modalities and thus facilitate the correlation, without the need to use manually chosen coordinates from the cell contour (see Chapter 3). These experiments belong to further efforts in order to obtain additional results and eliminate sources of uncertainty in the correlation and co-localisation analysis with the help of clearly visible fiducials.

Notably, none of the above two protocols used for this sample group include ice steps, in comparison with the previous 40 nm (10 nm) AuNP-SA(A488):Bi-Tf samples, as there is no need for sequential labelling here.

4.3.2 Results and discussion

The experimental results are presented in two separate paragraphs corresponding to the sample preparation protocols and the chronological order of the measurements. *First results* include data sets of the 15nm AuNP-PC-Tf(A488) sample prepared by our collaborators following Protocol 1, while *Further studies* comprise results of the 115nm AuNP-PC-Tf(A488) sample embedded with multi-fluorescent polystyrene beads prepared following Protocol 2.

First results

Figure 4.16 shows example images of reflection, FWM and confocal fluorescence microscopy for HeLa cells embedded with 15nm AuNP-PC-Tf(A488). As in previous cases, the sample was imaged first via confocal fluorescence in Cardiff School of Pharmacy on the same regions of interest mapped by the aid of a gridded coverslip and DIC also available in the confocal fluorescence microscope. Dashed rectangles on the DIC image obtained on our FWM set-up highlight the ROIs. The co-polarised reflection amplitude images (A_{2r}^+) can easily be correlated with the DIC highlighted regions. For the FWM/reflection images the following settings were used: pump (probe) power at the sample of 31 μW (15.5 μW), pump-probe delay time of 0.5 ps, 2ms pixel dwell time and in plane pixel size of 94 nm. Figure 4.16 comprises image sets of maximum intensity projection images originating from the

co-polarised FWM amplitude (A_{FWM}^+) alongside single xy reflection images (A_{2r}^+) and the corresponding maximum intensity projection of the confocal fluorescence ones. The re-registered overlay of FWM-fluorescence is shown as a product of the re-registration algorithm described in Chapter 3. For each region the calculated co-localisation coefficients of Pearson's (r_p) and Mander's (M_{FWM}) for the FWM channel based on the re-registered overlay image are given next to each analysed data set. Similar to previous results the calculated values indicate negligible values of correlation for both coefficients resulting in very poor co-localisation of AuNPs and the fluorophores.

Among the reasons for such a result, could again be the possibility of unbound fluorophores (A488) in the stock (and hence incubation) AuNP solution. Despite the fact that the AuNPs-PC construct was developed following centrifugation and purification steps, it is still possible that there were unbound fluorescence tags in the solution which would explain the lack of correlation between the internalised Tf-A488 and the AuNPs shown on the FWM images. In addition, the preparation protocol included a 2 hours 'chase' step which could potentially lead to the construct being broken down in lysosomes. Furthermore, there is the possibility of quenching of the fluorophore tag due to its close proximity to the AuNP surface. Another important factor to be considered, is the very low fluorescence signal of the Tf-A488 captured on the confocal fluorescence microscope. The fluorophore tag A488 attached to the PC-AuNP exhibited weak fluorescent signal (in many sample regions comparable to autofluorescence background coming from the cell and glass autofluorescence) and even after background subtraction, did not show the clearly punctuated spatial pattern expected from clathrin-mediated internalised Tf (see Figure 4.17). The excitation/detection conditions for Alexa488 are known to result in large cellular autofluorescence backgrounds. As mentioned, there can also be quenching due to non radiative energy transfer observed when colloidal gold nanoparticles are in close proximity to fluorescent molecules [114] [115] [51] [52].

Notably, a significant cellular uptake of AuNPs ($> 1 \text{ AuNP}/\mu\text{m}^3$), is observed for this sample which is consistent with the high concentration of the incubating solution used ($\sim 10^{13} \text{ AuNP}/\text{ml}$) and the long (2 hours) incubation time. Moreover, it is likely that the fluorescently PC-AuNPs form aggregates owing to the FWM signal strength which is larger than the value that we would expect for AuNPs of such diameter⁸. With the aim to improve image clarity towards visualising individual AuNPs, we decreased the incubation concentration to 1 in 30 dilution (compared to the initially used of 1 in 10) in the next sample (Protocol 2- *Further Studies*).

⁸The expected dependence of FWM signal with the radius of the NP is discussed in [116].

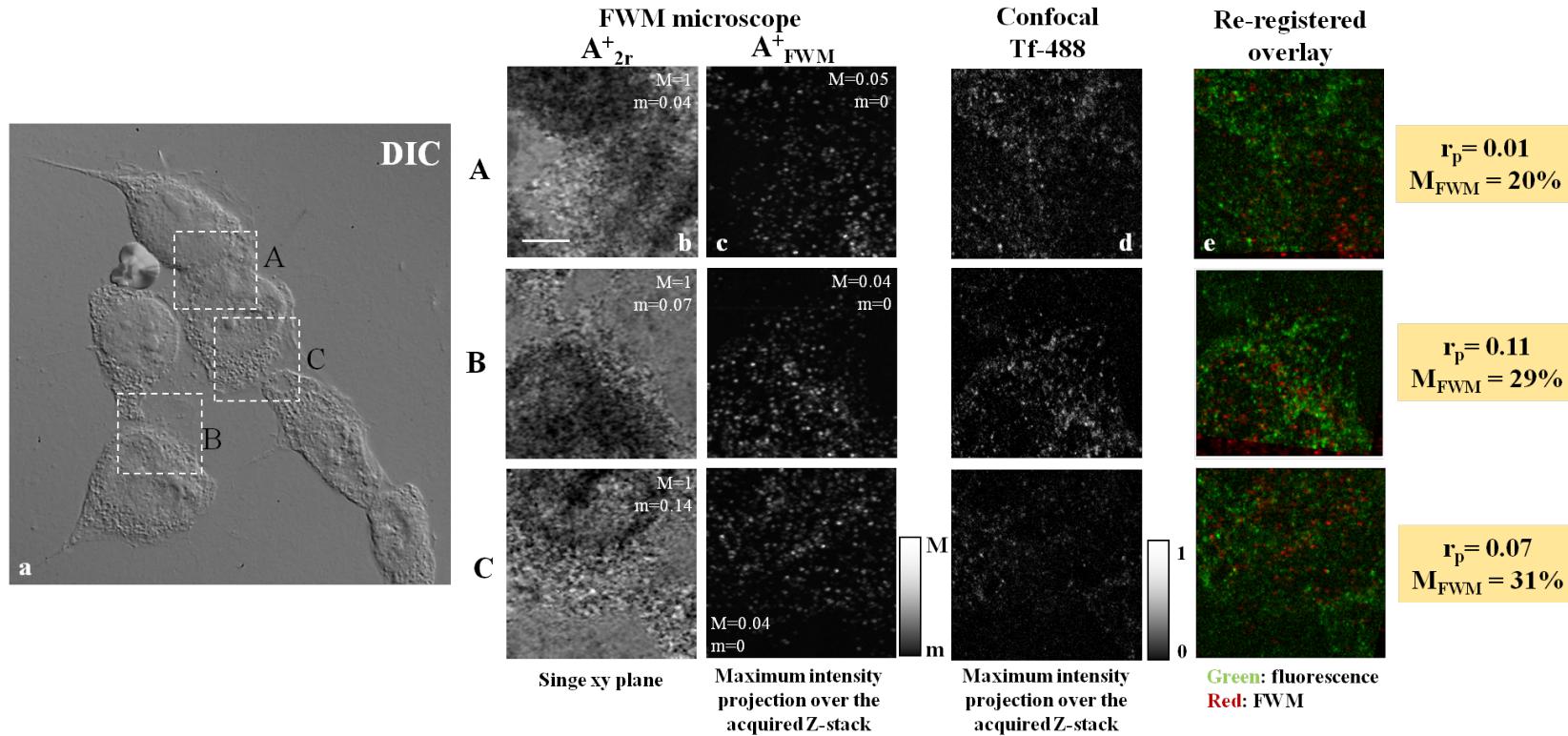


Figure 4.16: 15nm AuNP-PC-Tf(A488)

(a) DIC image of fixed HeLa cells where three dashed rectangles (A, B, C) show $20 \times 20 \mu\text{m}$ cellular regions imaged in 3D via FWM (b,c) and confocal fluorescence (d). The co-circularly polarised reflection (b), A_{2r}^+ , is shown as a single (x,y) plane while the co-circularly polarised FWM, A_{FWM}^+ , (c) and confocal fluorescence (d) channels are shown as maximum intensity projections over $5 \mu\text{m}$ axial direction. Amplitude scales from m to M are indicated in each image for the FWM acquisition while in fluorescence the scale bar spans from 0 to 1 corresponding to 255 grey levels. The scale bar for the FWM and reflection images is $5 \mu\text{m}$. Probe (Pump) power was measured $15.5 \mu\text{W}$ ($31 \mu\text{W}$) at the sample. The re-registered overlay (e) of the confocal fluorescence (green) –representing the fluorescently labelled Tf– on top of the FWM signal (red) –representing the location of gold NPs in the cell– is shown alongside the calculated Pearson's and Mander's correlation coefficients.

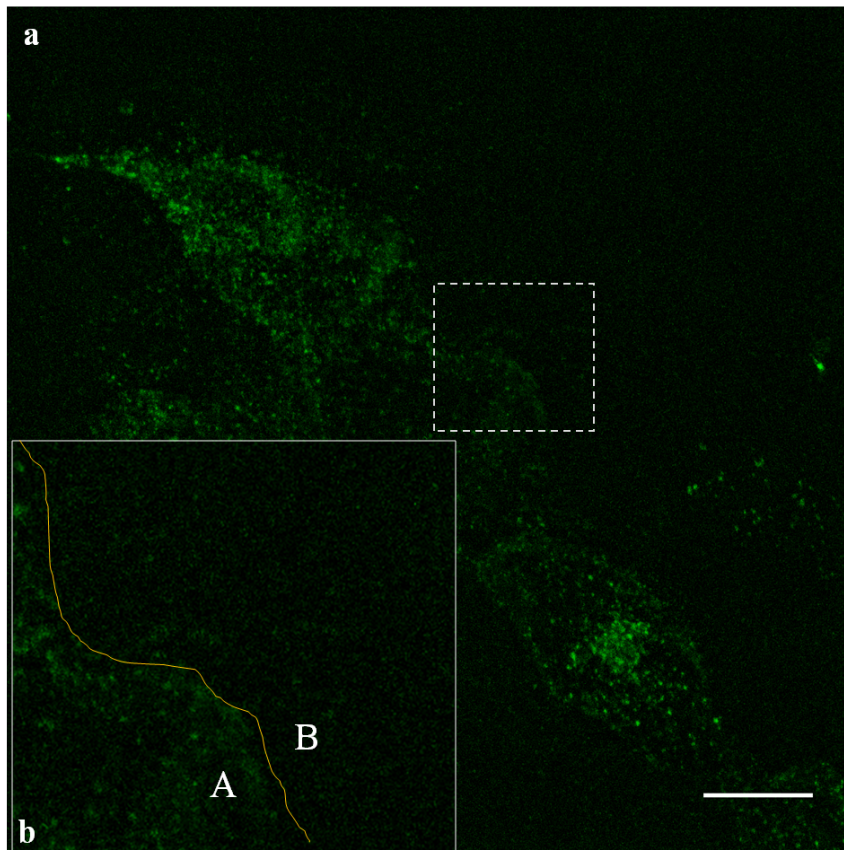


Figure 4.17: (a) An overview of the cellular region imaged on the confocal fluorescence microscope of Cardiff School of Pharmacy. This is a maximum intensity projection image over 6 μm on the z axis after background subtraction. Scale bar is 10 μm . (b) Zoom-in ROI where two regions A and B are separated based on the cell contour (yellow freehand line) retrieved by the simultaneous acquired DIC on the confocal microscope. The level of autofluorescence signal coming from the glass is comparable to the fluorescence signal coming from the cellular region making the correlation analysis very challenging on this sample.

Further studies

As mentioned on section 4.3.1 these samples intended to address the re-registration between fluorescence and FWM images obtained on two different microscopes via the use of fluorescent beads as fiducials, instead of relying on the manual selection of coordinates in the cell contour discussed in Chapter 3. In this case, the 200 nm diameter multifluorescent polystyrene beads are expected to strongly scatter and hence be easily detected in reflection whilst being also visible via fluorescence microscopy. We would therefore expect to have common unambiguous points of reference between the two modalities (FWM set-up and fluorescence) which could facilitate the correlation of the two signals.

Figure 4.18 reflects the results obtained on this sample. The presented data set

is composed of FWM, reflection and confocal fluorescence images of a whole cell region. FWM imaging parameters were set to pump (probe) power at the sample equal to 31 μW (15.5 μW), pump-probe delay time of 0.5 ps, 1 ms pixel dwell time and in plane pixel size of 94 nm. A DIC image (a) is shown along with two smaller ROIs highlighted with dashed rectangles. Co-polarised amplitude reflection, A_{2r}^+ , (b), maximum intensity projections of the co-polarised FWM field amplitude, A_{FWM}^+ , (c) and the confocal fluorescence overlay (d) are also shown for each region over the acquired z-stacks. Indeed, the fluorescent polymeric beads are visible via reflectometry (A_{2r}^+), although only when they are found outside the cell as shown on region B with the yellow arrow. The fluorescence intensity from the A488 tag in the 15nm AuNP-PC-Tf(A488) construct was, however, indistinguishable from the cellular autofluorescence in these samples. Despite several meticulous experimental efforts on this sample, the negligible fluorescent signal coming from A488 did not allow to proceed with a correlation analysis between FWM and fluorescence coming from the 15nm AuNP-PC-Tf(A488) construct. Figure 4.19 further highlights the fact that there is no "confident" fluorescent signal detected from the A488 which can be correlated with the FWM signal detected from the AuNPs. It is also worth mentioning that the green fluorescent signal surrounding the DAPI stained nucleus is typical cellular autofluorescence observed in the wavelength range (≈ 532 nm) used for detection of the A488. Notably, the 1 in 30 diluted concentration of the 15nm AuNP-PC-Tf(A488) used in this sample resulted –as expected– in lower density of AuNPs/ μm^3 and more distinct cellular uptake of the bio-conjugated AuNPs. It is possible that such reduced AuNP concentration in turn led to the reduction in the level of fluorescence from the A488 tag, which then became indistinguishable from the autofluorescence. Interestingly in this sample, AuNPs are detected even outside the cell region (Figure 4.18 c) which can be attributed to the lack of washing steps following the incubation part of Protocol 2, as well as the fact that the stock solution could have been degraded resulting in loss of the protein's (Tf) functionality. Note that, in those regions outside the cell (thus not dominated by cellular autofluorescence) where AuNPs were observed there was still no detectable A488 at the NP location, suggesting quenching of the dye or dissociation from the AuNP. All in all, the findings on both 15nm AuNP-PC-Tf(A488) samples (*First results and Further studies*) exemplify the argument that fluorescence labelling can be non reproducible severely affected by autofluorescence backgrounds, prone to photobleaching and quenching when tags are attached in close proximity to metallic NPs.

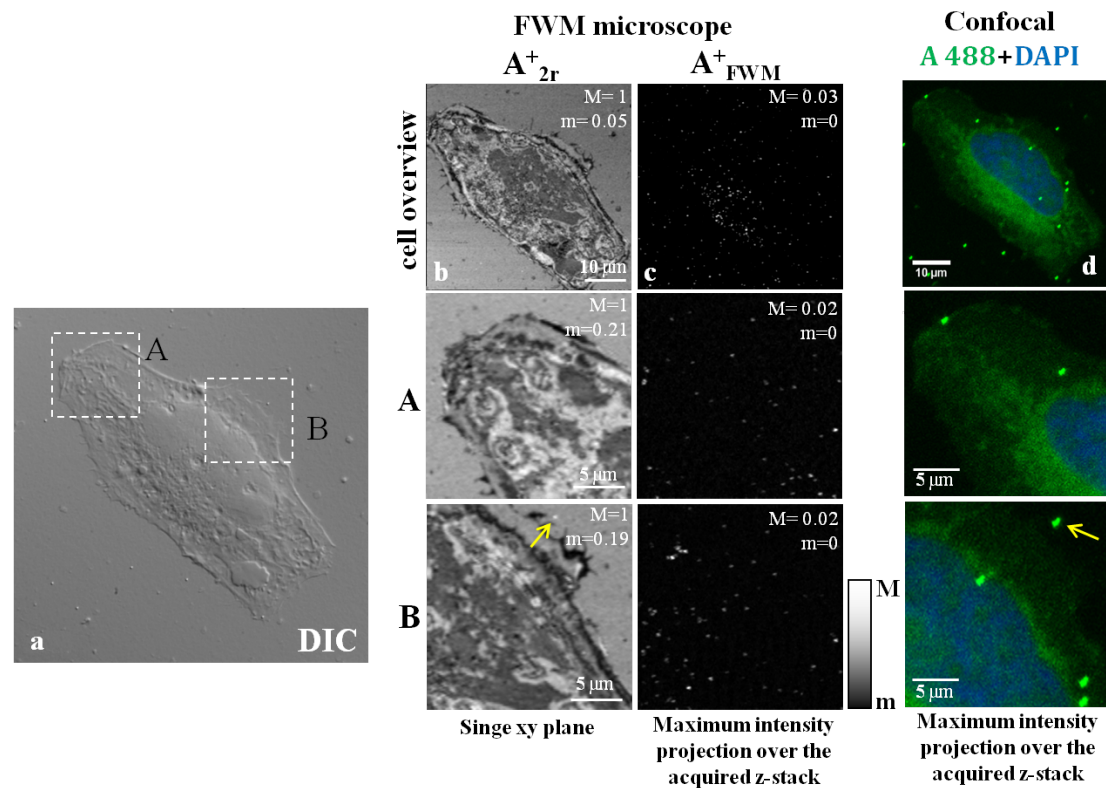


Figure 4.18: 15nm AuNP-PC-Tf(A488) with DAPI nuclear counterstain

(a) DIC image of a fixed HeLa cell embedded with 15nm AuNP-PC-Tf(A488) and stained with DAPI. A cell overview is given on the first row of images where the cell was imaged via FWM (reflection and FWM amplitude) after confocal fluorescence imaging acquisition. The dashed rectangles (A, B) show $20 \times 20 \mu\text{m}$ cellular regions imaged in 3D via FWM (b,c) and confocal fluorescence (d). The co-circularly polarised reflection (b), A_{2r}^+ , is shown as a single (x,y) plane while the co-circularly polarised FWM, A_{FWM}^+ , (c) and confocal fluorescence (d) channels are shown as maximum intensity projections over $3 \mu\text{m}$ axial direction for the FWM imaging and over $6 \mu\text{m}$ for the confocal with 300 nm z-step (apart from the FWM image of the cell overview imaging which is on a single xy plane). Amplitude scales from m to M are indicated in each image for the FWM acquisition while in fluorescence the scale bar spans from 0 to 1 corresponding to 255 grey levels. Probe (Pump) power was measured $15.5 \mu\text{W}$ ($31 \mu\text{W}$) at the sample. The yellow arrow on region B highlights a multifluorescent polystyrene bead of 200 nm diameter visible on both reflection and fluorescence imaging.

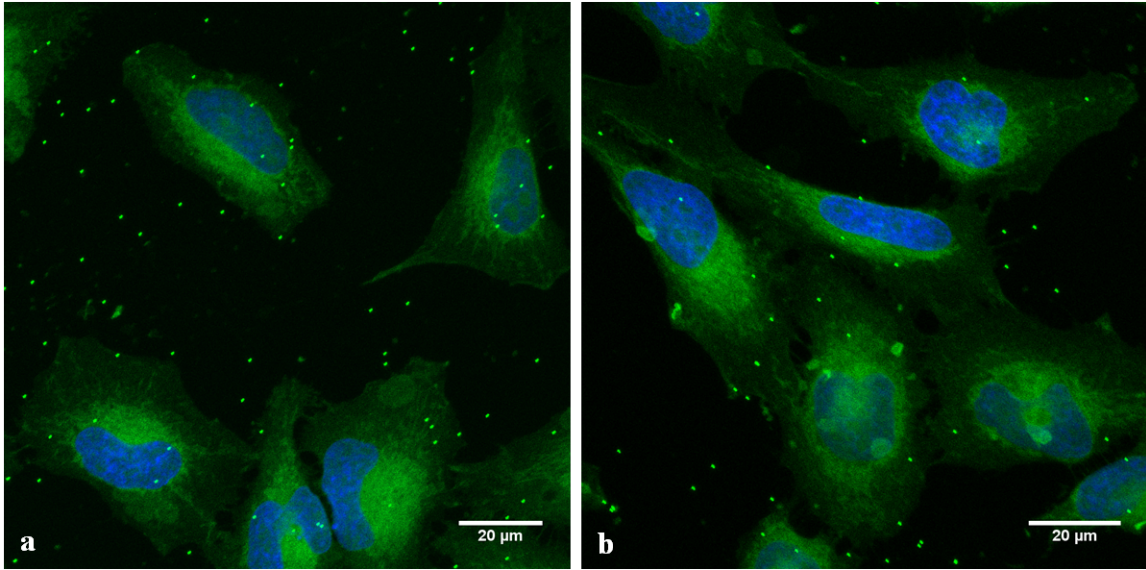


Figure 4.19: Representative examples (a, b) of merged confocal fluorescence images of fixed HeLa cells embedded with 15nm AuNP-PC-Tf(A488) (green) and stained with DAPI (blue) and mounted with multifluorescent beads (green). (a) and (b) are shown on a maximum intensity projection over 6 μm in the z direction. Scale bars are indicated on the image.

Proof of FWM signal

Following our standard experimental practice, proof of FWM signal for both PC-AuNPs samples were performed either via a pump-probe delay dependence of the FWM field amplitude Figure 4.21 (*First studies*) or via acquiring lateral scans with negative pump-probe delay times which results in absence of FWM signal as shown on Figure 4.20 (*Further studies*).

Figure 4.21 is a representative example of the pump-probe delay dependence reflecting the pump-induced change of a AuNP's polarisability as extensively discussed in previous work of our group [45]. Here, the co-polarised FWM field amplitude for a 15nm AuNP-PC-Tf(A488) at the focus center is plotted versus pump-probe delay time τ for a pump (probe) power measured at the sample of 31 μW (15.5 μW). Briefly, the observed dependence indicates the transient change of the electron and lattice temperature following the absorption of the pump pulse by the AuNP. Due to the electron's gas ultrafast heating, the transient FWM field amplitude reaches its maximum at a pump-probe delay τ of about 500 fs. The subsequent decay (1-5 ps timescale) represents the cooling of the electron gas via electron-phonon coupling [116],[14],[45]. The subsequent thermalisation of the NP with the surrounding medium is achieved at > 100 ps timescales[45].

Figure 4.20 shows another representation of the same 'check' where FWM signal is detected for a pump-probe delay set to 0.5 ps but not for a negative delay.

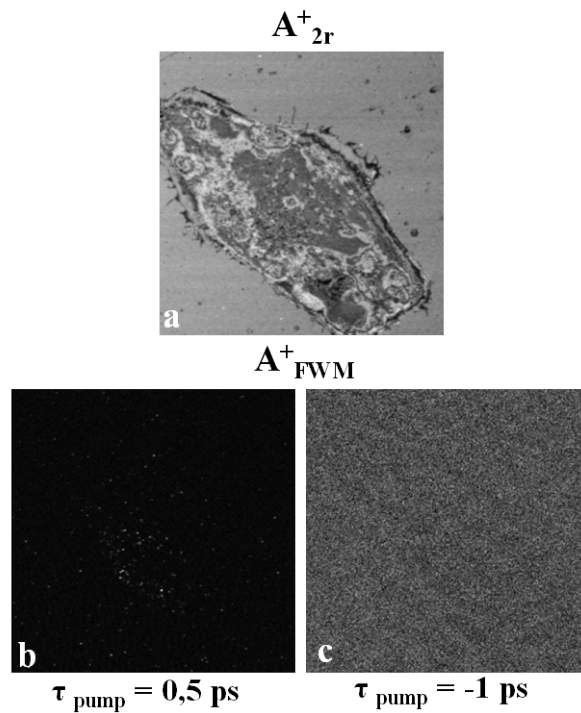


Figure 4.20: Example of raster reflection/FWM imaging on the 115nm AuNP-PC-Tf(A488) (*Further studies*) sample with 0.5 ps and -1 ps pump-probe delay. Image (a) refers to the co-circularly polarized amplitude reflection, A_{2r}^+ , while images (b) and (c) refer to the co-circularly polarized FWM amplitude, A_{FWM}^+ . When the pump-probe delay is negative (c) there is no emission of FWM signal from the AuNPs.

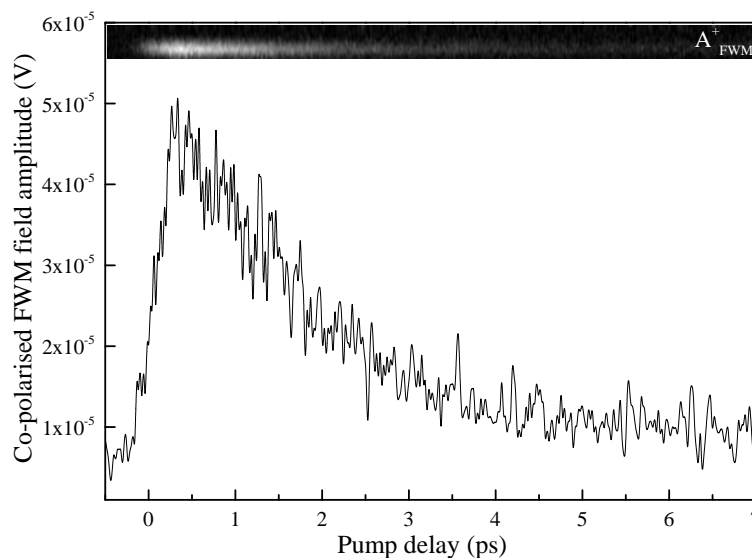


Figure 4.21: Co-polarised FWM field amplitude, A_{FWM}^+ , for a 15nm AuNP-PC-Tf(A488) at the focus center versus pump-probe delay time τ for a pump (probe) power at the sample of 31 μ W (15.5 μ W).

4.4 Imaging 20 nm AuNPs conjugated with antibodies in 3T3-L1 cells

In the two previous sections fluorescence and FWM measurements were not acquired on the same microscope. This led to the implementation of a custom registration analysis (see Chapter 3) in order to correlate position information derived from FWM microscopy of AuNPs with fluorescence microscopy of fluorophores attached onto the AuNPs acquired on a separate microscope. In order to avoid this post-acquisition registration (and its intrinsic uncertainty limits), this section describes the application of simultaneous acquisition of FWM and confocal fluorescence on the same set-up and, in turn, the correlation of these signals on a new series of samples.

In addition, the samples of this section were developed using two different antibodies and a commercially available bio-conjugation kit producing three different samples. The aim was to investigate further the co-localisation between fluorescence and FWM signal on state of the art samples on the same microscope without the need of gridded coverslips and post-measurement registration analysis.

4.4.1 Sample description

The preparation of these samples was realized by my co-supervisor Dr. Peter Watson.

As mentioned above, driven by the need to use state of the art bio-conjugation techniques in order to further investigate the question as to whether fluorescence is a reliable readout when using AuNP-fluorophore constructs, we came across the recent work of I. Cabezón et al. [117]. In their work, they studied via Transmission Electron Microscopy (TEM) the intracellular trafficking of 20 nm AuNPs coated with the 8D3 anti-TfR antibody at the mouse blood-brain barrier in the context of a possible delivery strategy of neurotherapeutics across it. Their sample protocol involved the use of a commercial bio-conjugation kit with proven internalization of AuNPs-8D3 shown on their publication.

The InnovaCoat 20 nm GOLD (20 OD) Conjugation Kit by Innova Biosciences (Cambridge, UK) was purchased in order to covalently attach antibodies on the coated surface of 20 nm diameter AuNPs in a few steps.

Formation of the AuNP-Antibody conjugate:

As the 8D3 anti-TfR antibody is mouse specific we had to use mouse cell lines. 3T3-L1 cells were grown on No. 1.5 thickness 25 mm diameter circular coverslips

(not gridded) (Fisher Scientific). Cells were incubated for 30 min in serum-free media, incubated for 15 min with 2.6×10^{10} AuNPs/ml of Antibody-AuNP solution and washed 3 times with PBS pH 7.4. Finally the cells were fixed in 3% PFA for 10 min at room temperature, washed 3 times in PBS pH 7.4 at room temperature and then mounted onto glass slides in Mowiol.

Table 4.2 alongside Figure 4.22 summarizes the protocol and the properties of the three samples investigated with our multi-modal imaging set-up via correlative FWM and confocal fluorescence.

Overall, we expect that on **Sample 1** (*non specific antibody*) the bioconjugated AuNPs may enter the cell via unspecific endocytosis or may not enter at all; on **Sample 2** (*specific antibody*) we expect to observe FWM signal of AuNPs only in the cells (the sample is not fluorescently labelled so no fluorescence is expected); and on **Sample 3** (*50:50*) we expect to see FWM signal of internalized AuNPs –via Tf-mediated endocytosis driven by the 8D3 antibody– co-localized with the fluorescence emission from the A647 tag on the unspecific antibody also present on the AuNPs surface.

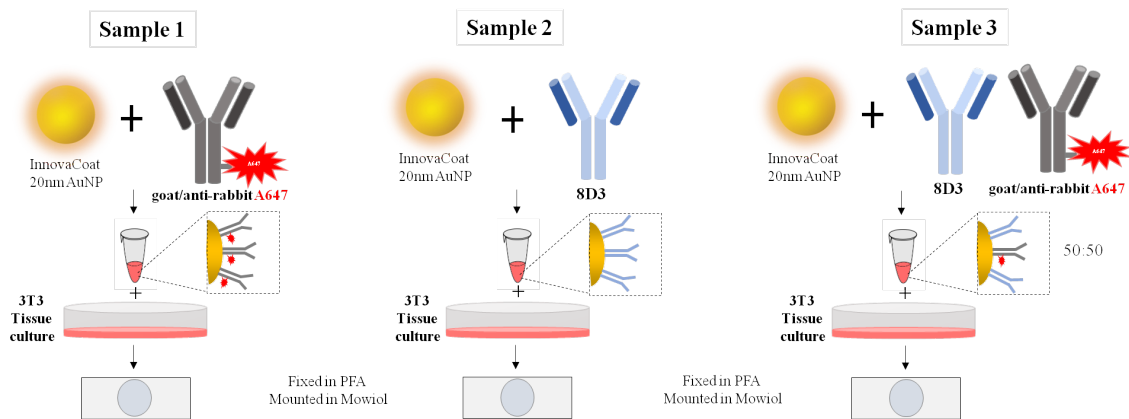


Figure 4.22: Illustration of the three different types of samples used for simultaneous FWM and confocal imaging on our multi-modal imaging set up.

Sample	Antibody type	Endocytic pathway	Labelling
Sample 1	Goat/Anti-rabbit	non receptor-mediated	A 647
Sample 2	8D3	receptor-mediated	No
Sample 3	8D3 + Goat/Anti-rabbit	receptor-mediated	A 647

Table 4.2: Samples' specifications according the antibody and labelling bio-conjugation achieved.

4.4.2 Results and discussion

In this section results for all three samples along with an explanation of the experimental work flow and analysis are presented.

All three samples were imaged on the multi-modal microscope in School of Biosciences via DIC, FWM and confocal fluorescence, the latter being a new modality added on our epi-detection scheme for the purposes of these measurements as explained in 3.1.2.

After optimizing the parameters of the experiment and having identified the cell regions to study, FWM and confocal fluorescence were acquired simultaneously in 3D. Higher power and smaller dwell time, than the ones used in the previous sections, were used here in order to image large cell regions in shorter time. Notably, 3T3-L1 cells are much larger and flatter than HeLa cells. Regarding the settings used, the power of pump (probe) beam was set 62 μW (31 μW) at the sample plane and the dwell time was set between 0.3 ms to 1 ms (each image caption contains the exact information) in order to maintain a sufficiently high signal to noise ratio. A Nikon 100x oil immersion objective with 1.45 NA with 1.5x tube lens was used for focusing of the pump and probe beams as well as for the epi-collection of the detected signals (FWM, reflection and fluorescence). FWM (A_{FWM}^+), reflection (A_{2r}^+) and confocal fluorescence channels were acquired simultaneously enabling detection of AuNPs background free in 3T3-L1 cells, detection of the cell structure and detection of fluorescence in 3D cellular environments. The fluorescence signal was epi-collected and guided into a PMT module Hamamtsu (H10770-40) with a Semrock filter (FF02-650/100) aiming to reject the excitation laser and collect only wavelengths in the range of 600-700 nm.

For all three samples various cell regions of different cells were imaged via z-stacks resulting in 3D images of the cellular environment presented here as (xy-z) montages or/and maximum intensity projections. The z-stack was initiated from the cell-coverslip interface ($z = 0$) where the maximum reflection is usually observed and then move upwards inside the sample ($z > 0$). The pixel size and dwell time can be slightly different for each data set and therefore the exact specifications are given at each Figure's caption.

Sample 1 - Results

Figures 4.23, 4.24 and 4.25 are representative for Sample 1 (*non specific antibody*). As expected for a sample where the AuNPs are attached to an unspecific antibody the number of the internalized AuNPs is very low with many of them to be observed outside the cellular regions. This can be easily seen by comparing the reflection

(c) and FWM (d) images of Figure 4.24 which is shown as a false color overlay on Figure 4.23 and indicates that AuNPs are not effectively internalized within this incubation time (15 min) via non-specific endocytosis. Observing the confocal fluorescence images of the two examples shown on Figures 4.24 and 4.25 one can distinguish intense fluorescent signals coming from structures with a diameter of about 1 μm . This is much larger than the PSF of the 1.45 NA objective expected in one-photon fluorescence ($\lambda/2\text{NA} \approx 200 \text{ nm}$). The structures are largely uncorrelated with the FWM from the AuNPs, and their fluorescence intensity is comparable to the autofluorescence observed in sample 2, particularly when imaging regions near the cell nucleus (see Figure 4.28).

Limited by the cell's autofluorescence and in order to further verify the origin of these fluorescent structures we imaged the sample on the wide-field fluorescence microscope in Cardiff School of Biosciences. The wide-field epi-fluorescence imaging of the sample was realized after the FWM experiments and it was optimized both for A647 and A568 detection (see Table 3.1 for the excitation/detection bandwidth corresponding to these channels) by setting 600 ms acquisition time and pixel binning 4. The A568 channel was additionally acquired to the A647 in order to 'simulate' the wavelength excitation of the FWM set-up and be able to qualitatively compare the cell's autofluorescence at this wavelength regime (note however that the detection range for the A568 channel in the widefield fluorescence microscope is from 580 nm to 630 nm while the confocal fluorescence detection range implemented in the FWM set-up is 600-700 nm). As shown on Figure 4.26 the sample exhibited autofluorescence on both channels. The fluorescent structures observed on our home-built microscope were also visible in Figure 4.33 around similar regions; clearly strong autofluorescence was observed around the nucleus. By further looking into the literature the origin of this signal can be attributed to vesicles or/and mitochondria which are known to exhibit autofluorescence under similar imaging conditions as presented by Dellinger et al. [118] and Andersson et al. [119]. Figure 4.26 shows some dotted structures appearing more pronounced in the red channel, which suggests that some A647-related fluorescence is actually visible, above the autofluorescence level. In particular, dotted structures are observed outside cell, consistent with the observation from FWM imaging that the AuNPs are not being efficiently internalised and are found mostly outside the cells. However, in these samples, A647 gives a weak fluorescence signal as the settings were not the ones typically used when a good concentration of fluorophore is present (600 ms acquisition time is a high interval in our experience when imaging on this microscope). To that end, we noticed that fixation of these cells was accompanied by a significant quenching of the fluorescence of the A647 as compared to imaging the cells live.

In summary, it appears that (i) fluorescence excitation at 550 nm and detection at 600-700 nm, as used in the FWM microscope, is accompanied by significant cellular autofluorescence, especially near the nucleus; (ii) fluorescence detection of $\approx 1 \mu\text{m}$ wide structures is probably due to vesicular/mitochondrial autofluorescence; (iii) some (punctuated) structures could be related to the A647 labelling but they are hard to distinguish from the autofluorescence background. Therefore in regions inside the cells, we cannot conclusively correlate FWM measured on AuNPs with the fluorescence signal as the latter is significantly affected by cellular autofluorescence. Notably, when looking in regions outside the cell where AuNPs are visible in FWM and cellular autofluorescence is not present, we still did not observe any clear fluorescence above background that could be correlated with the AuNPs. These results thus suggest that either the A647 is bleached, to the extent of making it undetectable against the background even outside the cell, or is actually not attached to the AuNP. It should be pointed out that since A647-related fluorescence appears to be visible in Figure 4.26 (both inside and outside the cell region) when using wide-field epifluorescence excitation/detection, the lack of any fluorescence from A647 being detected with the confocal modality implemented in the FWM microscope suggests additional fluorophore photobleaching induced by the pulsed laser scanning excitation where high peak field intensities are used ($\sim \text{GW}/\text{cm}^2$), compared to the mild widefield excitation ($\sim \text{W}/\text{cm}^2$). Future additional studies should be devoted to clarify this point.

Sample 2 - Results

Sample 2 (*specific antibody*) consists of non fluorescent 8D3-AuNP conjugates which are expected to be internalized via receptor-mediated endocytosis in the cell. The only way to evaluate the uptake behaviour of this sample is via our FWM imaging set-up based on the FWM signal coming from the AuNPs in absence of fluorophore. The results in Figures 4.27 and 4.28 support the expectation of a more efficient internalisation in this sample compared to Sample 1. On both examples an overall DIC image of the cell is shown alongside a smaller cellular region where the reflection (A_{2r}^+), FWM (A_{FWM}^+) and confocal fluorescence channels (no fluorescence from A647 is expected here but was acquired simultaneously for background reference and as autofluorescence control) for each z step/position. It is clear from both the FWM channel (Figures 4.27(c), 4.28(c)) and the false colour overlay images where the maximum intensity projection of the FWM channel is merged with a single x,y reflection channel (Figures 4.27(e), 4.28(e)) that the AuNPs are visible in all the z-steps indicating that the AuNPs are internalized in vesicles throughout the whole cell volume. Also no particles appear in regions outside the cell which is an addi-

tional indicator of the targeted receptor-mediated endocytosis. As mentioned, at the fluorescent channel of Figure 4.28 we observed similar autofluorescent features and intensity levels as in Figure 4.24 which supports their attribution to endogenous subcellular organelles such as mitochondria, as discussed previously. Notably, as previously mentioned, the autofluorescence is significant near the cell nucleus (Figure 4.28) while much lower in more peripheral cellular regions (Figure 4.27).

Sample 3 - Results

Figures 4.29 - 4.33 correspond to Sample 3 (50:50). All these examples involve similar measurements to the ones for the previous two samples where large cell regions were imaged simultaneously via FWM and confocal fluorescence imaging. The large numbers of NPs internalised by the cells observed in all FWM images for the examples of Sample 3 – which contains both antibodies used in Samples 1 and 2 in equal quantities– compared to Sample 1 suggests that the combined antibody conjugation was successful and that the conjugates entered the cells via receptor-mediated endocytosis. The false colour overlay image in Figure 4.30(c), where the maximum intensity projection of the FWM channel is merged with a single x,y reflection channel, strengthens further the above argument as only two NPs were imaged outside a $50 \times 50 \mu\text{m}$ region. All the images/results for Sample 3 are consistent with the previous remarks. A video showing the FWM channel of Figure 4.29 can be found at <https://youtu.be/Pg4i0etlvks>. In particular, similar to Sample 1 autofluorescence coming from the cell and subcellular organelles dominated the confocal fluorescence detection, and thus hindered any conclusive correlation of the A647 label with the AuNPs in cellular regions. As a result, we did not perform the correlation analysis in terms of Pearson and Manders coefficients (note that for these sample no image re-registration (i.e. rotation and translation, see Chapter 3) would be required as the images are acquired simultaneously). By merging the maximum intensity projection of the FWM with the confocal fluorescence channel (as appears in all the examples of Figures 4.29–4.32) it is straightforwardly observed that the two signals are not correlated. Following the experimental work flow on Sample 1 we performed wide-field fluorescence imaging as shown on Figure 4.33 where two cell regions of Sample 3 are illustrated on channels A647 (fluorophore tag) and A568 (mimicking the laser beam excitation at 550nm of the FWM). The imaging parameters were the same to the ones for Sample 1; 600 ms acquisition time and binning 4. The same attributes to the ones described for Sample 1 are also observed here by comparing the wide-field fluorescence images Figure 4.33 to the fluorescence obtained on our home-built microscope Figures 4.29–4.32.

In all samples, confocal fluorescence was dominated by autofluorescence coming

either from the cell's nucleus or $\approx 1\mu\text{m}$ fluorescent structures which are ascribed to either aggregated fluorescently tagged constructs or subcellular organelles like mitochondria or vesicles. This fact imposed significant limitations on detecting fluorescence emitted by the A647 fluorophore inside the cell and therefore made impossible a direct comparison and correlation analysis of the two channels (FWM-confocal fluorescence).

Overall, these results also highlight the limitations of fluorescence microscopy largely affected by problems including background autofluorescence and photobleaching, and confirm the superior performance of background free FWM imaging to located gold NPs specifically and unambiguously inside cells.

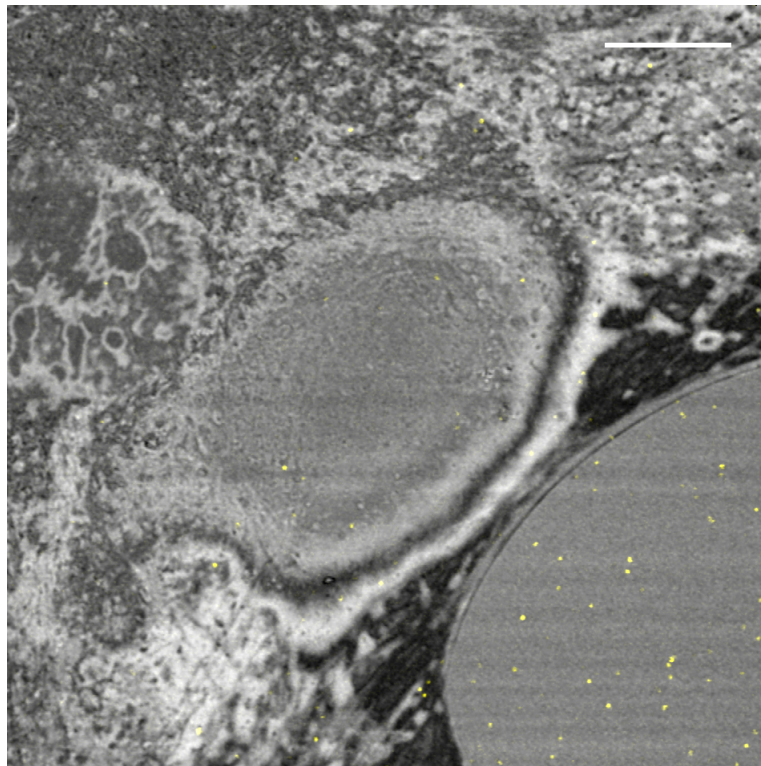


Figure 4.23: Sample 1 False colour overlay images of reflection (grey) and the maximum intensity projection of FWM (yellow) channel of Figure 4.24 where the AuNPs are depicted with yellow dots in adjusted scale to enhance visibility. Scale bar is 10 μm .

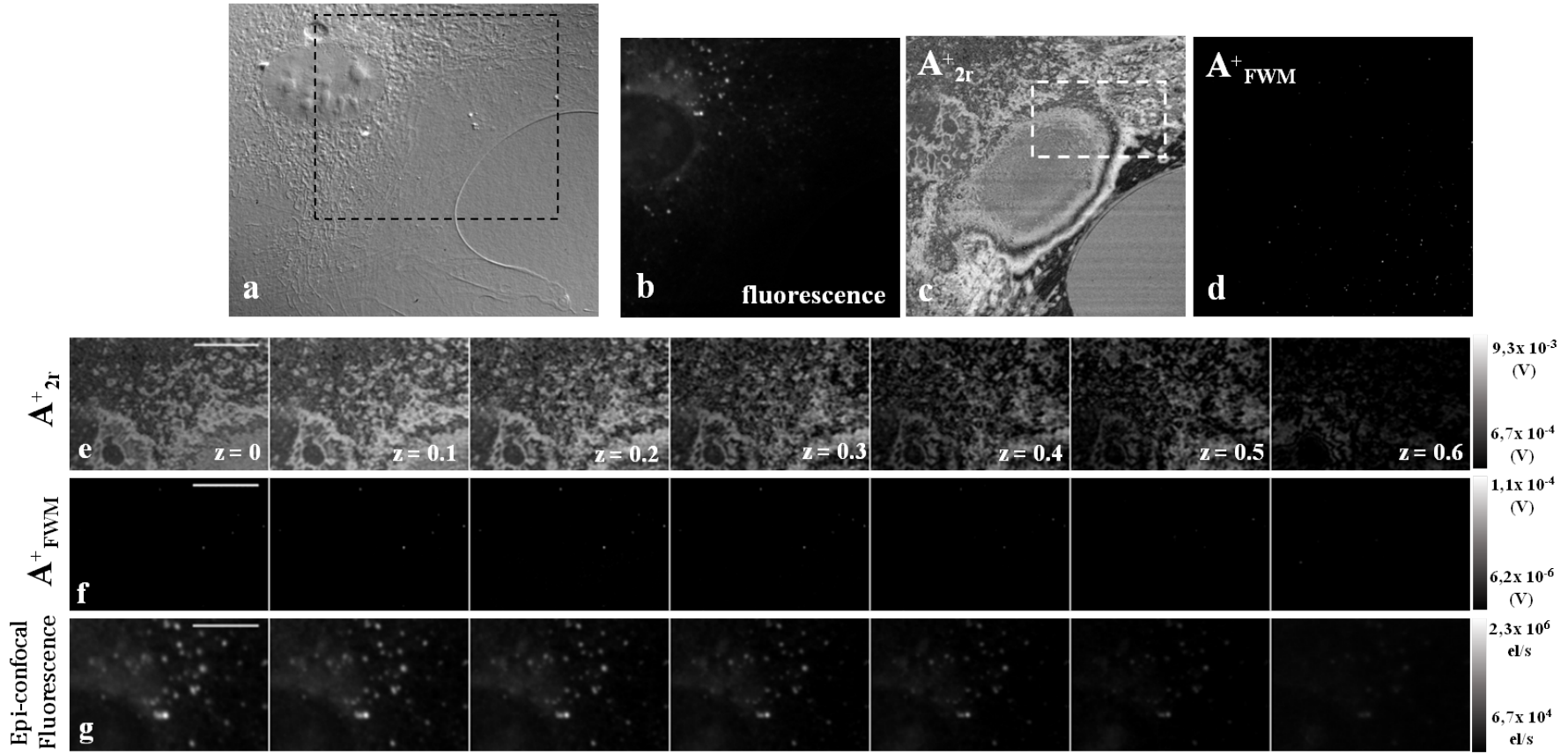


Figure 4.24: Sample 1 - Example 1

(a) DIC image of a cell region where the highlighted rectangular shows a $60 \times 60 \mu\text{m}$ cellular region imaged simultaneously via confocal fluorescence (b) and FWM (c,d). The co-polarised reflection, A_{2r}^+ , (c) and co-polarised FWM, A_{FWM}^+ , (d) and fluorescence (b) channels were acquired with 0.4 ms dwell time and 64 nm pixel size. A smaller region (indicated with white rectangular on (c)) was thereafter imaged as z-stack with 100 nm z-step size, 0.5 ms dwell time and 63 nm pixel size. Reflection (e), FWM (f), fluorescence (g) channels are shown as montages over the different z with their intensity scale bars on the right (as measured in Volts for FWM and reflection and in photoelectron/sec for fluorescence). The scale bar for e,f and g is 10 μm.

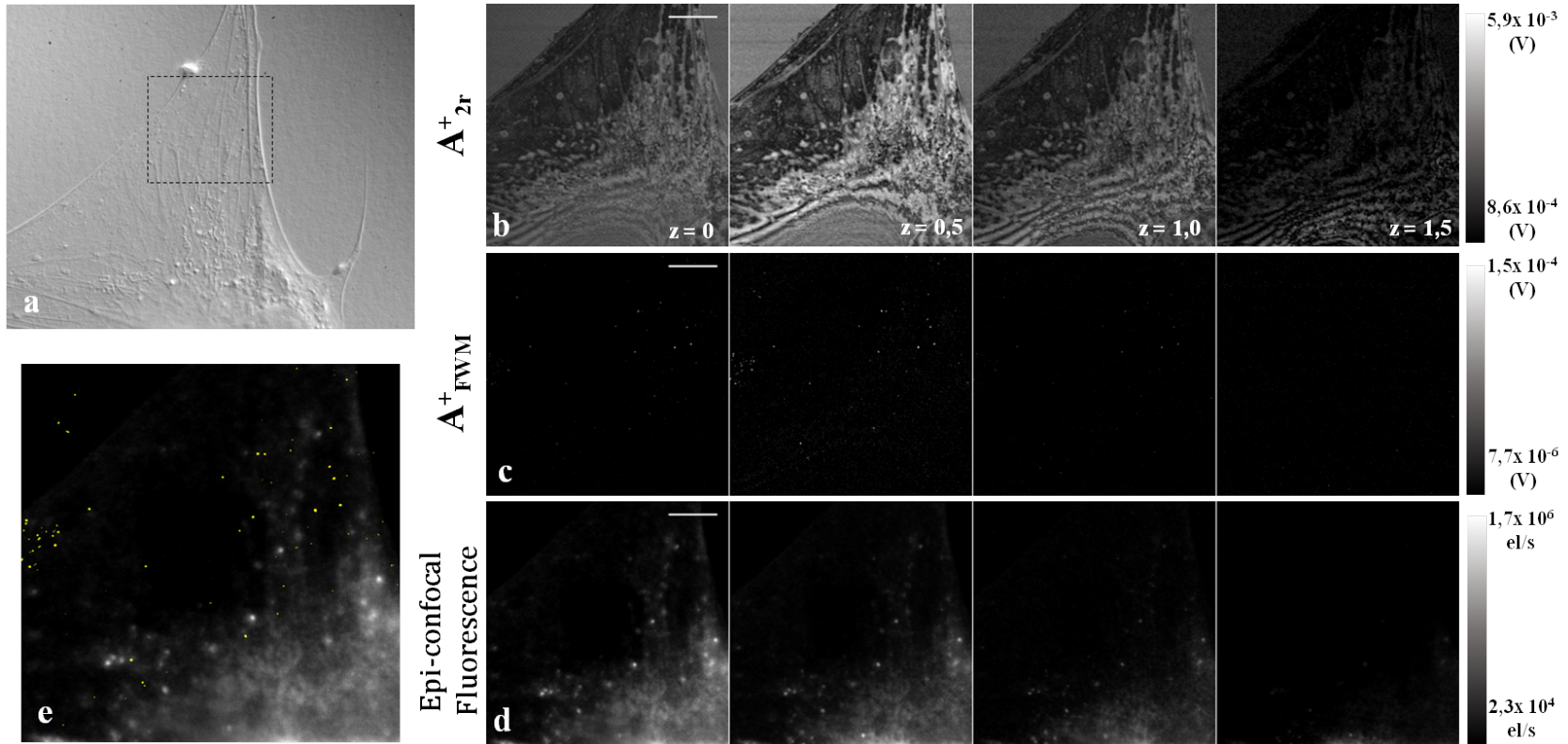


Figure 4.25: Sample 1 - Example 2

(a) DIC image of another cell region where the highlighted rectangular shows a $50 \times 50 \mu\text{m}$ cellular region imaged in 3D simultaneously via FWM (b,c) confocal and fluorescence (d). The co-polarised reflection, A_{2r}^+ , (b) and co-polarised FWM, A_{FWM}^+ , (c) and fluorescence (d) channels were acquired with 0.4 ms dwell time and 63 nm pixel size. The z-stacks with 500 nm z-step size are shown as montages over the different z with their intensity scale bars on the right. The scale bar for e,f and g is 10 μm . A false color overlay image (e) of the maximum intensity projection of the confocal fluorescence (grey) on top of the FWM one (yellow dots indicate the FWM signal originating from AuNPs) on adjusted scale indicates lack of co-localization of the two signals.

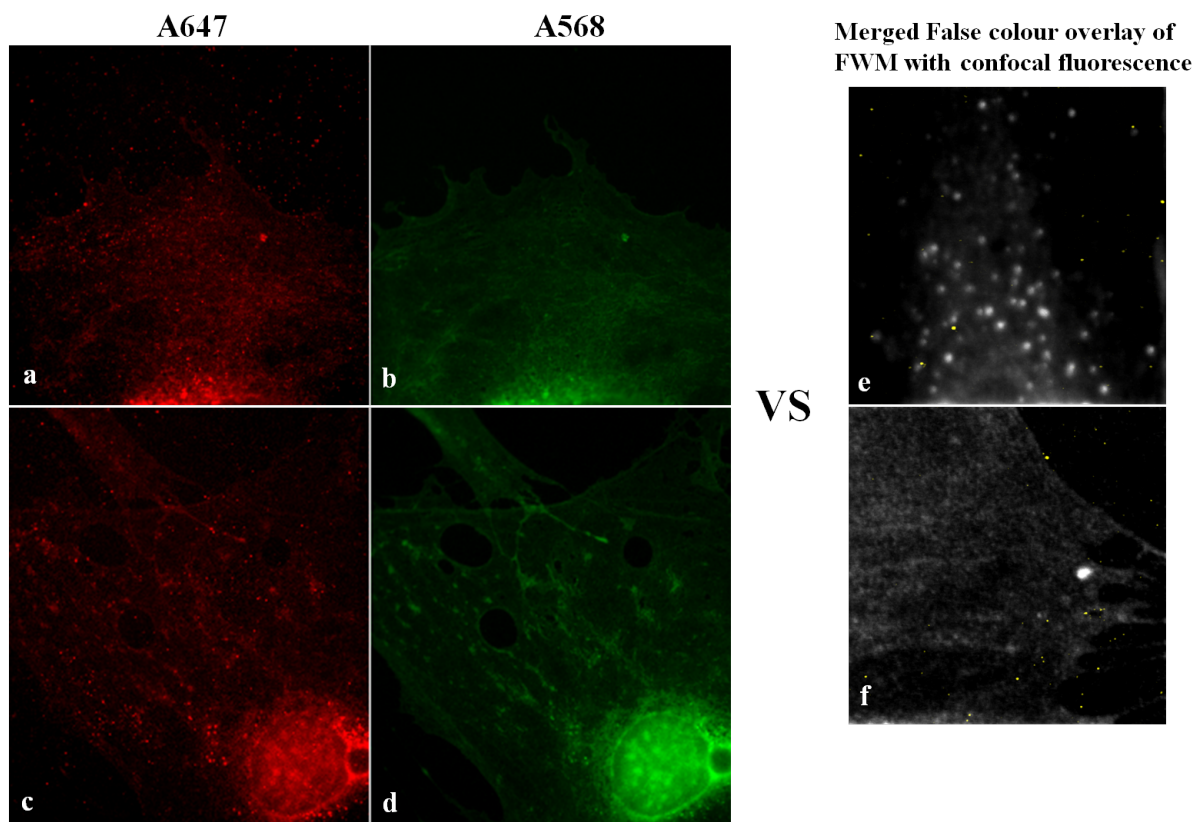


Figure 4.26: Qualitative comparison of fluorescence images acquired in our home-built microscopy set-up (e, f) with the ones acquired on the commercially available wide-field epi fluorescence microscope (a-d) for different cell regions on Sample 1. On the left, fluorescence images for the A647 (a, c) and A568 (b, d) channels on the commercially available microscope are shown on a 0-255 intensity scale. On the right, two merged images (different examples to the ones shown on Figures 4.24 and 4.25) of the maximum intensity projection of the FWM and fluorescence channels are shown in false colour (e, f); grey colour depicts the fluorescence while the yellow dots represent the AuNPs.

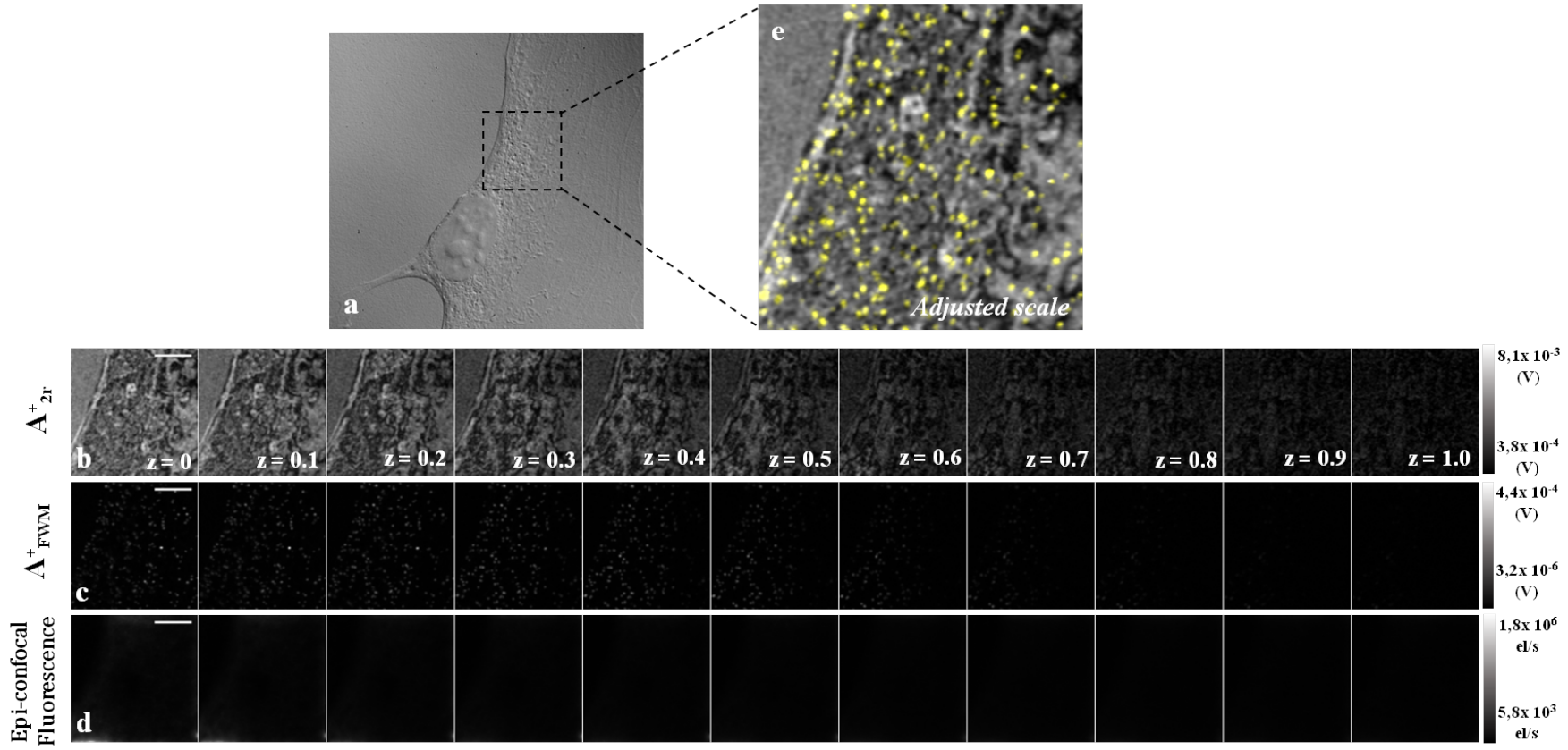


Figure 4.27: Sample 2 - Example 1

(a) DIC image of a cell region where the highlighted rectangular shows a $17 \times 17 \mu\text{m}$ cellular region imaged in 3D simultaneously via FWM (b,c) and confocal fluorescence (d). The co-polarised reflection, A_{2r}^+ , (b) and co-polarised FWM, A_{FWM}^+ , (c) and fluorescence (d) channels were acquired with 1 ms dwell time and 62 nm pixel size. The z-stacks with 100 nm z-step size are shown as montages over the different z with their intensity scale bars on the right. The scale bar for b,c and d is 5 μm . False color overlay image (e) of the maximum intensity projection of the the FWM channel of the whole stack (yellow dots in adjusted scale indicate the FWM signal originating from AuNPs) on top of a single xy reflection plane. All the AuNPs have been internalized and are located inside the cell as FWM (c) channel shows.

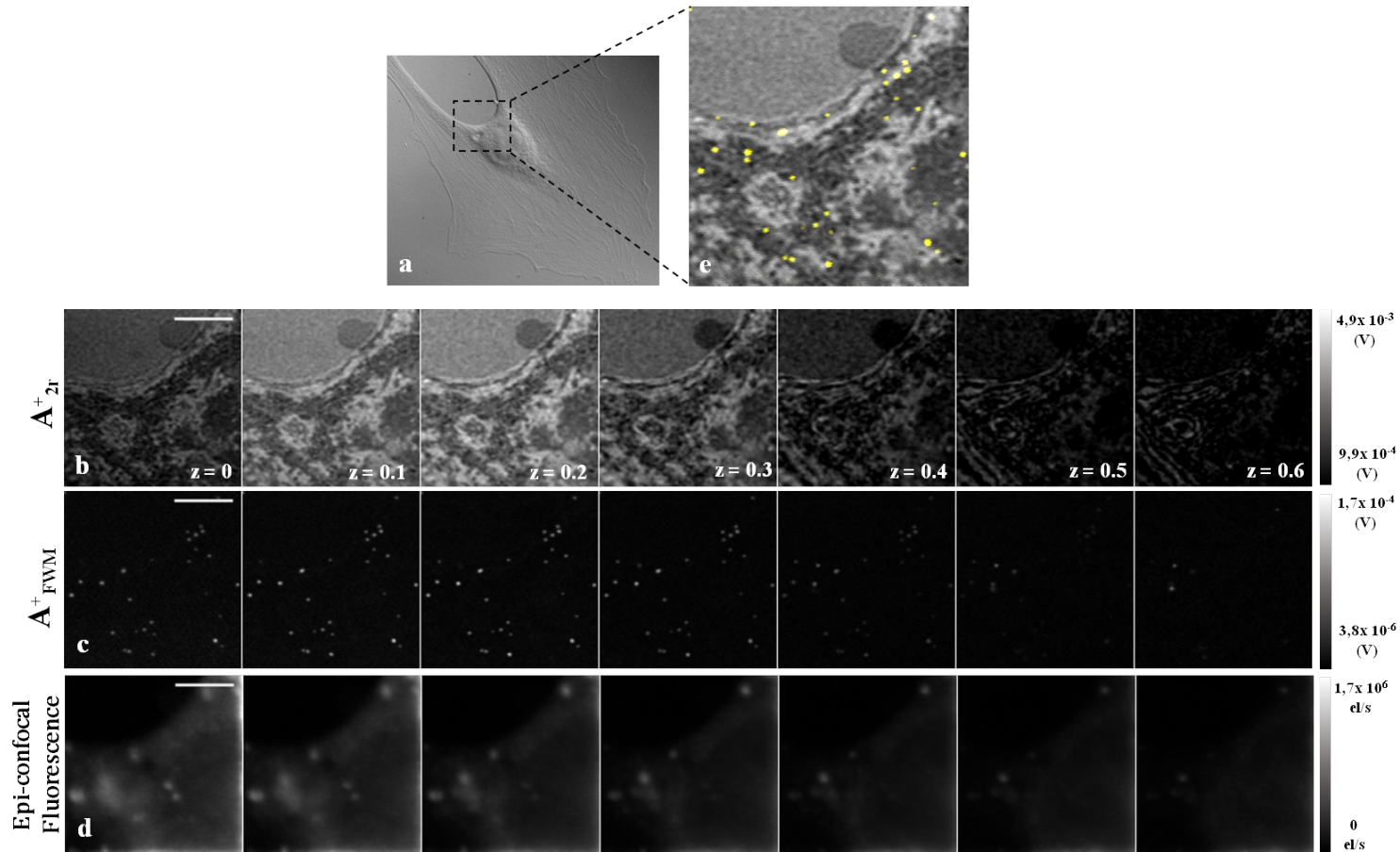


Figure 4.28: Sample 2 - Example 2

(a) DIC image of a cell region where the highlighted rectangular shows a $15 \times 15 \mu\text{m}$ cellular region imaged in 3D simultaneously via FWM (b,c) and confocal fluorescence (d). The co-polarised reflection, A_{2r}^+ , (b) and co-polarised FWM, A_{FWM}^+ , (c) and fluorescence (d) channels were acquired with 1 ms dwell time and 47 nm pixel size. The z-stacks with 200 nm z-step size are shown as montages over the different z with their intensity scale bars on the right. The scale bar for b,c and d is 5 μm . False color overlay image (e) of the maximum intensity projection of the the FWM channel of the whole stack (yellow dots in adjusted scale indicate the FWM signal originating from AuNPs) on top of a single xy reflection plane.

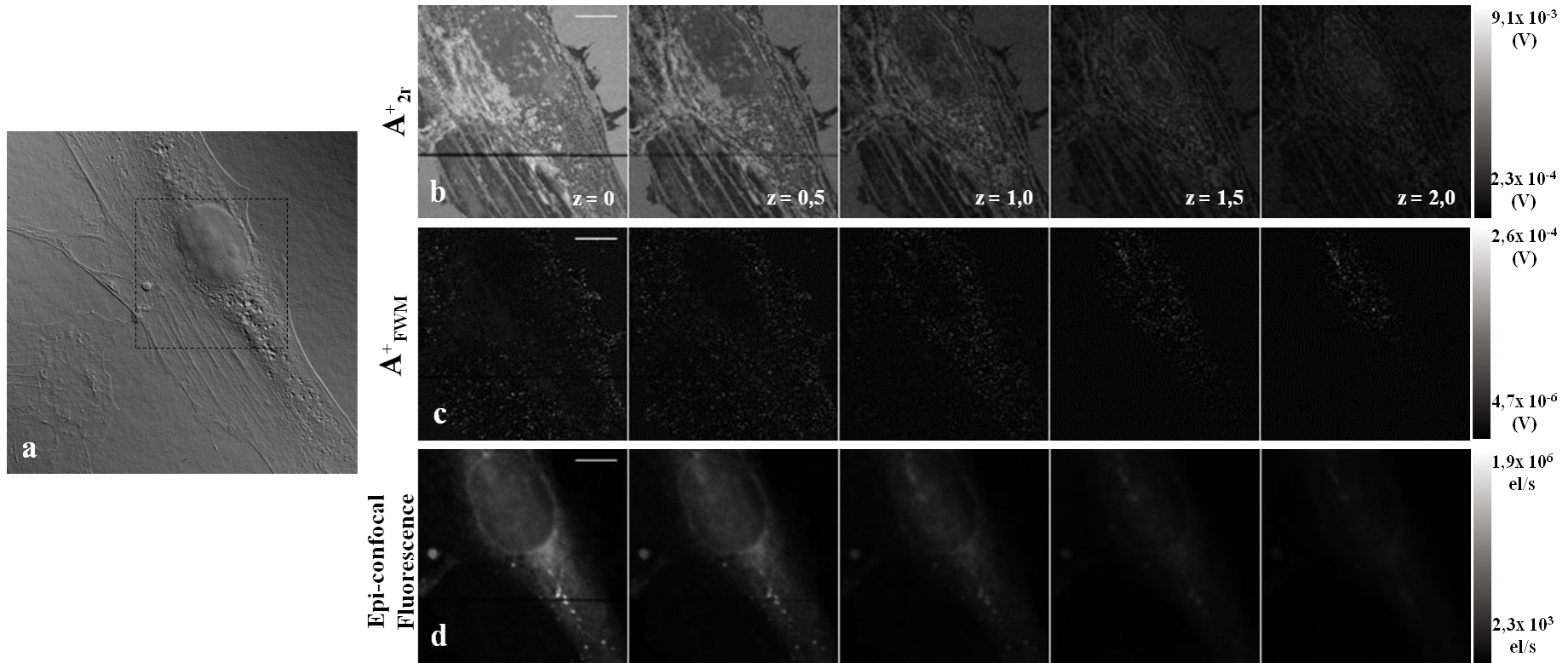


Figure 4.29: Sample 3 - Example 1

(a) DIC image of a cell region where the highlighted rectangular shows a $50 \times 50 \mu\text{m}$ cellular region imaged in 3D simultaneously via FWM (b,c) confocal and fluorescence (d). The co-polarised reflection, A_{2r}^+ , (b) and co-polarised FWM, A_{FWM}^+ , (c) –video can be found at <https://youtu.be/Pg4i0etlvks>– and fluorescence (d) channels were acquired with 0.4 ms dwell time and 63 nm pixel size. The z-stacks with 500 nm z-step size are shown as montages over the different z with their intensity scale bars on the right. The scale bar for b,c and d is 10 μm . Notably, the AuNPs have been internalized and are located inside the cell as FWM shows (c). The black line on the zero step originated from sudden loss of the laser beam due to the laser’s auto-alignment maintenance.

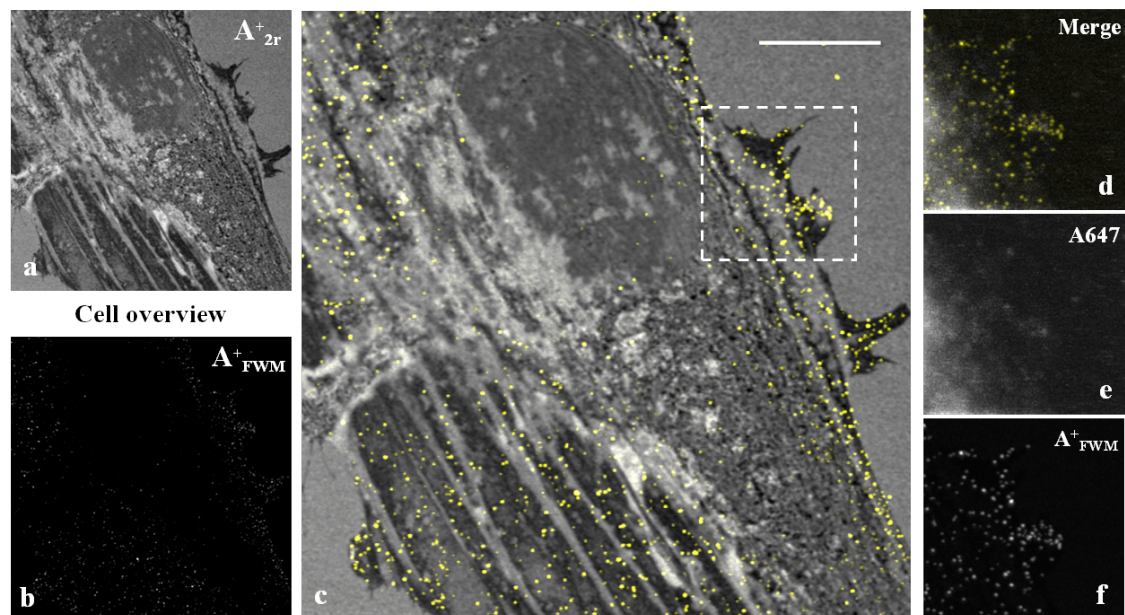


Figure 4.30: Sample 3 - Example 1 overlay The cell region of Figure 4.29 is shown on the reflection channel, A_{2r}^+ , (a), the FWM channel, A_{FWM}^+ , (b) and as a false colour overlay of the previous two channels (c) where the AuNPs appear as yellow single dots on the cell membrane. FWM channels are shown as maximum intensity projection over 6 μm z-stack while the reflection is shown on a single xy plane. On the right we can see the rectangular region highlighted on (c). The merged false colour overlay (d) is composed of the maximum intensity projection of the fluorescence channel (e) on top of the FWM one (f). Scale bar is 10 μm .

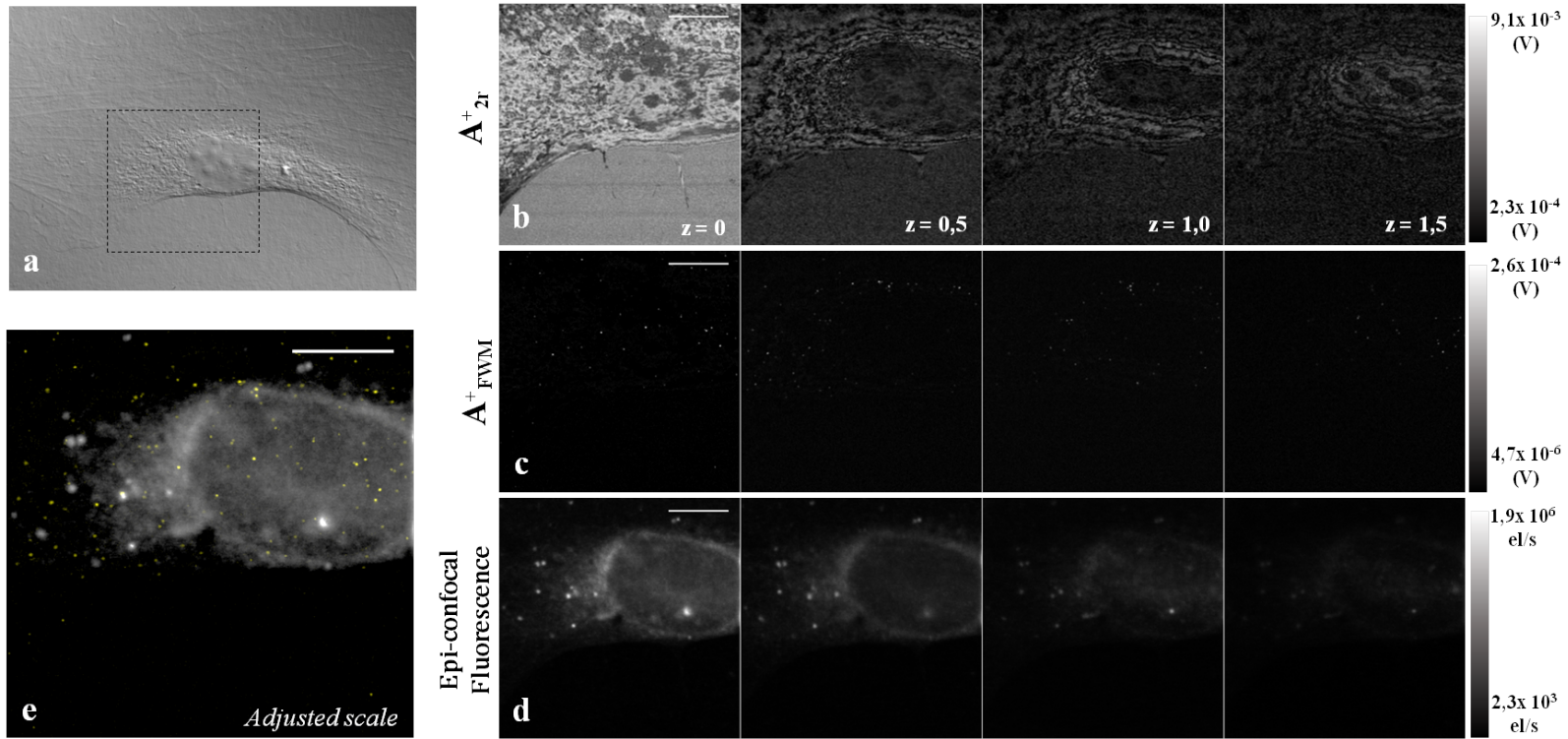


Figure 4.31: Sample 3 - Example 2

(a) DIC image of a cell region where the highlighted rectangular shows a $40 \times 40 \mu\text{m}$ cellular region imaged in 3D simultaneously via FWM (b,c) confocal and fluorescence (d). The co-polarised reflection, A_{2r}^+ , (b) and co-polarised FWM, A_{FWM}^+ , (c) and fluorescence (d) channels were acquired with 0.5 ms dwell time and 63 nm pixel size. The z-stacks with 500 nm z-step size are shown as montages over the different z with their intensity scale bars on the right. The scale bar for b,c and d is 10 μm . False colour overlay image (e) of the maximum intensity projection of the the FWM channel of the whole stack (yellow dots in adjusted scale indicate the FWM signal originating from AuNPs) on top of the confocal fluorescence one (shown in gray). AuNPs are shown to be homogeneously internalized and located inside the cell as FWM channel shows(c).

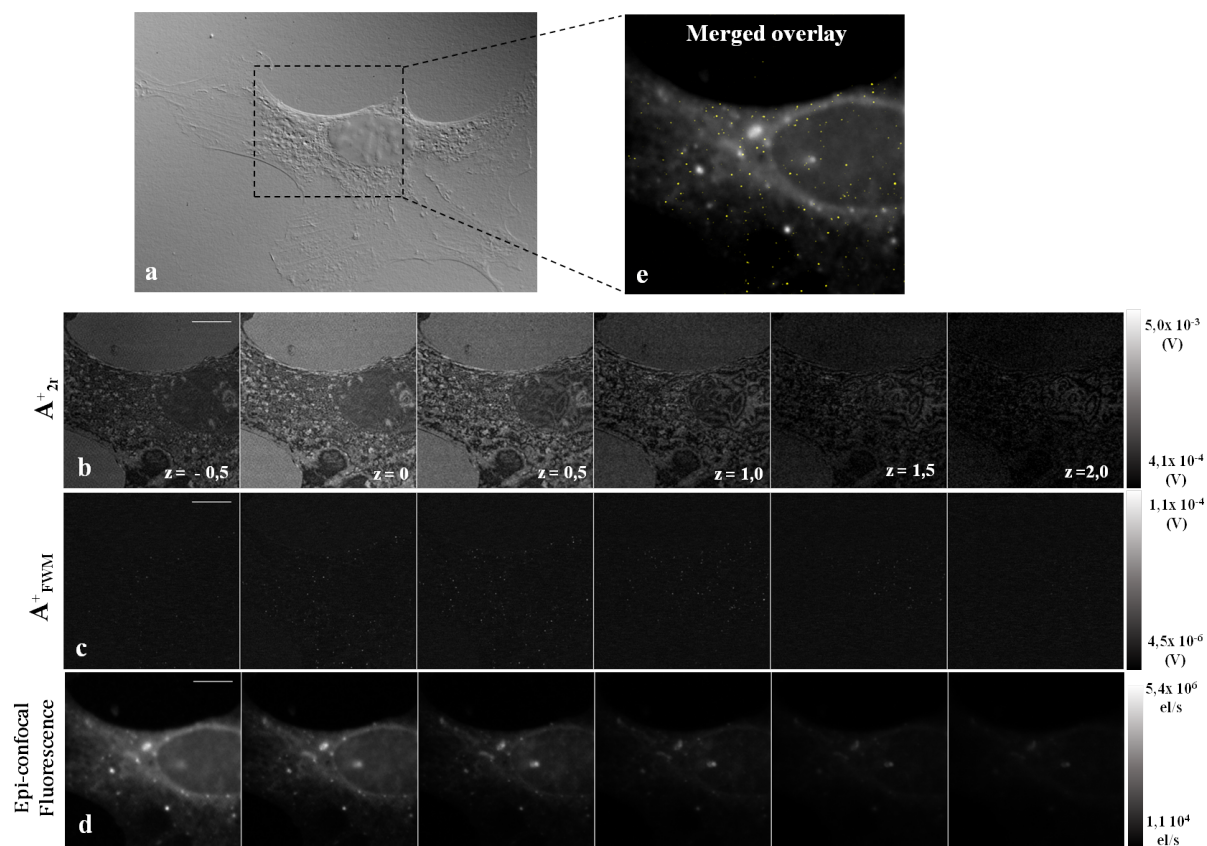


Figure 4.32: Sample 3 - Example 3

(a) DIC image of a cell region where the highlighted rectangular shows a $45 \times 45 \mu\text{m}$ cellular region imaged in 3D simultaneously via FWM (b,c) confocal and fluorescence (d). The co-polarised reflection, A_{2r}^+ , (b) and co-polarised FWM, A_{FWM}^+ , (c) and fluorescence (d) channels were acquired with 0.3 ms dwell time and 63 nm pixel size. The z-stacks with 500 nm z-step size are shown as montages over the different z with their intensity scale bars on the right. The scale bar for b,c and d is 10 μm . False color overlay image (e) of the maximum intensity projection of the the FWM channel of the whole stack (yellow dots in adjusted scale indicate the FWM signal originating from AuNPs) on top of the confocal fluorescence one (shown in gray).

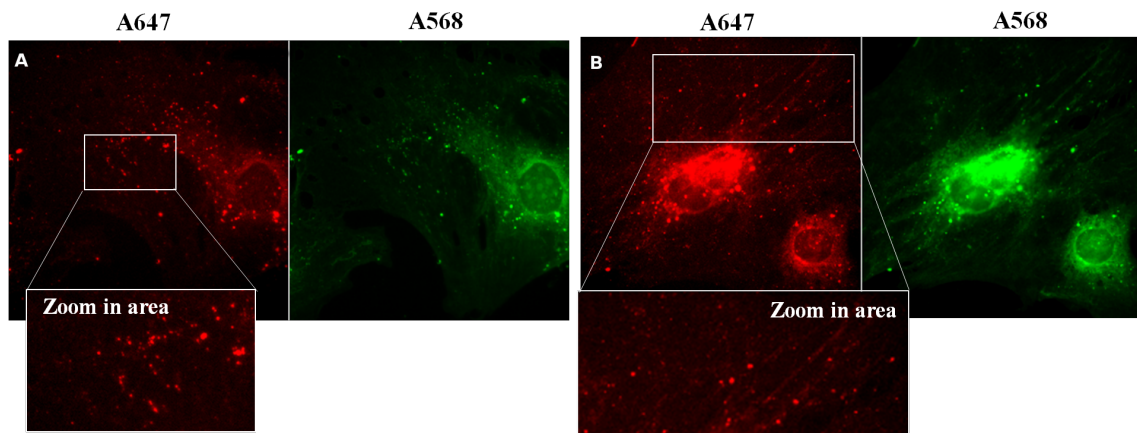


Figure 4.33: Two cell regions (A and B) of Sample 3 imaged on the commercially available wide-field epi fluorescence microscope for A647 and A568 channels. Zoom in regions are displayed and show strong fluorescence coming from similar structures to the ones observed via our confocal fluorescence on our home-built microscope.

Proof of FWM signal

The FWM signal was once again verified during each imaging session via either pump-probe delay scans (Figure 4.35) or via xy raster scans with a negative pump-probe delay (Figure 4.34) for two different cellular regions. Similar to previous measurements, the FWM origin of the signal as due to the free electron gas in the AuNPs undergoing ultrafast heating/cooling dynamics is shown in the below figures.

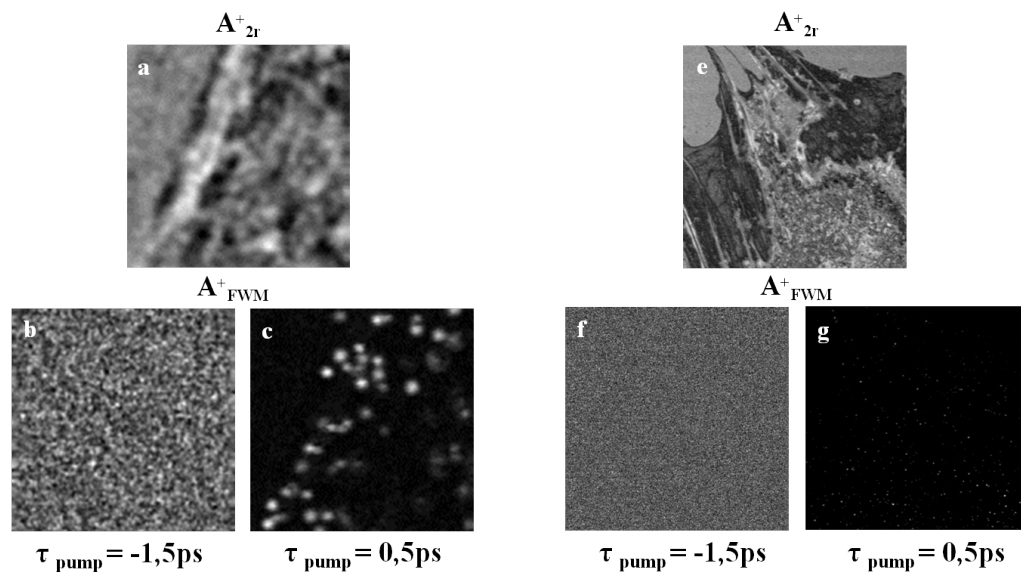


Figure 4.34: Two examples of xy raster scans with 0.5 ps and -1.5 ps pump-probe delay. Channels (a),(e) refer to the co-polarized reflection while the (b-c) and (f-g) refer to the co-polarized FWM one. Where the pump-probe delay is negative we do not observe FWM signal coming from AuNPs.

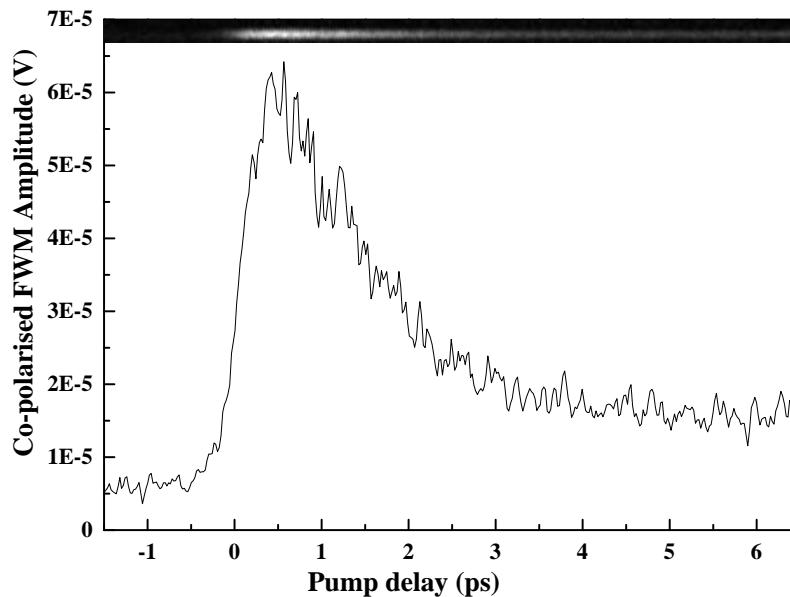


Figure 4.35: Co-polarized FWM field amplitude (V) for a 20 nm diameter AuNP at the laser beam's focus center versus pump-probe delay time τ for a pump (probe) power at the sample of 62 μW (31 μW).

4.5 Summary

Overall this chapter dealt with correlative FWM-fluorescence imaging measurements performed on an array of AuNP-fluorophore conjugate constructs both developed in house and commercially available with the scope to investigate their integrity in cells. Samples were divided, based on the bioconjugating type of labelling of the AuNPs into three groups:

- In section *Measurements of AuNPs conjugated with Transferrin in HeLa cells*, **the sequential labelling SA:Bi in house protocol** was used in order to bound AuNPs-SA conjugates (with SA covalently attached –40 nm AuNP sample– or non-covalently –10 nm AuNP sample–) with the biotinylated fluorescently labelled Tf.
- In section *Measurements of polymer coated 15nm AuNPs uptaken by HeLa cells*, **polymer coated AuNPs** were attached to a fluorescently labelled Tf.
- In section *Imaging of 20 nm AuNPs conjugated with various types of antibodies in 3T3-L1 cells*, **AuNPs were bound to antibodies** (a fluorescently

labelled-TfR antibody and a non-fluorescent unspecific antibody were used) via a commercially available bio-conjugation kit.

Common findings are that large areas of the cell that exhibit fluorescence do not show AuNPs in the same spatial location, and AuNPs (observed by FWM) are in spatial locations that are not fluorescent (or the observed fluorescence is indistinguishable from endogenous autofluorescence). This was quantified by a correlation analysis, where the degree of co-localisation measured via Pearson's and Mander's overlapping coefficient (for the FWM channel) was generally very poor. Moreover, due to limitations such as photobleaching and cellular autofluorescence a quantitative correlation analysis was not performed on a number of samples as was deemed not meaningful.

Explanations for the results shown in this chapter can vary and strongly depend on the construct used, the sample preparation protocol and the experimental imaging parameters as discussed in each sample group's result section. Overall, the possible reasons of lack of co-localisation observed in this study between fluorescence and FWM signal and hence negligible spatial correlation between fluorophores and AuNPs belonging to the same construct, can be summarised as follows: (i) break down (dissociation) of the constructs during internalization or several washing steps, (ii) presence of unbound fluorophores and/or proteins (SA) in the initial solutions applied to cells, (iii) degradation of the fluorophore where the 'chase' part of the biological protocol was very long (i.e. the 40 nm AuNP-SA:Bi-Tf-A647 sample which was chased for 6 hours), (iv) fluorescence quenching due to fluorophores being attached in close proximity to AuNPs (e.g 15 nm AuNPs-PC-Tf-A488), and (v) photobleaching effects due to high photo-excitation intensities (i.e. 20 nm AuNPs-Antibody-A647).

Importantly, these results are consistent with a very recent publication of Miles et al. [48] which showed no correlation between fluorescence and scattering signal coming from commercially available 10 nm AuNP-SA-A633 (similar construct to the ones used in the samples undergoing sequential labelling). In this published work, a diluted solution of the fluorescently labelled AuNPs was drop-deposited onto a coverslip and the sample was imaged on an interferometric cross-polarised microscope (IPCM) [50] combining the ability to detect scattering from single 10 nm AuNP and single molecule fluorescence at very low powers (less than 20 μ W). They concluded that there was a "complete absence of co-localisation" between the two signals and that most likely the AuNP quenches the fluorescence signal as was also previously reported by Kandela et al. [52]. Ref [52] had examined –among others– bulk solutions of 5 - 18 nm AuNP conjugated with fluorescently labelled antibodies and proved that the fluorescence signal of the construct was "nearly completely

quenched ($> 99\%$).

All in all, these findings highlight on the one hand the limitations of fluorescence labelling, and on the other hand the advantage of the background-free FWM technique used in this thesis as a reliable way to locate non-fluorescent AuNPs inside cells.

This study is of great importance to the cell imaging community which is traditionally based on fluorescence methods. Researchers shall keep in mind that fluorescence labelling is not always a reliable mean of following the cellular uptake of AuNPs and that biological probes have to be carefully chosen and characterized, not only as being biologically adequate but also in terms of photophysical behaviour and imaging detection properties, in order to avoid misinterpretation of results derived solely from fluorescence imaging.

5

STUDY OF AUNP'S DIFFUSION IN AGAROSE MATRIX GEL

5.1 Motivation

So far the thesis has discussed the high selectivity and background free capability of the FWM technique leading to correlative observations between intracellular uptake of various types of AuNPs and their fluorescently labeled attached ligands inside cells, at fixed time points. However, many questions that biomedical scientists aim to answer refer to understanding dynamic processes in living systems. To do so, there has been a tremendous progress in the physics community in developing techniques and data analysis methods that can elucidate these dynamic mechanisms inside cells. Among the most popular ones are the Single Particle Tracking (SPT) using optical microscopy. An updated scientific review on the progress on this field can be found in [120].

Probably the most widespread SPT methods are fluorescence based techniques which can achieve high localization precision and sufficient contrast against heterogeneous background using the single-emitter localisation principle [29],[28]. Alternative to those, key enabling techniques to access dynamics in living cells include fluorescence recovery after photobleaching (FRAP) which uses photobleaching in order to selectively switch off a fluorescently labeled molecule and has been applied to study protein dynamics in the cytoplasm or cellular structures in cells. In addi-

tion, Fluorescence correlation spectroscopy (FCS) is a correlation analysis method that analyses the intensity fluorescence fluctuations arising from a diluted solution observed in tiny volumes ($\sim 1 \mu\text{m}^3$) and provides information on the average dynamics (diffusion time) of the molecules under study [121], [122]. Of note is also the super resolution techniques cited also above: stimulated emission depletion microscopy (STED) that has allowed FCS measurements of individual molecules on nanoscale regions ($\sim 50 \text{ nm}$) in living cell membranes [123].

Alternative to the above mentioned far-field optical microscopy techniques are the near-field optic methods which can achieve spatial resolution down to 10 nm by localising the light field using metal coated tips [124], optical fiber probes with sub-wavelength apertures [30] or plasmonic nano-antennas [125]. All techniques using fluorescence are however limited by the intrinsic photophysical properties of single quantum emitters like saturation, photobleaching and photoblinking which provoke restrictions on the achievable photon fluxes. Moreover the induced phototoxicity and perturbation (due to the labeling) further hinders their practical applicability to living specimens. Ultimately, low photon fluxes result in low imaging quality and loss of localization precision which is of great importance in SPT applications [126].

A different approach is the exploitation of the unique optical properties of metallic nanoparticles by the means of far-field optical microscopy. It has been shown that 2D detection and localisation of (relatively big, e.g. 40-50 nm diameter) gold nanoparticles in living cells is possible via wide-field techniques such as DF microscopy [127] [33] and DIC microscopy [128]. The simple implementation of these techniques provides a relatively facile way for SPT applications; they are however limited by the scattering of the cellular environments.

By detecting the thermally induced refractive index change of the surrounding of a AuNP, photothermal imaging (PTI) has recently tracked 5 nm gold beads in 2D in live cells [129]. PTI is a pump-probe technique where a resonant (to the LSPR) pump-heating beam is superimposed with a non resonant probe beam. However it also suffers from background, namely photothermal contrast due to endogenous cell absorption [41]. Furthermore the need to acquire from multiple spatial points in order to localise the nanoparticle brings limitations to the acquisition speed of this method.

A key point of the highly selective and background-free FWM technique used during my PhD project that has not yet been showcased in this thesis is the the dual-polarisation detection of FWM and reflection field in amplitude and phase. In a very recent publication from Borri's lab [44] Zorinians et al. utilized this dual polarization detection to demonstrate a novel method to determine the position of a single AuNP –both theoretically and experimentally– with nanometric precision

from scanless far-field optical measurements. The concept behind this approach relies on the fact that a NP displaced from the focus center of the circularly polarized input laser beam focused with high NA objective experiences a field distribution with a non negligible cross-polarised component and as a result emits an electromagnetic field directly associated to the NP's radial and angular position. Although this is the case for both reflected ($2r$) and FWM fields (FWM) it is only the FWM signal that is background free and therefore suitable to be used for tracking in complex biological environments. As shown on Figure 5.1, the ratios of amplitude and phase $\mathbf{E}_{FWM}^-/\mathbf{E}_{FWM}^+$ (A_{FWM}^-/A_{FWM}^+ and $\Phi_{FWM}^- - \Phi_{FWM}^+$) are associated with the displacement of the AuNP from the center focus while the axial position of the NP is directly proportional to the co-polarised FWM field phase (Φ_{FWM}^+).

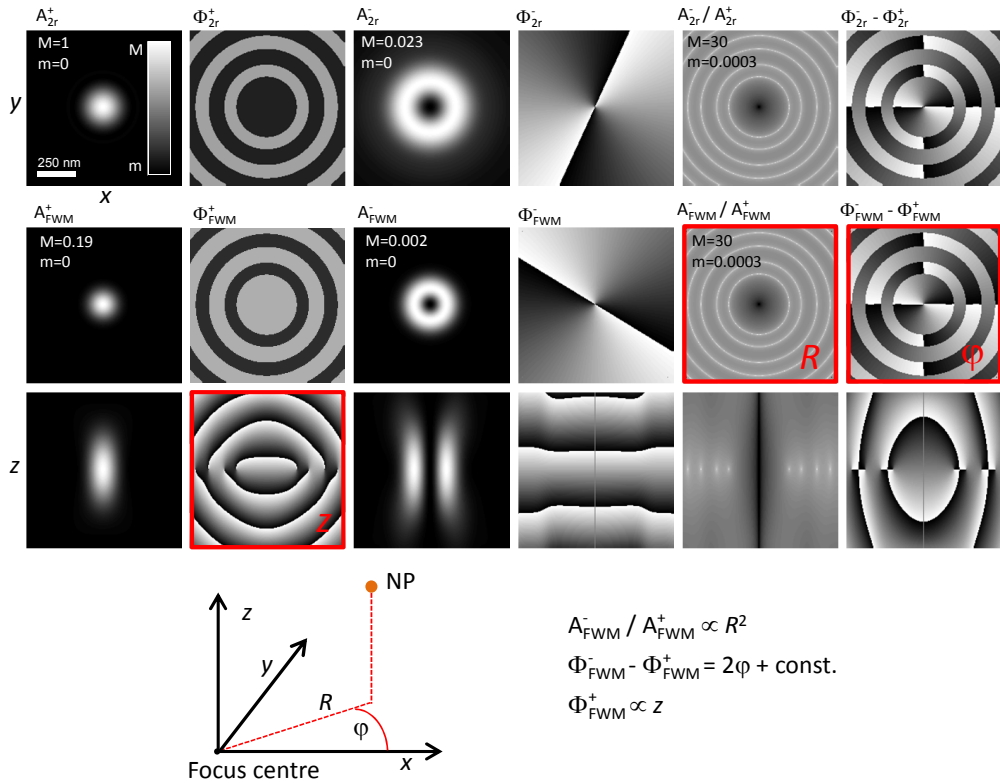


Figure 5.1: Nanometric localisation using optical vortices. Calculated amplitude (phase) components of the reflected probe field and FWM field A_{2r}^\pm and A_{FWM}^\pm (Φ_{2r}^\pm and Φ_{FWM}^\pm) respectively, as a function of particle position in the sample focal plane (x, y), and in a section along the axial direction (x, z) through the focus, where + refers to the co-polarised component and - to the cross-polarised component relative to the left-circularly polarised incident probe. The calculation assumes a perfectly spherical gold NP in the dipole approximation. The inset shows a sketch of how the amplitude and phase of the FWM field ratio and the phase of the co-polarised FWM field can be used to locate in 3D the spatial position of the NP relative to the focus center. Linear gray scale from $-\pi$ to π for all phases, and from m to M for field amplitudes, as indicated. The amplitude ratio of reflected probe and FWM are shown on a logarithmic grayscale over 5 orders of magnitudes. FIGURE AND CAPTION REPRODUCED WITH PERMISSION FROM REF. [44].

Importantly, Ref [44] also demonstrates that the nanoparticle's shape asymmetry is a limitation in this technique, as an ellipticity of as little as 0.5 % can induce a cross-circularly polarised field and eventually limits the accuracy of the in-plane localisation. A way to overcome this issue is to have the nanoparticle freely rotating in order to average the effect caused by the particle's asymmetry over the acquisition time. This idea alongside the need to mimic the diffusion of a nanoparticle in a biological environment such as the cytosolic network led to performing fast FWM measurements of AuNP of 50 nm diameter embedded in agarose gel where the nanoparticle may freely rotate but not diffuse out of focus. These experiments showed that it is possible to retrieve the in-plane position of the particle with nanometric position precision, as discussed in detail in Ref [44]. In my PhD project however I have only exploited the ability of the technique to provide the axial position z , which is discussed in the following.

In this chapter, FWM and reflection images of freely rotating nominally spherical 50 nm diameter AuNPs in a 3D agarose water solution are shown, alongside a preliminary study on the AuNPs dynamics in this matrix gel environment. This has been done by analyzing the autocorrelation function of the z position derived directly by the phase of co-polarised E_{FWM} .

5.2 Sample description

An overview of the sample layout is shown on Figure 5.2 and the sample description is given below. All glass slides and coverslips that were used had been previously cleaned thoroughly with acetone (purchased from Sigma-Aldrich®) and wiped with high quality cleanroom wipes. The agarose-in-water solution (AS) was formulated as follow: Firstly, 500 mg of agarose powder (Bioline Cat. 41025) was placed in a conical glass beaker filled with 10 mL of deionized H_2O in order to achieve a 5% w/v AS concentration. The mixture was then boiled in a microwave for several intervals of 20 s each until a homogeneous liquid was formed. Spherical AuNPs of nominal 50 nm diameter suspended in water were purchased from BBI Solutions™(Cardiff, UK). They were diluted and added to the mixture in order to achieve an estimated concentration of 10^9 NPs/mL. In order to have a well defined 3D volume of the agarose gel-AuNPs emulsion, we created a chamber by using an adhesive imaging spacer purchased from Grace Bio-Labs (SecureSeal™ imaging spacer). Specifically, an adhesive imaging chamber of 0.12 mm thickness and a 13 mm diameter hole was attached onto the glass coverslip used. 16 μL of the AS-AuNPs mixture was pipetted into the chamber's hole and then sealed with a glass coverslip of No. 1.5 bought from ThermoFisher Scientific™(by Menzel Gläser).

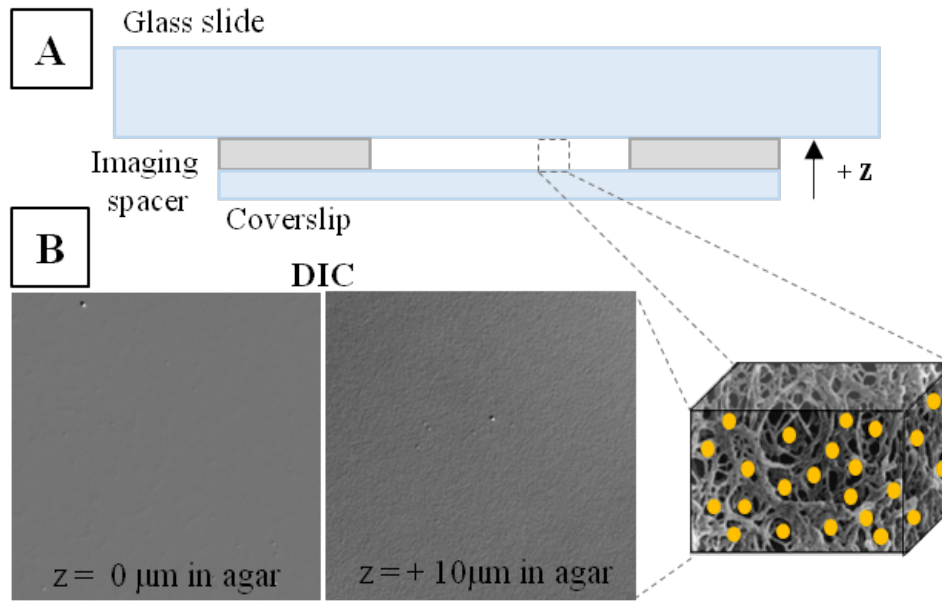


Figure 5.2: **A.** Sketch of the sample's layout showing the chamber which enclosed the AuNPs - AS gel mixture. **B.** High contrast DIC images taken on the FWM multimodal microscope using a high speed CMOS PCO.edge 5.5 camera. Both images were obtained by averaging 256 images with 100 fps speed and using the below formula $I_c = (I^+ - I^-)/(I^+ + I^-)$, where I^+ stands for an image obtained with +10 degree angle while I^- stands for an image obtained with -10 degree angle of the polariser in the de Senarmont compensator (see also Ref. [130]). The left image corresponds to the AS mixture-inner coverslip interface while the right one to an image obtained at +10 μm axial depth in the gel's volume.

5.3 Experimental details

As always before the measurements of the sample under investigation, the set up was aligned using the reference sample of gold film as described in section 3.1.3. A Nikon - Plan Apo 60x water immersion objective with 1.27 NA (Nikon CFI Plan Apochromat lamda series, super resolution) was used for focusing the overlapped pump and probe beams as well as the signals' (\mathbf{E}_{2f} and \mathbf{E}_{FWM}) epi collection. The images and tracing scans were performed by moving the sample over the fixed laser spot by means of the piezo-scanner. The results shown in this Chapter include: i) 3D scans, where an xy (lateral) scan was acquired in sequentially step defined z positions and ii) very rapid scans over time. The later scans will be named as *tracing* scans and refer to measurements where after we have carefully identified a freely rotating AuNP by 3D scan (or even by simple xy scan); we then give to one of the lateral axis small movements (e.g 50 points over 50 nm) and the other lateral axis an even smaller movement (e.g 1000 points over 10 nm) with less than 1 ms pixel dwell time. This experimental approach makes the tracing scans being almost

scanless over the NP area.

5.4 Data Analysis

In Zorinats et al. [44] experimental findings are shown on FWM measurements of rotating 50 nm diameter size AuNPs embedded in 5% w/v AS and 3D single particle tracking. Xy scans on various NPs revealed a central node at the A_{FWM}^- and a phase vortex pattern with $l=1$ ¹ (Figure 5.3). By comparing these results with theoretical simulations (also shown in Figure 5.3), the rotational averaging hypothesis was corroborated. As shown on Figure 5.1 the retrieval of the NP's position in a 3D domain is feasible via the calculation of the ratios of amplitude and phase of the FWM field as well as via the co-polarised FWM phase.

Notably these relations in Figure 5.1 refer to an $l=2$ vortex, hence are altered for the experimentally observed $l=1$ vortex and take the forms below [5.4.1 - 5.4.3].

$$A_{FWM}^-/A_{FWM}^+ \propto R \quad (5.4.1)$$

$$\Phi_{FWM}^- - \Phi_{FWM}^+ = -\phi + const \quad (5.4.2)$$

$$\Phi_{FWM}^+ \propto z \quad (5.4.3)$$

Using these dependencies the 3D coordinates of a 50 nm nominally spherical AuNP were extracted and compared with the ones taken from the piezoelectric stage of our set-up. Importantly, a precision of 16 nm in x, y and 3 nm in z, at 1 ms acquisition time per point were deduced from the experiment. The value in plane is consistent with the estimated shot-noise limit, while the measured precision in z is larger than the estimated shot-noise limit, and is dominated by the precision of the positioning stage.

¹An optical vortex has usually a topological charge number (l) which corresponds to an integer indicating how many twists the field exhibits in one wavelength. This number is an integer multiple to 2π . When projected in 2D, an optical vortex has an amplitude which is zero in the center and radially symmetric nonzero away from the center (i.e. looks like a ring), and a phase changing with l times the in-plane polar angle.

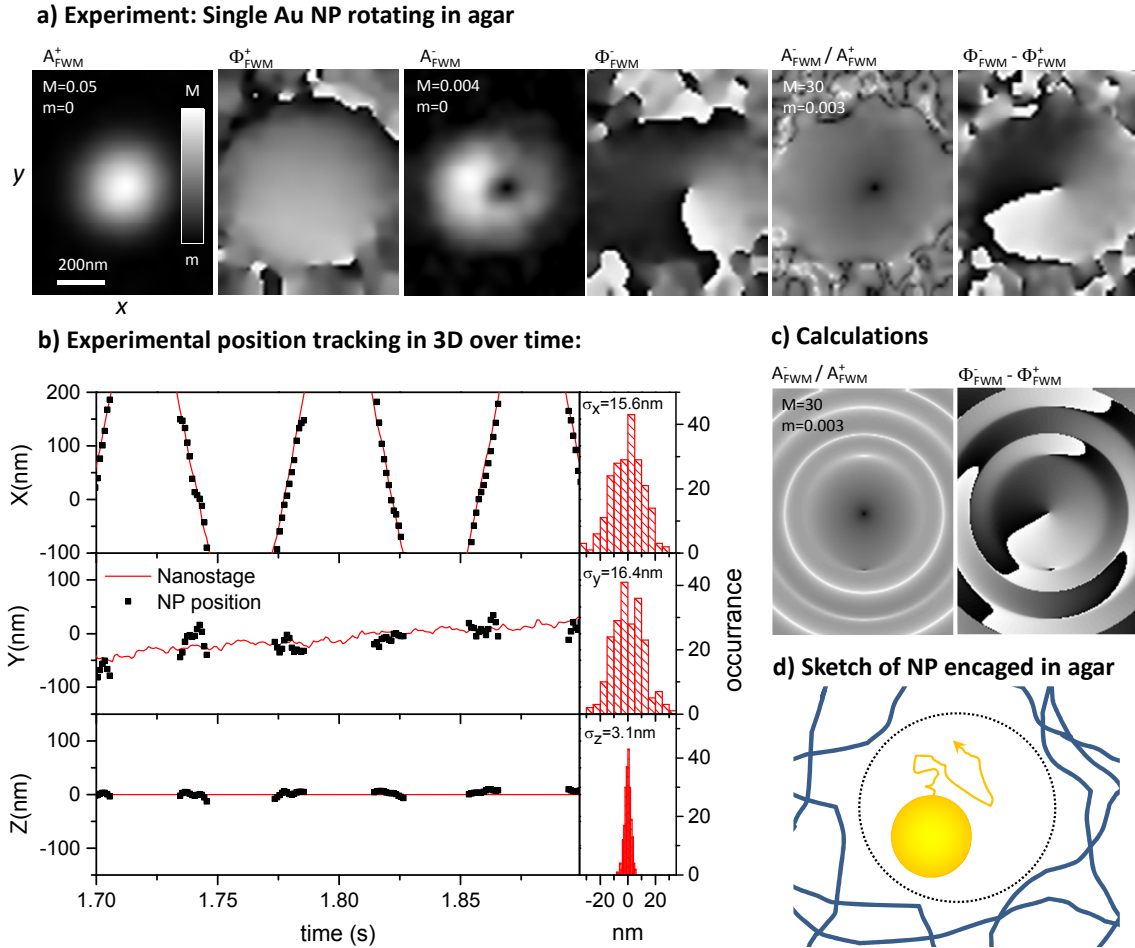


Figure 5.3: Rotational averaging of nanoparticle asymmetry. Single 25 nm radius gold NP freely rotating while ‘engaged’ in an agarose gel pocket (see sketch). **a)** Experimental x,y scan of the cross and co-circularly polarised FWM field in the focal plane, using a 1.27 NA water-immersion objective. Linear grey scale from $-\pi$ to π for phases, and from m to M for field amplitudes with M given relative to the maximum A_{2r}^+ . The amplitude ratio is on a logarithmic scale over 4 orders of magnitudes. Pump (probe) power at the sample was $70 \mu\text{W}$ ($10 \mu\text{W}$) with pump (probe) filling factor 2.15 (0.97). Measurements were performed with 0.5 ms pixel dwell time, 0.5 ps pump-probe delay time, and 13 nm pixel size in-plane. Data are shown as spatial averages over an effective area of 3×3 pixels. **b)** Time traces of the retrieved particle position coordinates in 3D from the measured FWM amplitude and phase (symbols) compared with the coordinates recorded from the scanning piezoelectric sample stage (lines). Traces are binned to an equivalent 1 ms acquisition time. **c)** Calculated FWM field ratio assuming a polarisation tensor that projects the longitudinally polarised field component into the x,y plane. [FIGURE AND CAPTION REPRODUCED WITH PERMISSION FROM [44]]

For the results shown on section 5.5 the following analysis was performed.

For the determination of the NP's z position; the co-polarised FWM phase (Φ_{FWM}^+) was used, as this phase is linear along the z -axis (5.4.3) and directly associated with the displacement between the NP and focus centre. As explained in the supplementary material of Zoriniantz et al. [116] the linearity was verified experimentally from rapid 3D scans as shown on Fig 5.4 and results in a slope $\partial z/\partial\Phi = 37$ nm/rad.

For each tracing scan the raw data were extracted as \Re and \Im part of the co-polarised FWM field (\mathbf{E}_{FWM}^+) from the MultiCARS analysis software (see Chapter 3). From those we calculated the co-polarised amplitude and phase as $A_{FWM}^+ = \sqrt{\Re^2 + \Im^2}$ and $\Phi_{FWM}^+ = \text{atan2}(\Im, \Re)$. The z position was then retrieved via $\Phi_{FWM}^+ \times 37$ nm/rad. All the calculations and graphic plots were made in Origin [®]. After repeating the same procedure for each time repetition of the tracing scan, a new Origin file with all the repetitions stitched one after the other was created and interpreted. Histograms of the z position of the AuNP were also produced in order to assess the frequency distribution (shown as counts for each bin) of the particle's axial position. In addition some further statistical analysis was performed in order to evaluate the probability of the NP to exist in each dominant frequency-position.

In the last part of the results section we also show autocorrelation plots ($G(t)$) of the retrieved z position of the AuNP. This is a common tool (also used in FCS analysis) in order to extract quantities of interest (such as diffusion coefficients) usually by fitting the autocorrelation function with known functions. In our case

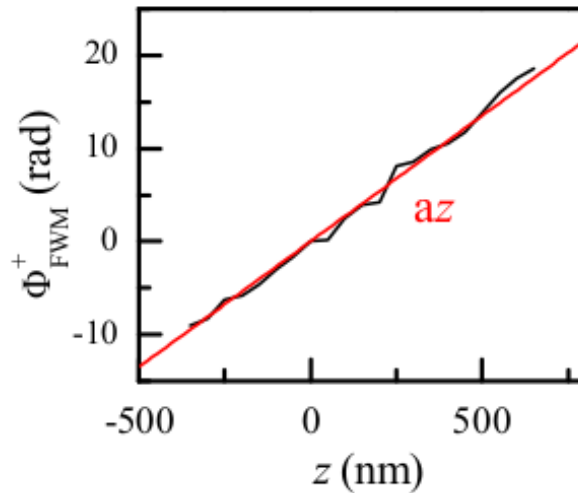


Figure 5.4: Axial dependence of the co-polarised FWM field phase (Φ_{FWM}^+) versus z (black line - experimental data) together with a linear fit (red line) giving a slope of 37 nm/rad. [TAKEN WITH PERMISSION FROM SM OF ZORINIANTS ET AL.]

the $G(t)$ was computed via the in-built fast correlation algorithm of Origin *corr1*², normalised and then with 1 subtracted in order to have values going asymptotically to zero.

5.5 Results and discussion

The results of the investigation of the axial fluctuations retrieved from the phase Φ_{FWM}^+ of the co-polarised FWM are shown alongside their interpretation and an outlook on the applications of our technique in the research field of SPT and NP characterisation.

Beginning with xy raster scans and z-stacks we imaged nominally spherical 50 nm AuNPs in 5 % AS as shown in Figure 5.5 and noted their positions (given by the piezoelectric stage) in order to later investigate each one and perform more imaging and tracing scans. Importantly observing the montage of Figure 5.5 made by single xy scans over 15 z steps - starting from the interface and moving inside the AS - one can see that the FWM channel is not affected by scattering provoked by the agar network while the reflection channel reveals a structured background coming from the agarose matrix gel throughout the imaged volume.

FWM imaging of a single 50 nm diameter size AuNP is shown in Figure 5.6 where xy raster scanned images of the co-polarised FWM (A_{FWM}^+) and reflection amplitude (A_{2r}^+) along with the cross-polarised FWM Amplitude (A_{FWM}^-) and phase (Φ_{FWM}^-). Similar to the results shown on Figure 5.3 one can observe an optical vortex $l=1$ with a central node in the cross-polarised FWM enabled by the rotational averaging. Zorinians and co-workers have shown via theoretical simulations that the $l=1$ pattern can be tentatively attributed to NP's chirality (see also Figure 5.3) [44]. Notably for the FWM imaging results shown in this thesis pump and probe beams have the same diameter size unlike the results shown on Figure 5.3 where the pump beam PSF at the sample was increased by a factor of two to enlarge the region where a single NP could diffuse while still being excited by the pump field, hence giving rise to FWM (this also increases the maximum cross-polarized FWM amplitude).

Observing the experimental findings and after starting to analyse our data by trying to retrieve the AuNP's axial position, we formed the hypothesis shown on Figure 5.7 where an initially immobile AuNP once illuminated with a tight focused laser beam in our FWM set-up experiment, is become mobile through a local delta-

²Fast algorithm based on the correlation theorem. Let $f(n)$ and $g(n)$ be the input signals of the same length M and $y(m)$ the output signal which is calculated as:
 $y(m) = \sum_{n=0}^{M-1} f(n)g(n-m)$. In our case both $f(n)$ and $g(n)$ refer to the axial position time series $z(t)$

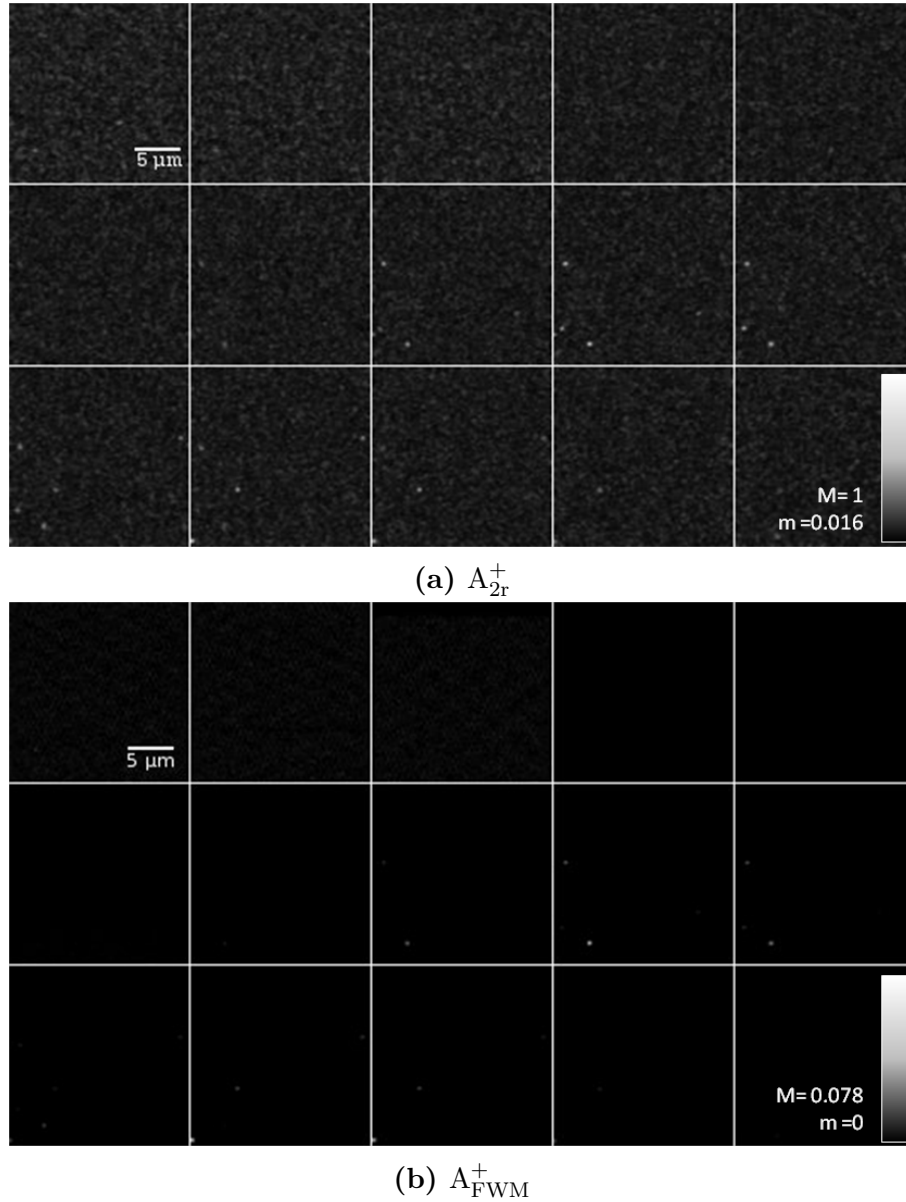


Figure 5.5: Montage of experimental xy scans over 15 z steps (0.5 μm step size) of the co-polarised reflection (A_{2r}^+) and FWM (A_{FWM}^+) fields showing the distribution of 50 nm AuNPs in 5 % AS. Pump (Probe) power at the sample was 10 μW (5 μW). Experimental data were acquired with 0.5 ms pixel dwell time, 0.5 ps pump-probe delay time and 11.7 nm pixel size in-plane.

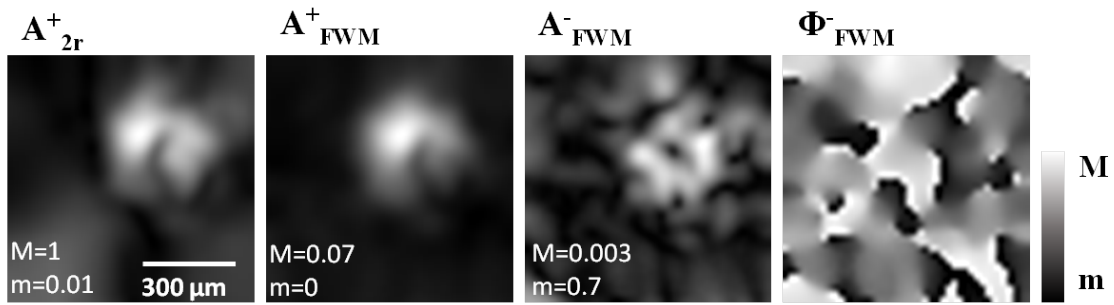


Figure 5.6: Raster scan images indicating rotational motion leading to field averaging of nanoparticle asymmetry. Single xy images of a single 50 nm AuNP in 5 % AS of [left to right] the co-polarised reflection A_{2r}^+ and FWM A_{FWM}^+ amplitude as well as the cross-polarised amplitude A_{FWM}^- and phase Φ_{FWM}^- . Pump (Probe) power at the sample was 7.5 μ W (3.75 μ W). Experimental data were acquired with 1 ms pixel dwell time, 0.5 ps pump-probe delay time and 18 nm pixel size in-plane. Linear grey scale from $-\pi$ to π for phases, and from m to M for field amplitudes, with M given relative to the maximum A_{2r}^+ .

bility of the AS and can eventually become freely rotating while being enclosed in a confined pocket (**‘caged’ particle behavior**) or jump between two (**‘jumping’ particle behavior**). The rest of the results shown in this chapter are a preliminary analysis based on the axial position of the particle in order to derive conclusions on the NP’s diffusion mechanism inside the agar matrix gel.

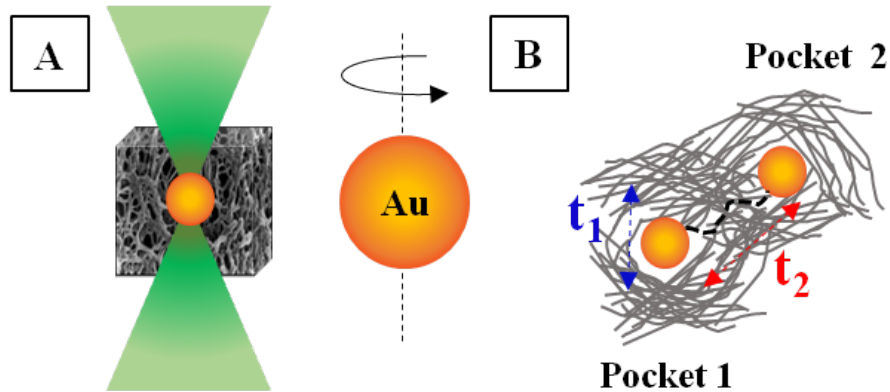


Figure 5.7: **A.** A tight focused laser beam locally melts the AS and set ‘free’ the AuNP **B.** Diffusion of AuNP between two pockets of the Agar network. On the sketch we have identified with t_1 the characteristic time constant of the constraint diffusion within one pocket and with t_2 the characteristic time constant of the ‘jumping’ between two pockets.

As mentioned in the previous sections, I measured the z coordinates directly by the co-circularly polarised FWM phase Φ_{FWM}^+ and by simply plotting an histogram of the axial coordinates as shown on Figure 5.8 the NP's diffusion behavior can be observed. One can easily distinguish that the AuNP is 'caged' in two gel pockets located around the axial positions $z \sim 60$ nm and $z \sim 150$ nm while also 'jumps' between them. In each pocket the co-circularly polarised FWM amplitude (shown in the top part of Figure 5.8) is significant strong indicating that the AuNP remains in focus while the scan was acquired.

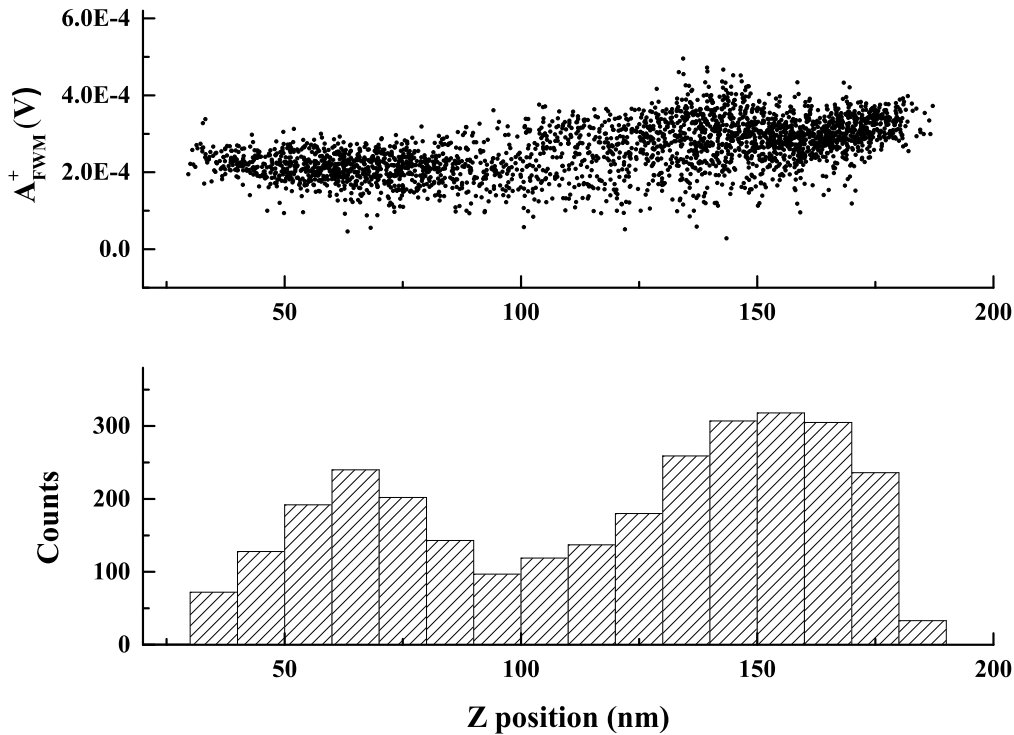


Figure 5.8: Histogram of the derived AuNP's axial position alongside the corresponding amplitude co-circularly polarised field (A_{FWM}^+) indicating that the NP is 'caged' and jumps between two pockets. Data were acquired with 1 ms dwell time and and pump (probe) power 7.5 (3.75) μ W before entering the microscope.

Multiple *tracing* scans were acquired over time enabling us to perform some further statistical analysis regarding our hypothesis that, following NP heating from the laser beam and melting of the local AS environment, the particle diffuses between pockets formed by the agarose matrix. To that end, we plotted the histogram of six repeated *tracing* scans which were 'stitched' in time one after the other and the result of this was fitted as shown on Figure 5.9. On these plots, the overall histogram of the axial position is firstly shown (5.9) where the two peaks –indicating the two gel pockets– cannot easily be distinguished. Therefore we fitted the two center 'pocket' peaks shown as *Fit Peak 1* and *Fit Peak 2* respectively on 5.9 on top of a cumulative

fit including all the center bins of the histogram. Thus, we calculated the probability of the AuNP to reside in each pocket as:

$$P_{\text{pocket 1}} = \frac{\text{Area of Fit Peak 1}}{\text{Overall cumulative Fit area}} = 59.3 \pm 18.9\% \quad (5.5.1)$$

$$P_{\text{pocket 2}} = \frac{\text{Area of Fit Peak 2}}{\text{Overall cumulative Fit area}} = 48 \pm 18\% \quad (5.5.2)$$

We thus deduce that the AuNP has about an equal probability to reside in each pocket.

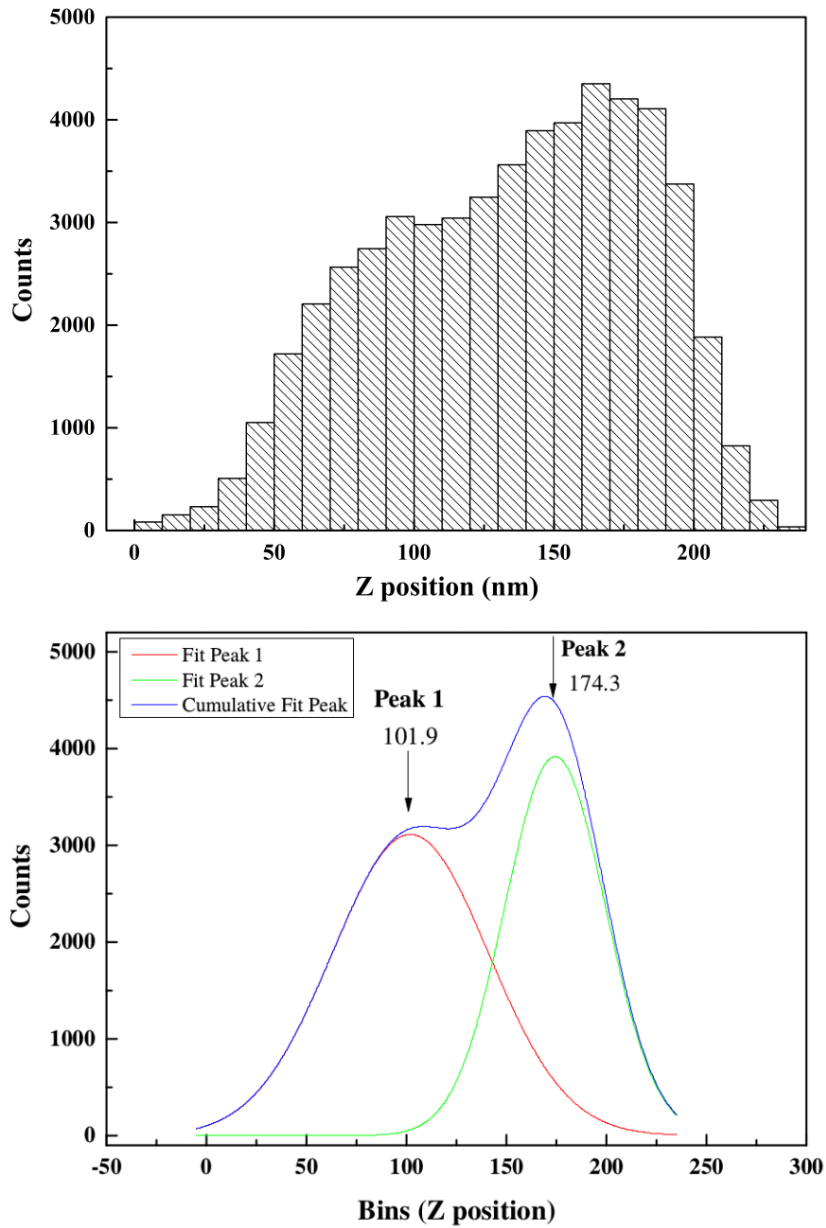


Figure 5.9: (Top) Histogram of the z coordinates of multiple *tracing* scans (Bottom) Fitted lines for each of the center bin peaks alongside a cumulative fit for all the center bins of the above histogram. From the areas underneath the fitted lines the probability of the AuNP to be each pocket was calculated as explained in the text.

As a next step of the NP's diffusion study based on the particle's axial position we autocorrelated the time series of the retrieved NP's z position. In order to be able to gain some further information on the type of diffusion that we observe, we fitted the autocorrelated experimental data of $z(t)$ (*shown with black line*) with two formulas as shown in Figure 5.11. We used an exponential fitting formula 5.5.3 (green colour in Figure 5.11) and a common anomalous diffusion fitting formula 5.5.4 (magenta colour in Figure 5.11).

$$G(t) = G_1 e^{-(t/t_1)^2} + G_2 e^{-(t/t_2)} \quad (5.5.3)$$

$$G(t) = G_1 \frac{1}{1 + (t/t_1)^{a_1}} + G_2 \frac{1}{1 + (t/t_2)^{a_2}} \quad (5.5.4)$$

Both formulas seem to come in agreement with our experimental data giving similar values of the two characteristic times of our systems with average values of $t_1 = 2.3$ ms for **constraint diffusion time** and $t_2 = 2.9$ s for **jumping time** as also shown on Figure 5.11.

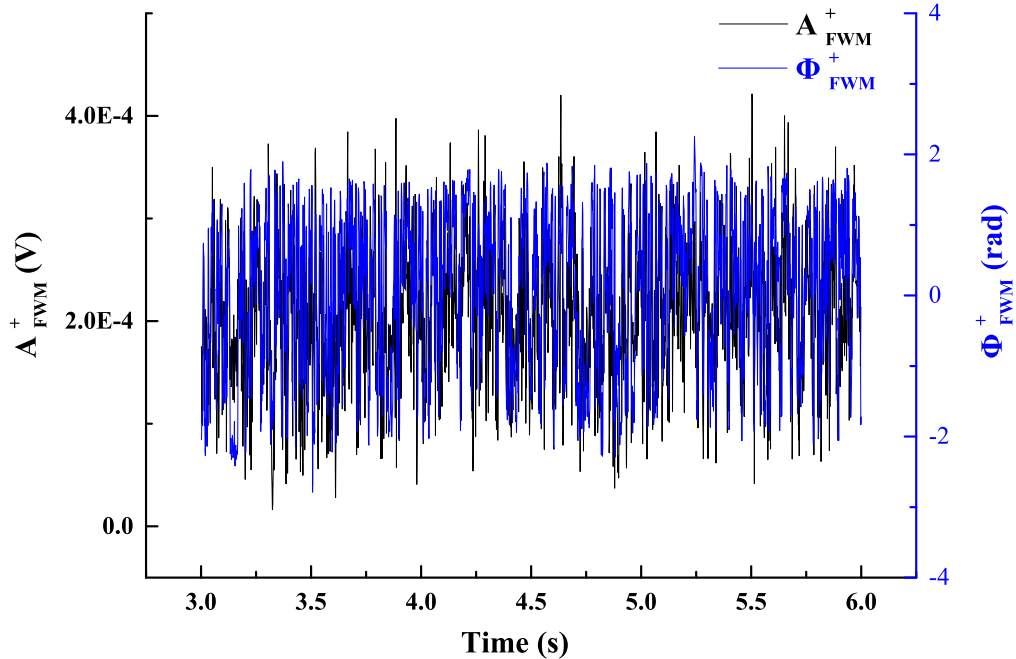


Figure 5.10: Time traces of the amplitude (A_{FWM}^+) and phase (Φ_{FWM}^+) of co-circularly polarised FWM signal derived from *tracing* scans obtained with 1 ms dwell time and pump (probe) power at 7.5 (3.75) μW before entering the microscope. The axial position time series $z(t)$ follows the behaviour of the co-circularly polarised phase (Φ_{FWM}^+) as is derived by that.

In addition to these results, traces were also analysed by calculating the mean

square displacement (MSD)³ as a function of time lag (t_{lag}) ([120],[131]) which showed a sub-linear dependence and saturation of the MSD versus t_{lag} as outlined in Zorinants et al.[44] where the Figure 5.12 is taken from.

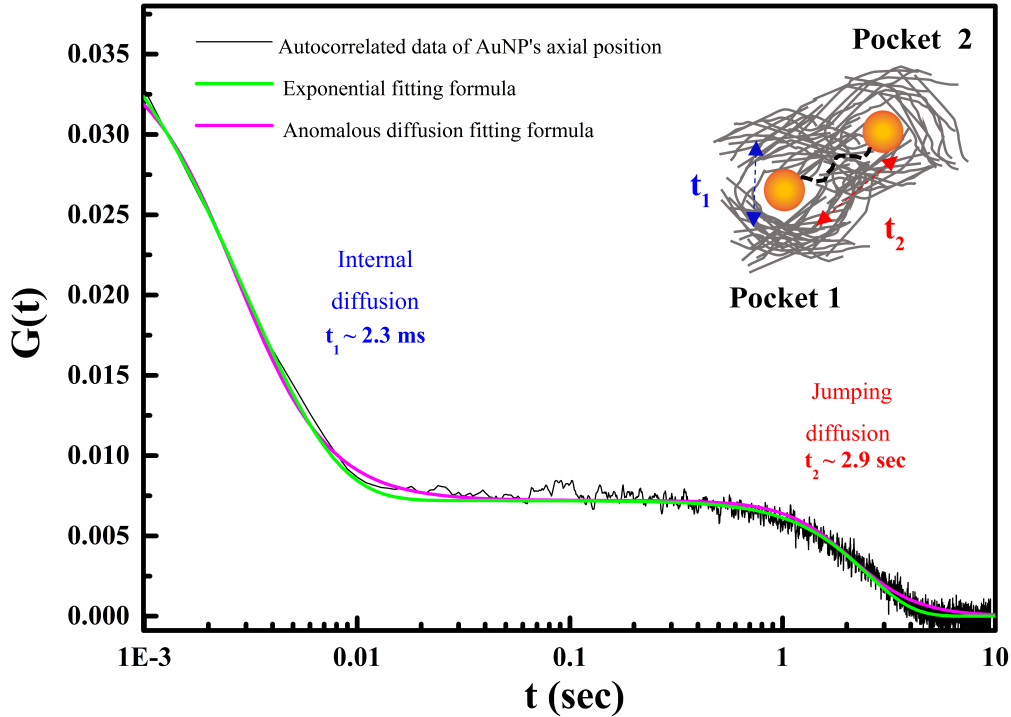


Figure 5.11: Autocorrelated data of the retrieved axial position (black line) of a single AuNP in agarose gel fitted with two different type of anomalous diffusion models (colored lines) indicating an internal diffusion time (t_1) and a jumping time (t_2) between the two agar pockets as explained in our hypothesis.

The observed behaviour suggests a confined diffusion mechanism within a matrix agarose gel 'pocket' and a jumping mechanism for diffusion between two (or even more) gel 'pockets'. This interesting behaviour has also been the subject a recent publication of Cai et al. [132] where they propose a hopping mechanism for NP's diffusion defined by topological constrains in untangled or entangled polymer environments (such in our case is the agarose matrix gel) and entangled polymer liquids.

In conclusion, this Chapter highlights the additional capability of axially tracking of single AuNPs with the FWM technique used in my PhD project and comprises a preliminary analysis on the study of the diffusion mechanism of a single 50 nm AuNP embedded in an agarose gel environment.

³more details can be found in [116]

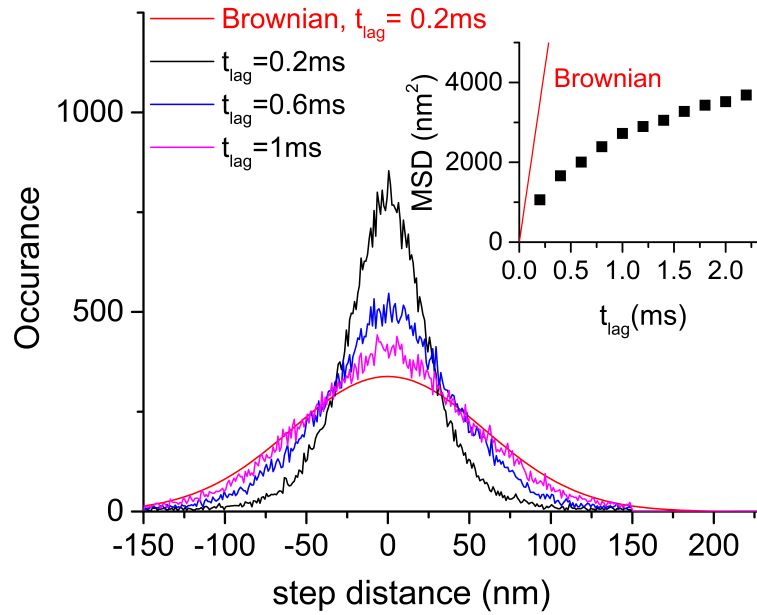


Figure 5.12: Analysis of axial position time traces acquired at 0.2 ms time per point. [FIGURE AND CAPTION TAKEN WITH PERMISSION FROM REF [116]]

Specifically, we have demonstrated experimentally axial tracking of nominally spherical 50 nm AuNPs in 5% AS based on the detection of the co-polarised FWM field phase. By analysing the time traces of a single particle’s axial position and performing statistical and autocorrelation analysis we observe that the AuNP diffuses within one gel pocket with a characteristic time constant of 2.3 ms while it can also ‘jump’ to another pocket with a 2.9 s characteristic time constant.

Owing to the background-free capability of our FWM detection, this technique opens new frontiers towards single particle tracking in complex and heterogeneous environments.

6

SUMMARY AND OUTLOOK

In this thesis, we have demonstrated the application of our recently developed dual-polarisation FWM imaging modality in heterodyne detection, in order to image a variety of AuNP-fluorophore conjugates ($10\text{nm} < \text{AuNP} < 40\text{nm}$) in cells and ultimately investigate their intracellular fate via correlation with the fluorescence emission from the labelled part of the construct. The technique enabled us to image background free and selectively AuNPs down to 10 nm diameter in highly scattering and autofluorescent cellular environments with high 3D spatial resolution owing to the nature of the detected FWM signal originating from the nonlinear light-matter interaction with the free electron gas of the metal. The main goal of this work was to spatially correlate the FWM signal of the AuNP for each construct with the fluorescence signal coming from the fluorescently labelled part of it and investigate the cellular fate of the AuNP construct for each sample. This was done in a range of samples synthesized both in-house, in collaboration with Cardiff School of Pharmacy and Nottingham School of Pharmacy, as well as by using commercially available constructs. Despite the fact that fluorescently labelled gold nanoparticles are widely used in correlative microscopy techniques, detailed studies regarding the integrity of these constructs following their cellular entry are only a few [133], [134]. An overview of the current research landscape and the scientific motivation of the thesis was given in Chapter 1. There, the recent advances of nanotechnology in biomedical applications, focusing on AuNPs and specifically their use in linear and nonlinear microscopy as well as their bioimaging applications were discussed. The remarkable progress in the design and study of nanomaterials towards biological applications

points out that the implementation of plasmonic metallic NPs is among the most promising platforms for target-specific delivery of therapeutic agents, cancer diagnosis, photothermal therapy and optical labeling. The above assets are related to the strong and photostable optical properties of AuNPs at their localised surface plasmon resonance (LSPR). Overall, the results of this work further demonstrate the capabilities of AuNPs to act as unique optical probes, in this case owing to their resonant four-wave-mixing nonlinearity at the LSPR.

Chapter 4 encompasses all the major results on spatially correlative FWM - fluorescence microscopy and demonstrates FWM detection of nominally spherical gold NPs of various sizes (10 nm to 40 nm in diameter) in fixed human and mice cells fluorescently labelled with plasma membrane receptors targeting endocytosis mechanisms. Tables 4.1 and 4.2 summarise the different types of conjugated AuNPs-fluorophore which were synthesised via both in house and commercially available protocols and were examined via correlative FWM-fluorescence microscopy. In conclusion, the samples exhibited very poor signal correlation resulting in lack of colocalisation between the FWM and fluorescence signals. Wherever possible, this was quantified via calculating the image's cross correlation coefficient, r_p , (also known as Pearson's) and Mander's overlapping coefficient for the FWM channel, M_{FWM} , after implementing a series of steps which comprised our correlation analysis. The reasons for this lack of correlation can vary depending on the construct and sample preparation used, thus an in depth analysis can be found at the results and discussion section for each sample. Overall, the possible reasons for the lack of colocalisation between fluorescence and FWM signal belonging to the same construct for this study can be summarised here as follows: inherent limitations of fluorescence detection, such as photobleaching effects because of high photo-excitation intensities; fluorescence quenching when in close proximity to metallic NPs; unbound fluorophores and/or proteins in the initial stock solutions used in cells during the sample preparation protocols; break down (dissociation) of the construct (AuNP-fluorophore) during cellular internalisation or the several washing steps; degradation of the AuNP-fluorophore conjugate as a result of the long 'chase' times in some of our sample cases (i.e. for the 40nm AuNP-SA:Bi-Tf-A647 sample, 'chase' time was 6 hours); lack of contrast in the presence of cellular autofluorescence limiting the applicability of our correlation analysis for some of the samples.

These observations manifest the limitations of only relying on fluorescence imaging for bioimaging studies and emphasise the need for detailed study of the fluorescently labelled bioconjugated construct prior the final sample preparation and imaging stages. The influence of the construct's spacer, the bond type of conjugation between the constructs alongside the whole construct;s size as well as the NPs'

size itself, are factors that need to be examined and taken into consideration in early stages of the research. As indicated by the thesis' outcome, it is of paramount importance that the fluorescently labelled AuNP constructs are equally tested for their photophysical properties as for their biological properties and intracellular behaviour. If fluorescently bioconjugated gold NPs are chosen as fiducial markers for biological studies, we suggest imaging of the labelled NP solution itself, prior to the biological sample preparation and cellular imaging. For example, correlative wide-field fluorescence and extinction measurements could be performed in order to properly examine the colocalisation of the NP (extinction) with the fluorophore before the cellular experiments. Importantly, our results are consistent with the recent publication of Miles et al. [48], which further highlights the drawbacks of fluorophore tagging that can lead to misinterpretations.

In addition to imaging, in Chapter 5 we exemplified the application of FWM for single particle tracking. As demonstrated in Ref. [135], [44], our technique is able to track single NPs with nanometric precision in 3D by exploiting the optical vortex field pattern in the focal plane of a high numerical aperture objective lens. In this work, a freely rotating AuNP of 25 nm radius in a dense agar network (5% w/v) was studied and the diffusion of it based on the axial coordinate was retrieved from the information carried by the phase of the co-circularly polarised FWM signal. The results showed that the NP is 'caged' in an agarose pocket withing a couple of milliseconds and then 'jumps' to a neighbor pocket in a timescale of a couple of seconds (Figure 5.11). All in all, the set-up features simultaneous correlative FWM-confocal fluorescence and alongside its capability for nanometric precision in 3D (shown in Chapter 5 -only for axial position- and further analysed in Zorininats et al.), our technique is able to image and locate AuNPs down to 10nm radius in a way that was previously not feasible, especially in highly scattering cellular environments. This approach opens new prospects towards an in-depth understanding of the intracellular fate and integrity of bio-conjugated AuNPs within biological networks.

As a proof-of-principle that our technique is applicable for live cell imaging, a few preliminary experiments were performed, toward the end of this project achieving FWM imaging of 20 nm AuNPs in live 3T3-L1 cells (see Appendix D). The aim of these experiments were to explore the feasibility of our FWM imaging technique in live cells and assist our research group to establish a set of experimental steps for FWM imaging in live cells. The first observations were encouraging and since there are no equipment or hardware limitations, more experiments should be performed in this research area to identify all the experimental parameters for live cell imaging in our set-up. Importantly, some of the first factors that will need to be determined are: optimisation of the power levels on the sample in order to keep signal-to-noise

ratio high but also keep the cells in healthy state, optimisation of the acquisition and dwell times, as well as identifying the limitations of the sample's viability under various imaging parameters on our set-up.

All in all, the results in this work suggest that future work should be devoted to demonstrate FWM imaging and tracking of single AuNPs in living cells, addressing, for example, the kinetics of bio-conjugated metallic NPs in confined biological regions such as intracellular vesicles, or synapses of neurons. Another very promising future direction of FWM imaging is also its applicability to correlative light electron microscopy, using the AuNP as a single optical probe without the need for dual labeling.



APPENDIX A

A.1 Investigation of thermoresponsive PC-50 nm AuNPs via absorption spectroscopy

A.1.1 Introduction

The project initially involved monitoring of thermoresponsive PC-AuNPs functionalised with Tf in order to demonstrate transport of the Tf-PC-AuNP into the recycling cell pathway upon temperature stimulation. Being able to primarily characterise test-solutions based on their linear optical properties and get a better understanding of their temperature dependent behaviour with a simple Vis spectroscopy set-up was the goal of the measurements presented in this section. To do so, several batches of thermoresponsive PC-AuNPs of 50 nm diameter in buffer solutions were fabricated by our collaborator at Nottingham School of Pharmacy and were tested via temperature-dependent absorption spectroscopy measurements in Cardiff.

It is worth mentioning that nowadays huge research interest is focused on the polymer-decoration of AuNPs for various purposes in the fields of biomedicine [109], [136], [137], [138], [139] and advanced material science [110], [140]. In concept, the ‘stimuli-responsive’ polymers grafted on the surface of the NPs are meant to undergo relatively large and abrupt conformational changes (Fig. A.1) owing to an external stimulus. For an extensive description of different polymer modified AuNPs used in recent years refer to the reviews by D.Li et al.[141], M.Ward et al. [110] and F.Liu et

al. [140]. In our case, the stimuli response of the polymer chain is attributed to the temperature change in the solution, leading to an hydrophobic phase (and in turn polymer chain collapse) above a specific temperature pre-defined for each polymer solution. As previously mentioned, with these measurements we aimed to verify not only the reversibility of the thermoresponsiveness of different polymers grafted onto the 50 nm AuNPs but also test if there is aggregation upon temperature increase.

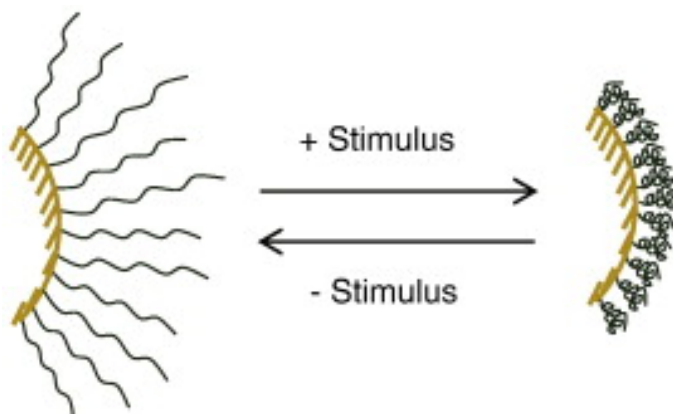


Figure A.1: Scheme of the change of the conformational structure of the polymer chain on the AuNP's surface. In our case the external stimulus of the PC-AuNPs under investigation is the temperature. [FIGURE REPRODUCED WITH PERMISSION FROM REF [141].]

A.1.2 Samples

The PC-AuNPs were fabricated following chemistry protocols from expertise available in house in collaboration with the group of C. Alexander at the School of Pharmacy at Nottingham University [113], [111], [136]. They have previously shown with in vitro studies that heating (40 °C) of PNIPAm¹-coated AuNPs above their lower critical solution temperature (LCST) (37 °C) resulted in cellular internalisation [112]. They have also proved that thermoresponsive polymers can be used to reversibly mask ligands –such as thiolated biotin or folic acid- by a local temperature gradient application [111].

Several samples were received during the initial stage of the project, the ones reported here are shown on Table A.1.

The common characteristic of these samples is the type of thermoresponsive polymer used to coat the metallic surface. In general, thermoresponsive polymers belong to the wide group of ‘smart’ materials and are able to respond to a change in temperature. Thermoresponsive polymers can be classified into two main groups,

¹Poly(N-isopropylacrylamide)

Sample	Diameter of AuNP (nm)	Tf ligand	Fluorescent Label
JPM 400	50 nm	No	No
JPM 487	50 nm	Yes	A488
JPM 491	50 nm	Yes	A488

Table A.1: Summary of thermoresponsive PC-AuNPs measured via absorption microscopy manufactured by our collaborators at Nottingham University.

lower critical solution temperature (LCST)-type phase transition and upper critical solution temperature (UCST)-type phase based on whether their wettability decrease (increase) upon increase (decrease) of temperature respectively [110], [140]. In our case, the thermoresponsive polymer is a LCST type, i.e. upon heating above a specific transition temperature, the state of an LCST polymer changes from more hydrophilic to less hydrophilic. In terms of change of the sample’s structure, the polymer brushes (LCST part of the sample) are expected to ‘collapse’ and ‘reveal’ the Tf ligand (*‘hide-reveal’ property*).

Although all the samples consist of the same AuNP size (50 nm diameter), the thermoresponsive polymer (LCST) which surrounds the particle changes based on the synthetic chemistry planned by our collaborators at Nottingham University. The first solution (JPM 400) was composed of 50 nm AuNPs coated with a primary LCST polymer. The other two samples (JPM 487, JPM 491) were additionally fluorescently labeled with A488 which was bound to the Tf. In addition, JPM 491 was functionalised with an extra amphiphilic polymer (MPC) aiming at exhibiting a stronger hydrophilic behaviour than the previous batches. In theory, upon transition the LCST part of this sample would collapse while the additional MPC shell is still hydrated. In this case the solution was expected to aggregate significantly less than JPM 400 and JPM 487 upon heating.

All the samples were diluted in PBS (pH 7.4) resulting in a final concentration of 1.36×10^{11} AuNPs/mL for JPM 400 and in a 0.45×10^{11} AuNPs/mL for JPM 487 and JPM 491. The solutions were placed in a 1 cm path length plastic disposable cuvette (macro type, Greiner bio-one). Absorbance spectra were recorded over a temperature range of 20 °C to 70 °C with 5 °C steps. At each temperature, the sample was allowed to equilibrate for an average time of 5 minutes before the spectra were recorded.

A.1.3 Temperature dependent spectroscopy measurements

In this section a series of temperature-dependent absorption spectra are shown for all three samples: JPM 400, JPM 487 and JPM 491.

All the samples at room temperature present an absorbance peak around 531 nm, as expected for spherical AuNPs of this size in aqueous environment [142]. In more details, for the JPM 400, upon temperature increase, a red shift and broadening of the peak is observed along with a significant decrease of the intensity. Previous studies have shown that nanoparticle aggregates of growing size exhibit an increasing red shift and broadening of the surface plasmon band [143],[67]. This suggests that the red shift, broadening and decreasing absorption intensity exhibited by the JPM 400 sample (Fig. A.2) is due to the formation of aggregated particles as the temperature is increased. In Fig. A.3 the temperature-dependence of the absorption of the sample at 531 nm is displayed. The transition temperature of the sample can be extracted by the first derivative of this curve. Using this method, a transition temperature of 50 °C is calculated for JPM 400, which is very high for cell applications. Extended absorption measurements upon several heating cycles (Fig. A.4 - A.6) have been made in order to understand the time-response of the change of the polymer's state from hydrophilic to hydrophobic. All lead to the result that the phenomenon is neither reversible nor reproducible for this sample. The sample appears to form aggregates upon heating, as would be expected due to the more hydrophobic nature of the polymer, however it does not recover to its initial state upon cooling. Control measurements acquiring absorption spectra over time (in a 45 minutes total) at constant temperature were also taken and are shown in Fig. A.7 indicating that in these conditions the spectra are stable over time, hence the observed changes in Fig A.2, A4-A6 are due to the effect of temperature. As a result, JPM 400 was not investigated further as its behaviour was not suited for further applications in cells.

Samples JPM 487 and JPM 491 appear to have a transition temperature around 34 °C - 35 °C (determined by the synthetic chemistry lab in Nottingham) which is biocompatible for future live cell applications. In terms of absorption spectra they appear not to form aggregations over temperature rise as shown in Fig. A.8 and Fig. A.9. This suggests that the addition of the hydrophilic MPC² shell indeed was preventing aggregation after collapse of the LCST polymer.

²2-Methacryloyloxyethyl phosphorylcholine

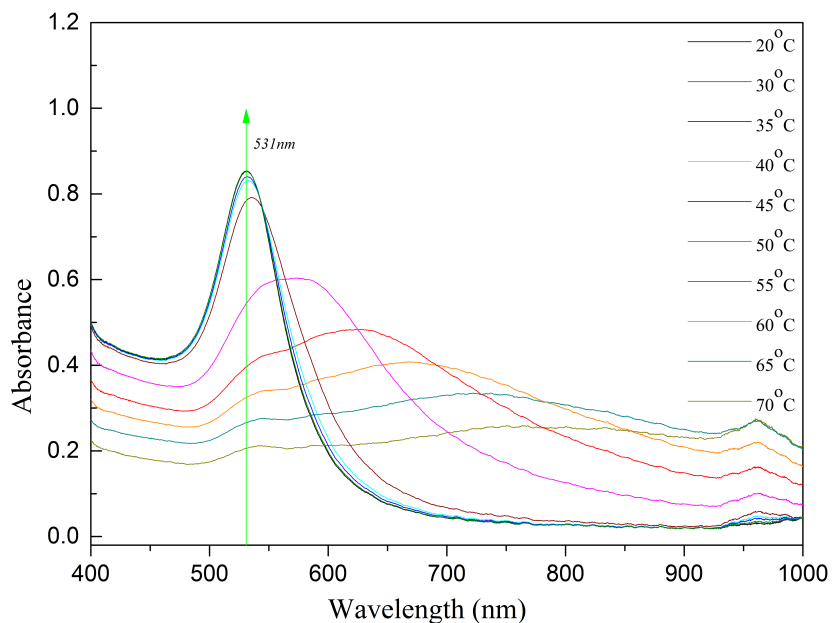


Figure A.2: Vis-NIR absorption spectra of the firstly received 50 nm polymer coated AuNP sample, JPM 400, from 20 °C to 70 °C.

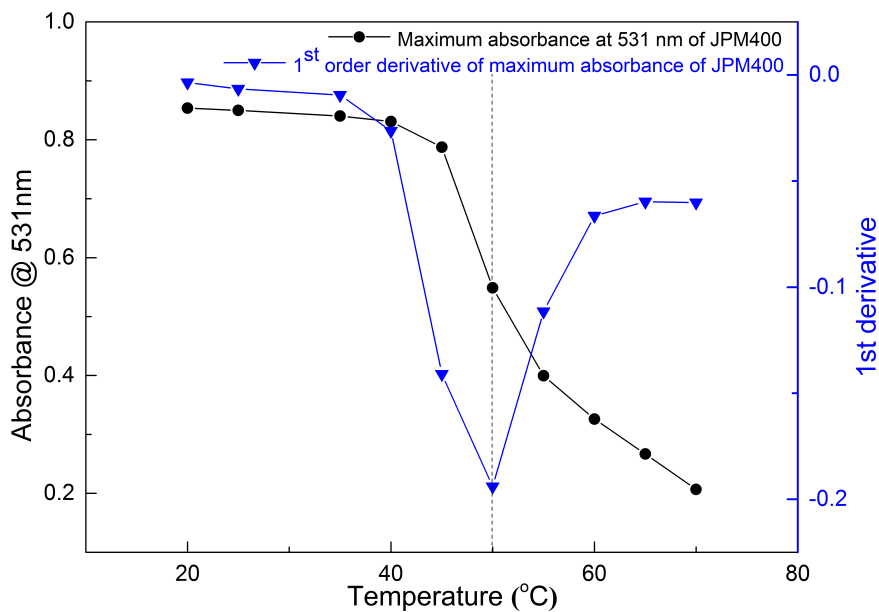


Figure A.3: Maximum absorbed intensity at the LSPR peak of 531 nm versus temperature. The transition temperature is found to occur at 50 °C.

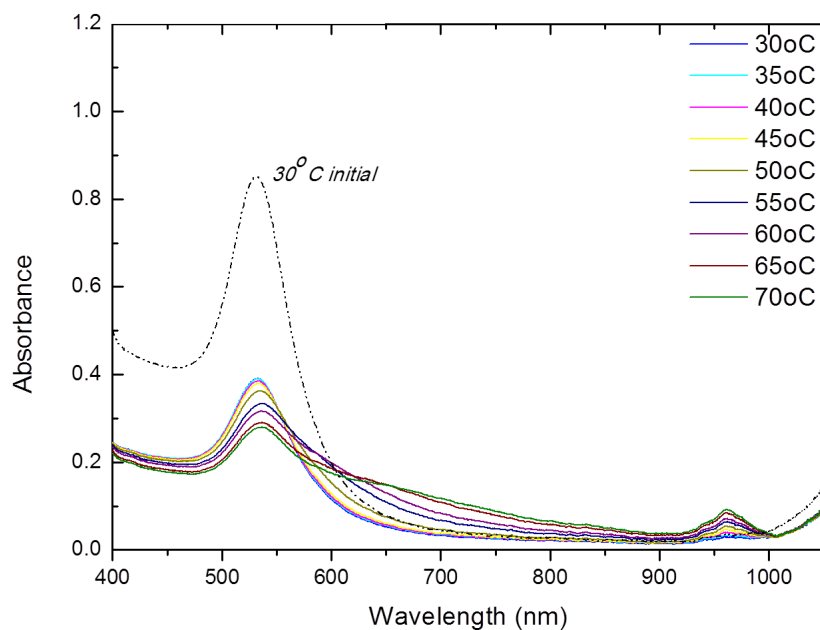


Figure A.4: Vis-NIR absorption spectra of the firstly received 50 nm polymer coated AuNP sample, JPM 400, from 30 °C to 70 °C one day after the first cycle of heating shown on Fig. A.2.

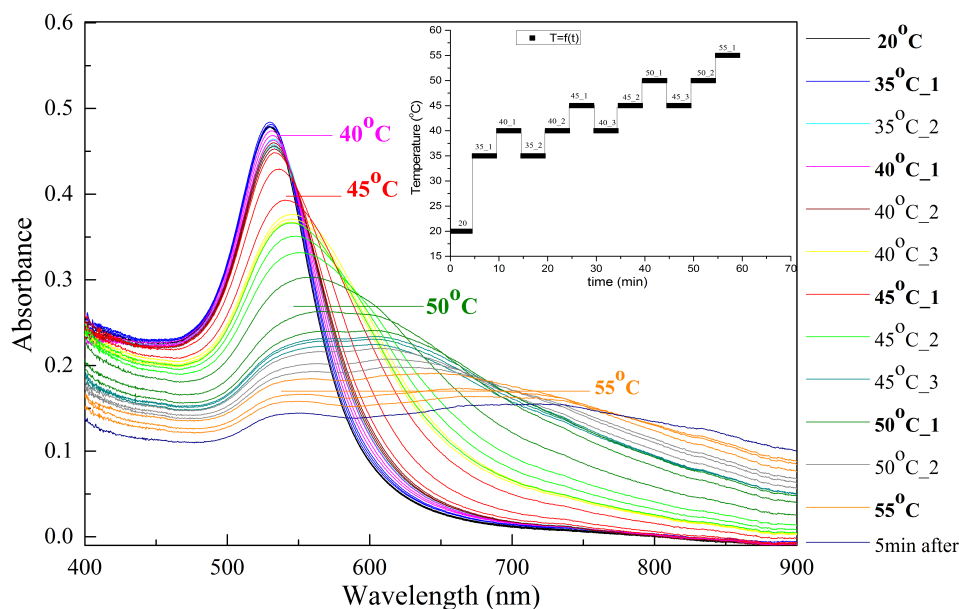


Figure A.5: Vis-NIR absorption spectra of JPM 400 at temperatures between 35 °C and 55 °C with 5 minutes intervals at each temperature. The temperature was changed every 5 minutes going from lower to higher temperatures and then back as the inset graph shows. The smaller graph $T=f(t)$ on the top right indicates the temperature steps and the time intervals staying at each temperature.

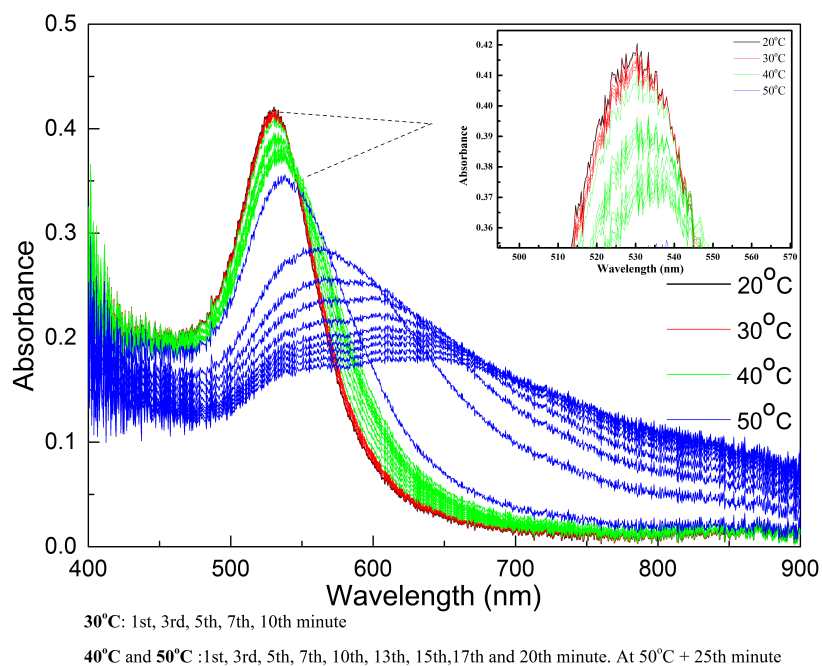


Figure A.6: Multiple Vis-NIR absorption spectra of JPM 400 sample at each of the shown temperatures for longer timescale (indicated at the bottom).

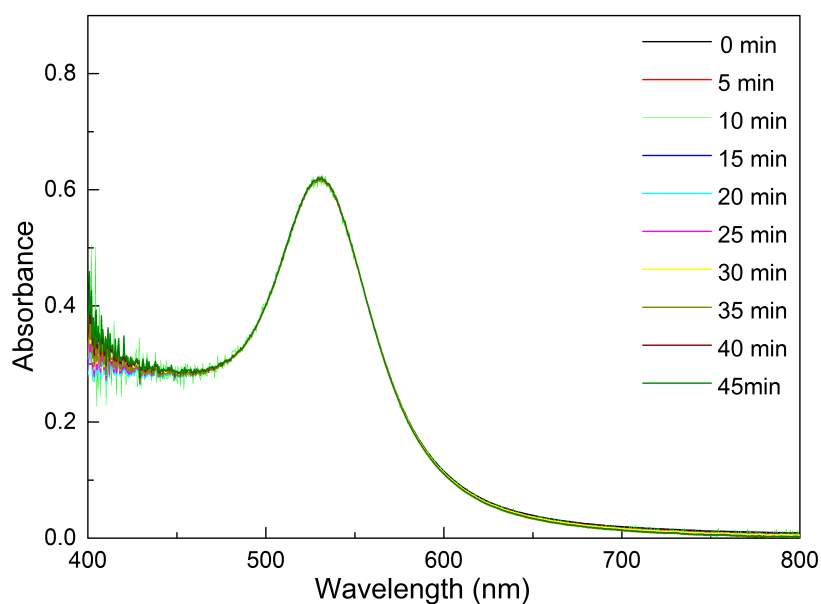


Figure A.7: Control measurement. Vis-NIR absorption spectra of JPM 400 for 45 minutes at constant temperature (room temperature). The behaviour of the investigated solution, i.e. PBS, was found to be stable over time.

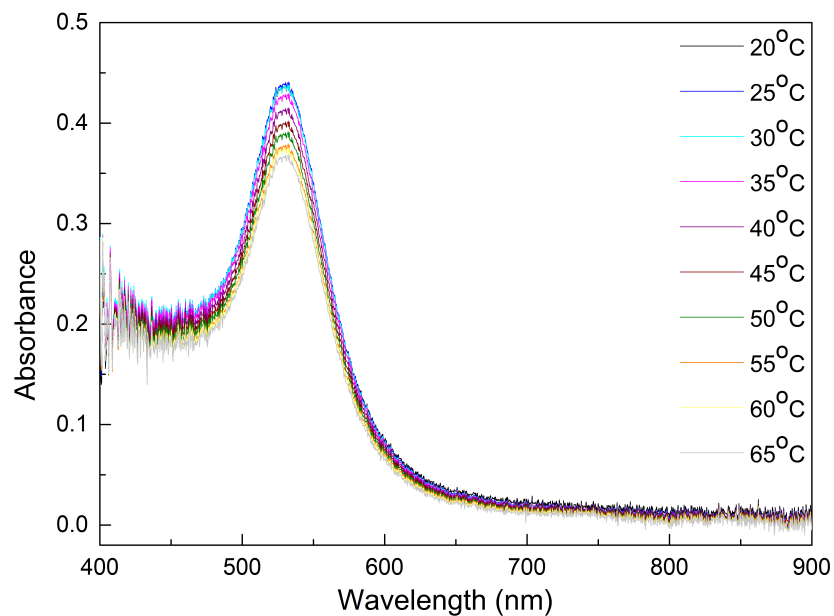


Figure A.8: Vis-NIR absorption spectra of sample JPM 487 from 20 °C to 65 °C.

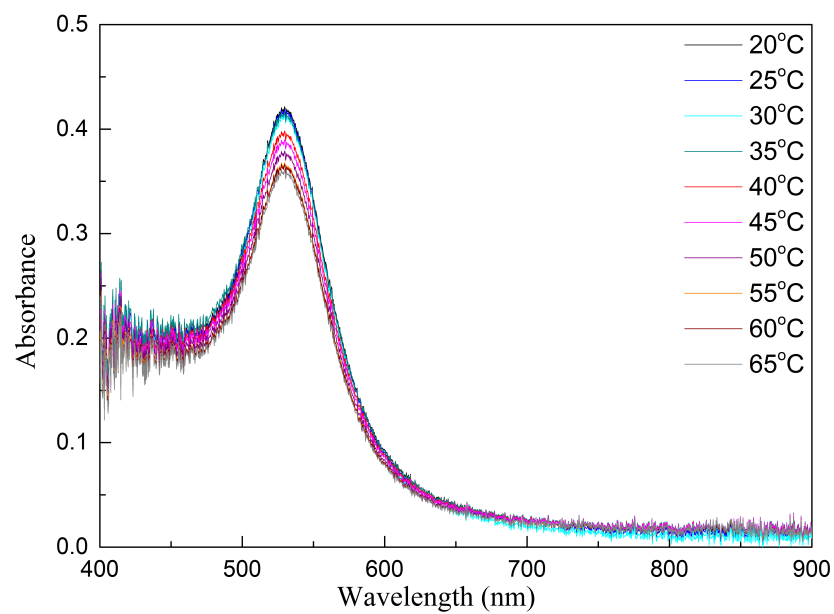


Figure A.9: Vis-NIR absorption spectra of sample JPM 491 from 20 °C to 65 °C.

A.1.4 Summary

Although we received several samples of PC-AuNPs from our collaborators; unfortunately most of them did not match basic requirements for monitoring their uptake in cells based on the ‘hide-reveal’ property of the thermoresponsive polymer coated shell. To conclude, a batch of PC-AuNP without Tf (JPM 400) was initially characterized in its thermo-responsiveness by absorption spectroscopy upon several heating cycles. The sample was prone to formation of aggregates, exhibited a non-physiological transition temperature at 50 °C, and showed a non sufficiently reversible behaviour. Therefore it was discarded, being unsuited for subsequent use in cellular applications. Two more PC-AuNPs solutions functionalised with Tf (JPM 487 and JPM 491) were measured exhibiting a more physiological transition temperature and a stable behaviour without the formation of aggregates upon temperature increase. They were later tested by our co-workers in order to examine their cellular uptake. Despite the fact that the PC-AuNPs-Tf³ were internalized via clathrin-mediated endocytosis, it was also proved that their cellular uptake was not temperature dependent and therefore no further research took place on these samples within my PhD project.

Finally, this specific collaboration with Nottingham and Cardiff School of Pharmacy ended in December 2015, and we had no access to additional samples.

³the experiments of cellular uptake were performed with AuNPs of 15 nm diameter

B

APPENDIX B

B.1 Optical resolution of FWM imaging

Here are displayed some experimental measurements of the resolution of our FWM imaging modality in two different samples. A single nominally spherical 60 nm AuNPs covalently bound onto glass (Figures B.1 and B.2) and single 20 nm bioconjugated AuNPs embedded in cells –Sample 3 of 20 nm AuNP-8D3-A647 in 3T3-L1 cells- (Figure B.3) were imaged on our multi-modal microscope via FWM using a 100x, 1.45 NA oil-immersion objective. The experimental determination of the full width at half maximum (FWHM) from the co-polarised FWM field amplitude provides an estimate of our optical resolution. Note that in our technique, the field amplitude is measured, as opposed to its intensity. In other words the measured widths are larger (by a factor $\sqrt{2}$ if we assume Gaussian profiles) than what would be obtained by measuring the intensity point-spread function. Notably fluorescence detection techniques are typically based on detecting intensities, and accordingly quote intensity PSF widths.

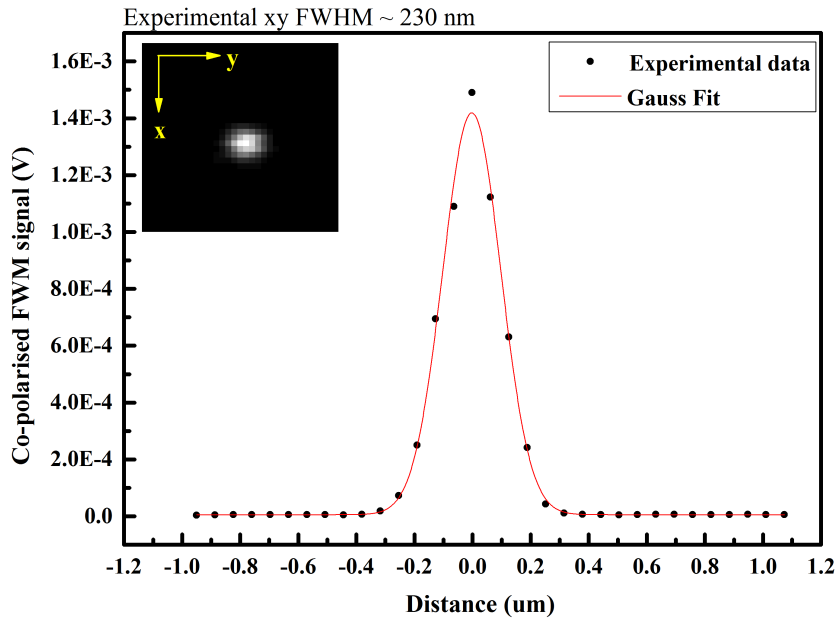


Figure B.1: Lateral resolution (xy) of our FWM imaging modality experimentally determined by the FWHM of the FWM co-polarised field amplitude on a single 60 nm spherical AuNP at the center of the laser focus beam collected with an oil-immersion 100x, 1.45 NA objective.

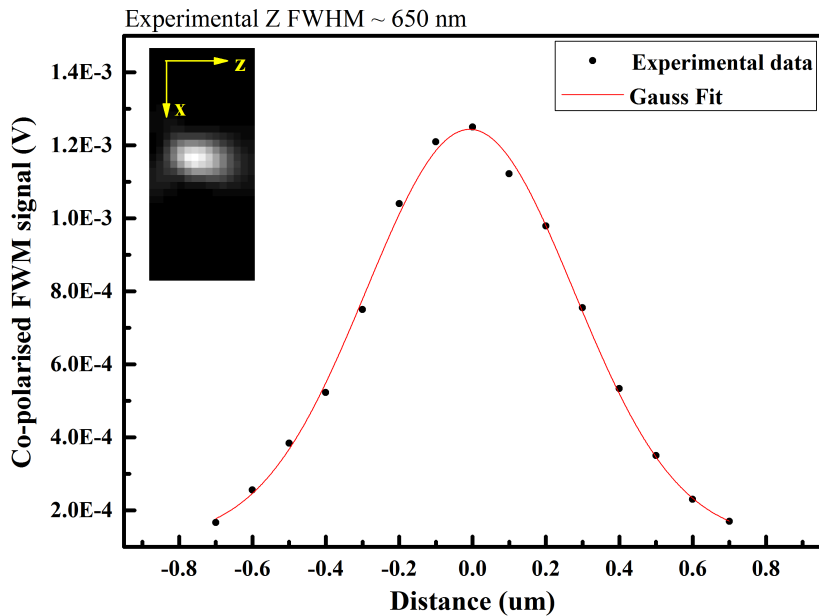


Figure B.2: Axial resolution (xz) of our FWM imaging modality experimentally determined by the FWHM of the FWM co-polarised field amplitude on a single 60 nm spherical AuNP at the center of the laser focus beam collected with an oil-immersion 100x, 1.45 NA objective.

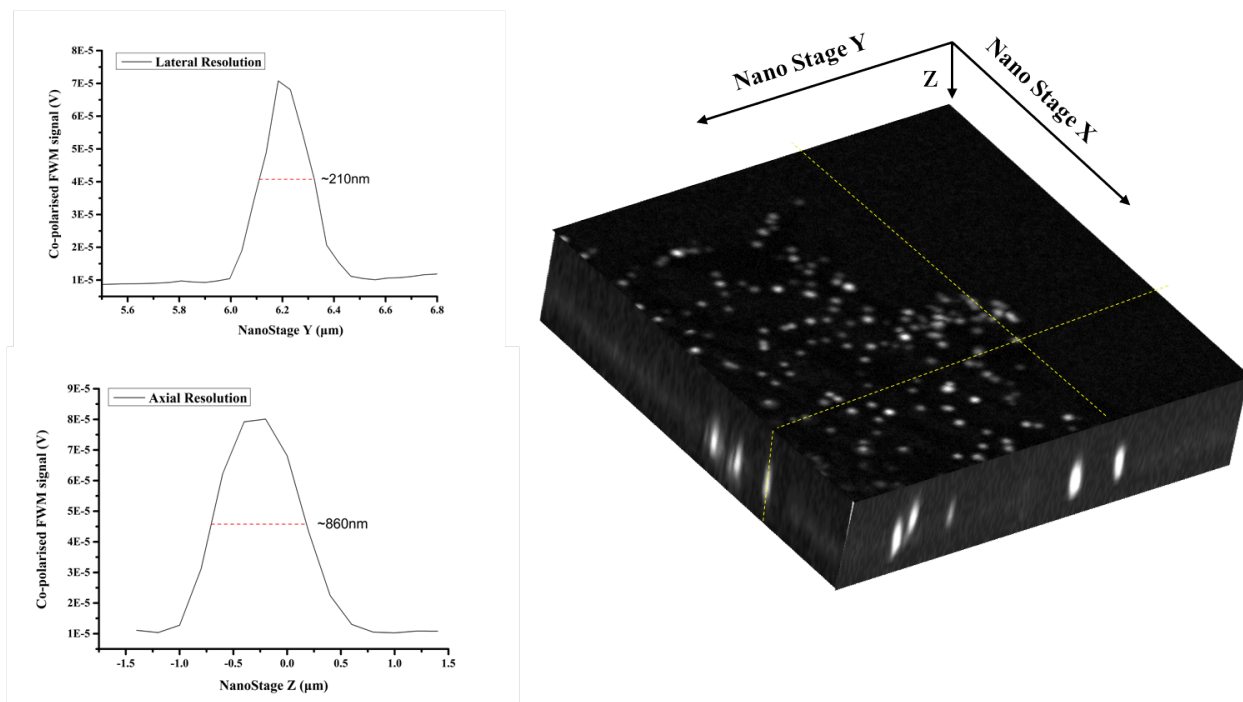


Figure B.3: Experimental determination of both lateral and axial resolution of FWM when imaging AuNPs in cells.

Lateral (top left) and axial (bottom left) resolution determined from the FWHM of the FWM co-polarised field amplitude on a single 20 nm spherical AuNP embedded in cells at the center of the laser focus beam. On the right a 3D representation of a FWM raster scan of the sample where the yellow dashed lines represent the xz and yz slices of one AuNP. The difference in the axial resolution seen here compared to the value shown for the 60 nm AuNP in oil (Figure B2) could be possibly attributed to the lower index of the cell medium due to their high concentration in water (compared to the mowiol medium surrounding). This would lead to additional spherical aberrations when going into the cells.

C

APPENDIX C

C.1 Competition of 15nm AuNP-PC-Tf(A488) with excess Tf

To determine whether 15 nm AuNPs-PC-Tf-A488 are internalized in a receptor-mediated (TfR) or independent manner, Tf competition experiments were performed. These experiments were done by our collaborators in Cardiff School of Pharmacy and further analysis on those can be found at Ref. [109].

The images below show fluorescence images of live HeLa cells with or without Tf-Bi solution under 488 nm excitation and a 100x, 1.45 NA oil objective in the confocal fluorescence microscopy of Cardiff School of Cardiff. The protocol included seeding of HeLa cells on MatTek dishes for 48h. Fig. C1 (Fig. C2) was incubated with 0 $\mu\text{g}/\text{ml}$ (50 $\mu\text{g}/\text{ml}$) non-fluorescent Tf-Bi in medium (DMEM with BSA and HEPES) and a concentration of 4.25×10^{12} AuNPs/mL of 15 nm AuNP-PC-Tf(A488) sample reference name JPM521 for 2h at 37° C. Addition of the free Tf was expected to out-compete the 15 nm AuNP-PC-Tf(A488) binding to Tf-receptors (note the excess concentration of Tf-Bi, nearly 100 times larger than the AuNP concentration), and thus reduce internalization of the AuNPs through Tf-mediated route. These results confirmed that the main route of internalisation of the 15 nm AuNPs-PC-Tf-A488 was via the Tf-mediated endocytic pathway.

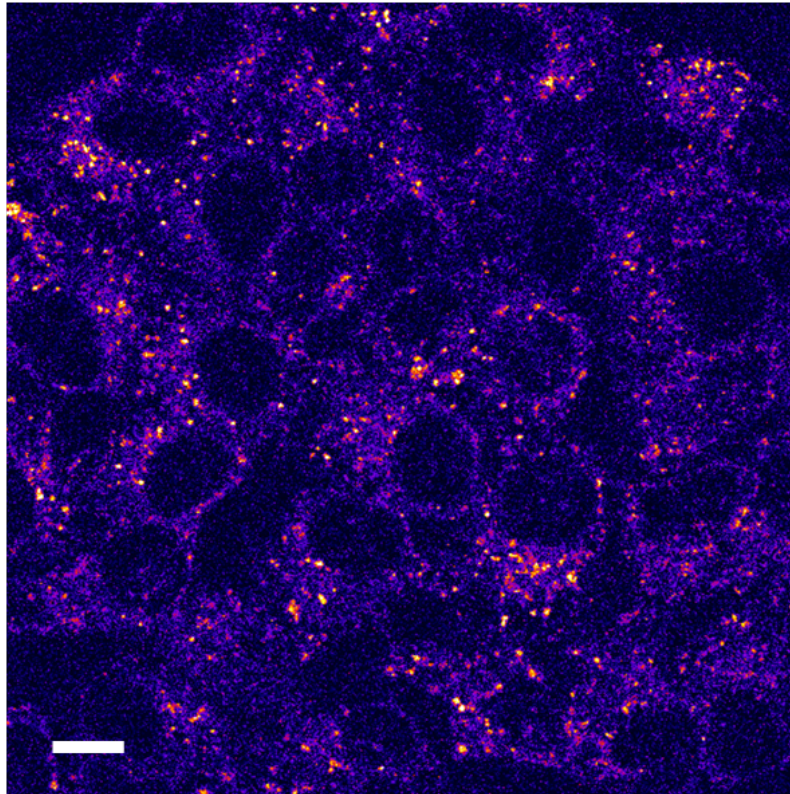


Figure C.1: 0 µg/ml non-fluorescent Tf-Bi. 10 µm scalebar.

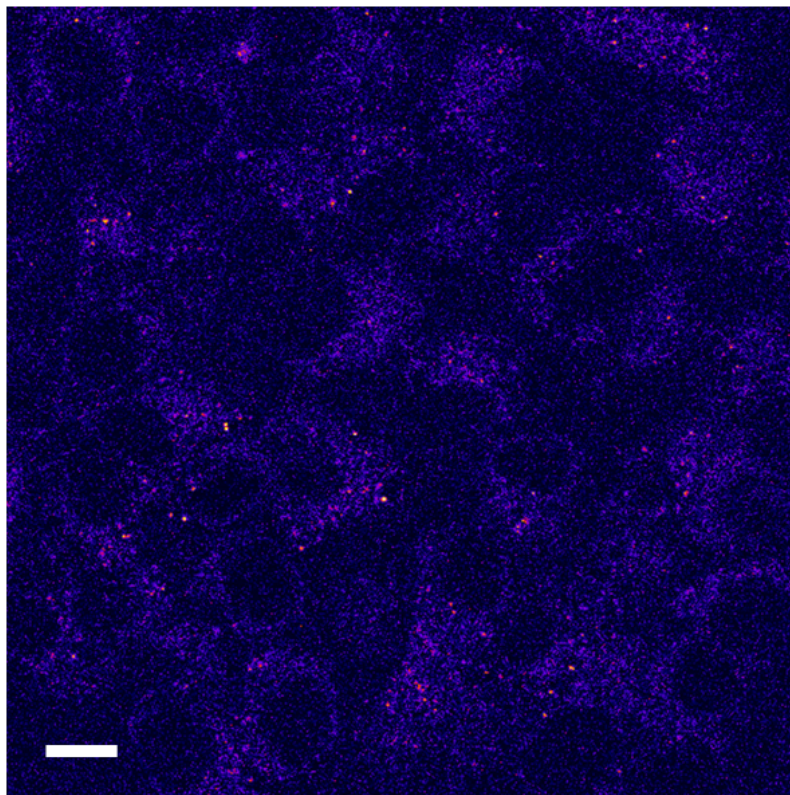


Figure C.2: 50 µg/ml non-fluorescent Tf-Bi. 10 µm scalebar.

D

APPENDIX D

D.1 Preliminary experiments on FWM imaging of 20nm AuNPs in live 3T3-L1 cells

Preliminary experiments of simultaneous FWM and epi-confocal fluorescence imaging on 20 nm AuNPs covalently attached to fluorescently labelled (A647) 8D3 anti-TfR antibody in live 3T3-L1 cells (see Sample 3 of Section 4.4) are presented.

3T3-L1 cells were grown on No. 1.5 thickness 25 mm diameter circular coverslips (Fisher Scientific) and on the day of the experiment were incubated for 30 min in serum free media and then with the Antibody-AuNP solution while mounted on a glass slide using an adhesive imaging spacer¹ of 0.12 mm thickness and a 13 mm diameter hole. The sample was then mounted onto the microscope's sample holder. In order to heat and keep the sample's temperature as close to 37°C as possible, objective and condenser heaters were used. The heaters were purchased by K.F.Technology and have the form of strips which can be wrapped around the optical components (in our case condenser and objective) and secured by means of a velcro strip. The temperature of the sample was monitored by temperature sensors attached onto the sample and kept at 37°C.

The set-up was aligned using the reference sample of gold film as described in section 3.1.3. A Nikon - Plan Apo 60x water immersion objective with 1.27 NA (Nikon CFI Plan Apochromat lamda series, super resolution) was used for focusing

¹described in Section 5.2

the overlapped pump and probe beams as well as the signals' (FWM and fluorescence) epi collection. The 1.34 NA oil condenser was used for DIC imaging alongside the 1.5x tube lens. Pump and probe laser power were measured at the sample to be 50 μW and 25 μW respectively. Two types of scans were acquired: (i) xy raster scans which gave an overview of the cell region (see Figure D.1), (ii) '*fast scans*' in temporal sequence which gave an overview of the live kinetics of the AuNPs in the scanning region (see Figure D.2). A video comprising 15 temporal repetitions of a $10 \times 10 \mu\text{m}$ scan of this sample can be found at this link: <https://youtu.be/DVJJwjpV1o>.

Despite the preliminary nature of these experiments, it is noted that the fluorescence signal is not colocated with the FWM signal from the AuNPs.

The aim of this experiment was to explore the feasibility of our FWM imaging technique in live cells and establish a practice towards that direction. The images presented here are examples of FWM imaging and tracking of AuNPs and show the potential of our technique in addressing kinetics of bio-conjugated of AuNPs in biological environments.

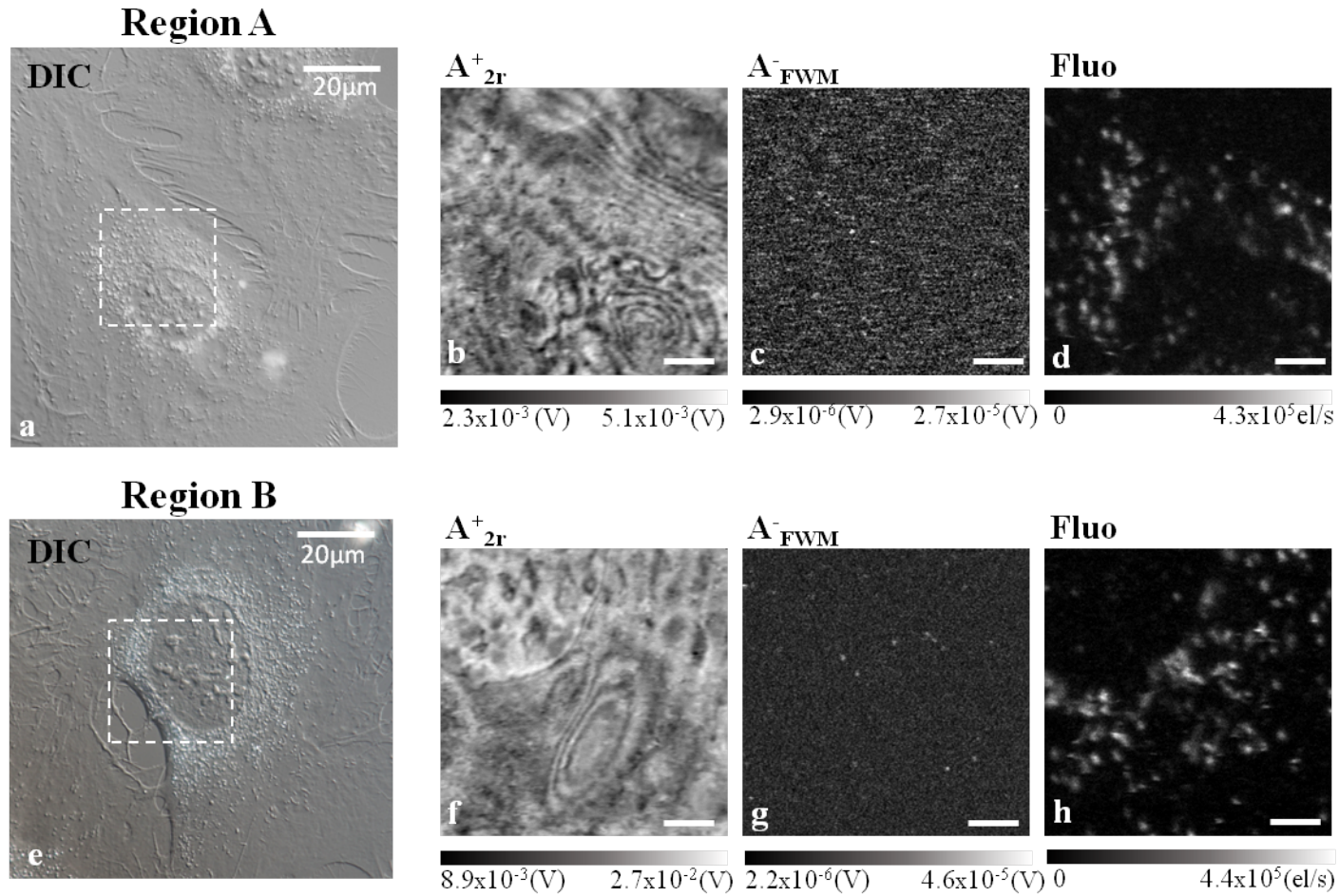


Figure D.1: Preliminary experimental results on simultaneous FWM-fluorescence imaging of 20nm AuNPs in live 3T3-L1 cells. DIC images (a, e) of two different cell regions (Region A and B) where the highlighted rectangular shows a $30 \times 30 \mu\text{m}$ cellular region imaged simultaneously via FWM (b,c and f,g) and epi-confocal fluorescence (d, h). The co-polarised reflection, A_{2r}^+ , (b,f) and cross-polarised FWM, A_{FWM}^- , (c,g) and fluorescence channels (d,h) were acquired with 0.5 (0.4) ms dwell time for Region A (B) and 72 nm pixel size. The scale bar for the FWM/confocal images is $5 \mu\text{m}$. The intensity scales in measured units (Volts, and photoelectron/s) are shown alongside the respective images.

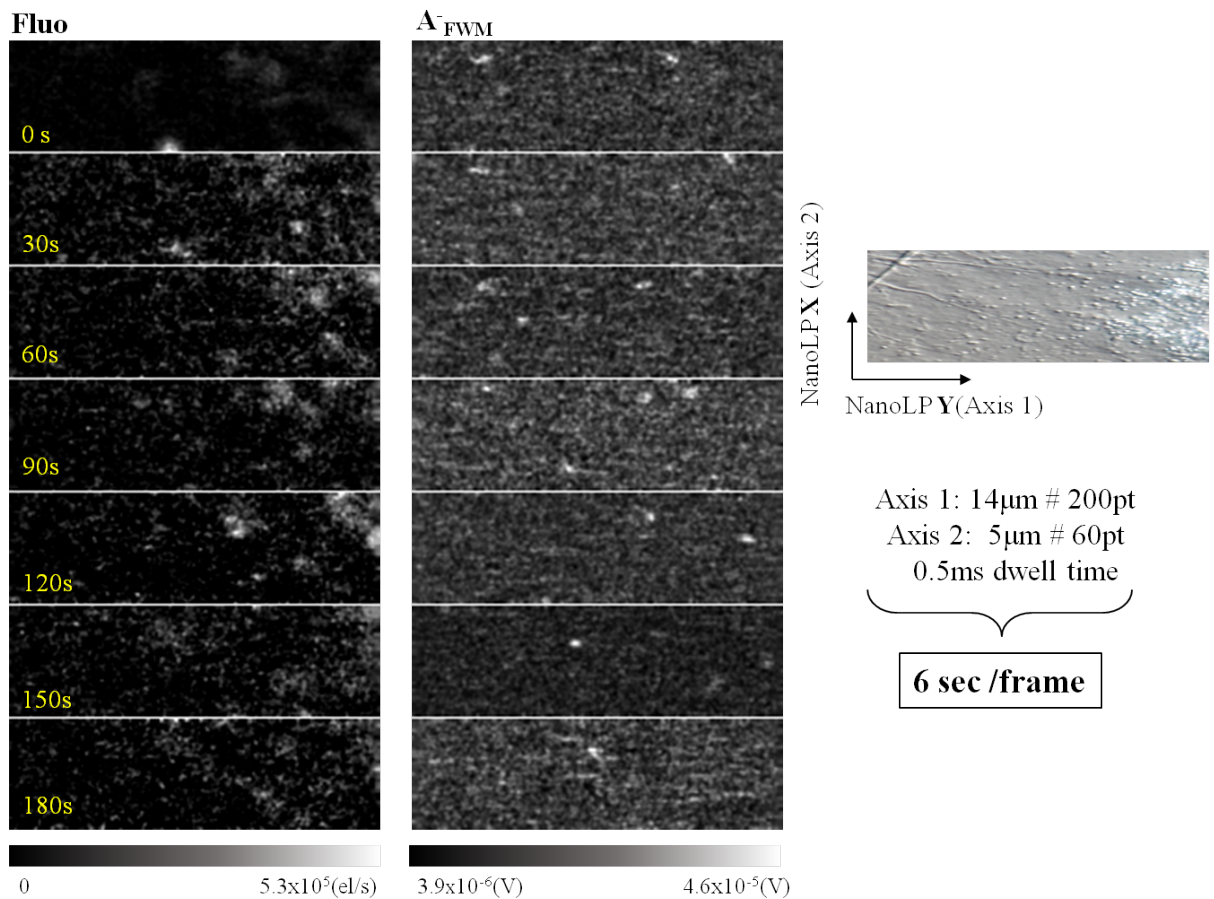


Figure D.2: Montage of *fast scans* on simultaneous FWM-fluorescence of 20nm AuNPs in live 3T3-L1 cells. Rectangular raster scans of $14 \times 5 \mu\text{m}$ acquired with 0.5 ms dwell time leading to a 6s per frame speed are shown every 5 repetitions (equal to 30s) side by side. Single 20 nm AuNPs undergoing endocytosis are detected simultaneously with confocal fluorescence.

BIBLIOGRAPHY

- [1] Omid C. Farokhzad and Robert Langer. “Impact of Nanotechnology on Drug Delivery”. In: *ACS Nano* 3.1 (2009), pp. 16–20. ISSN: 1936-0851. DOI: 10.1021/nn900002m. URL: <http://dx.doi.org/10.1021/nn900002m>.
- [2] W. P. Faulk and G. M. Taylor. “An immunocolloid method for the electron microscope”. In: *Immunochemistry* 8.11 (1971), pp. 1081–3. ISSN: 0019-2791 (Print) 0019-2791.
- [3] Solmaz Maleki Dizaj, Samira Jafari, and Ahmad Yari Khosroushahi. “A sight on the current nanoparticle-based gene delivery vectors”. In: *Nanoscale research letters* 9.1 (2014), p. 252.
- [4] Sha Jin and Kaiming Ye. “Nanoparticle-Mediated Drug Delivery and Gene Therapy”. In: *Biotechnology progress* 23.1 (2007), pp. 32–41.
- [5] S. Rana et al. “Monolayer coated gold nanoparticles for delivery applications”. In: *Adv Drug Deliv Rev* 64.2 (2012), pp. 200–16.
- [6] G. Han, P. Ghosh, and V. M. Rotello. “Functionalized gold nanoparticles for drug delivery”. In: *Nanomedicine (Lond)* 2.1 (2007), pp. 113–23. ISSN: 1743-5889. DOI: 10.2217/17435889.2.1.113.
- [7] Partha Ghosh et al. “Gold nanoparticles in delivery applications”. In: *Advanced Drug Delivery Reviews* 60.11 (2008), pp. 1307–1315. ISSN: 0169-409X. DOI: <http://dx.doi.org/10.1016/j.addr.2008.03.016>. URL: <http://www.sciencedirect.com/science/article/pii/S0169409X08000999>.
- [8] Robert Wilson. “The use of gold nanoparticles in diagnostics and detection”. In: *Chemical Society Reviews* 37.9 (2008), pp. 2028–2045. ISSN: 0306-0012. DOI: 10.1039/B712179M. URL: <http://dx.doi.org/10.1039/B712179M>.
- [9] Lev Dykman and Nikolai Khlebtsov. “Gold nanoparticles in biomedical applications: recent advances and perspectives”. In: *Chem. Soc. Rev.* 41 (6 2012), pp. 2256–2282. DOI: 10.1039/C1CS15166E. URL: <http://dx.doi.org/10.1039/C1CS15166E>.

- [10] C. Leduc et al. “Direct investigation of intracellular presence of gold nanoparticles via photothermal heterodyne imaging”. In: *ACS Nano* 5.4 (2011), pp. 2587–92. ISSN: 1936-0851. DOI: 10.1021/nm1023285.
- [11] Katrin Kneipp et al. “Surface-enhanced Raman scattering and biophysics”. In: *J. Phys.: Condens. Matter* 14 (2002), R597–R624.
- [12] Satish K. Nune et al. “Nanoparticles for biomedical imaging”. In: *Expert opinion on drug delivery* 6.11 (2009), pp. 1175–1194. ISSN: 1742-5247 1744-7593. DOI: 10.1517/17425240903229031. URL: <http://www.ncbi.nlm.nih.gov/pmc/articles/PMC3097035/>.
- [13] X. Huang et al. “Cancer cell imaging and photothermal therapy in the near-infrared region by using gold nanorods”. In: *J Am Chem Soc* 128.6 (2006), pp. 2115–20. ISSN: 0002-7863 (Print) 0002-7863. DOI: 10.1021/ja057254a.
- [14] Gregory V. Hartland. “Optical Studies of Dynamics in Noble Metal Nanostructures”. In: *Chemical Reviews* 111.6 (2011), pp. 3858–3887. ISSN: 0009-2665. DOI: 10.1021/cr1002547. URL: <http://dx.doi.org/10.1021/cr1002547>.
- [15] K. Lance Kelly et al. “The Optical Properties of Metal Nanoparticles: The Influence of Size, Shape, and Dielectric Environment”. In: *The Journal of Physical Chemistry B* 107.3 (2003), pp. 668–677. ISSN: 1520-6106. DOI: 10.1021/jp026731y. URL: <http://dx.doi.org/10.1021/jp026731y>.
- [16] Erik C Dreaden et al. “The golden age: gold nanoparticles for biomedicine”. In: *Chemical Society Reviews* 41.7 (2012), pp. 2740–2779.
- [17] E. Boisselier and D. Astruc. “Gold nanoparticles in nanomedicine: preparations, imaging, diagnostics, therapies and toxicity”. In: *Chem Soc Rev* 38.6 (2009), pp. 1759–82. ISSN: 0306-0012 (Print) 0306-0012. DOI: 10.1039/b806051g.
- [18] Xiaohua Huang et al. “Gold nanoparticles: interesting optical properties and recent applications in cancer diagnostics and therapy”. In: *Nanomedicine* 2.5 (2007), pp. 681–693. ISSN: 1743-5889. DOI: 10.2217/17435889.2.5.681. URL: <http://dx.doi.org/10.2217/17435889.2.5.681>.
- [19] Xiaohua Huang and Mostafa A. El-Sayed. “Gold nanoparticles: Optical properties and implementations in cancer diagnosis and photothermal therapy”. In: *Journal of Advanced Research* 1.1 (2010), pp. 13–28. ISSN: 2090-1232. DOI: <http://dx.doi.org/10.1016/j.jare.2010.02.002>. URL: <http://www.sciencedirect.com/science/article/pii/S2090123210000056>.

- [20] Younan Xia and Naomi J. Halas. “Shape-Controlled Synthesis and Surface Plasmonic Properties of Metallic Nanostructures”. In: *MRS Bulletin* 30.5 (2005), 338–348. DOI: 10.1557/mrs2005.96.
- [21] M. C. Daniel and D. Astruc. “Gold nanoparticles: Assembly, supramolecular chemistry, quantum-size-related properties, and applications toward biology, catalysis, and nanotechnology”. In: *Chemical Reviews* 104.1 (2004), pp. 293–346. ISSN: 0009-2665. DOI: 10.1021/cr030698+. URL: <GotoISI>://WOS:000188217400009.
- [22] Babak Nikoobakht and Mostafa A. El-Sayed. “Preparation and Growth Mechanism of Gold Nanorods (NRs) Using Seed-Mediated Growth Method”. In: *Chemistry of Materials* 15.10 (2003), pp. 1957–1962.
- [23] Catherine J. Murphy et al. “Anisotropic Metal Nanoparticles: Synthesis, Assembly, and Optical Applications”. In: *The Journal of Physical Chemistry B* 109.29 (2005), pp. 13857–13870. DOI: 10.1021/jp0516846. eprint: <http://dx.doi.org/10.1021/jp0516846>. URL: <http://dx.doi.org/10.1021/jp0516846>.
- [24] John Turkevich, Peter Cooper Stevenson, and James Hillier. “A study of the nucleation and growth processes in the synthesis of colloidal gold”. In: *Discuss. Faraday Soc.* 11 (0 1951), pp. 55–75. DOI: 10.1039/DF9511100055. URL: <http://dx.doi.org/10.1039/DF9511100055>.
- [25] J. Kimling et al. “Turkevich Method for Gold Nanoparticle Synthesis Revisited”. In: *The Journal of Physical Chemistry B* 110.32 (2006), pp. 15700–15707. DOI: 10.1021/jp061667w. eprint: <https://doi.org/10.1021/jp061667w>. URL: <https://doi.org/10.1021/jp061667w>.
- [26] Stefan W. Hell. “Far-Field Optical Nanoscopy”. In: *Science* 316.5828 (2007), pp. 1153–1158. DOI: 10.1126/science.1137395. URL: <http://www.sciencemag.org/content/316/5828/1153.abstract>.
- [27] Stefan W. Hell and Jan Wichmann. “Breaking the diffraction resolution limit by stimulated emission: stimulated-emission-depletion fluorescence microscopy”. In: *Opt. Lett.* 19.11 (1994), pp. 780–782. DOI: 10.1364/OL.19.000780. URL: <http://ol.osa.org/abstract.cfm?URI=ol-19-11-780>.
- [28] Michael J Rust, Mark Bates, and Xiaowei Zhuang. “Sub-diffraction-limit imaging by stochastic optical reconstruction microscopy (STORM)”. In: *Nature methods* 3.10 (2006), pp. 793–796.

- [29] Eric Betzig et al. “Imaging Intracellular Fluorescent Proteins at Nanometer Resolution”. In: *Science* 313.5793 (2006), pp. 1642–1645. ISSN: 0036-8075. DOI: 10.1126/science.1127344. eprint: <http://science.sciencemag.org/content/313/5793/1642.full.pdf>. URL: <http://science.sciencemag.org/content/313/5793/1642>.
- [30] Eric Betzig and Jay K Trautman. “Near-field optics: microscopy, spectroscopy, and surface modification beyond the diffraction limit”. In: *Science* 257.5067 (1992), pp. 189–196.
- [31] Y. Sako, S. Minoghchi, and T. Yanagida. “Single-molecule imaging of EGFR signalling on the surface of living cells.” In: *Nature cell biology* 2.3 (Mar. 2000), pp. 168–172. ISSN: 1465-7392. DOI: 10.1038/35004044. URL: <http://dx.doi.org/10.1038/35004044>.
- [32] Prashant K. Jain et al. “Calculated Absorption and Scattering Properties of Gold Nanoparticles of Different Size, Shape, and Composition: Applications in Biological Imaging and Biomedicine”. In: *The Journal of Physical Chemistry B* 110.14 (2006), pp. 7238–7248. ISSN: 1520-6106. DOI: 10.1021/jp057170o. URL: <http://dx.doi.org/10.1021/jp057170o>.
- [33] Hiroshi Ueno et al. “Simple dark-field microscopy with nanometer spatial precision and microsecond temporal resolution”. In: *Biophysical journal* 98.9 (2010), pp. 2014–2023.
- [34] Sergiy Patskovsky, Eric Bergeron, and Michel Meunier. “Hyperspectral dark-field microscopy of PEGylated gold nanoparticles targeting CD44-expressing cancer cells”. In: *Journal of Biophotonics* 8.1-2 (2015), pp. 162–167. ISSN: 1864-0648. DOI: 10.1002/jbio.201300165. URL: <http://dx.doi.org/10.1002/jbio.201300165>.
- [35] W. Qian et al. “Dark-field light scattering imaging of living cancer cell component from birth through division using bioconjugated gold nanoprobess”. In: *J Biomed Opt* 15.4 (2010), p. 046025. ISSN: 1560-2281 (Electronic) 1083-3668 (Linking). DOI: 10.1117/1.3477179.
- [36] Xiaohua Huang and Mostafa A. El-Sayed. “Plasmonic photo-thermal therapy (PPTT)”. In: *Alexandria Journal of Medicine* 47.1 (2011), pp. 1–9. ISSN: 2090-5068. DOI: <https://doi.org/10.1016/j.ajme.2011.01.001>. URL: <http://www.sciencedirect.com/science/article/pii/S2090506811000029>.

- [37] Vladimir P Zharov et al. “Synergistic enhancement of selective nanophotothermolysis with gold nanoclusters: potential for cancer therapy”. In: *Lasers in surgery and medicine* 37.3 (2005), pp. 219–226.
- [38] D. Boyer et al. “Photothermal imaging of nanometer-sized metal particles among scatterers”. In: *Science* 297.5584 (2002), pp. 1160–3. ISSN: 0036-8075. DOI: 10.1126/science.1073765.
- [39] Stéphane Berciaud et al. “Photothermal Heterodyne Imaging of Individual Nonfluorescent Nanoclusters and Nanocrystals”. In: *Physical Review Letters* 93.25 (2004), p. 257402. URL: <http://link.aps.org/doi/10.1103/PhysRevLett.93.257402>.
- [40] Stéphane Berciaud et al. “Photothermal heterodyne imaging of individual metallic nanoparticles: Theory versus experiment”. In: *Physical Review B* 73.4 (2006), p. 045424. URL: <http://link.aps.org/doi/10.1103/PhysRevB.73.045424>.
- [41] David Lasne et al. “Label-free optical imaging of mitochondria in live cells”. In: *Opt. Express* 15.21 (2007), pp. 14184–14193. DOI: 10.1364/OE.15.014184. URL: <http://www.opticsexpress.org/abstract.cfm?URI=oe-15-21-14184>.
- [42] L. Cognet et al. “Single metallic nanoparticle imaging for protein detection in cells”. In: *Proceedings of the National Academy of Sciences* 100.20 (2003), pp. 11350–11355. ISSN: 0027-8424. DOI: 10.1073/pnas.1534635100. eprint: <http://www.pnas.org/content/100/20/11350.full.pdf>. URL: <http://www.pnas.org/content/100/20/11350>.
- [43] Ling Tong and Ji-Xin Cheng. “Label-free imaging through nonlinear optical signals”. In: *Materials Today* 14.6 (2011), pp. 264–273. ISSN: 1369-7021. DOI: [http://dx.doi.org/10.1016/S1369-7021\(11\)70141-9](http://dx.doi.org/10.1016/S1369-7021(11)70141-9). URL: <http://www.sciencedirect.com/science/article/pii/S1369702111701419>.
- [44] George Zorinants et al. “Background-Free 3D Nanometric Localization and Sub-nm Asymmetry Detection of Single Plasmonic Nanoparticles by Four-Wave Mixing Interferometry with Optical Vortices”. In: *Phys. Rev. X* 7 (4 2017), p. 041022. DOI: 10.1103/PhysRevX.7.041022. URL: <https://link.aps.org/doi/10.1103/PhysRevX.7.041022>.
- [45] F. Masia, W. Langbein, and P. Borri. “Measurement of the dynamics of plasmons inside individual gold nanoparticles using a femtosecond phase-resolved microscope”. In: *Physical Review B* 85.23 (2012). ISSN: 1098-0121. DOI: 10.1103/PhysRevB.85.235403. URL: <GotoISI>://WOS:000304693200005.

- [46] Francesco Masia, Wolfgang Langbein, and Paola Borri. “Polarization-resolved ultrafast dynamics of the complex polarizability in single gold nanoparticles”. In: *Phys. Chem. Chem. Phys.* 15 (12 2013), pp. 4226–4232. DOI: 10.1039/C2CP43451B. URL: <http://dx.doi.org/10.1039/C2CP43451B>.
- [47] Paul R. Moody et al. “Receptor Crosslinking: A General Method to Trigger Internalization and Lysosomal Targeting of Therapeutic Receptor:Ligand Complexes”. In: *Mol Ther* (2015). ISSN: 1525-0024. DOI: 10.1038/mt.2015.178. URL: <http://dx.doi.org/10.1038/mt.2015.178>.
- [48] Benjamin Miles et al. “Direct Evidence of Lack of Colocalisation of Fluorescently Labelled Gold Labels Used in Correlative Light Electron Microscopy”. In: *Scientific Reports* 7 (2017), p. 44666.
- [49] Benjamin T. Miles et al. “Sensitivity of Interferometric Cross-Polarization Microscopy for Nanoparticle Detection in the Near-Infrared”. In: *ACS Photonics* 2.12 (2015), pp. 1705–1711. DOI: 10.1021/acsp Photonics.5b00326. eprint: <https://doi.org/10.1021/acsp Photonics.5b00326>. URL: <https://doi.org/10.1021/acsp Photonics.5b00326>.
- [50] Benjamin T Miles et al. “All-optical method for characterizing individual fluorescent nanodiamonds”. In: *ACS Photonics* 3.3 (2016), pp. 343–348.
- [51] E. Dulkeith et al. “Fluorescence Quenching of Dye Molecules near Gold Nanoparticles: Radiative and Nonradiative Effects”. In: *Phys. Rev. Lett.* 89 (20 2002), p. 203002. DOI: 10.1103/PhysRevLett.89.203002. URL: <https://link.aps.org/doi/10.1103/PhysRevLett.89.203002>.
- [52] Irawati K. Kandela and Ralph M. Albrecht. “Fluorescence quenching by colloidal heavy metals nanoparticles: implications for correlative fluorescence and electron microscopy studies.” In: *Scanning* 29 (2007), pp. 152–161. DOI: 10.1002/sca.20055.
- [53] Irawati K. Kandela, Reiner Bleher, and Ralph M. Albrecht. “Multiple Correlative Immunolabeling for Light and Electron Microscopy Using Fluorophores and Colloidal Metal Particles”. In: *Journal of Histochemistry & Cytochemistry* 55.10 (2007), pp. 983–990. DOI: 10.1369/jhc.6A7124.2007. eprint: <https://doi.org/10.1369/jhc.6A7124.2007>. URL: <https://doi.org/10.1369/jhc.6A7124.2007>.
- [54] Ian Freestone et al. “The Lycurgus cup—a roman nanotechnology”. In: *Gold Bulletin* 40.4 (2007), pp. 270–277.
- [55] URL: <http://www.amusingplanet.com/2016/12/lycurgus-cup-piece-of-ancient-roman.html>.

- [56] Meindert Alexander van Dijk. “Nonlinear-optical studies of single gold nanoparticles”. In: *PhD Thesis* (2007-2010).
- [57] Aurelien Crut et al. “Optical absorption and scattering spectroscopies of single nano-objects”. In: *Chem. Soc. Rev.* 43 (11 2014), pp. 3921–3956. DOI: 10.1039/C3CS60367A. URL: <http://dx.doi.org/10.1039/C3CS60367A>.
- [58] Andreas Trügler. “Optical properties of metallic nanoparticles”. PhD thesis. Institut für Physik, Fachbereich Theoretische Physik, 2011.
- [59] C.F. Bohren and D.R. Huffman. *Absorption and scattering of light by small particles*. Ed. by John Wiley and Sons. Wiley Science, 1982.
- [60] R. Gans. “Über die Form ultramikroskopischer Silberteilchen”. In: *Annalen der Physik* 352.10 (1915), pp. 270–284. ISSN: 1521-3889. DOI: 10.1002/andp.19153521006. URL: <http://dx.doi.org/10.1002/andp.19153521006>.
- [61] Susie Eustis and Mostafa A. El-Sayed. “Determination of the aspect ratio statistical distribution of gold nanorods in solution from a theoretical fit of the observed inhomogeneously broadened longitudinal plasmon resonance absorption spectrum”. In: *Journal of Applied Physics* 100.4 (2006), p. 044324. DOI: 10.1063/1.2244520. eprint: <https://doi.org/10.1063/1.2244520>. URL: <https://doi.org/10.1063/1.2244520>.
- [62] Lukas M. Payne. “Optical extinction and coherent multiphoton micro-spectroscopy of single nanoparticles”. PhD thesis. Cardiff University, 2015.
- [63] P. B. Johnson and R. W. Christy. “Optical Constants of the Noble Metals”. In: *Phys. Rev. B* 6 (12 1972), pp. 4370–4379. DOI: 10.1103/PhysRevB.6.4370. URL: <https://link.aps.org/doi/10.1103/PhysRevB.6.4370>.
- [64] M. A. van Dijk et al. “Absorption and scattering microscopy of single metal nanoparticles”. In: *Physical Chemistry Chemical Physics* 8.30 (2006), pp. 3486–3495. ISSN: 1463-9076. DOI: 10.1039/B606090K. URL: <http://dx.doi.org/10.1039/B606090K>.
- [65] Maria Dienerowitz, Michael Mazilu, and Kishan Dholakia. “Optical manipulation of nanoparticles: a review”. In: *Journal of Nanophotonics* 2.1 (2008), pp. 2–32. ISSN: 1934-2608. DOI: 10.1117/1.2992045. URL: <http://dx.doi.org/10.1117/1.2992045>.
- [66] Stephan Link and Mostafa A. El-Sayed. “Size and Temperature Dependence of the Plasmon Absorption of Colloidal Gold Nanoparticles”. In: *The Journal of Physical Chemistry B* 103.21 (1999), pp. 4212–4217. ISSN: 1520-6106. DOI: 10.1021/jp984796o. URL: <http://dx.doi.org/10.1021/jp984796o>.

- [67] Peter N. Njoki et al. “Size Correlation of Optical and Spectroscopic Properties for Gold Nanoparticles”. In: *The Journal of Physical Chemistry C* 111.40 (2007), pp. 14664–14669. ISSN: 1932-7447. DOI: 10.1021/jp074902z. URL: <http://dx.doi.org/10.1021/jp074902z>.
- [68] Lindsey J. E. Anderson et al. “Quantitative Measurements of Individual Gold Nanoparticle Scattering Cross Sections”. In: *The Journal of Physical Chemistry C* 114.25 (2010), pp. 11127–11132. DOI: 10.1021/jp1040663. eprint: <http://dx.doi.org/10.1021/jp1040663>. URL: <http://dx.doi.org/10.1021/jp1040663>.
- [69] Catherine J Murphy and Nikhil R Jana. “Controlling the aspect ratio of inorganic nanorods and nanowires”. In: *Advanced Materials* 14.1 (2002), pp. 80–82.
- [70] C. J. Orendorff, T. K. Sau, and C. J. Murphy. “Shape-dependent plasmon-resonant gold nanoparticles”. In: *Small* 2.5 (2006), pp. 636–9. ISSN: 1613-6810. DOI: 10.1002/smll.200500299.
- [71] Roejarek Kanjanawarut, Bo Yuan, and Su XiaoDi. “UV-Vis Spectroscopy and Dynamic Light Scattering Study of Gold Nanorods Aggregation”. In: *Nucleic Acid Therapeutics* 23.4 (2013), pp. 273–280. ISSN: 2159-3337 2159-3345. DOI: 10.1089/nat.2013.0421. URL: <http://www.ncbi.nlm.nih.gov/pmc/articles/PMC3723236/>.
- [72] Cecilia Noguez. “Surface Plasmons on Metal Nanoparticles: The Influence of Shape and Physical Environment”. In: *The Journal of Physical Chemistry C* 111.10 (2007), pp. 3806–3819. DOI: 10.1021/jp066539m. eprint: <http://dx.doi.org/10.1021/jp066539m>. URL: <http://dx.doi.org/10.1021/jp066539m>.
- [73] Iván O. Sosa, Cecilia Noguez, and Rubén G. Barrera. “Optical Properties of Metal Nanoparticles with Arbitrary Shapes”. In: *The Journal of Physical Chemistry B* 107.26 (2003), pp. 6269–6275. DOI: 10.1021/jp0274076. eprint: <http://dx.doi.org/10.1021/jp0274076>. URL: <http://dx.doi.org/10.1021/jp0274076>.
- [74] Luis M. Liz-Marzán. “Tailoring Surface Plasmons through the Morphology and Assembly of Metal Nanoparticles”. In: *Langmuir* 22.1 (2006), pp. 32–41. ISSN: 0743-7463. DOI: 10.1021/la0513353. URL: <http://dx.doi.org/10.1021/la0513353>.

- [75] Mona B. Mohamed et al. “The ‘lightning’ gold nanorods: fluorescence enhancement of over a million compared to the gold metal”. In: *Chemical Physics Letters* 317.6 (2000), pp. 517–523. ISSN: 0009-2614. DOI: [https://doi.org/10.1016/S0009-2614\(99\)01414-1](https://doi.org/10.1016/S0009-2614(99)01414-1). URL: <http://www.sciencedirect.com/science/article/pii/S0009261499014141>.
- [76] Shuhua Yue, Mikhail N. Slipchenko, and Ji-Xin Cheng. “Multimodal Non-linear Optical Microscopy”. In: *Laser & photonics reviews* 5.4 (2011). ISSN: 1863-8880 1863-8899. DOI: 10.1002/lpor.201000027. URL: <http://www.ncbi.nlm.nih.gov/pmc/articles/PMC3863942/>.
- [77] Jérémy Butet, Pierre-Francois Brevet, and Olivier JF Martin. “Optical second harmonic generation in plasmonic nanostructures: From fundamental principles to advanced applications”. In: *Acs Nano* 9.11 (2015), pp. 10545–10562.
- [78] P.J. Campagnola and C.-Y. Dong. “Second harmonic generation microscopy: principles and applications to disease diagnosis”. In: *Laser & Photonics Reviews* 5.1 (2011), pp. 13–26. ISSN: 1863-8899. DOI: 10.1002/lpor.200910024. URL: <http://dx.doi.org/10.1002/lpor.200910024>.
- [79] G. Bachelier et al. “Origin of optical second-harmonic generation in spherical gold nanoparticles: Local surface and nonlocal bulk contributions”. In: *Phys. Rev. B* 82 (23 2010), p. 235403. DOI: 10.1103/PhysRevB.82.235403. URL: <https://link.aps.org/doi/10.1103/PhysRevB.82.235403>.
- [80] Markus Lippitz, Meindert A. van Dijk, and Michel Orrit. “Third-Harmonic Generation from Single Gold Nanoparticles”. In: *Nano Letters* 5.4 (2005), pp. 799–802. DOI: 10.1021/nl0502571. eprint: <https://doi.org/10.1021/nl0502571>. URL: <https://doi.org/10.1021/nl0502571>.
- [81] M. W. Klein et al. “Lineshape of harmonic generation by metallic nanoparticles and metallic photonic crystal slabs”. In: *Phys. Rev. B* 72 (11 2005), p. 115113. DOI: 10.1103/PhysRevB.72.115113. URL: <https://link.aps.org/doi/10.1103/PhysRevB.72.115113>.
- [82] Yong Wang et al. “Four-wave mixing microscopy of nanostructures”. In: *Advances in Optics and Photonics* 3.1 (2011), pp. 1–52. DOI: 10.1364/AOP.3.000001. URL: <http://aop.osa.org/abstract.cfm?URI=aop-3-1-1>.
- [83] Yookyung Jung et al. “Imaging Gold Nanorods by Plasmon Resonance Enhanced Four Wave Mixing”. In: *The Journal of Physical Chemistry C* 113.7 (2009), pp. 2657–2663. ISSN: 1932-7447. DOI: 10.1021/jp810852c. URL:

<http://dx.doi.org/10.1021/jp810852c>
<http://pubs.acs.org/doi/pdfplus/10.1021/jp810852c>.

- [84] Francesco Masia et al. “Resonant four-wave mixing of gold nanoparticles for three-dimensional cell microscopy”. In: *Optics Letters* 34.12 (2009), pp. 1816–1818. DOI: 10.1364/OL.34.001816. URL: <http://ol.osa.org/abstract.cfm?URI=ol-34-12-1816><http://www.opticsinfobase.org/ol/abstract.cfm?uri=ol-34-12-1816>.
- [85] Iestyn Pope et al. “Coherent anti-Stokes Raman scattering microscopy of single nanodiamonds”. In: *Nature nanotechnology* 9.11 (2014), p. 940.
- [86] Robert W. Boyd. *Nonlinear Optics*. 3rd. Elsevier, 2008.
- [87] B.E.A. Saleh and M.C. Teich. *Fundamentals of Photonics*. Second. John Wiley & Sons Inc., 2007.
- [88] Partha P. Banerjee. *Nonlinear Optics: Theory, Numerical Modeling, and Applications*. CRC Press, 2003.
- [89] Stefan A. Maier. *Plasmonics: Fundamentals and Applications*. Springer, 2007.
- [90] Naveen Kumar Balla et al. “Polarized Nonlinear Nanoscopy of Metal Nanostructures”. In: *ACS Photonics* 4.2 (2017), pp. 292–301. DOI: 10.1021/acsp Photonics.6b00635. eprint: <https://doi.org/10.1021/acsp Photonics.6b00635>. URL: <https://doi.org/10.1021/acsp Photonics.6b00635>.
- [91] Otto L. Muskens, Natalia Del Fatti, and Fabrice Vallée. “Femtosecond Response of a Single Metal Nanoparticle”. In: *Nano Letters* 6.3 (2006), pp. 552–556. DOI: 10.1021/nl0524086. eprint: <https://doi.org/10.1021/nl0524086>. URL: <https://doi.org/10.1021/nl0524086>.
- [92] Christophe Voisin et al. “Ultrafast Electron Dynamics and Optical Nonlinearities in Metal Nanoparticles”. In: *The Journal of Physical Chemistry B* 105.12 (2001), pp. 2264–2280. DOI: 10.1021/jp0038153. eprint: <https://doi.org/10.1021/jp0038153>. URL: <https://doi.org/10.1021/jp0038153>.
- [93] Payne Lukas, Langbein Wolfgang, and Borri Paola. “Polarization-resolved extinction and scattering cross-sections of individual gold nanoparticles measured by wide-field microscopy on a large ensemble”. In: *Applied Physics Letters* 102.13 (2013). DOI: <http://dx.doi.org/10.1063/1.4800564>.
- [94] Lukas M. Payne, Wolfgang Langbein, and Paola Borri. “Wide-Field Imaging of Single-Nanoparticle Extinction with Sub-nm² Sensitivity”. In: *Phys. Rev. Applied* 9 (3 2018), p. 034006. DOI: 10.1103/PhysRevApplied.9.034006. URL: <https://link.aps.org/doi/10.1103/PhysRevApplied.9.034006>.

- [95] P. Hariharan. *Basics of Interferometry*. Second edition. Elsevier, 2007.
- [96] Philippe Thévenaz. *An ImageJ plugin for the recursive alignment of a stack of images*. <http://bigwww.epfl.ch/thevenaz/stackreg/>. 1998.
- [97] S. Bolte and F. P. Cordelieres. “A guided tour into subcellular colocalization analysis in light microscopy”. In: *J Microsc* 224.Pt 3 (2006), pp. 213–32. ISSN: 0022-2720 (Print) 0022-2720 (Linking). DOI: 10.1111/j.1365-2818.2006.01706.x.
- [98] EMM Manders et al. “Four-dimensional imaging of chromatin dynamics during the assembly of the interphase nucleus”. In: *Chromosome research* 11.5 (2003), pp. 537–547.
- [99] Sylvain V Costes et al. “Automatic and quantitative measurement of protein-protein colocalization in live cells”. In: *Biophysical journal* 86.6 (2004), pp. 3993–4003.
- [100] Qi Li et al. “A syntaxin 1, G α , and N-type calcium channel complex at a presynaptic nerve terminal: analysis by quantitative immunocolocalization”. In: *Journal of Neuroscience* 24.16 (2004), pp. 4070–4081.
- [101] Zhong Ming Qian et al. “Targeted Drug Delivery via the Transferrin Receptor-Mediated Endocytosis Pathway”. In: *Pharmacological Reviews* 54.4 (2002), pp. 561–587. URL: <http://pharmrev.aspetjournals.org/content/54/4/561.abstract>.
- [102] Joshua Z. Rappoport and Sanford M. Simon. “Real-time analysis of clathrin-mediated endocytosis during cell migration”. English (US). In: *Journal of Cell Science* 116.5 (Mar. 2003), pp. 847–855.
- [103] Lisa M. Bareford and Peter W. Swaan. “Endocytic mechanisms for targeted drug delivery”. In: *Advanced Drug Delivery Reviews* 59.8 (2007), pp. 748–758. ISSN: 0169-409X. DOI: <http://dx.doi.org/10.1016/j.addr.2007.06.008>. URL: <http://www.sciencedirect.com/science/article/pii/S0169409X07000968>.
- [104] Joshua Z. Rappoport. “Focusing on clathrin-mediated endocytosis”. In: *Biochemical Journal* 412.3 (2008), pp. 415–423. DOI: 10.1042/bj20080474. URL: <http://www.biochemj.org/ppbiochemj/412/3/415.full.pdf>.
- [105] Anand Gole and Catherine J. Murphy. “BiotinStreptavidin-Induced Aggregation of Gold Nanorods: Tuning RodRod Orientation”. In: *Langmuir* 21.23 (2005), pp. 10756–10762. DOI: 10.1021/la0512704. eprint: <https://doi.org/10.1021/la0512704>. URL: <https://doi.org/10.1021/la0512704>.

- [106] Sigma-Aldrich. URL: <https://www.sigmaaldrich.com/catalog/product/aldrich/81381?lang=en®ion=GB>.
- [107] N. Michael Green. “Avidin”. In: *Advances in Protein Chemistry* 29 (1975), pp. 85–133. ISSN: 0065-3233. DOI: [http://dx.doi.org/10.1016/S0065-3233\(08\)60411-8](http://dx.doi.org/10.1016/S0065-3233(08)60411-8). URL: <http://www.sciencedirect.com/science/article/pii/S0065323308604118>.
- [108] Xiaochen A. Wu et al. “Intracellular Fate of Spherical Nucleic Acid Nanoparticle Conjugates”. In: *Journal of the American Chemical Society* 136.21 (2014), pp. 7726–7733. DOI: 10.1021/ja503010a. eprint: <https://doi.org/10.1021/ja503010a>. URL: <https://doi.org/10.1021/ja503010a>.
- [109] Edward Sayers et al. “Switching of macromolecular ligand display by thermoresponsive polymers mediates endocytosis of multi-conjugate nanoparticles”. In: *Bioconjugate Chemistry* 0.ja (2018), null. DOI: 10.1021/acs.bioconjchem.7b00704. eprint: <https://doi.org/10.1021/acs.bioconjchem.7b00704>. URL: <https://doi.org/10.1021/acs.bioconjchem.7b00704>.
- [110] Mark A. Ward and Theoni K. Georgiou. “Thermoresponsive Polymers for Biomedical Applications”. In: *Polymers* 3.3 (2011), pp. 1215–1242. ISSN: 2073-4360. URL: <http://www.mdpi.com/2073-4360/3/3/1215>.
- [111] Francesca Mastrotto et al. “Polymer control of ligand display on gold nanoparticles for multimodal switchable cell targeting”. In: *Chemical Communications* 47.35 (2011), pp. 9846–9848. ISSN: 1359-7345. DOI: 10.1039/C1CC12654G. URL: <http://dx.doi.org/10.1039/C1CC12654G>.
- [112] Stefano Salmaso et al. “Cell up-take control of gold nanoparticles functionalized with a thermoresponsive polymer”. In: *Journal of Materials Chemistry* 19.11 (2009), pp. 1608–1615. ISSN: 0959-9428. DOI: 10.1039/B816603J. URL: <http://dx.doi.org/10.1039/B816603J>.
- [113] Samer R. Abulateefeh et al. “Facile synthesis of responsive nanoparticles with reversible, tunable and rapid thermal transitions from biocompatible constituents”. In: *Chemical Communications* 40 (2009), pp. 6068–6070. ISSN: 1359-7345. DOI: 10.1039/B911986H. URL: <http://dx.doi.org/10.1039/B911986H>.
- [114] Richard D. Powell et al. “A Covalent Fluorescent–Gold Immunoprobe: Simultaneous Detection of a Pre-mRNA Splicing Factor by Light and Electron Microscopy”. In: *Journal of Histochemistry & Cytochemistry* 45.7 (1997), pp. 947–956. DOI: 10.1177/002215549704500704. eprint: <https://doi.org/10.1177/002215549704500704>.

org/10.1177/002215549704500704. URL: <https://doi.org/10.1177/002215549704500704>.

- [115] Pascal Anger, Palash Bharadwaj, and Lukas Novotny. “Enhancement and Quenching of Single-Molecule Fluorescence”. In: *Phys. Rev. Lett.* 96 (11 2006), p. 113002. DOI: 10.1103/PhysRevLett.96.113002. URL: <https://link.aps.org/doi/10.1103/PhysRevLett.96.113002>.
- [116] G. Zorinians et al. “Background-Free 3D Nanometric Localization and Sub-nm Asymmetry Detection of Single Plasmonic Nanoparticles by Four-Wave Mixing Interferometry with Optical Vortices”. In: *Phys. Rev. X* (2017). Supplementary material.
- [117] Itsaso Cabezón et al. “Trafficking of Gold Nanoparticles Coated with the 8D3 Anti-Transferrin Receptor Antibody at the Mouse Blood–Brain Barrier”. In: *Molecular Pharmaceutics* 12.11 (2015), pp. 4137–4145. DOI: 10.1021/acs.molpharmaceut.5b00597. eprint: <http://dx.doi.org/10.1021/acs.molpharmaceut.5b00597>. URL: <http://dx.doi.org/10.1021/acs.molpharmaceut.5b00597>.
- [118] M. Dellinger and M. Gèze. “Detection of mitochondrial DNA in living animal cells with fluorescence microscopy”. In: *Journal of Microscopy* 204.3 (2001), pp. 196–202. ISSN: 1365-2818. DOI: 10.1046/j.1365-2818.2001.00954.x. URL: <http://dx.doi.org/10.1046/j.1365-2818.2001.00954.x>.
- [119] Andersson et al. “Autofluorescence of living cells”. In: *Journal of Microscopy* 191.1 (1998), pp. 1–7. ISSN: 1365-2818. DOI: 10.1046/j.1365-2818.1998.00347.x. URL: <http://dx.doi.org/10.1046/j.1365-2818.1998.00347.x>.
- [120] Carlo Manzo and Maria F Garcia-Parajo. “A review of progress in single particle tracking: from methods to biophysical insights”. In: *Reports on Progress in Physics* 78.12 (2015), p. 124601. URL: <http://stacks.iop.org/0034-4885/78/i=12/a=124601>.
- [121] Elliot L. Elson. “Fluorescence Correlation spectroscopy: Past, Present, Future”. In: *Biophysical Journal* 101.12 (2011), pp. 2855–2870. DOI: <http://dx.doi.org/10.1016/j.bpj.2011.11.012show>.
- [122] Kirsten Bacia, Sally A Kim, and Petra Schwille. “Fluorescence cross-correlation spectroscopy in living cells”. In: *Nature methods* 3.2 (2006), pp. 83–89.
- [123] Christian Eggeling et al. “Direct observation of the nanoscale dynamics of membrane lipids in a living cell”. In: *Nature* 457.7233 (2009), p. 1159.

- [124] Erik J. Sánchez, Lukas Novotny, and X. Sunney Xie. “Near-Field Fluorescence Microscopy Based on Two-Photon Excitation with Metal Tips”. In: *Phys. Rev. Lett.* 82 (20 1999), pp. 4014–4017. DOI: 10.1103/PhysRevLett.82.4014. URL: <https://link.aps.org/doi/10.1103/PhysRevLett.82.4014>.
- [125] P. J. Schuck et al. “Improving the Mismatch between Light and Nanoscale Objects with Gold Bowtie Nanoantennas”. In: *Phys. Rev. Lett.* 29 (2005). URL: http://foundry.lbl.gov/schuckgroup/page3/assets/29_Schuck05_BowtieTPPL_PRL94_017402.pdf.
- [126] WE Moerner and David P Fromm. “Methods of single-molecule fluorescence spectroscopy and microscopy”. In: *Review of Scientific instruments* 74.8 (2003), pp. 3597–3619.
- [127] Ivan H. El-Sayed, Xiaohua Huang, and Mostafa A. El-Sayed. “Surface Plasmon Resonance Scattering and Absorption of anti-EGFR Antibody Conjugated Gold Nanoparticles in Cancer Diagnostics: Applications in Oral Cancer”. In: *Nano Letters* 5.5 (2005), pp. 829–834. ISSN: 1530-6984. DOI: 10.1021/nl050074e. URL: <http://dx.doi.org/10.1021/nl050074e>.
- [128] Yan Gu et al. “Three-Dimensional Super-Localization and Tracking of Single Gold Nanoparticles in Cells”. In: *Analytical Chemistry* 84.9 (2012), pp. 4111–4117. ISSN: 0003-2700. DOI: 10.1021/ac300249d. URL: <http://dx.doi.org/10.1021/ac300249d>.
- [129] David Lasne et al. “Single Nanoparticle Photothermal Tracking (SNaPT) of 5-nm Gold Beads in Live Cells”. In: *Biophysical Journal* 91.12 (2006), pp. 4598–4604. ISSN: 0006-3495 1542-0086. DOI: 10.1529/biophysj.106.089771. URL: <http://www.ncbi.nlm.nih.gov/pmc/articles/PMC1779909/>.
- [130] CI McPhee et al. “Measuring the lamellarity of giant lipid vesicles with differential interference contrast microscopy”. In: *Biophysical journal* 105.6 (2013), pp. 1414–1420.
- [131] Ralf Metzler et al. “Anomalous diffusion models and their properties: non-stationarity, non-ergodicity, and ageing at the centenary of single particle tracking”. In: *Phys. Chem. Chem. Phys.* 16 (44 2014), pp. 24128–24164. DOI: 10.1039/C4CP03465A. URL: <http://dx.doi.org/10.1039/C4CP03465A>.
- [132] Li-Heng Cai, Sergey Panyukov, and Michael Rubinstein. “Hopping Diffusion of Nanoparticles in Polymer Matrices”. In: *Macromolecules* 48.3 (2015), pp. 847–862. DOI: 10.1021/ma501608x. eprint: <http://dx.doi.org/10.1021/ma501608x>. URL: <http://dx.doi.org/10.1021/ma501608x>.

- [133] Mengmeng Liu et al. “Real-time visualization of clustering and intracellular transport of gold nanoparticles by correlative imaging”. In: *Nature Communications* 8 (2017), p. 15646.
- [134] Elisa Panzarini et al. “Intracellular Transport of Silver and Gold Nanoparticles and Biological Responses: An Update”. In: *International Journal of Molecular Sciences* 19.5 (2018). ISSN: 1422-0067. DOI: 10.3390/ijms19051305. URL: <http://www.mdpi.com/1422-0067/19/5/1305>.
- [135] P. Borri et al. “Imaging and Tracking Single Plasmonic Nanoparticles in 3D Background-Free with Four-Wave Mixing Interferometry”. In: *2018 20th International Conference on Transparent Optical Networks (ICTON)*. 2018, pp. 1–4. DOI: 10.1109/ICTON.2018.8473874.
- [136] Xuan Xue et al. “Upper critical solution temperature thermo-responsive polymer brushes and a mechanism for controlled cell attachment”. In: *J. Mater. Chem. B* 5 (25 2017), pp. 4926–4933. DOI: 10.1039/C7TB00052A. URL: <http://dx.doi.org/10.1039/C7TB00052A>.
- [137] Henna Vihola et al. “Drug release characteristics of physically cross-linked thermosensitive poly(N-vinylcaprolactam) hydrogel particles”. In: *Journal of Pharmaceutical Sciences* 97.11 (2008), pp. 4783–4793. ISSN: 1520-6017. DOI: 10.1002/jps.21348. URL: <http://dx.doi.org/10.1002/jps.21348>.
- [138] Y. M. Zhou et al. “Deposition transfection technology using a DNA complex with a thermoresponsive cationic star polymer”. In: *J Control Release* 123.3 (2007), pp. 239–46. ISSN: 0168-3659. DOI: 10.1016/j.jconrel.2007.08.026.
- [139] R. A. Stile and K. E. Healy. “Thermo-responsive peptide-modified hydrogels for tissue regeneration”. In: *Biomacromolecules* 2.1 (2001), pp. 185–94. ISSN: 1525-7797 (Print) 1525-7797.
- [140] Fang Liu and Marek W. Urban. “Recent advances and challenges in designing stimuli-responsive polymers”. In: *Progress in Polymer Science* 35.1 (2010), pp. 3 –23. ISSN: 0079-6700. DOI: <https://doi.org/10.1016/j.progpolymsci.2009.10.002>. URL: <http://www.sciencedirect.com/science/article/pii/S0079670009001002>.
- [141] Dongxiang Li, Qiang He, and Junbai Li. “Smart core/shell nanocomposites: Intelligent polymers modified gold nanoparticles”. In: *Advances in Colloid and Interface Science* 149.1 (2009), pp. 28 –38. ISSN: 0001-8686. DOI: <https://doi.org/10.1016/j.cis.2008.12.007>. URL: <http://www.sciencedirect.com/science/article/pii/S0001868609000025>.

- [142] Stephan Link and Mostafa A. El-Sayed. “Size and Temperature Dependence of the Plasmon Absorption of Colloidal Gold Nanoparticles”. In: *The Journal of Physical Chemistry B* 103.21 (1999), pp. 4212–4217. DOI: 10.1021/jp984796o. eprint: <http://dx.doi.org/10.1021/jp984796o>. URL: <http://dx.doi.org/10.1021/jp984796o>.
- [143] Wolfgang Haiss et al. “Determination of Size and Concentration of Gold Nanoparticles from UVVis Spectra”. In: *Analytical Chemistry* 79.11 (2007), pp. 4215–4221. ISSN: 0003-2700. DOI: 10.1021/ac0702084. URL: <http://dx.doi.org/10.1021/ac0702084>.

PUBLICATIONS, ORAL AND POSTER PRESENTATIONS

Publications

Parts of this work is published in the following articles:

1. G.Zorinants, F.Masia, **N.Giannakopoulou**, W. Langbein and P.Borri, “Background-Free 3D Nanometric Localization and Sub-nm Asymmetry Detection of Single Plasmonic Nanoparticles by Four-Wave Mixing Interferometry with Optical Vortices”, *Phys. Rev. X* (2017), doi: 10.1103/PhysRevX.7.041022.
2. P. Borri, G. Zorinants, **N. Giannakopoulou**, F. Masia, I. Pope and W. Langbein, "Imaging and Tracking Single Plasmonic Nanoparticles in 3D Background-Free with Four-Wave Mixing Interferometry," 2018 20th International Conference on Transparent Optical Networks (ICTON), Bucharest, 2018, pp. 1-4. doi: 10.1109/ICTON.2018.8473874
3. **N. Giannakopoulou**, J.B. Williams, P. Moody, J.P. Magnusson, I. Pope, C. Alexander, A.T. Jones, W. Langbein, P. Watson, and P. Borri, “Shedding new light on gold nanoparticle-fluorophore conjugates for applications in cell biology with correlative four-wave-mixing microscopy” (to be submitted)

Oral and Poster presentations

Parts of this work were presented at the following conferences:

1. P. Borri, G. Zorinants, **N. Giannakopoulou**, F. Masia, I. Pope, P. Watson, and W. Langbein, “Imaging and tracking single plasmonic nanoparticles in 3D background-free with four-wave mixing interferometry ”, *Oral presentation*, SPIE BiOS, San Francisco, California United States. (5 February 2019)
2. **N. Giannakopoulou**, P.Moody, J.P.Magnusson, C.Alexander, A.T.Jones, P. Watson, W. Langbein and P. Borri, “Studying internalisation of bio-conjugated 20nm AuNPs in cancer cells via Correlative Four-wave mixing and confocal fluorescence microscopy”, *Poster presentation*, BioNano Photonics Symposium, Cardiff, United Kingdom (18-19 September 2017)

3. **N. Giannakopoulou**, P.Moody, J.P.Magnusson, C.Alexander, A.T.Jones, P. Watson, W. Langbein and P. Borri, "Cellular uptake of gold nanoparticles studied via correlative Four-Wave-Mixing Imaging and confocal fluorescence microscopy", *Oral presentation*, Focus on Microscopy, Bordeaux, France (9 - 12 April 2017)
4. G.Zoriniants, F.Masia, **N.Giannakopoulou**, W.Langbein, and P.Borri, "Scan-less background free 3D localisation of plasmonic nanoparticles using optical vortices", *Oral presentation*, Focus on Microscopy, Bordeaux, France (9 - 12 April 2017)
5. **N. Giannakopoulou**, P.Moody, J.P.Magnusson, C.Alexander, A.T.Jones, P. Watson and P. Borri, "Studying cellular uptake of protein-coated gold nanoparticles via Four-Wave mixing imaging and fluorescence Confocal microscopy", Photon, Leeds, United Kingdom (5 - 8 September 2016)
6. **N. Giannakopoulou**, P.Moody, J.P.Magnusson, C.Alexander, A.T.Jones, P. Watson and P. Borri, "Resonant Four-Wave Mixing microscopy of AuNPs in cells correlative with confocal fluorescence", *Poster presentation*, BioNano Photonics Symposium, Cardiff, United Kingdom (5 - 6 September 2015)

CURRICULUM VITAE

Naya was born in the coastal town of Patras in Greece in 1990. After achieving outstanding marks in the field of natural science in national exams she entered 2nd in the Department of Physics in University of Patras and was granted an Honorary Scholarship from the States Scholarships Foundation. She graduated in the top 6% of her class with a major in Solid State Physics where she also carried out her senior thesis in studying X-ray reflectivity of films versus temperature. In 2013 she received an MSc in Laser and Photonics with Distinction where she completed her MSc thesis (2011-2013) in the Laboratory of Nonlinear and Quantum Optics. There she studied the nonlinear optical properties of various materials such as BODIPY derivatives, graphene oxide and azobenzene based materials. As a postgraduate student she undertook an Erasmus Exchange Scholarship and joined S. Haacke's and J. Leonard's group in the Institute de Physique et Materiaux de Strasbourg (IPCMS). She was involved in implementing time-resolved fluorescence measurements in a droplet-based microfluidic chip towards high throughput screening.

In 2014 she joined the group of Biophotonics and Quantum optoelectronics in Cardiff University as a Marie Curie Fellow of the ITN FINON Network. She carried out research on correlative Four-Wave Mixing (FWM) and fluorescence microscopy as an imaging tool for investigation of a variety of functionalised AuNPs' uptake in cancer cells. As part of her training in FINON she also spent one month as a research intern at the MOSAIC group in the Institute of Fresnel comprising polarization resolved nonlinear microscopy of gold nanoparticles in cells.

Naya's research interests are focused on nonlinear microscopy, biophotonics applications and AuNP functionalisation techniques for drug delivery purposes.